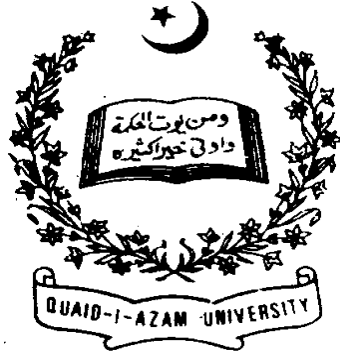# Flows of Nanofluids in Rotating Frame

By

Arsalan Aziz

Department of Mathematics
Quaid-i-Azam University
Islamabad, Pakistan
2020

Flows of Nanofluids in Rotating Frame

By

Arsalan Aziz

Supervised By

Prof. Dr. Tasawar Hayat

Department of Mathematics
Quaid-i-Azam University
Islamabad, Pakistan
2020

Flows of Nanofluids in Rotating Frame

By

Arsalan Aziz

A THESIS SUBMITTED IN THE PARTIAL FULFILLMENT OF THE REQUIREMENT FOR THE DEGREE OF

DOCTOR OF PHILOSOPHY

IN

MATHEMATICS

Supervised By

Prof. Dr. Tasawar Hayat

Department of Mathematics
Quaid-i-Azam University
Islamabad, Pakistan
2020

Author's Declaration

I, **Arsalan Aziz**, hereby state that my PhD thesis titled **Flows of Nanofluids in Rotating Frame** is my own work and has not been submitted previously by me for taking any degree from the Quaid-I-Azam University Islamabad, Pakistan or anywhere else in the country/world.

At any time if my statement is found to be incorrect even after my graduate the university has the right to withdraw my PhD degree.

Name of Student: **Arsalan Aziz**

Date: **08-Sep-2020**

Plagiarism Undertaking

I solemnly declare that research work presented in the thesis titled "**Flows of Nanofluids in Rotating Frame**" is solely my research work with no significant contribution from any other person. Small contribution/help wherever taken has been duly acknowledged and that complete thesis has been written by me.

I understand the zero tolerance policy of the HEC and **Quaid-i-Azam University** towards plagiarism. Therefore, I as an Author of the above titled thesis declare that no portion of my thesis has been plagiarized and any material used as reference is properly referred/cited.

I undertake that if I am found guilty of any formal plagiarism in the above titled thesis even afterward of PhD degree, the University reserves the rights to withdraw/revoke my PhD degree and that HEC and the University has the right to publish my name on the HEC/University Website on which names of students are placed who submitted plagiarized thesis.

Student/Author Signature

Name: **Arsalan Aziz**

Flows of Nanofluids in Rotating Frame

By

Arsalan Aziz

CERTIFICATE

A THESIS SUBMITTED IN THE PARTIAL FULFILLMENT OF THE
REQUIREMENTS FOR THE DEGREE OF THE

DOCTOR OF PHILOSOPHY IN MATHEMATICS

We accept this thesis as conforming to the required standard

1. _____
   Prof. Dr. Sohail Nadeem
   (Chairman)

2. _____
   Prof. Dr. Tasawar Hayat
   (Supervisor)

3. _____
   Prof. Dr. Saleem Asghar
   (External Examiner)

4. _____
   Dr. Nasir Ali
   (External Examiner)

Department of Mathematics, COMSATS
University, Park Road Chak Shahzad,
Islamabad.

Department of Mathematics & Statistics,
International Islamic University,
Sector H-10 Islamabad.

Department of Mathematics
Quaid-I-Azam University
Islamabad, Pakistan
2020

Certificate of Approval

This is to certify that the research work presented in this thesis entitled **Flows of Nanofluids in Rotating Frame** was conducted by **Mr. Arsalan Aziz** under the kind supervision of **Prof. Dr. Tasawar Hayat**. No part of this thesis has been submitted anywhere else for any other degree. This thesis is submitted to the Department of Mathematics, Quaid-i-Azam University, Islamabad in partial fulfillment of the requirements for the degree of Doctor of Philosophy in field of Mathematics from Department of Mathematics, Quaid-i-Azam University Islamabad, Pakistan.

Student Name: **Arsalan Aziz**   Signature: _____

External committee:

a) **External Examiner 1**:   Signature: _____
   Name: **Prof. Dr. Saleem Asghar**
   Designation: Professor
   Office Address: Department of Mathematics, COMSATS University, Park Road Chak Shahzad, Islamabad.

b) **External Examiner 2**:   Signature: _____
   Name: **Dr. Nasir Ali**
   Designation: Associate Professor
   Office Address: Department of Mathematics & Statistics, International Islamic University, Sector H-10 Islamabad.

c) **Internal Examiner**   Signature: _____
   Name: **Prof. Dr. Tasawar Hayat**
   Designation: Professor
   Office Address: Department of Mathematics, Quaid-i-Azam University, Islamabad.

   Supervisor Name: Signature: _____
   Prof. Dr. Tasawar Hayat

   Name of Dean/ HOD   Signature: _____

   Prof. Dr. Sohail Nadeem

Preface

Low thermal efficiency of working fluids is a main problem for several heat transport mechanisms in the engineering applications. Thus several researchers are engaged to develop an innovative way for improvement of thermal efficiency of working fluids. Many researchers have suggested different mechanisms to enhance the thermal efficiency of working fluids. Out of these, the insertion of nanoparticles in the working fluid known as nanomaterial is quite attractive. In addition the nanoliquid has vital role for cooling rate requirements with high thermal efficiency. Presently nanofluid dynamics has received remarkable attention of researchers due to its thermal transport in several areas. Nanofluids have applications in engine cooling, transformer cooling, microwave tubes, impingement jets, high-power lasers, renewable energies, lubrication, cooling of welding, thermal storage and solar water heating, heat exchangers, automotive, heating and tempering process, nuclear reactors, combustion and medicine and electronic chips cooling etc. High efficient oils and lubricants can be developed by the use of nanofluid. Magnetonanofluid dynamics is an attractive field of research in which physics of electrically conducting liquids like plasma and electrolytes or salt water and liquid metals has been analyzed. Mixture of working liquid and magnetic nanoparticles is termed as magnetonanofluid. Magnetonanofluids execute intrinsic role in MHD pumps and accelerators, some arterial diseases and hyperthermia, cancer tumor treatment, reduction of blood during surgeries and sink float separation etc.

Heat transfer in rotating flows is interesting area of research. It is because of their enormous applications in manufacturing of crystal growth, computer storage device, thermal power generation, gas turbine rotors etc. It is recognized fact that the nanofluids have pivotal role in the intensification of heat transfer. Thus we inspired to study nonlinear rotating flow problems in the

presence of nanoparticles. It is noted that two-dimensional nonlinear flow problems subject to fixed frame in literature are much studied when compared with the three-dimensional nonlinear flow problems in rotating frame. Keeping such facts in mind the present thesis is organized for three-dimensional nonlinear flow problems of nanofluids subject to rotating frame. The present thesis is designed as follows.

Chapter one has literature review of relevant previous published works and relations for conservations of mass, momentum, energy and concentration. Tensor forms for non-Newtonian fluids (Maxwell, Oldroyd-B and Jeffrey) are presented. Fundamental concept of optimal homotopy analysis method is included in this chapter.

Chapter two elaborates three dimensional rotating flow of nanoliquid induced by a stretchable sheet. Darcy-Forchheimer porous space is considered. Thermophoretic diffusion and random motion aspects are retained. Heat and mass flux conditions are implemented at stretchable surface. Convergent series solutions have been derived for velocities, temperature and concentration. Optimal homotopy analysis technique (OHAM) is implemented for the solutions development. Further surface drag coefficients and heat and mass transfer rates are presented via plots. The contents of this chapter are published in **International Journal of Numerical Methods for Heat and Fluid Flow 28 (2018) 2895-2915.**

Chapter three is the extension of chapter two for convective boundary conditions, heat generation/absorption, binary chemical reaction and activation energy. The nonlinear differential systems are numerically tackled by built-in shooting technique. Observations of this chapter are published in **Journal of Thermal Analysis and Calorimetry 136 (2019) 1769-1779.** Chapter four generalizes contents of chapter two for homogeneous-heterogeneous reactions. The results of this chapter are published in **Physica Scripta 94 (2019) 115708.**

Chapter five addresses the Darcy-Forchheimer three dimensional flow of nanoliquid induced by an exponentially stretchable surface in rotating frame. Thermophoretic diffusion and random motion aspects are retained. Prescribed surface heat and mass fluxes are implemented at stretchable surface. The governing systems are solved numerically by built-in shooting technique. Moreover temperature, concentration, surface drag coefficients and local Nusselt and Sherwood numbers are graphically illustrated. The data of this chapter is published in **Journal of Thermal Analysis and Calorimetry 136 (2019) 2087-2095.**

Chapter six illustrates the novel feature of entropy generation for three-dimensional rotating flow of nanoliquid with porous medium, velocity slip condition and activation energy. Thermophoretic dispersion and an irregular motion phenomena are also analyzed. Numerical solution is determined via efficient numerical method namely built-in shooting method. The obtained results for involved pertinent variables are examined through graphs for velocities, entropy generation, nano-concentration, temperature, skin-friction, local Nusselt number, Bejan number and local Sherwood numbers. Material of this chapter is submitted for publication in **International Communications in Heat and Mass Transfer.** Chapter seven extends the analysis of previous chapter for convective heat and mass conditions, magnetohydrodynamics (MHD), Joule heating and heat generation/absorption. Outcomes of this chapter are submitted for publication in **Journal of Non-Equilibrium Thermodynamics.**

Chapter eight examines the impact of activation energy on three dimensional rotating flow of Maxwell nanoliquid with nonlinear radiative heat flux. Thermophoretic dispersion and irregular motion are investigated. Convective conditions of heat and mass are employed at the boundary.

Shooting technique is implemented for solutions development. Influences of numerous emerging flow parameters on nano-concentration, temperature and mass and heat transfer rates are elaborated through graphs. The findings of this chapter have been submitted for publication in **Journal of the Brazilian Society of Mechanical Sciences and Engineering.**

Chapter nine describes three dimensional rotating flow of an Oldroyd-B nanoliquid due to linearly extendable surface. Brownian movement and thermophoresis are explored. Thermal convective condition and a condition associated with zero nanomaterials flux are implemented at the boundary. The nonlinear differential expressions are solved through optimal homotopy analysis method (OHAM). Moreover velocities, temperature, concentration and transfer of heat rate are discussed graphically. The observations of this chapter have been published in **Journal of the Brazilian Society of Mechanical Sciences and Engineering 41 (2019) 236.**

Chapter ten communicates three-dimensional rotating flow of Jeffrey nanoliquid in the presence of binary chemical reaction and activation energy. Impact of heat generation/absorption is also examined. Furthermore thermophoretic dispersion and irregular motion phenomena are investigated. Thermal convective and zero flux of nanoparticles conditions are accounted at the surface. Optimal homotopy analysis technique is utilized for solutions construction. Impacts of pertinent variables on velocities, nano-concentration, temperature and rate of heat transfer are interpreted through plots. The results of this research have been submitted for publication in **Journal of Thermal Analysis and Calorimetry.**

Contents

Chapter 1

Literature survey and some basic definitions

1.1 Introduction

Here survey of existing literature about nanoliquid, Darcy-Forchheimer porous medium, homogeneous-heterogeneous reactions, entropy generation, rotating flow, non-Newtonian fluids and binary chemical mechanism and activation energy is presented. Some relevant fundamental laws are included. Mathematical models of rate type non-Newtonian fluids are given. Further the fundamental concepts of optimal homotopy and built-in shooting techniques are also presented to develop the series and numerical solutions respectively.

1.2 Background

The addition of nanosized $(1 - 100 nm)$ metallic or any other particles in common fluids makes nanofluids. Nanofluids have the capability to elevate the heat transfer rate through increasing thermal efficiency of common liquids. For this purpose the nanoparticles are dispersed in common liquids to improve the efficiency of heat transport procedure. Nanofluids have numerous applications in nanoscale technology, like in air-conditioners, combustors, melt spinning, medicine manufacturing, microelectronics, computer processors and heat exchangers etc. Further in cancer therapy, wound treatment, hyperthermia and resonance imaging are more support-

able for the case of magneto nanofluids (MNFs). The fundamental investigations regarding increment of thermal characteristics due to nanoparticles suspension into ordinary liquids was performed by Choi [1]. Afterward Buongiorno [2] formulated the nanofluid model by considering the effects of Brownian dispersion and thermophoretic diffusion. Chamkha et al. [3] developed similarity solution for time-dependent flow from a moving sheet with porous space effect. Analytical methods for MHD nanofluids flow with heat and mass transport aspects are reported by Turkyilmazoglu [4]. Rashidi et al. [5] computed homotopic solutions of nanoliquid flow induced by a non-linearly stretching isothermal porous surface. Hayat et al. [6] examined hydromagnetic properties in 3D non-Newtonian nanoliquid flow. Raju et al. [7] constructed dual solutions for 3D nanomaterials hydromagnetic flow induced by a variable permeable accelerating sheet. Influence of hydromagnetic flow of nanoliquid by nonlinear convectively heated stretching sheet is elaborated by Hayat et al. [8]. Impact of MHD on 3D radiative flow of nanofluid over permeable linear actuating surface is deliberated by Nayak et al. [9]. Impact of combined Fourier's and Fick's expressions in Burgers nanoliquid flow is due to Hayat et al. [10]. Numerical treatment for magnetohydrodynamic three-dimensional radiative slip flow of nanofluids caused by a nonlinear accelerating sheet is elaborated by Mahanthesh et al. [11]. An optimal study for non-Darcian 3D flow of Carreau nanoliquid is done by Hayat et al. [12]. Sheikholeslami [13] investigated the influence of MHD in Al_2O_3-water nanoliquid transportation inside a porous space utilizing innovative computer technique. Heat and mass transfer features of 3D Maxwell nanoliquid by an exponentially moving sheet is scrutinized by Ali et al. [14]. Recently numerical study for thermoelectro-hydrodynamic convection in a horizontal dielectric nanoliquid layer using the power series method is done by Yadav et al. [15].

Chemical mechanisms are associated with abundant artificially responding structures like catalysis, consuming and biochemical frameworks. These mechanisms respond distinctively in the presence or nonappearance of an impetus. In homogeneous mechanism, both impetus and substances work in the comparable stage (strong, fluid or gas) while for heterogeneous response, both impetus and substances work in various stage. Examples in this direction may include polymer creation, hydro-metallurgical devices, assembling of earthenware production, biochemical structures, refining process, digestion of sustenance in body, blast of firecrackers and so forth. Boundary layer stream of thick fluid subject to heterogeneous-homogeneous responses is

examined by Merkin [16]. Chaudary and Merkin [17] researched heterogeneous-homogeneous responses with comparable diffusivities. Kameswaran et al. [18] contemplated the nanoliquid flow initiated due to a porous surface with heterogeneous-homogeneous responses. Imtiaz et al. [19] examined homogeneous-heterogeneous impacts in magnetohydrodynamic flow by an exponential sheet. Hayat et al. [20] inspected impact of Cattaneo-Christov fluxes in 3D second grade liquid flow with heterogeneous-homogeneous responses. An adjusted homogeneous-heterogeneous model for magnetohydrodynamic stagnation flow subject to dispersal and Ohmic heating is elaborated by Khan et al. [21]. An optimization analysis for non-Darcian 3D nanoliquid flow subject to convective effect and heterogeneous-homogeneous responses is reported by Hayat et al. [22]. Heterogeneous-homogeneous model for blended convection in gravity-driven film flow of nanofluids is due to Raees et al. [23]. Alzahrani [24] discussed non-Darcian 3D flow of carbon nanotubes with heterogeneous-homogeneous reactions. Numerical treatment of liquefying exchange of warmth and heterogeneous-homogeneous model in flow with carbon nanotubes is examined by Hayat et al. [25]. Recently Almutairi et al. [26] elaborated MHD flow of nanoliquid with heterogeneous-homogeneous reactions and second order slip velocity embedded in a porous space.

Rotating flow of nanoliquid over a stretching surface has become one of the most important topics. It is because to its versatile utilizations in industrial and engineering mechanisms. Such flows have a prominent role in rotor-systems, air-cleaning machines, thermal-power generation, medical equipment, electronic devices and computer storage devices etc. Initially Wang [27] explained stretching of surface in a rotating fluid. Local similar solution for swirling flow induced by an exponentially movable continuous sheet is developed by Javed et al. [28]. Nanoliquid swirling flow by an exponentially stretched permeable sheet is due to Rosali et al. [29]. Mustafa et al. [30] employed generalized Fourier's law for swirling Maxwell liquid flow. Maqsood et al. [31] analyzed the influence of heterogeneous-homogeneous mechanisms in viscoelastic fluid flow subject to rotating frame. Non-Darcian flow of nanoliquid in a rotating frame of reference is explained by Hayat et al. [32]. Jusoh et al. [33] examined ferroliquid flow by an exponentially squeezing/actuating surface in a rotating frame of reference. Numerical treatment for non-Darcian 3D swirling flow subject to activation energy and binary chemically reactive mechanism is discussed by Hayat et al. [34]. Characteristics of 3D swirling flow of hybrid carbon nanotube

past an exponentially deformed sheet are elaborated by Hayat et al. [35]. Aziz et al. [36] computed optimal solutions for 3D swirling flow of Oldroyd-B nanoliquid with convective effect. Impact of activation energy on rotating Maxwell nanomaterial flow is illustrated by Rashid et al. [37]. Numerical study for non-Darcian three-dimensional swirling flow of nanoliquid with prescribed fluxes is done by Hayat et al. [38]. Impacts of ion slip and Hall on hydromagnetic swirling flow of nanoliquid induced by an infinite vertical plate through permeable space are examined by Krishna and Chamkha [39].

Entropy production has prominent role in the study of heat transfer mechanisms. Entropy is a measure of the randomness or molecular disorder of a system. Entropy produces due to various causes of forces like magnetic forces, viscous dissipation, porous medium, thermal gradient, chemical and diffusion reactions. Entropy production refers to irreversible thermodynamical deterioration of thermal systems. The performance of engineering equipment is depreciated for higher rate of entropy production. Therefore, the minimization of entropy production is the prime perception to elevate the fertility of the thermal systems in industrial sector. Bejan [40, 41] was the first who initiated the concept of entropy optimization. Noghrehabadi et al. [42] analyzed entropy production for nanoliquid flow considering heat source/sink effect. Entropy production optimization for non-Newtonian nanoliquid flow with passive control of nanomaterials at the moving sheet is elucidated by Rehman et al. [43]. Bhatti et al. [44] examined entropy production optimisation for flow of non-Newtonian nanomaterial flow generated by a porous moving surface employing Successive Linearization method. Entropy production in second grade hydromagnetic radiative flow of nanoliquid induced by a convectively heated moving sheet with viscous dissipation is explained by Sithole et al. [45]. Alharbi et al. [46] presented entropy production in hydromagnetic Eyring-Powell liquid flow induced by a time-dependent oscillatory moving sheet with thermal radiation. Seyyedi et al. [47] constructed computational framework for free convective MHD flow in view of entropy generation. Rashid et al. [48] carried out analysis for ferromagnetic liquid flow with nonlinear radiation and entropy production. Irreversibility analysis for hydromagnetic flow of third order nanoliquid through a permeable space is examined by Hayat et al. [49].

Mass transfer analysis involving chemically reactive mechanism with activation energy has acheived much attention among the researchers. It is due to its various implications in met-

allurgy and chemical engineering processes. The occurrence of mass transfer is based on mass species concentration difference. First of all, the analysis of binary chemically reactive mechanism was investigated by Bestman [50]. Chemical reaction effect on binary mixture of convective liquid induced by a permeable surface is reported by Makinde and Olanrewaju [51]. Effectiveness of activation energy on hydrodynamic flow subject to viscous heating and heat source/sink is scrutinized by Maleque [52]. Consequences of binary chemically reactive mechanism on CNTs and buoyancy effects is presented by Lu et al. [53]. Zaib et al. [54] computed numerical solution of second law of thermodynamics for hydromagnetic Casson nanoliquid with binary chemically reactive mechanism. Anuradha and Sasikala [55] elaborated MHD impact on natural convective flow of nanoliquid caused by a porous shrinking sheet with activation energy and binary chemically reactive mechanism. Effect of activation energy in MHD Maxwell nanoliquid is explained by Ramesh et al. [56]. Impact of activation energy and binary chemically reactive mechanism on non-Darcian 3D rotating nanofluid flow due to Hayat et al. [57]. Reddy et al. [58] discussed impact of nonlinear radiative heat flux in 3D magneto slip flow of Eyring-Powell nanoliquid flow induced by a stretch up surface with binary chemically reactive mechanism. Consequences of magnetohydrodynamic flow of squeezed fluid with activation energy and binary chemically reactive mechanism are discussed by Ahmad et al. [59].

The study of fluid flow and heat transport process in a porous media has received much attention of the researchers. It is because of its ample utilizations in chemical, industrial and technological manufacturing goods such as contaminant pollution control, hydrocarbon exploitation, nuclear waste document, ground water pollution, water resource management, welding and casting in manufacturing mechanisms, permeable bearings, sustainable urban drainage, solar power systems and hazardous waste isolation etc. In 1856, Darcy developed a law which states that there exists a direct relation between volumetric flux of fluid through medium and pressure gradient. Basically Darcy expression [60] is used widely in the previous problems associated to modelling, simulation and study of flow saturating permeable space. Features of weaker porosity and smaller velocity are elaborated through only traditional Darcy's model. Both boundary and inertia impacts are ignored by this model. Non-Darcian porous space is modern form of classical Darcy's model accomodates both boundary and inertia impacts. Hence Forchheimer [61] analyzed inertia through the inclusion of a square velocity term in momentum

expression. Muskat [62] titled such term as Forchheimer factor. Many researchers have done incredible works on flow in non-Darcian porous space (see [63 − 80]).

The investigations related to non-Newtonian materials have acquired immense importance due to their widespread utilizations in industrial and engineering mechanisms. Those fluids which do not follow the traditional Newton's viscosity relation are non-Newtonian fluids. Examples of this kind of fluid may contain custard, blood, condensed milk, tomato paste, printing ink, specific grease, sugar solution, cosmetic products, polymer melts and many more. Non-Newtonain liquids are classified into three types i.e. (a) differential type (b) integral type and (c) rate type. Only rate type non-Newtonian liquids have been discussed in this thesis. These rate type non-Newtonian models exhibit the main features of stress retardation and relaxation. Maxwell liquid model [81, 82] is the most simplest category of rate type non-Newtonian liquid. This model explores remarkable properties of relaxation time. Effect of retardation time cannot be predicted by Maxwell model. In order to compensate this discrepensy offered by Maxwell relation, the Oldroyd-B model [83, 84] is proposed. The features of both retardation and relaxation times are generally not exhibited by most of the organic and polymeric structures. An another adopted model (Jeffrey liquid [85, 86]) falls in the category of such liquids which has time derivative instead of convective derivative. This model shows the features of relaxation to retardation time ratio and retardation time.

1.3   Basic relations

1.3.1   Conservation of mass

Mathematical form of continuity expression for compressible liquid is

$$\boldsymbol{\nabla} \cdot \left(\rho_{\hat{f}} \bar{\mathbf{V}}^{\star\star} \right) + \frac{\partial \rho_{\hat{f}}}{\partial t} = 0, \tag{1.1}$$

where velocity, density and time are symbolized by $\bar{\mathbf{V}}^{\star\star}$, $\rho_{\hat{f}}$ and t respectively. For incompressible liquid ($\rho_{\hat{f}} = $ constant) and the above relation (1.1) reduces to

$$\boldsymbol{\nabla} \cdot \bar{\mathbf{V}}^{\star\star} = 0. \tag{1.2}$$

1.3.2 Conservation of momentum

Equation of motion for non-rotating system is

$$\rho_{\hat{f}} \frac{d\bar{\mathbf{V}}^{\star\star}}{dt} = \boldsymbol{\nabla} \cdot \boldsymbol{\tau} + \rho_{\hat{f}} \bar{\mathbf{b}}^{\star\star}, \tag{1.3}$$

where $\rho_{\hat{f}}$ depicts density, d/dt material time derivative, $\boldsymbol{\tau} = -p\bar{\mathbf{I}}^{\star\star} + \breve{\mathbf{S}}^{\star\star}$ Cauchy stress tensor, p pressure, $\breve{\mathbf{S}}^{\star\star}$ extra stress tensor, $\bar{\mathbf{I}}^{\star\star}$ identity tensor and $\bar{\mathbf{b}}^{\star\star}$ body force vector. Equation of motion in rotating frame can be written as

$$\rho_{\hat{f}} \left(\frac{d\bar{\mathbf{V}}^{\star\star}}{dt} + 2(\boldsymbol{\omega} \times \bar{\mathbf{V}}^{\star\star}) + \boldsymbol{\omega} \times (\boldsymbol{\omega} \times \mathbf{r}) \right) = \boldsymbol{\nabla} \cdot \boldsymbol{\tau} + \rho_{\hat{f}} \bar{\mathbf{b}}^{\star\star}, \tag{1.4}$$

in which $\boldsymbol{\omega}$ represents the angular velocity, $\boldsymbol{\omega} \times (\boldsymbol{\omega} \times \mathbf{r})$ and $2(\boldsymbol{\omega} \times \bar{\mathbf{V}}^{\star\star})$ the centrifugal and Coriolis forces respectively.

1.3.3 Conservation of energy

Nanoliquid energy expression is

$$(\rho c)_{\hat{f}} \frac{d\tilde{T}}{dt} = I_p \boldsymbol{\nabla} \cdot \tilde{\mathbf{j}}_p - \boldsymbol{\nabla} \cdot \hat{\mathbf{q}}. \tag{1.5}$$

In above relation $(\rho c)_{\hat{f}} \frac{d\tilde{T}}{dt}$, I_p, $\hat{\mathbf{q}}$, $\tilde{\mathbf{j}}_p$ denote internal energy, nanoparticles specific enthalpy, heat and mass fluxes for nanoparticles diffusion respectively. The expressions of $\tilde{\mathbf{j}}_p$ and $\hat{\mathbf{q}}$ are

$$\tilde{\mathbf{j}}_p = -\rho_p D_B \boldsymbol{\nabla} \tilde{C} - \rho_p D_T \frac{\boldsymbol{\nabla} \tilde{T}}{\tilde{T}_\infty}, \tag{1.6}$$

$$\hat{\mathbf{q}} = \tilde{\mathbf{j}}_p I_p - k \boldsymbol{\nabla} \tilde{T}. \tag{1.7}$$

By employing (1.6) and (1.7), the energy expression for nanoliquids satisfies

$$(\rho c)_{\hat{f}} \frac{d\tilde{T}}{dt} = k \boldsymbol{\nabla}^2 \tilde{T} + (\rho c)_p \left(D_T \frac{\boldsymbol{\nabla} \tilde{T}.\boldsymbol{\nabla} \tilde{T}}{\tilde{T}_\infty} + D_B \boldsymbol{\nabla} \tilde{C}.\boldsymbol{\nabla} \tilde{T} \right), \tag{1.8}$$

1.3.4 Conservation of concentration

Concentration relation for nanoliquid can be expressed as

$$\bar{\mathbf{V}}^{\star\star}.\boldsymbol{\nabla}\tilde{C} + \frac{\partial \tilde{C}}{\partial t} = -\frac{1}{\rho_p}\boldsymbol{\nabla}.\tilde{\mathbf{j}}_p. \tag{1.9}$$

After implementing Eq. (1.6), one obtains

$$\bar{\mathbf{V}}^{\star\star}.\boldsymbol{\nabla}\tilde{C} + \frac{\partial \tilde{C}}{\partial t} = D_T\frac{\boldsymbol{\nabla}^2\tilde{T}}{\tilde{T}_\infty} + D_B\boldsymbol{\nabla}^2\tilde{C}. \tag{1.10}$$

1.4 Non-Newtonian liquids

1.4.1 Maxwell liquid model

Extra stress tensor ($\check{\mathbf{S}}^{\star\star}$) is

$$\left(1 + \lambda_1^{\star\star}\frac{D}{Dt}\right)\check{\mathbf{S}}^{\star\star} = \lambda_1^{\star\star}\frac{D\check{\mathbf{S}}^{\star\star}}{Dt} + \check{\mathbf{S}}^{\star\star} = \mu\bar{\mathbf{A}}_1^{\star\star}, \tag{1.11}$$

where $\lambda_1^{\star\star}$, D/Dt, μ and $\bar{\mathbf{A}}_1^{\star\star}$ represent relaxation time, covariant differentiation, absolute viscosity and first Rivlin-Erickson tensor respectively. Here $\bar{\mathbf{A}}_1^{\star\star}$ can be written as

$$\bar{\mathbf{A}}_1^{\star\star} = \left(\mathrm{grad}\,\bar{\mathbf{V}}^{\star\star}\right)^{\bar{T}} + (\mathrm{grad}\,\bar{\mathbf{V}}^{\star\star}), \tag{1.12}$$

in which $\bar{T}$ expresses transpose of matrix and

$$(\mathrm{grad}\,\bar{\mathbf{V}}^{\star\star}) = \begin{bmatrix} \frac{\partial u}{\partial x} & \frac{\partial u}{\partial y} & \frac{\partial u}{\partial z} \\ \frac{\partial v}{\partial x} & \frac{\partial v}{\partial y} & \frac{\partial v}{\partial z} \\ \frac{\partial w}{\partial x} & \frac{\partial w}{\partial y} & \frac{\partial w}{\partial z} \end{bmatrix}, \quad \left(\mathrm{grad}\,\bar{\mathbf{V}}^{\star\star}\right)^{\bar{T}} = \begin{bmatrix} \frac{\partial u}{\partial x} & \frac{\partial v}{\partial x} & \frac{\partial w}{\partial x} \\ \frac{\partial u}{\partial y} & \frac{\partial v}{\partial y} & \frac{\partial w}{\partial y} \\ \frac{\partial u}{\partial z} & \frac{\partial v}{\partial z} & \frac{\partial w}{\partial z} \end{bmatrix}, \tag{1.13}$$

1.4.2 Oldroyd-B liquid model

Extra stress tensor ($\check{\mathbf{S}}^{\star\star}$) for this model can be defined as

$$\left(1 + \lambda_1^{\star\star}\frac{D}{Dt}\right)\check{\mathbf{S}}^{\star\star} = \lambda_1^{\star\star}\frac{D\check{\mathbf{S}}^{\star\star}}{Dt} + \check{\mathbf{S}}^{\star\star} = \mu\left(1 + \lambda_2^{\star\star}\frac{D}{Dt}\right)\bar{\mathbf{A}}_1^{\star\star}, \tag{1.14}$$

in which $(\lambda_2^{**}, \lambda_1^{**})$ signify (retardation, relaxation) times respectively.

1.4.3 Jeffrey liquid model

Extra stress tensor $(\check{\mathbf{S}}^\star)$ for Jeffrey liquid is

$$\check{\mathbf{S}}^{**} = \frac{\mu}{1 + \lambda_1^{**}} \left(\lambda_2^{**} \frac{d\bar{\mathbf{A}}_1^{**}}{dt} + \bar{\mathbf{A}}_1^{**} \right), \tag{1.15}$$

where $(\lambda_2^{**}, \lambda_1^{**})$ are (retardation, relaxation to retardation ratio) times respectively.

1.5 Solution methodologies

1.5.1 Optimal homotopic technique (OHAM)

The optimal homotopic scheme (OHAM) [87−93] is employed to develope approximate solutions of highly nonlinear partial/ordinary system. The convergence of approximate series solution is controlled and also adjusted by (OHAM) scheme. In order to perceive the preliminary concept of (OHAM), we assume a strong nonlinear differential expression

$$\check{\mathcal{N}}\left[u\left(\xi\right)\right] = 0, \tag{1.16}$$

in which $\check{\mathcal{N}}$ exhibits the non-linear operator and $u\left(\xi\right)$ the unknown function of independent variable ξ.

Deformation at zeroth-order

The expression of zeroth-order deformation is

$$\left(1 - \check{\mathsf{P}}^{\star\star\star}\right) \tilde{\mathcal{L}} \left[\hat{u}\left(\xi; \check{\mathsf{P}}^{\star\star\star}\right) - \hat{u}_0\left(\xi\right) \right] = \check{\mathsf{P}}^{\star\star\star} \bar{\hbar} \check{\mathcal{N}} \left[\hat{u}\left(\xi; \check{\mathsf{P}}^{\star\star\star}\right) \right], \tag{1.17}$$

in which $\hat{u}_0\left(\xi\right)$, $\tilde{\mathcal{L}}$, $\check{\mathsf{P}}^{\star\star\star} \in [0, 1]$, $\bar{\hbar}$ and $\hat{u}\left(\xi; \check{\mathsf{P}}^{\star\star\star}\right)$ denote the initial guess, auxiliary linear operator, embedding parameter, nonzero auxiliary parameter and unknown function of ξ and $\check{\mathsf{P}}^{\star\star\star}$ respectively.

$\mathring{m}^\star$th-order deformation

For $\mathring{m}^\star$th-order deformation, we differentiate Exp. (1.17) w.r.t $\check{\mathrm{P}}^{\star\star\star}$ then divide by $\mathring{m}^\star!$ and finally putting $\check{\mathrm{P}}^{\star\star\star} = 0$, one obtains

$$\tilde{\mathcal{L}}\left[u_{\mathring{m}^\star}\left(\xi\right) - \chi_{\mathring{m}^\star} u_{\mathring{m}^\star - 1}\left(\xi\right)\right] = \bar{\hbar}\mathcal{R}_{\mathring{m}^\star}\left(\xi\right), \tag{1.18}$$

$$\mathcal{R}_{\mathring{m}^\star}\left(\xi\right) = \frac{1}{(\mathring{m}^\star - 1)!}\frac{\partial^{\mathring{m}^\star}\check{\mathcal{N}}\left[\hat{u}\left(\xi; \check{\mathrm{P}}^{\star\star\star}\right)\right]}{\partial\check{\mathrm{P}}^{\star\star\star}}\Bigg|_{\check{\mathrm{P}}^{\star\star\star}=0}, \tag{1.19}$$

where

$$\chi_{\mathring{m}^\star} = \begin{cases} 0, & \mathring{m}^\star \leq 1 \\ 1, & \mathring{m}^\star > 1 \end{cases}. \tag{1.20}$$

Inserting $\check{\mathrm{P}}^{\star\star\star}$ and $\check{\mathrm{P}}^{\star\star\star} = 1$, one has

$$\hat{u}\left(\xi; 0\right) = \hat{u}_0\left(\xi\right) \quad \text{and} \quad \hat{u}\left(\xi; 1\right) = u\left(\xi\right). \tag{1.21}$$

Applying the concept of Taylor series, we obtain

$$\hat{u}\left(\xi; \check{\mathrm{P}}^{\star\star\star}\right) = u_0\left(\xi\right) + \sum_{\mathring{m}^\star=1}^{\infty} u_{\mathring{m}^\star}\left(\xi\right)\check{\mathrm{P}}^{\star\star\star\mathring{m}^\star}, \quad u_{\mathring{m}^\star}\left(\xi\right) = \frac{1}{\mathring{m}^\star!}\frac{\partial^{\mathring{m}^\star}\hat{u}\left(\xi; \check{\mathrm{P}}^{\star\star\star}\right)}{\partial\check{\mathrm{P}}^{\star\star\star\mathring{m}^\star}}\Bigg|_{\check{\mathrm{P}}^{\star\star\star}=0}. \tag{1.22}$$

For $\check{\mathrm{P}}^{\star\star\star} = 1$ we get

$$u\left(\xi\right) = u_0\left(\xi\right) + \sum_{\mathring{m}^\star=1}^{\infty} u_{\mathring{m}^\star}\left(\xi\right). \tag{1.23}$$

Optimal convergence control parameter

Both convergence region and homotopic solution rate are regulated by non-zero auxiliary variable ($\hbar$). To acquire optimal value of convergence control variable ($\hbar$), we have utilized the concept of minimization by considering the average squared residual errors as recommended by Liao [87].

$$\tilde{\varepsilon}_{\mathring{m}^\star} = \frac{1}{k+1}\sum_{j=0}^{k}\left[\check{\mathcal{N}}\left(\sum_{\mathring{i}=0}^{\mathring{m}^\star} u_{\mathring{m}^\star}\left(\xi\right)\right)_{\zeta=j\delta\xi}\right]^2, \tag{1.24}$$

where total squared residual error is symbolized by $\tilde{\varepsilon}_{\mathring{m}^\star}$.

13

1.5.2　Numerical approach

The numerical solutions of differential equations are presented in chapters 3 and 5 to 8. The solutions have been constructed in MATHEMATICA by using built-in shooting technique [93 − 100]. The differential systems can be directly solved by this technique.

Chapter 2

Darcy-Forchheimer flow of nanofluid subject to rotating frame

This chapter focuses on non-Darcian three-dimensional rotating flow of nanoliquid with constant thermal and mass fluxes. Buongiorno model is employed for thermophoresis and Brownian diffusion. Ordinary differential systems are constructed by appropriate transformations. Resulting mathematical systems are computed by optimal homotopic procedure. The velocity components, temperature and nano-concentration are analyzed graphically. In addition surface drag coefficients and local Nusselt and Sherwood numbers are sketched and analyzed. Our observations indicate that an elevation in rotation parameter and Forchheimer number leads to weaker velocity fields while an inverse trend is noticed for temperature and nano-concentration.

2.1 Statement

Here we intend to study three-dimensional rotating flow of nanoliquid due to a linearly stretchable surface. Darcy-Forchheimer porous medium is considered. Heat and mass flux conditions are imposed. Impacts of thermophoresis and random motion are also studied. Cartesian framework is employed. Let $U_w(x) = ax$ be surface moving velocity. Furthermore fluid rotates along

$z-$direction with uniform angular velocity ω (see Fig. 2.1). Resulting relations satisfy
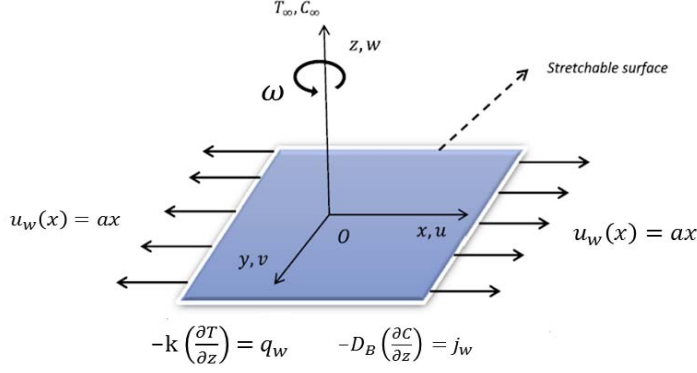
Fig. 2.1 : Flow configuration.

$$\frac{\partial u}{\partial x} + \frac{\partial v}{\partial y} + \frac{\partial w}{\partial z} = 0, \qquad (2.1)$$

$$u\frac{\partial u}{\partial x} + v\frac{\partial u}{\partial y} + w\frac{\partial u}{\partial z} - 2\omega v = \nu\frac{\partial^2 u}{\partial z^2} - \frac{\nu}{k^\star}u - Fu^2, \qquad (2.2)$$

$$u\frac{\partial v}{\partial x} + v\frac{\partial v}{\partial y} + w\frac{\partial v}{\partial z} + 2\omega u = \nu\frac{\partial^2 v}{\partial z^2} - \frac{\nu}{k^\star}v - Fv^2, \qquad (2.3)$$

$$u\frac{\partial T}{\partial x} + v\frac{\partial T}{\partial y} + w\frac{\partial T}{\partial z} = \alpha^\star\frac{\partial^2 T}{\partial z^2} + \frac{(\rho c)_p}{(\rho c)_f}\left(\frac{D_T}{T_\infty}\left(\frac{\partial T}{\partial z}\right)^2 + D_B\left(\frac{\partial T}{\partial z}\frac{\partial C}{\partial z}\right)\right), \qquad (2.4)$$

$$u\frac{\partial C}{\partial x} + v\frac{\partial C}{\partial y} + w\frac{\partial C}{\partial z} = \frac{D_T}{T_\infty}\left(\frac{\partial^2 T}{\partial z^2}\right) + D_B\left(\frac{\partial^2 C}{\partial z^2}\right), \qquad (2.5)$$

with

$$u = U_w(x) = ax, \ v = 0, \ w = 0, \ -k\left(\frac{\partial T}{\partial z}\right) = q_w, \ -D_B\left(\frac{\partial C}{\partial z}\right) = j_w \text{ at } z = 0, \qquad (2.6)$$

$$u \to 0, \quad v \to 0, \quad T \to T_\infty, \quad C \to C_\infty \quad \text{when } z \to \infty. \qquad (2.7)$$

16

Note that u, v and w symbolize velocity components in $x-$, $y-$ and $z-$directions while $\nu \left(= \mu/\rho_f\right)$, μ and ρ_f denote kinematic viscosity, absolute viscosity and density of base liquid, $k^\star$ for permeability of porous space, $F = C_b/xk^{\star 1/2}$ for inertia coefficient of porous space, C_b for drag coefficient, $\alpha^\star = k/(\rho c)_f$, k, $(\rho c)_f$ and $(\rho c)_p$ for thermal diffusion, thermal efficiency, thermal potential of liquid and effective thermal potential of nanomaterials, T for temperature, D_B the Brownian diffusivity, C for nano-concentration, D_T for thermophoretic dispersion coefficient and T_∞ and C_∞ the ambient fluid temperature and nano-concentration respectively. Selecting

$$\left.\begin{array}{c} u = axf'(\zeta), \ v = axg(\zeta), \ w = -(a\nu)^{1/2}f(\zeta), \ \zeta = \left(\frac{a}{\nu}\right)^{1/2} z, \\ T = T_\infty + \sqrt{\frac{\nu}{a}}\frac{q_w}{k}\theta(\zeta), \ C = C_\infty + \sqrt{\frac{\nu}{a}}\frac{j_w}{D_B}\phi(\zeta), \end{array}\right\} \tag{2.8}$$

equation (2.1) is justified while Eqs. (2.2) $-$ (2.7) become

$$f''' + ff'' - f'^2 + 2\Omega g - \lambda f' - Frf'^2 = 0, \tag{2.9}$$

$$g''' + fg' - f'g - 2\Omega f' - \lambda g - Frg^2 = 0, \tag{2.10}$$

$$\theta'' + \Pr\left(f\theta' + N_b\theta'\phi' + N_t\theta'^2\right) = 0, \tag{2.11}$$

$$\phi'' + Scf\phi' + \frac{N_t}{N_b}\theta'' = 0, \tag{2.12}$$

$$f(0) = g(0) = 0, \ f'(0) = 1, \ \theta'(0) = -1, \ \phi'(0) = -1, \tag{2.13}$$

$$f'(\infty) \to 0, \ g(\infty) \to 0, \ \theta(\infty) \to 0, \ \phi(\infty) \to 0. \tag{2.14}$$

Here rotation parameter, Prandtl number, porosity parameter, thermophoresis parameter, Forchheimer number, Schmidt number and Brownian motion parameter are symbolized by Ω, Pr, λ, N_t, Fr, Sc and N_b respectively. Nondimensional forms of these parameters are given below:

$$\left.\begin{array}{c} \lambda = \frac{\nu}{k^\star a}, \ Fr = \frac{C_b}{k^{\star 1/2}}, \ \Omega = \frac{\omega}{a}, \ \Pr = \frac{\nu}{\alpha^\star}, \ Sc = \frac{\nu}{D_B}, \\ Nb = \frac{(\rho c)_p D_B(C_w - C_\infty)}{(\rho c)_f \nu}, \ Nt = \frac{(\rho c)_p D_T(T_w - T_\infty)}{(\rho c)_f \nu T_\infty}. \end{array}\right\} \tag{2.15}$$

Dimensionless coefficients of skin friction and local Nusselt and Sherwood numbers are

$$
\left.
\begin{aligned}
(\mathrm{Re}_x)^{-1/2} C_f &= f''(0), \\
(\mathrm{Re}_x)^{-1/2} C_g &= g'(0), \\
(\mathrm{Re}_x)^{-1/2} Nu_x &= \tfrac{1}{\theta(0)}, \\
(\mathrm{Re}_x)^{-1/2} Sh_x &= \tfrac{1}{\phi(0)}.
\end{aligned}
\right\}
$$

Here $(\mathrm{Re}_x = U_w x/\nu)$ represents local Reynolds number.

2.2   Initial guesses

The suitable initial guesses and operators are

$$
f_0(\zeta) = 1 - e^{-\zeta}, \quad g_0(\zeta) = 0, \quad \theta_0(\zeta) = e^{-\zeta}, \quad \phi_0(\zeta) = e^{-\zeta}, \tag{2.17}
$$

$$
\ddot{\mathcal{L}}_f^\star = \frac{d^3 f}{d\zeta^3} - \frac{df}{d\zeta}, \quad \ddot{\mathcal{L}}_g^\star = \frac{d^2 g}{d\zeta^2} - g, \quad \ddot{\mathcal{L}}_\theta^\star = \frac{d^2 \theta}{d\zeta^2} - \theta, \quad \ddot{\mathcal{L}}_\phi^\star = \frac{d^2 \phi}{d\zeta^2} - \phi. \tag{2.18}
$$

Operators in above expressions have properties

$$
\left.
\begin{aligned}
\ddot{\mathcal{L}}_f^\star \left[\tilde{B}_1^{\star\star\star} + \tilde{B}_2^{\star\star\star} e^\zeta + \tilde{B}_3^{\star\star\star} e^{-\zeta} \right] &= 0, \quad \ddot{\mathcal{L}}_g^\star \left[\tilde{B}_4^{\star\star\star} e^\zeta + \tilde{B}_5^{\star\star\star} e^{-\zeta} \right] = 0, \\
\ddot{\mathcal{L}}_\theta^\star \left[\tilde{B}_6^{\star\star\star} e^\zeta + \tilde{B}_7^{\star\star\star} e^{-\zeta} \right] &= 0, \quad \ddot{\mathcal{L}}_\phi^\star \left[\tilde{B}_8^{\star\star\star} e^\zeta + \tilde{B}_9^{\star\star\star} e^{-\zeta} \right] = 0,
\end{aligned}
\right\} \tag{2.19}
$$

in which $\tilde{B}_1^{\star\star\star}$ $(j = 1 - 9)$ indicate arbitrary constants.

2.3   OHAM solutions

The non-zero auxiliary parameters $\hbar_f$, $\hbar_g$, $\hbar_\theta$ and $\hbar_\phi$ in solutions regulate the convergence portion and also rate of homotopic solutions. For optimal data of $\hbar_f$, $\hbar_g$, $\hbar_\theta$ and $\hbar_\phi$, concept of minimization via average squared residual errors suggested by Liao [87] is employed as follows:

$$
\varepsilon_{\mathring{m}^\star}^f = \frac{1}{\check{k}^\star + 1} \sum_{j=0}^{\check{k}^\star} \left[\mathcal{N}_f \left(\sum_{\mathring{i}=0}^{\mathring{m}^\star} \tilde{f}(\zeta), \sum_{\mathring{i}=0}^{\mathring{m}^\star} \tilde{g}(\zeta) \right)_{\zeta = j\delta\zeta} \right]^2, \tag{2.20}
$$

$$\varepsilon^{g}_{\mathring{m}^{\star}} = \frac{1}{\breve{k}^{\star}+1} \sum_{j=0}^{\breve{k}^{\star}} \left[\mathcal{N}_g \left(\sum_{\mathring{i}=0}^{\mathring{m}^{\star}} \tilde{f}\left(\zeta\right), \sum_{\mathring{i}=0}^{\mathring{m}^{\star}} \tilde{g}\left(\zeta\right) \right)_{\zeta=j\delta\zeta} \right]^2, \tag{2.21}$$

$$\varepsilon^{\theta}_{\mathring{m}^{\star}} = \frac{1}{\breve{k}^{\star}+1} \sum_{j=0}^{\breve{k}^{\star}} \left[\mathcal{N}_\theta \left(\sum_{\mathring{i}=0}^{\mathring{m}^{\star}} \tilde{f}\left(\zeta\right), \sum_{\mathring{i}=0}^{\mathring{m}^{\star}} \tilde{g}\left(\zeta\right), \sum_{\mathring{i}=0}^{\mathring{m}^{\star}} \tilde{\theta}\left(\zeta\right), \sum_{\mathring{i}=0}^{\mathring{m}^{\star}} \tilde{\phi}\left(\zeta\right) \right)_{\zeta=j\delta\zeta} \right]^2, \tag{2.22}$$

$$\varepsilon^{\phi}_{\mathring{m}^{\star}} = \frac{1}{\breve{k}^{\star}+1} \sum_{j=0}^{\breve{k}^{\star}} \left[\mathcal{N}_\phi \left(\sum_{\mathring{i}=0}^{\mathring{m}^{\star}} \tilde{f}\left(\zeta\right), \sum_{\mathring{i}=0}^{\mathring{m}^{\star}} \tilde{g}\left(\zeta\right), \sum_{\mathring{i}=0}^{\mathring{m}^{\star}} \tilde{\theta}\left(\zeta\right), \sum_{\mathring{i}=0}^{\mathring{m}^{\star}} \tilde{\phi}\left(\zeta\right) \right)_{\zeta=j\delta\zeta} \right]^2. \tag{2.23}$$

By Liao [87] :

$$\varepsilon^{t}_{\mathring{m}^{\star}} = \varepsilon^{f}_{\mathring{m}^{\star}} + \varepsilon^{g}_{\mathring{m}^{\star}} + \varepsilon^{\theta}_{\mathring{m}^{\star}} + \varepsilon^{\phi}_{\mathring{m}^{\star}}. \tag{2.24}$$

Here $\varepsilon^{t}_{\mathring{m}^{\star}}$ expresses total squared residual error, $\breve{k}^{\star} = 20$ and $\delta\zeta = 0.5$. At 2nd order of approximations, the optimal values of convergence control variables are $\hbar_f = -0.654264$, $\hbar_g = -1.34791$, $\hbar_\theta = -1.5552$ and $\hbar_\phi = -1.27278$ and total averaged squared residual error is $\varepsilon^{t}_{\mathring{m}^{\star}} = 2.10 \times 10^{-2}$. Figure 2.2 represents the plots of total residual error. Table 2.1 shows individual average squared residual errors. Clearly averaged squared residual errors exhibit decaying trend for higher order deformations.
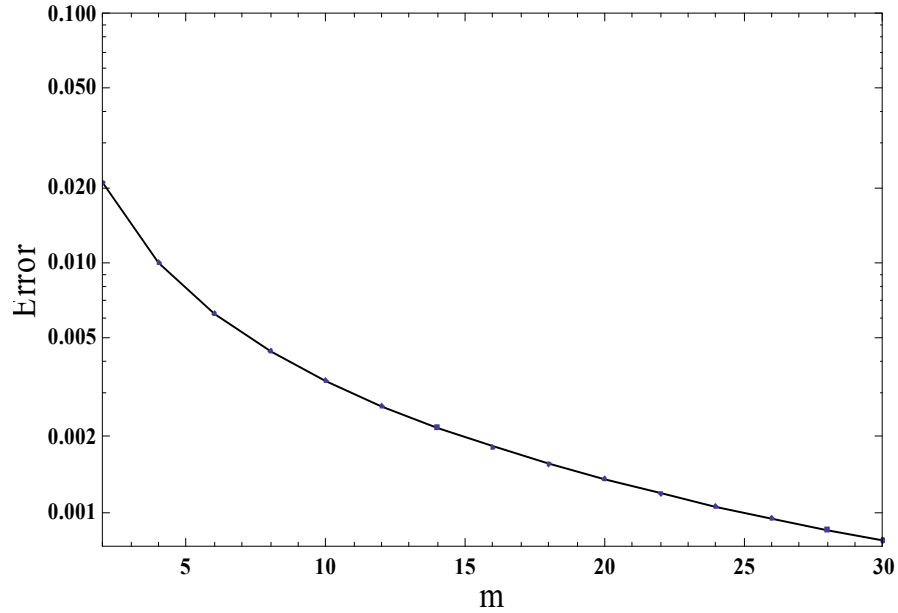
Figure 2.2 : Total residual error sketch.

Table 2.1. Optimal convergence control variables and total average squared residual errors.

$\mathring{m}^\star$	$\varepsilon^f_{\mathring{m}^\star}$	$\varepsilon^g_{\mathring{m}^\star}$	$\varepsilon^\theta_{\mathring{m}^\star}$	$\varepsilon^\phi_{\mathring{m}^\star}$
2	5.80×10^{-4}	3.20×10^{-4}	1.12×10^{-2}	8.91×10^{-3}
6	1.09×10^{-4}	4.04×10^{-5}	3.26×10^{-3}	2.84×10^{-3}
10	5.04×10^{-5}	1.34×10^{-5}	1.58×10^{-3}	1.72×10^{-3}
16	2.46×10^{-5}	4.32×10^{-6}	7.40×10^{-4}	1.06×10^{-3}
20	1.74×10^{-5}	2.42×10^{-6}	5.04×10^{-4}	8.31×10^{-4}
24	1.30×10^{-5}	1.46×10^{-6}	3.65×10^{-4}	6.76×10^{-4}
30	9.01×10^{-6}	7.66×10^{-7}	2.43×10^{-4}	5.21×10^{-4}

2.4 Discussion

This subsection consists of outcomes for interesting physical variables including porosity parameter $\lambda(0.1 \leqslant \lambda \leqslant 0.7)$, Brownian motion parameter $N_b(0.4 \leqslant N_b \leqslant 1.3)$, Forchheimer number $Fr(0.0 \leqslant Fr \leqslant 1.2)$, Schmidt number $Sc(0.6 \leqslant Sc \leqslant 1.5)$, rotation parameter $\Omega(0.0 \leqslant \Omega \leqslant 0.45)$, Prandtl number $\Pr(0.7 \leqslant \Pr \leqslant 1.6)$ and thermophoresis parameter $N_t(0.0 \leqslant N_t \leqslant 0.6)$ on nondimensional velocities $f'(\zeta)$ and $g(\zeta)$, temperature $\theta(\zeta)$ and concentration $\phi(\zeta)$ fields. Figure 2.3 displays change in $f'(\zeta)$ for λ. Reduction is noted in velocity field $f'(\zeta)$ against higher λ. Figure 2.4 is developed to examine the impact of Fr on velocity field $f'(\zeta)$. Higher Fr correspond to decay of $f'(\zeta)$. Effect of Ω on $f'(\zeta)$ is presented via Figure 2.5. Higher rotation parameter lead to lower velocity field. Physically the ratio of angular velocity to stretching rate is termed as rotation parameter. Larger Ω yield higher rotational rate which give rise to depreciate in $f'(\zeta)$ and momentum layer thickness. Figure 2.6 presents the outcome of λ for velocity $g(\zeta)$. Velocity field shows an increasing trend for higher λ. Figure 2.7 demonstrates that velocity $g(\zeta)$ reduces against Fr. Figure 2.8 shows curves of velocity $g(\zeta)$ against higher Ω. Decaying behavior is seen by higher Ω. Figure 2.9 displays that how λ varies $\theta(\zeta)$. Temperature $\theta(\zeta)$ is enhanced by higher values of λ. Figure 2.10 displays change in temperature $\theta(\zeta)$ for varying Forchheimer number Fr. Here temperature is increased through Fr. Figure 2.11 indicates that higher rotation parameter Ω yields stronger temperature field. Figure 2.12 shows temperature field $\theta(\zeta)$ for varying Prandtl number Pr. Temperature field $\theta(\zeta)$ is decreased

for higher Pr. Figure 2.13 elaborates outcome of thermophoresis parameter N_t on temperature field $\theta(\zeta)$. Here temperature field is enhanced for larger N_t. Figure 2.14 indicates impact of Brownian movement parameter N_b on temperature $\theta(\zeta)$. One can easily observe increasing behavior of $\theta(\zeta)$ via higher N_b. Figure 2.15 scrutinizes the variation in nano-concentration $\phi(\zeta)$ for larger λ. It has been noted that higher estimation of λ yields an increase in $\phi(\zeta)$. Figure 2.16 presents that nano-concentration $\phi(\zeta)$ is higher for larger Forchheimer number Fr. Fig. 2.17 shows an increase in nano-concentration $\phi(\zeta)$ via higher Ω. Effect of Schmidt number Sc on nano-concentration $\phi(\zeta)$ is exhibited in Figure 2.18. In this Figure, we can analyze that concentration field $\phi(\zeta)$ exhibits decreasing trend via larger Schmidt number Sc. Behavior of N_t on $\phi(\zeta)$ is presented in Figure 2.19. It is analyzed that larger N_t correspond to increasing trend of concentration field $\phi(\zeta)$. Figure 2.20 is developed to deliberate the consequences of N_b on $\phi(\zeta)$. An increment in N_b causes decay in nano-concentration field. Figure 2.21 displays the behaviors of Ω and Fr on $(\mathrm{Re}_x)^{-1/2}C_f$. It is noticed that $(\mathrm{Re}_x)^{-1/2}C_f$ enhances via Fr while reverse trend is seen for Ω. Figure2.22 demonstrates the influences of λ and Ω on $(\mathrm{Re}_x)^{-1/2}C_f$. Apparently $(\mathrm{Re}_x)^{-1/2}C_f$ exhibits decaying trend against Ω while reverse situation is observed for λ. Figure 2.23 depicts effects of Fr and Ω on $(\mathrm{Re}_x)^{-1/2}C_g$. Higher estimations of Ω and Fr declare diminishing behavior for $(\mathrm{Re}_x)^{-1/2}C_g$. Figure 2.24 displays the influences of Ω and λ on $(\mathrm{Re}_x)^{-1/2}C_g$. From this Figure it is examined that $(\mathrm{Re}_x)^{-1/2}C_g$ presents increasing trend for λ while reverse trend is analyzed via Ω. Properties of Pr and N_t on $(\mathrm{Re}_x)^{-1/2}Nu_x$ (rate of heat transfer)are disclosed through Figure 2.25. Interestingly $(\mathrm{Re}_x)^{-1/2}Nu_x$ reduces for both Pr and N_t. Figure 2.26 exhibits the behavior of N_b and Sc on $(\mathrm{Re}_x)^{-1/2}Sh_x$ (rate of mass transfer). Here it is noticed that $(\mathrm{Re}_x)^{-1/2}Sh_x$ enhances through N_b and Sc.
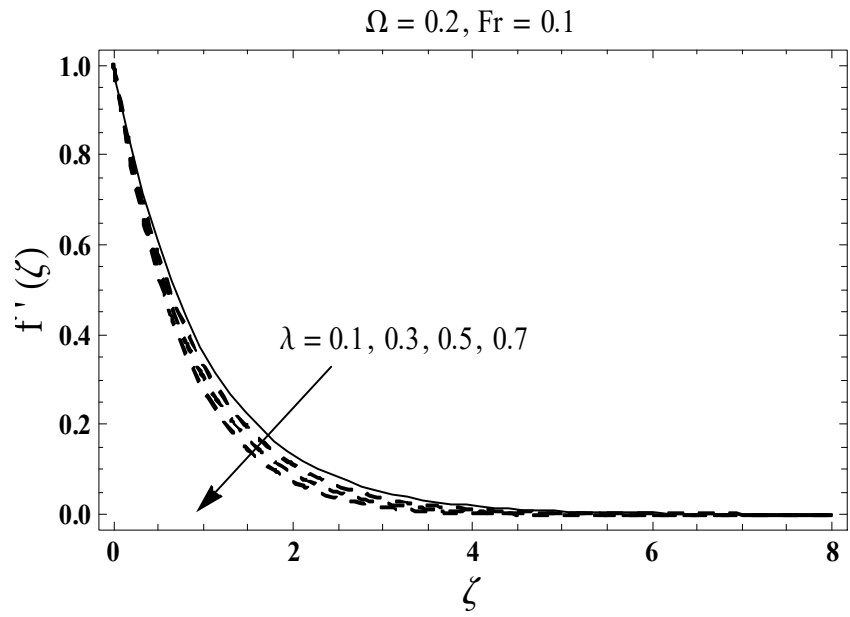
Figure 2.3 : Sketch for $f'(\zeta)$ against λ.
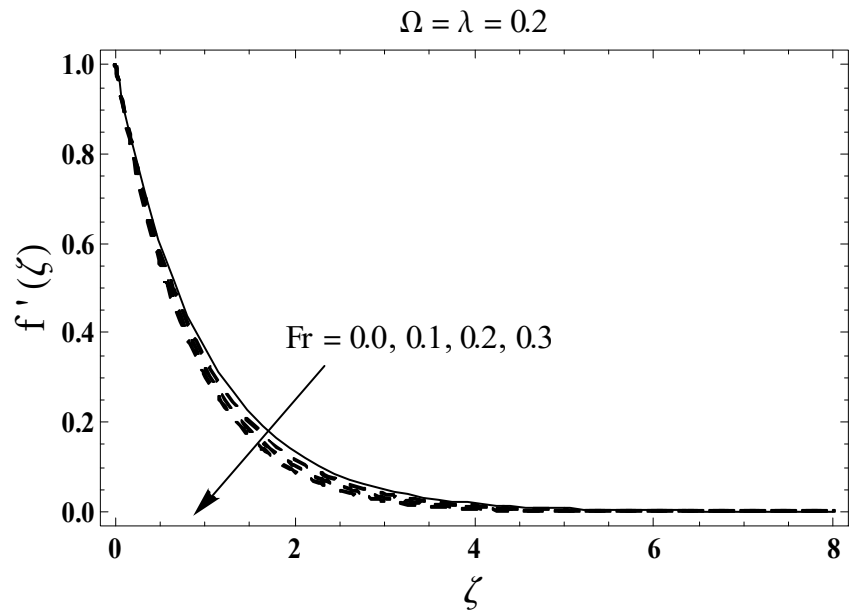
Figure 2.4 : Sketch for $f'(\zeta)$ against Fr.

22

$$\lambda = 0.2,\ Fr = 0.1$$

$$\Omega = 0.0, 0.15, 0.30, 0.45$$
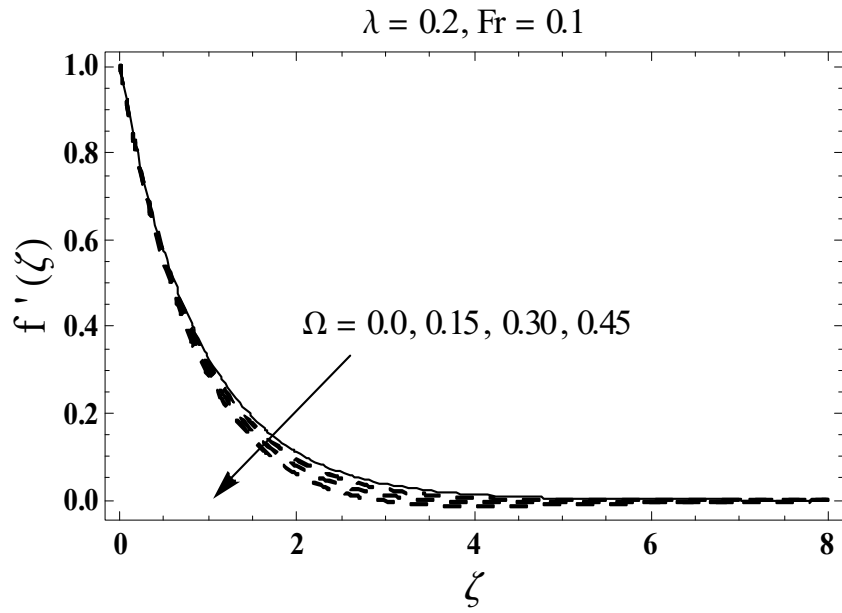
Figure 2.5 : Sketch for $f'(\zeta)$ against Ω.

$$\Omega = 0.2,\ Fr = 0.1$$

$$\lambda = 0.1, 0.3, 0.5, 0.7$$
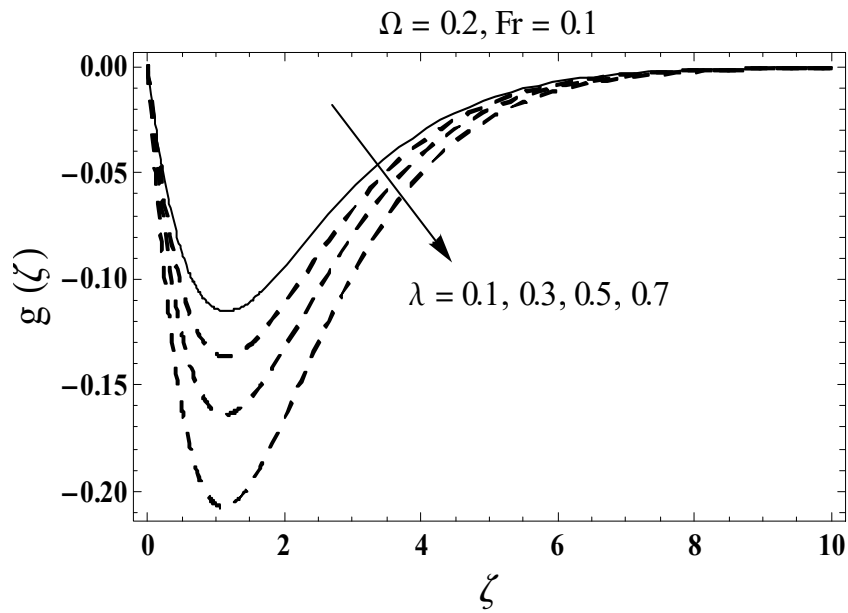
Figure 2.6 : Sketch for $g(\zeta)$ against λ.

$$\Omega = \lambda = 0.2$$

Fr = 0.0, 0.1, 0.2, 0.3
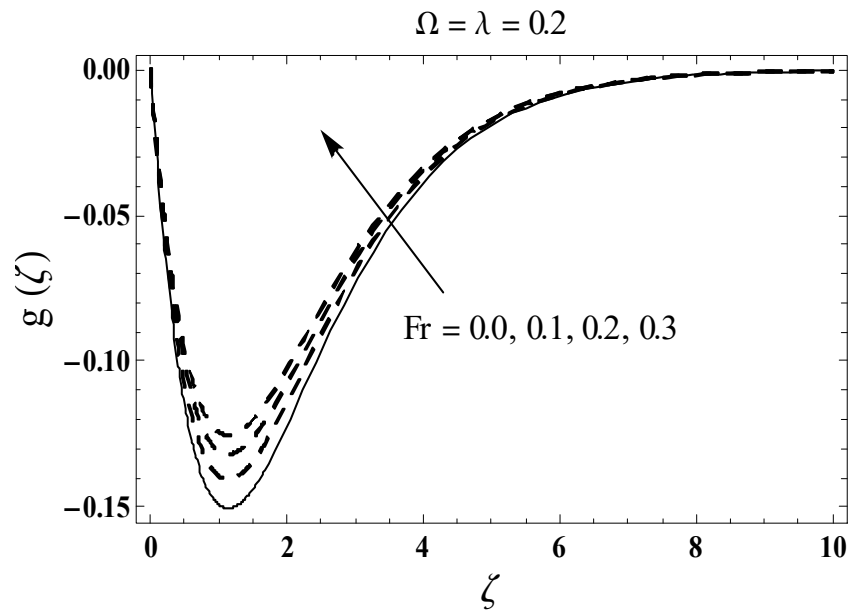
Figure 2.7 : Sketch for $g(\zeta)$ against Fr.

$$\lambda = 0.2, \text{Fr}=0.1$$

$\Omega = 0.0, 0.15, 0.30, 0.45$
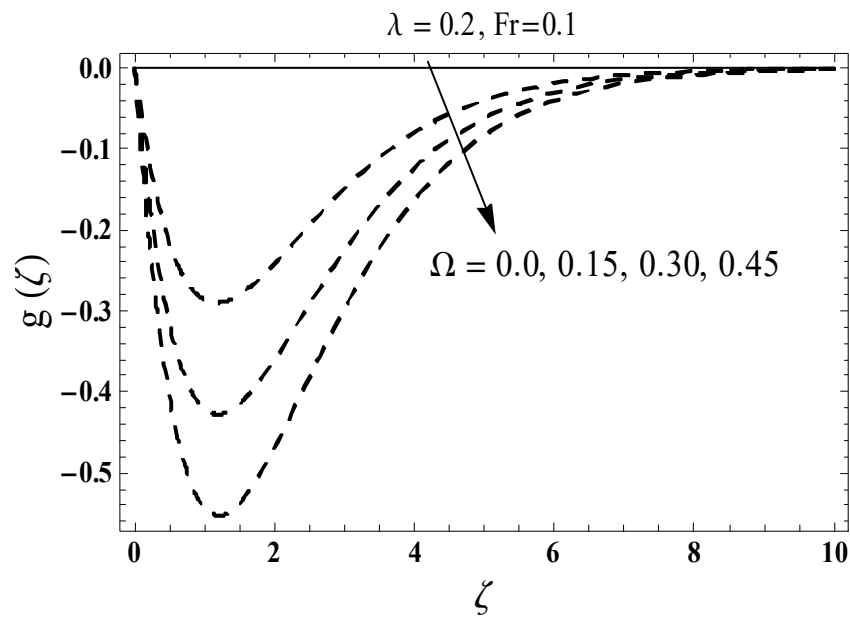
Figure 2.8 : Sketch for $g(\zeta)$ against Ω.

24
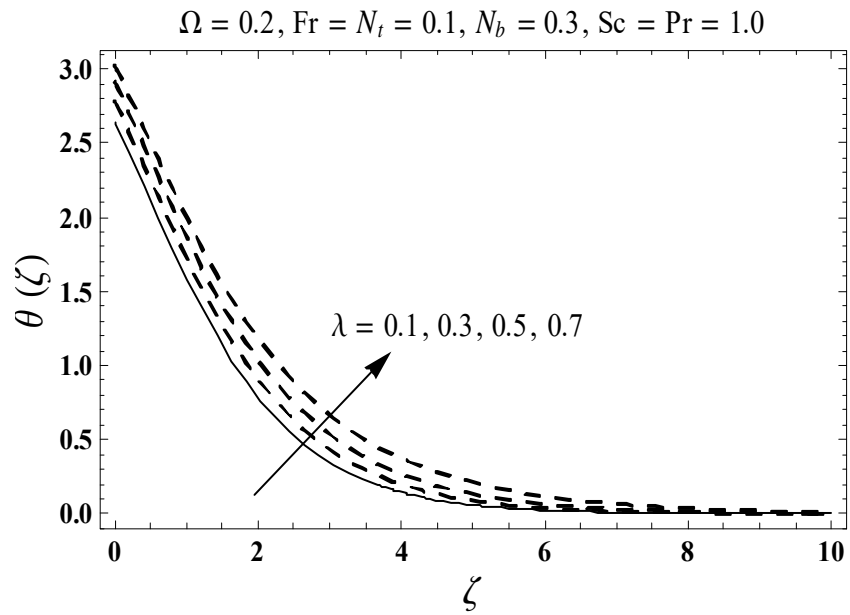
Figure 2.9 : Sketch for $\theta(\zeta)$ against λ.
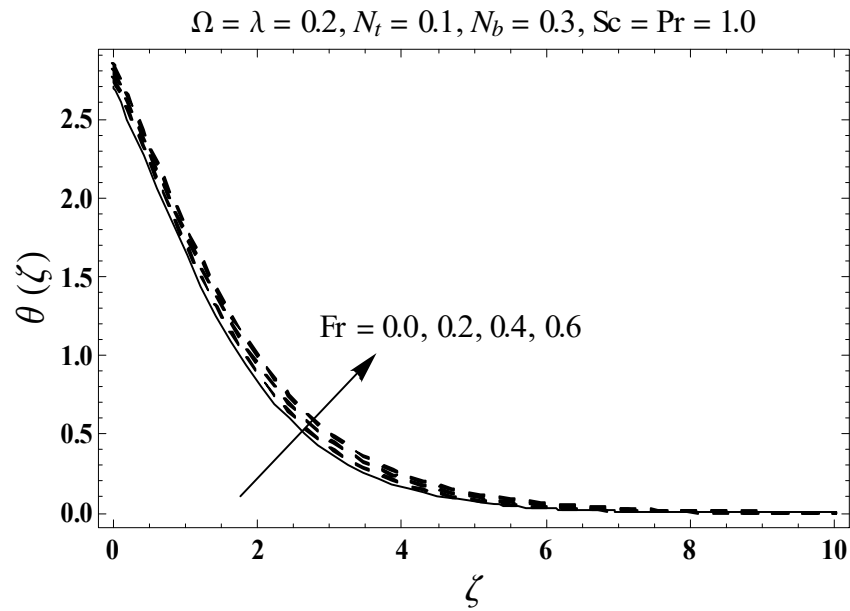
Figure 2.10 : Sketch for $\theta(\zeta)$ against Fr.

$\lambda = 0.2$, Fr $= N_t = 0.1$, $N_b = 0.3$, Sc $=$ Pr $= 1.0$

$\Omega = 0.0, 0.15, 0.30, 0.45$
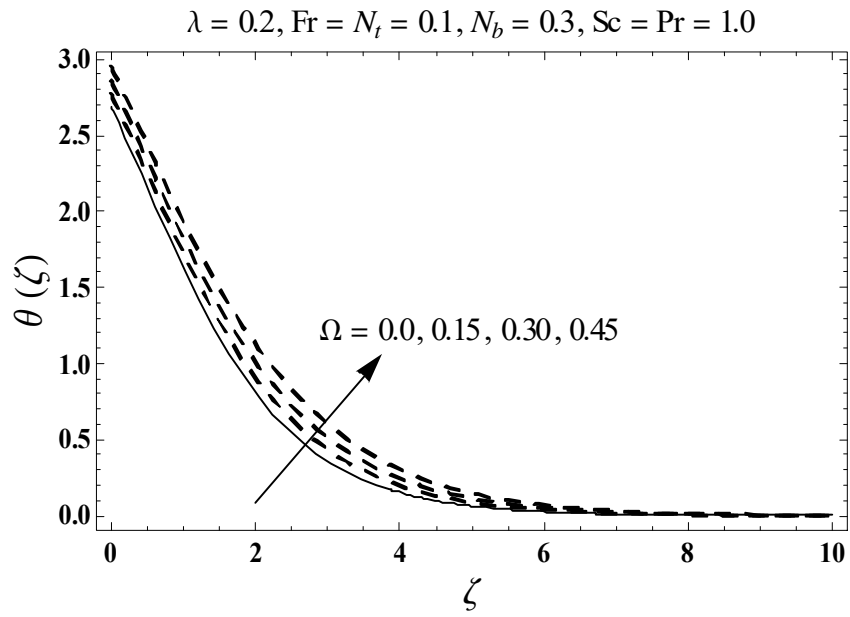
Figure 2.11 : Sketch for $\theta(\zeta)$ against Ω.

$\Omega = \lambda = 0.2$, Fr $= N_t = 0.1$, $N_b = 0.3$, Sc $= 1.0$

Pr $= 0.7, 1.0, 1.3, 1.6$
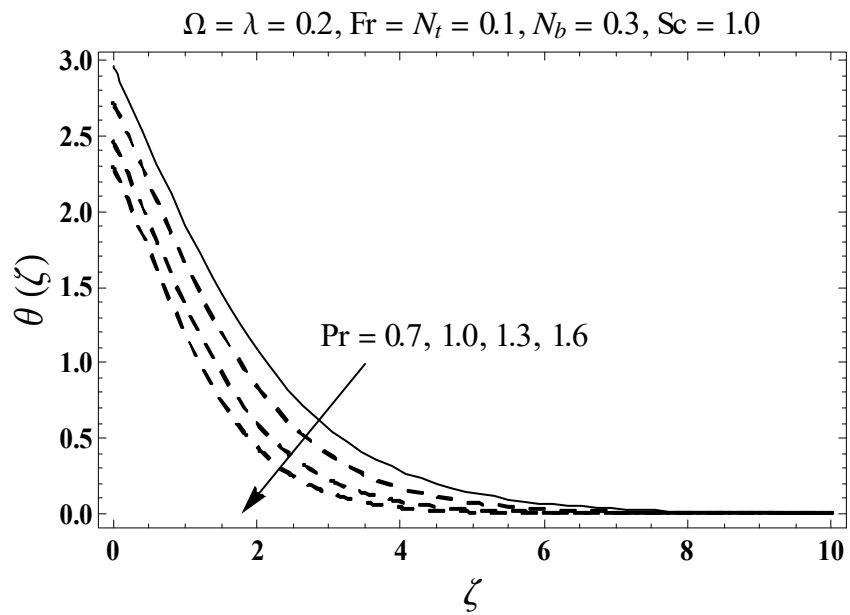
Figure 2.12 : Sketch for $\theta(\zeta)$ against Pr.

$\Omega = \lambda = 0.2$, Fr = 0.1, $N_b = 0.3$, Sc = Pr = 1.0

$N_t = 0.0, 0.2, 0.4, 0.6$
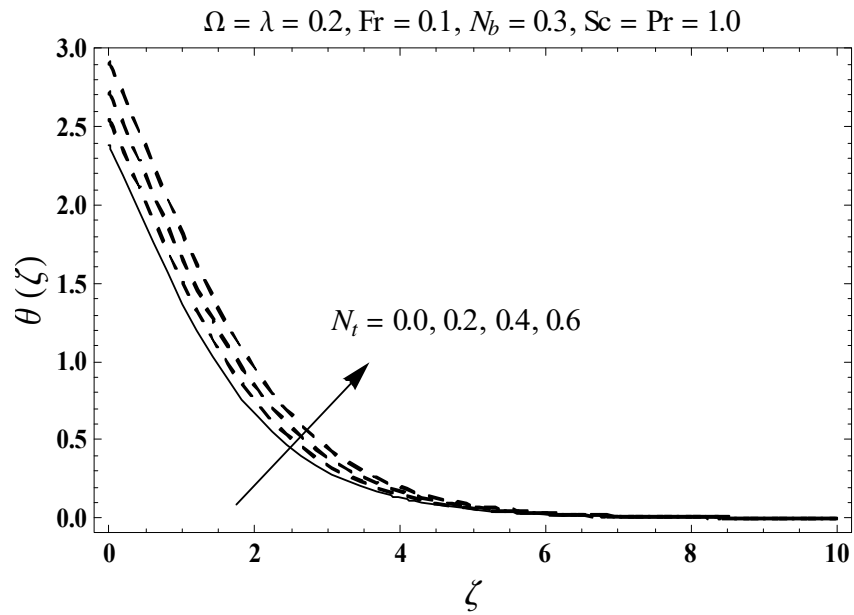
Figure 2.13 : Sketch for $\theta(\zeta)$ against N_t.

$\Omega = \lambda = 0.2$, Fr = $N_t = 0.1$, Sc = Pr = 1.0

$N_b = 0.4, 0.7, 1.0, 1.3$
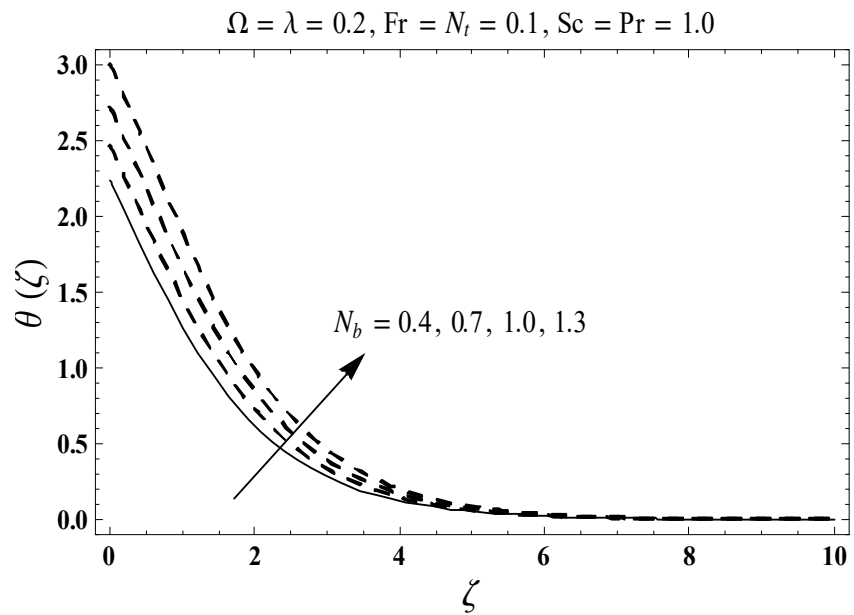
Figure 2.14 : Sketch for $\theta(\zeta)$ against N_b.

$\Omega = 0.2$, Fr $= N_t = 0.1$, $N_b = 0.3$, Sc $=$ Pr $= 1.0$
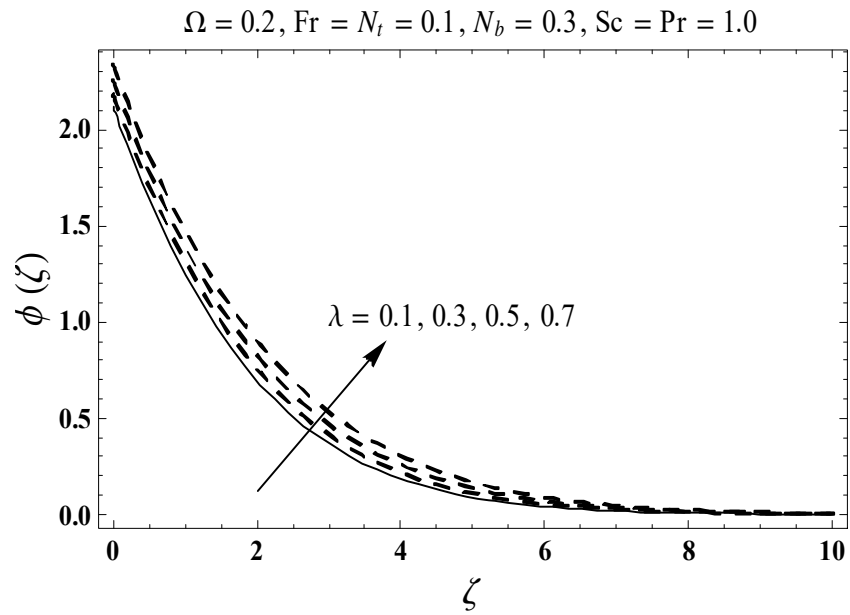
Figure 2.15 : Sketch for $\phi(\zeta)$ against λ.

$\Omega = \lambda = 0.2$, $N_t = 0.1$, $N_b = 0.3$, Sc $=$ Pr $= 1.0$
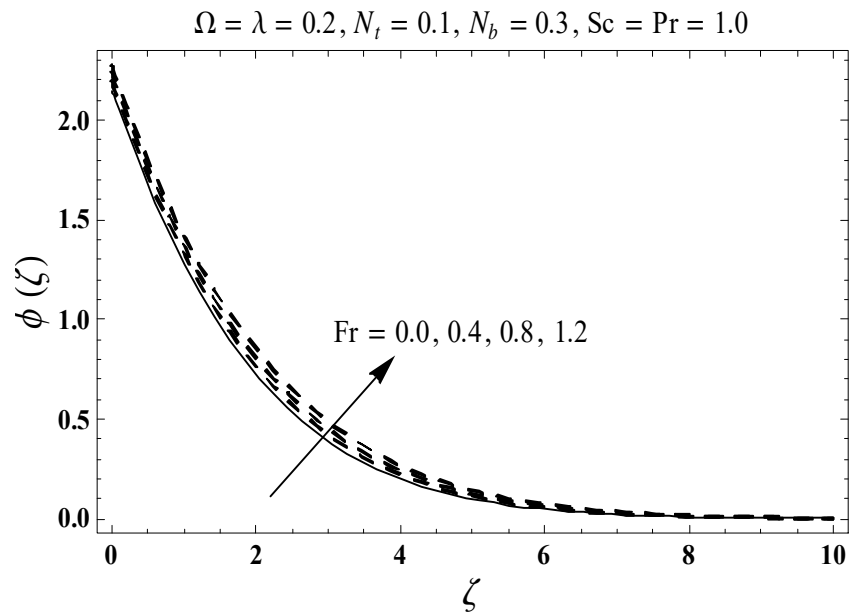
Figure 2.16 : Sketch for $\phi(\zeta)$ against Fr.

$$\lambda = 0.2, \text{Fr} = N_t = 0.1, N_b = 0.3, \text{Sc} = \text{Pr} = 1.0$$

$$\Omega = 0.0, 0.15, 0.30, 0.45$$
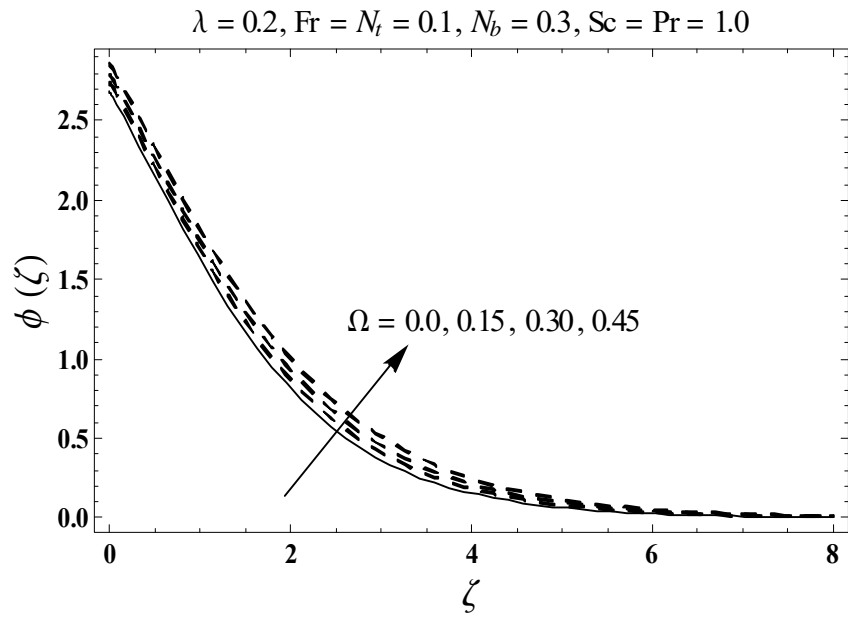
Figure 2.17 : Sketch for $\phi(\zeta)$ against Ω.

$$\Omega = \lambda = 0.2, \text{Fr} = N_t = 0.1, N_b = 0.3, \text{Pr} = 1.0$$

$$\text{Sc} = 0.8, 1.0, 1.2, 1.4$$
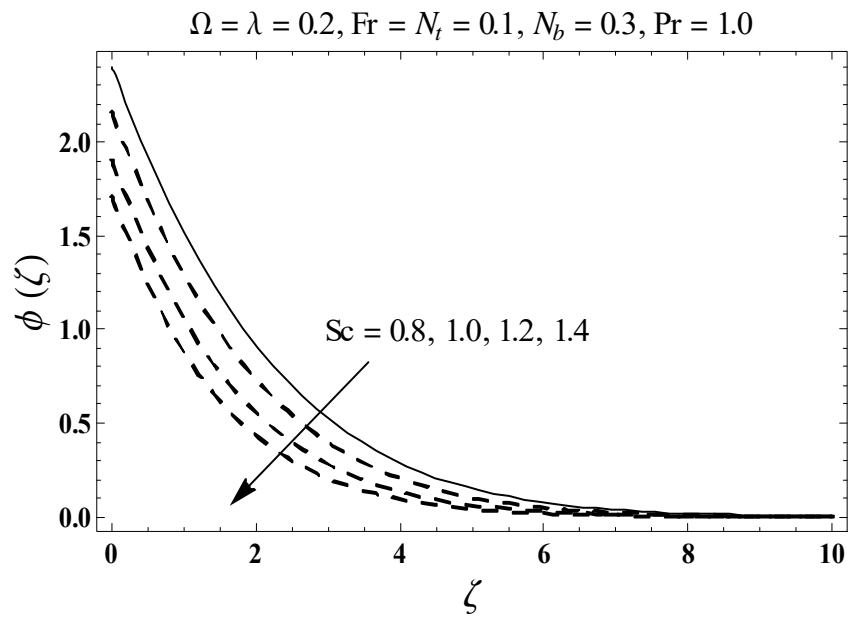
Figure 2.18 : Sketch for $\phi(\zeta)$ against Sc.

$\Omega = \lambda = 0.2$, Fr $= 0.1$, $N_b = 0.3$, Sc $=$ Pr $= 1.0$

$N_t = 0.0, 0.2, 0.4, 0.6$
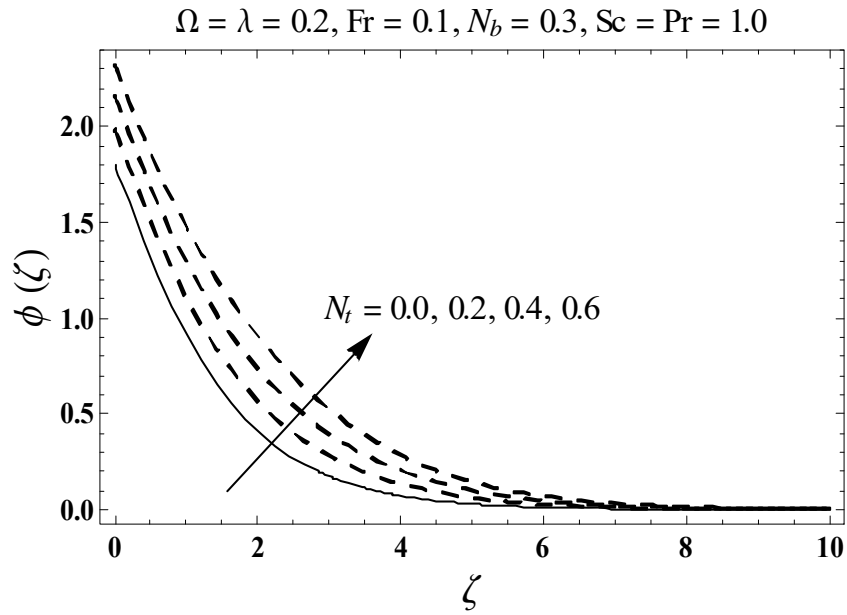
Figure 2.19 : Sketch for $\phi(\zeta)$ against N_t.

$\Omega = \lambda = 0.2$, Fr $= N_t = 0.1$, Sc $=$ Pr $= 1.0$

$N_b = 0.4, 0.7, 1.0, 1.3$
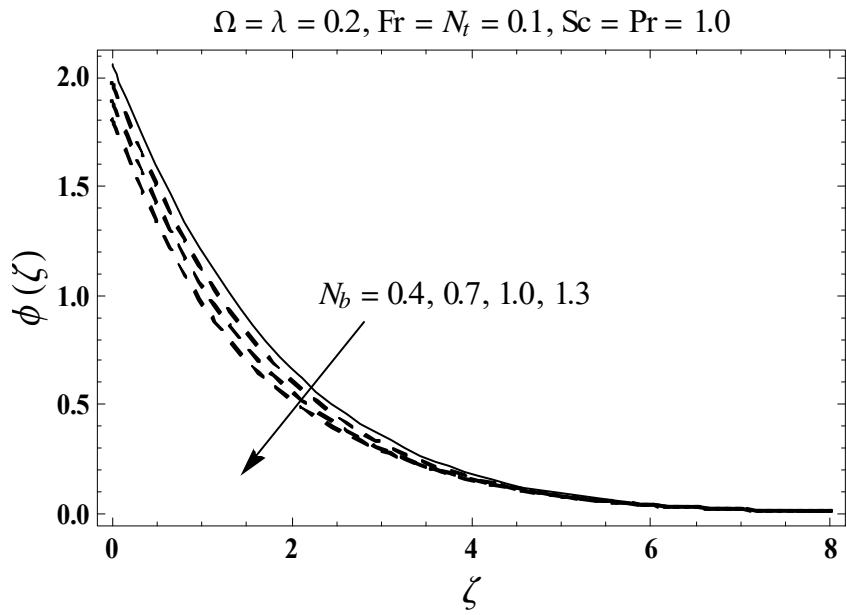
Figure 2.20 : Sketch for $\phi(\zeta)$ against N_b.

30
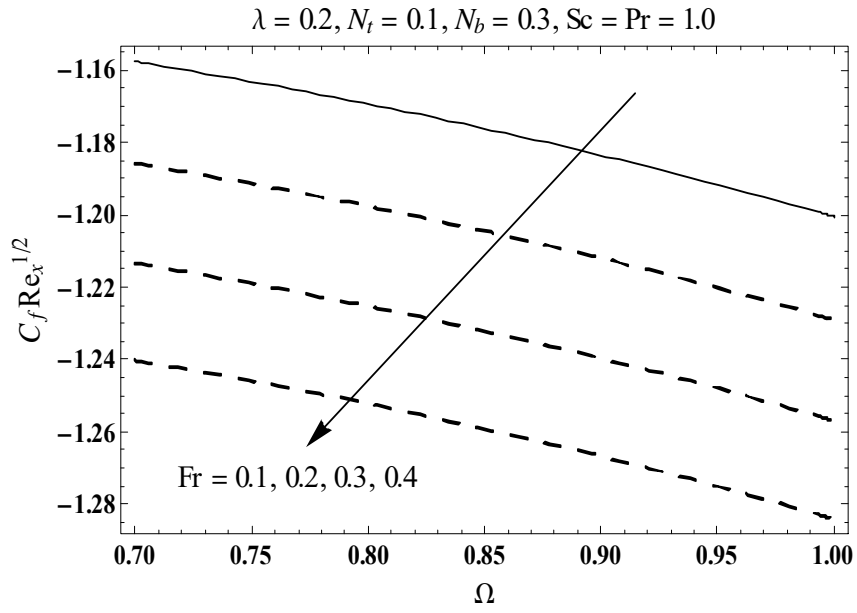
Figure 2.21 : Sketch for $C_f \operatorname{Re}_x^{1/2}$ against Ω and Fr.
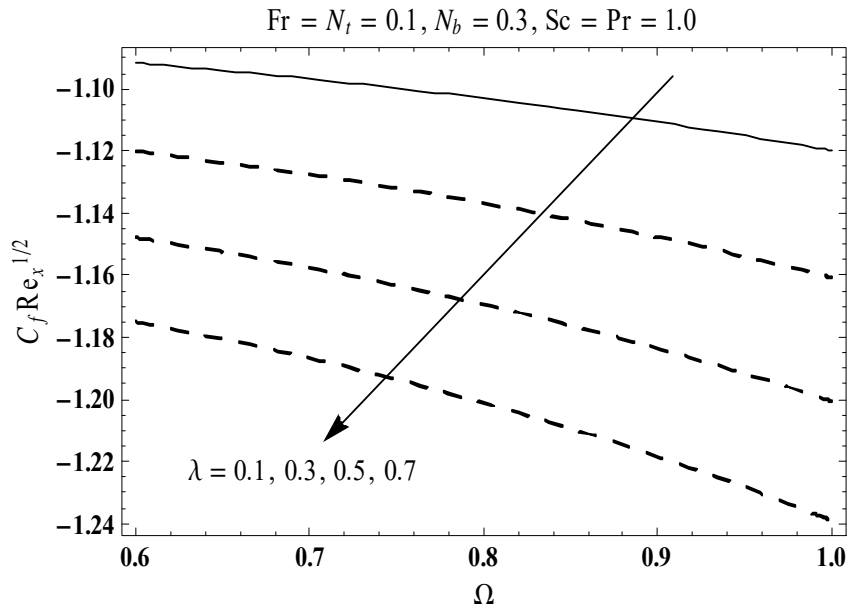
Figure 2.22 : Sketch for $C_f \operatorname{Re}_x^{1/2}$ against Ω and λ.

$\lambda = 0.2,\, N_t = 0.1,\, N_b = 0.3,\, \text{Sc} = \text{Pr} = 1.0$

Fr = 0.1, 0.2, 0.3, 0.4
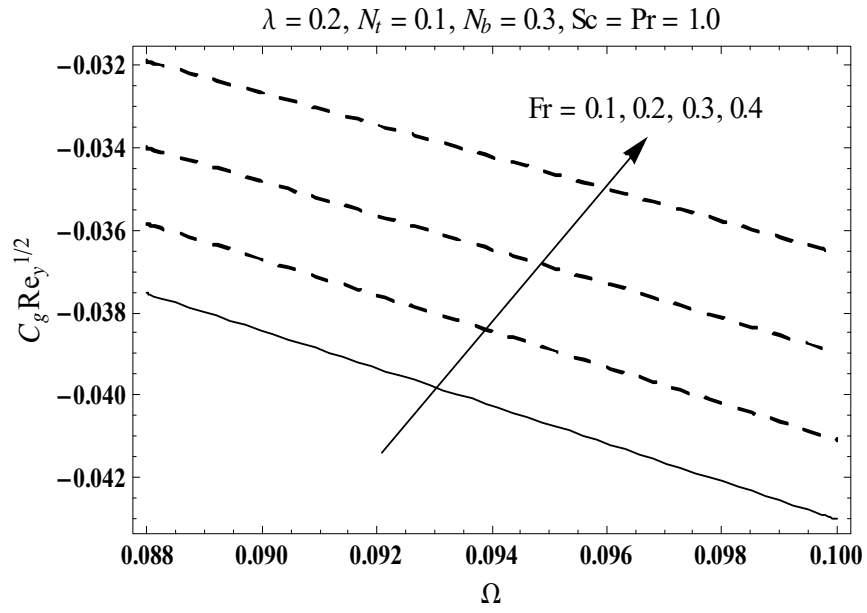
Figure 2.23 : Sketch for $C_g\,\mathrm{Re}_y^{1/2}$ against Ω and Fr.

$\text{Fr} = N_t = 0.1,\, N_b = 0.3,\, \text{Sc} = \text{Pr} = 1.0$

$\lambda = 0.1, 0.3, 0.5, 0.7$
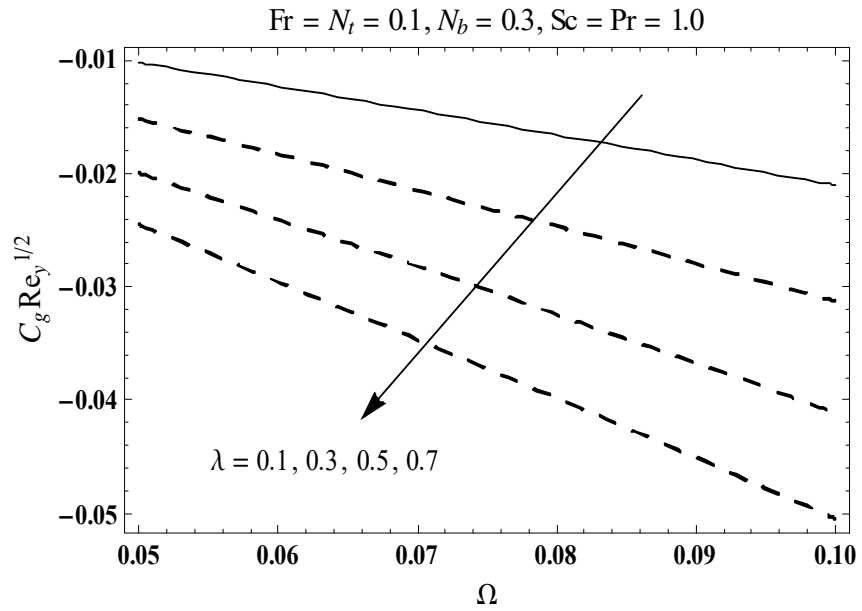
Figure 2.24 : Sketch for $C_g\,\mathrm{Re}_y^{1/2}$ against Ω and λ.
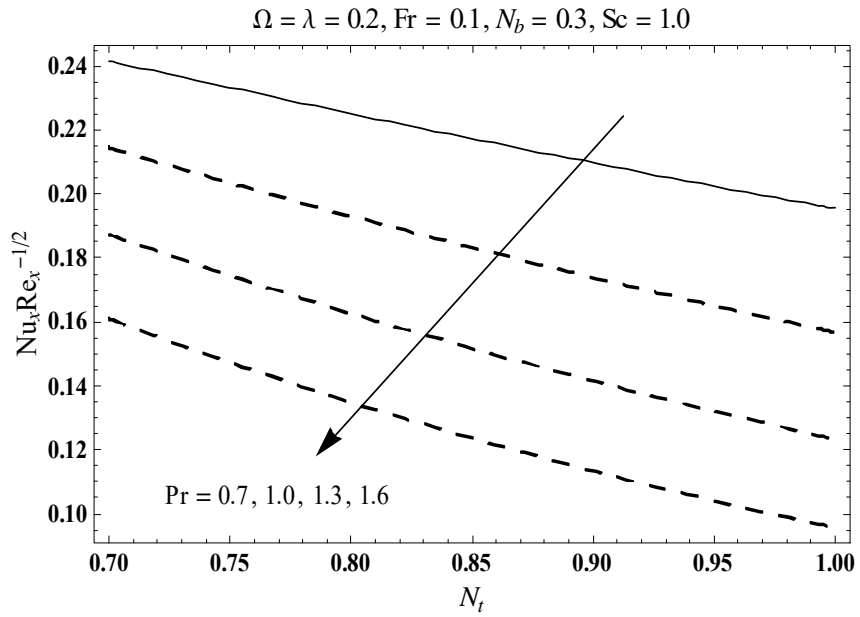
Figure 2.25 : Sketch for $Nu_x \operatorname{Re}_x^{-1/2}$ N_t and Pr.
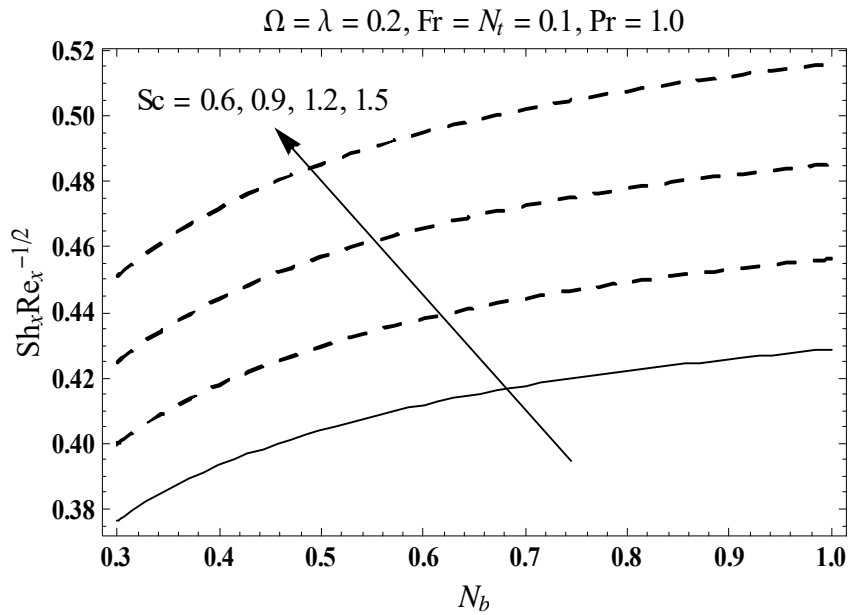
Figure 2.26 : Sketch for $Sh_x \operatorname{Re}_x^{-1/2}$ against N_b and Sc.

2.5 Major observations

Non-Darcian three-dimensional rotating flow of nanoliquid with constant thermal and mass fluxes is discussed. Main findings are summarized below:

- Larger porosity parameter λ show opposite behavior for both velocity profiles $f'(\zeta)$ and $g(\zeta)$ while similar trend is noticed for temperature $\theta(\zeta)$ and nano-concentration $\phi(\zeta)$.

- Both velocities $f'(\zeta)$ and $g(\zeta)$ have decreasing behavior for higher Forchheimer number Fr while increasing impact is found for temperature $\theta(\zeta)$ and nano-concentration $\phi(\zeta)$.

- An enhancement in rotation parameter Ω yields low velocity components while opposite holds for temperature and nano-concentration.

- Nano-concentration and temperature are increasing function of thermophoresis parameter N_t.

- An enhancement in Prandtl number Pr and Schmidt number Sc corresponds to low temperature and nano-concentration.

- Higher Brownian motion parameter N_b depict stronger temperature $\theta(\zeta)$ while opposite holds for nano-concentration $\phi(\zeta)$.

Chapter 3

Influences of heat generation/absorption and activation energy in Darcy-Forchheimer three-dimensional rotating flow of nanofluid

Non-Darcian three-dimensional rotating flow of nanoliquid in presence of activation energy and heat sink/source is examined in this chapter. Heat and mass transport via convective process is investigated. Buongiorno model is adopted to illustrate thermophoresis and Brownian diffusion. An efficient numerical technique namely NDSolve is employed for computations of nonlinear system. The graphical illustrations examine outcomes of various flow parameters. Local Nusselt and Sherwood numbers are computed and examined. It is noticed that temperature and nano-concentration are enhanced for Forchheimer number and porosity parameter.

3.1 Statement

Here non-Darcian three dimensional rotating flow of nanoliquid through binary chemical mechanism, Arrhenius activation energy and heat generation/absorption is addressed. Heat and mass transfer by convective conditions are examined. Nanoliquid has characteristics of Brownian movement and thermophoresis. It is further assume that the surface is heated by hot liquid with temperature T_f and concentration C_f (that provides heat and mass transport coefficients h_1 and h_2 respectively). Surface in Cartesian coordinate system is aligned with $xy-$plane and fluid occupies $z \geq 0$. Rate of stretching is c. Whole system rotates with constant angular velocity ω. Relevant problems for 3D flow satisfy

$$\frac{\partial u}{\partial x} + \frac{\partial v}{\partial y} + \frac{\partial w}{\partial z} = 0, \tag{3.1}$$

$$u\frac{\partial u}{\partial x} + v\frac{\partial u}{\partial y} + w\frac{\partial u}{\partial z} - 2\omega v = \nu\frac{\partial^2 u}{\partial z^2} - \frac{\nu}{k^*}u - Fu^2, \tag{3.2}$$

$$u\frac{\partial v}{\partial x} + v\frac{\partial v}{\partial y} + w\frac{\partial v}{\partial z} + 2\omega u = \nu\frac{\partial^2 v}{\partial z^2} - \frac{\nu}{k^*}v - Fv^2, \tag{3.3}$$

$$u\frac{\partial T}{\partial x} + v\frac{\partial T}{\partial y} + w\frac{\partial T}{\partial z} = \alpha^*\frac{\partial^2 T}{\partial z^2} + \frac{Q}{(\rho c)_f}(T - T_\infty) + \frac{(\rho c)_p}{(\rho c)_f}\left(\frac{D_T}{T_\infty}\left(\frac{\partial T}{\partial z}\right)^2 + D_B\left(\frac{\partial C}{\partial z}\frac{\partial T}{\partial z}\right)\right), \tag{3.4}$$

$$u\frac{\partial C}{\partial x} + v\frac{\partial C}{\partial y} + w\frac{\partial C}{\partial z} = D_B\left(\frac{\partial^2 C}{\partial z^2}\right) - k_r^2(C - C_\infty)\left(\frac{T}{T_\infty}\right)^n \exp\left(-\frac{E_a}{\kappa T}\right) + \frac{D_T}{T_\infty}\left(\frac{\partial^2 T}{\partial z^2}\right), \tag{3.5}$$

$$\left.\begin{array}{c} u = cx = U_w(x), \ v = 0, \ w = 0, \ -k\frac{\partial T}{\partial z} = h_1(T_f - T), \\ -D_B\frac{\partial C}{\partial z} = h_2(C_f - C) \text{ at } z = 0, \end{array}\right\} \tag{3.6}$$

$$u \to 0, \quad v \to 0, \quad T \to T_\infty, \quad C \to C_\infty \quad \text{when } z \to \infty. \tag{3.7}$$

In which permeability of porous space, variable inertial coefficient of permeable space, drag coefficient, thermal diffusivity, thermal potential of the liquid, specific thermal potential of the nanomaterials, heat generation/absorption coefficient, Brownian movement, thermophoretic dispersion coefficient, reaction rate, fitted rate constant, activation energy, Boltzmann constant, coefficients of mass and heat transfer are symbolized by k^*, $F = C_b/xk^{*1.2}$, C_b, $\alpha^* = k/(\rho c)_f$, $(\rho c)_f$, $(\rho c)_p$, Q, D_B, D_T, k_r, n, E_a, κ, h_2 and h_1 respectively. Setting

$$u = cxf'(\zeta), \; v = cxg(\zeta), \; w = -(c\nu)^{1/2} f(\zeta), \;\Big\}$$
$$\zeta = \left(\tfrac{c}{\nu}\right)^{1/2} z, \; \theta(\zeta) = \tfrac{T-T_\infty}{T_f - T_\infty}, \; \phi(\zeta) = \tfrac{C-C_\infty}{C_f - C_\infty}, \;\Big\} \tag{3.8}$$

expression (3.1) is automatically verified and Eqs. $(3.2) - (3.7)$ are reduced to

$$f''' + ff'' - f'^2 + 2\Omega g - \lambda f' - Fr f'^2 = 0, \tag{3.9}$$

$$g'' + fg' - f'g - 2\Omega f' - \lambda g - Fr g^2 = 0, \tag{3.10}$$

$$\theta'' + \mathrm{Pr}\left(f\theta' + N_b\theta'\phi' + N_t\theta'^2 + S_1\theta\right) = 0, \tag{3.11}$$

$$\frac{1}{Sc}\phi'' + f\phi' + \frac{1}{Sc}\frac{N_t}{N_b}\theta'' - \sigma\left(1 + \delta\theta\right)^n \phi \exp\left(-\frac{E}{1+\delta\theta}\right) = 0, \tag{3.12}$$

$$f(0) = g(0) = 0, \; f'(0) = 1, \; \theta'(0) = -\gamma_1(1 - \theta(0)), \; \phi'(0) = -\gamma_2(1 - \phi(0)), \tag{3.13}$$

$$f'(\infty) \to 0, \; g(\infty) \to 0, \; \theta(\infty) \to 0, \; \phi(\infty) \to 0. \tag{3.14}$$

Here porosity parameter, Forchheimer number, rotation parameter, heat generation/absorption parameter, Prandtl number, Schmidt number, Brownian movement parameter, thermal Biot number, thermophoresis parameter, chemical reaction parameter, concentration Biot number, temperature difference parameter and nondimensional activation energy are denoted by λ, Fr, Ω, S_1, Pr, Sc, N_b, γ_1, N_t, σ, γ_2, δ and E respectively. We set these definitions as follows:

$$\lambda = \tfrac{\nu}{k^* c}, \; Fr = \tfrac{C_b}{k^{*1/2}}, \; \Omega = \tfrac{\omega}{c}, \; S_1 = \tfrac{Q}{c(\rho c)_f}, \; \mathrm{Pr} = \tfrac{\nu}{\alpha^\star}, \; Sc = \tfrac{\nu}{D_B}, \;\Big\}$$
$$N_b = \tfrac{(\rho c)_p D_B (C_f - C_\infty)}{(\rho c)_f \nu}, \; \sigma = \tfrac{k_r^2}{c}, \; \gamma_1 = \tfrac{h_1}{k}\sqrt{\tfrac{\nu}{c}}, \; E = \tfrac{E_a}{\kappa T_\infty}, \;\Big\} \tag{3.15}$$
$$N_t = \tfrac{(\rho c)_p D_T (T_f - T_\infty)}{(\rho c)_f \nu T_\infty}, \; \gamma_2 = \tfrac{h_2}{D_B}\sqrt{\tfrac{\nu}{c}}, \; \delta = \tfrac{T_f - T_\infty}{T_\infty}. \;\Big\}$$

The physical quantities like skin friction coefficients and local Nusselt and Sherwood numbers are

$$(\mathrm{Re}_x)^{-1/2} C_{fx} = f''(0), \;\Big\}$$
$$(\mathrm{Re}_x)^{-1/2} C_{fy} = g'(0), \;\Big\}$$
$$(\mathrm{Re}_x)^{-1/2} Nu_x = -\theta'(0), \;\Big\} \tag{3.16}$$
$$(\mathrm{Re}_x)^{-1/2} Sh_x = -\phi'(0). \;\Big\}$$

Here the local Reynolds number is given by $Re_x = U_w x/\nu$.

3.2 Discussion

This portion contains contribution of interesting physical variables including porosity parameter λ, Forchheimer number Fr, rotational parameter Ω, Prandtl parameter Pr, Schmidt parameter Sc, heat generation $(S_1 > 0)$ or absorption $(S_1 < 0)$ parameter , Brownian movement parameter N_b, fitted rate constant n, thermophoresis number N_t, nondimensional activation energy E, thermal Biot parameter γ_1, nondimensional reaction rate σ, temperature difference parameter δ and concentration Biot parameter γ_2 on temperature $\theta(\zeta)$ and nano-concentration $\phi(\zeta)$ fields. Figure 3.1 depicts that how porosity parameter λ affects temperature $\theta(\zeta)$. Temperature $\theta(\zeta)$ is elevated by porosity parameter λ. Figure 3.2 is interpreted for impact of Fr on $\theta(\zeta)$. Higher estimations of Fr correspond to stronger $\theta(\zeta)$. Figure 3.3 indicates that higher rotation parameter Ω yield stronger $\theta(\zeta)$. Figure 3.4 exhibits effect of γ_1 on $\theta(\zeta)$. Here an increment in γ_1 generates more temperature. Figures 3.5 and 3.6 are sketched to analyze the impacts of heat generation parameter (when $S_1 > 0$) and heat absorption parameter (when $S_1 < 0$). From these Figures, it is observed that temperature and related thermal layer thickness show increasing behavior while considering heat generation but in the case of heat absorption it has opposite trend. Figure 3.7 presents estimations $\theta(\zeta)$ with respect to Pr. Higher estimation of Pr yield weaker temperature $\theta(\zeta)$ and less associated layer thickness. Figure 3.8 elaborates influence of thermophoresis parameter N_t on temperature $\theta(\zeta)$. Clearly temperature is enhanced via larger N_t. Figure 3.9 shows how temperature field $\theta(\zeta)$ gets affected with Brownian motion parameter N_b. For higher N_b, the temperature field $\theta(\zeta)$ shows increasing trend. Figure 3.10 portrays λ variation on nano-concentration $\phi(\zeta)$. Higher λ give rise to more $\phi(\zeta)$. An increment in Forchheimer number Fr shows elevation of $\phi(\zeta)$ (see Figure 3.11). Figure 3.12 exhibits variation in $\phi(\zeta)$ for varying Ω. Here $\phi(\zeta)$ elevates via higher Ω. Figure 3.13 exhibits the influence of γ_2 on nano-concentration $\phi(\zeta)$. Nano-concentration $\phi(\zeta)$ increases via higher γ_2. Figure 3.14 elaborates influence of E on nano-concentration $\phi(\zeta)$. An increment in E decays modified Arrhenius function $\left(\frac{T}{T_\infty}\right)^n \exp\left(-\frac{E_a}{\kappa T}\right)$. This finally develops the productive chemical mechanism due to which $\phi(\zeta)$ enhances. Figure 3.15 presents that an enhancement in chemical reaction

parameter σ exhibits a decay in nano-concentration $\phi(\zeta)$ and its associated layer. Figure 3.16 elucidates influence of temperature difference parameter δ on $\phi(\zeta)$. Here $\phi(\zeta)$ is noted decreasing function of δ. Figure 3.17 presents nano-concentration $\phi(\zeta)$ for changing n. Clearly $\phi(\zeta)$ decreases for higher estimation of n. Nano-concentration $\phi(\zeta)$ against Schmidt number Sc is shown in Figure 3.18. By higher Sc, weaker nano-concentration $\phi(\zeta)$ field is observed. Figure 3.19 exhibits nano-concentration $\phi(\zeta)$ for particular values of N_t. Clearly larger N_t give rise to more nano-concentration $\phi(\zeta)$. Figure 3.20 elucidates that nano-concentration $\phi(\zeta)$ reduces for N_b. Table 3.1 analyzed surface drag coefficients $-(\mathrm{Re}_x)^{-1/2}C_{fx}$ and $-(\mathrm{Re}_x)^{-1/2}C_{fy}$ for several estimations of Forchheimer number Fr, porosity parameter λ and rotation parameter Ω. Both $-(\mathrm{Re}_x)^{-1/2}C_{fx}$ and $-(\mathrm{Re}_x)^{-1/2}C_{fy}$ depict increasing trend for higher Ω while reverse behavior is observed for larger λ and Fr. Table 3.2 computed local Nusselt (heat transfer rate) via λ, Fr, Ω, N_t, γ_1, N_b and Pr. Rate of heat transfer decays via λ, Fr, Ω, S_1, N_t and N_b. Effects of γ_1 and Pr on local Nusselt (heat transfer rate) are quite similar. Table 3.3 exhibits numerical data of rate of solutal transfer (local Sherwood number) $(\mathrm{Re}_x)^{-1/2}Sh_x$ via σ, Sc, N_t, E, δ, N_b, n and γ_2. Clearly the mass transfer rate has lower and higher values for increasing (N_t, E) and $(\sigma, Sc, \delta, N_b, n, \gamma_2)$ respectively.
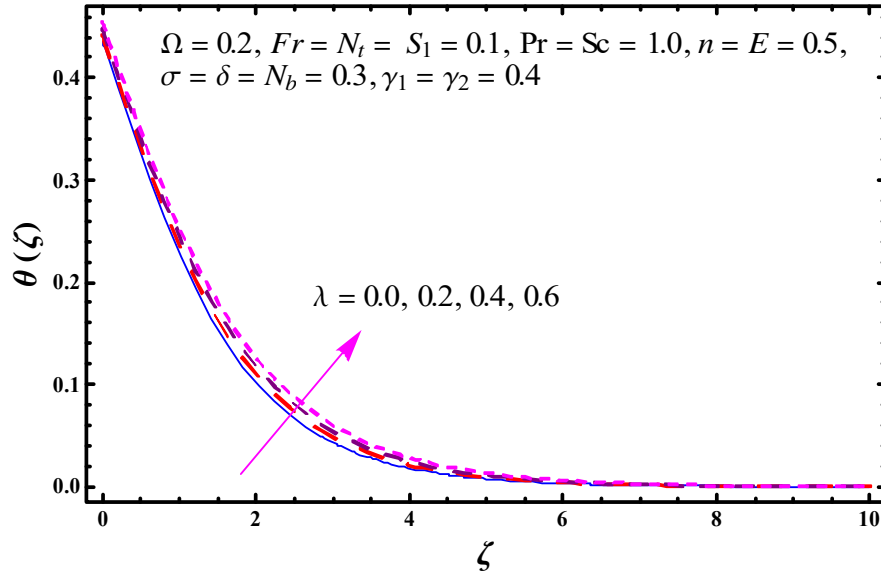
Figure 3.1 : Sketch for $\theta(\zeta)$ against λ.
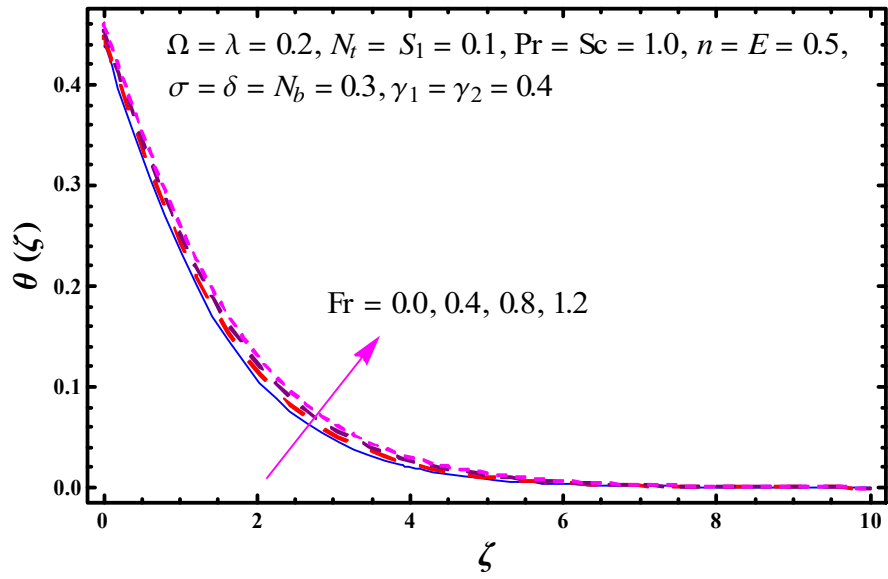
Figure 3.2 : Sketch for $\theta(\zeta)$ against Fr.
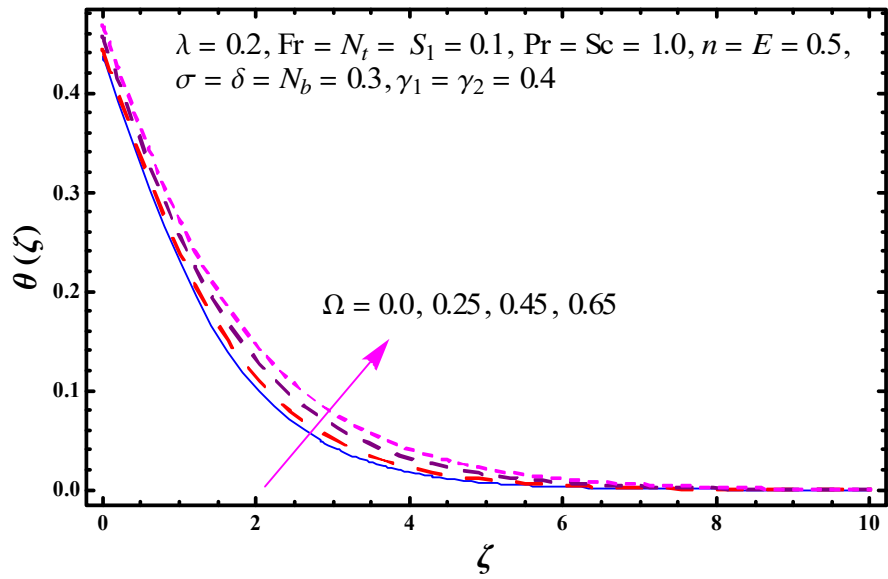
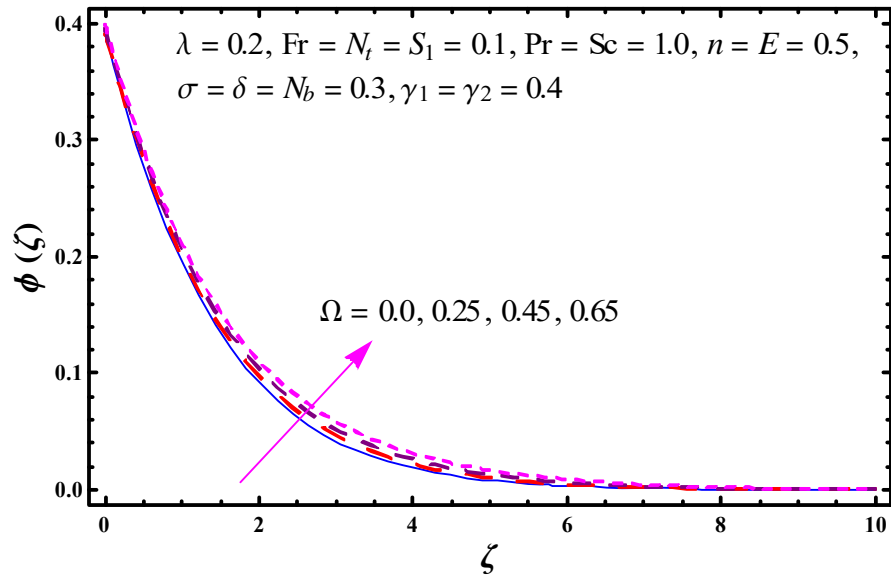Figure 3.3 : Sketch for $\theta(\zeta)$ against Ω.
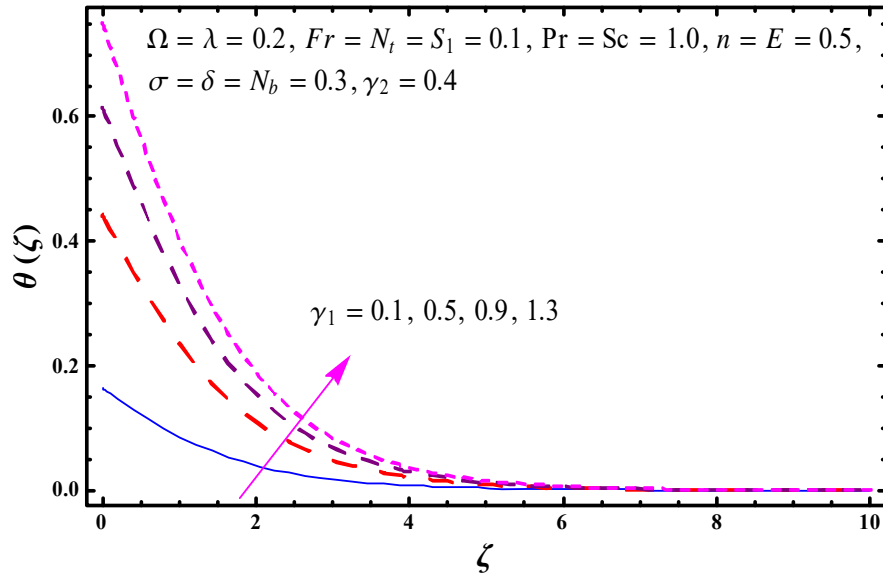
Figure 3.4 : Sketch for $\theta(\zeta)$ against γ_1.
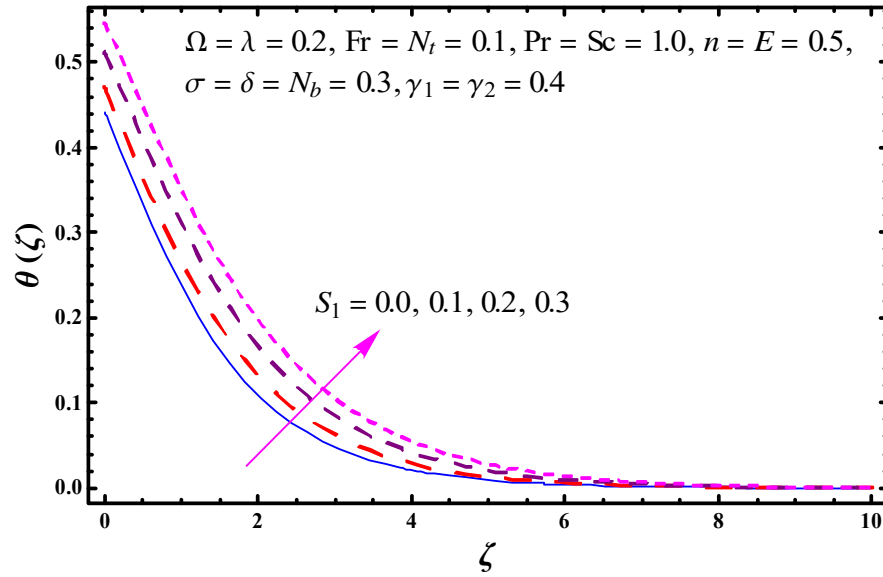
Figure 3.5 : Sketch for $\theta(\zeta)$ against $S_1 (> 0)$.

41
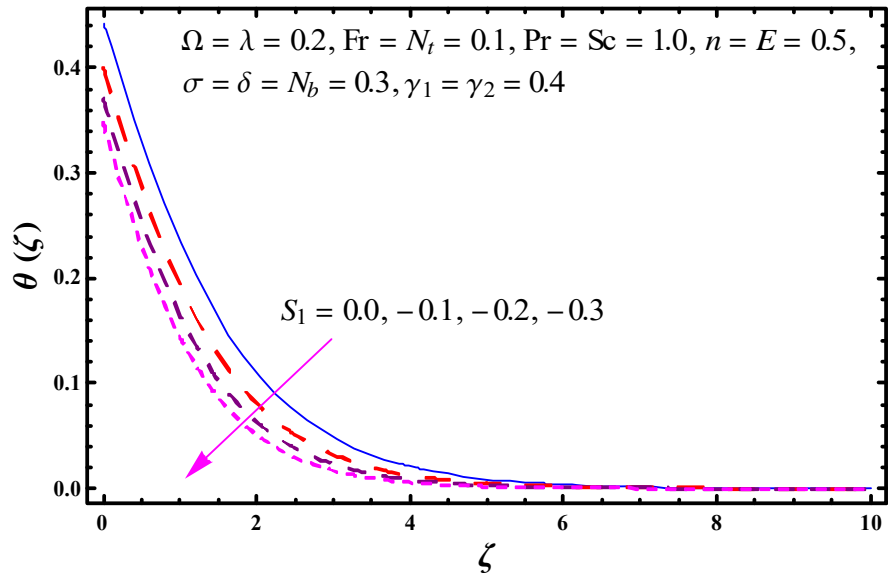
Figure 3.6 : Sketch for $\theta(\zeta)$ against $S_1(< 0)$.
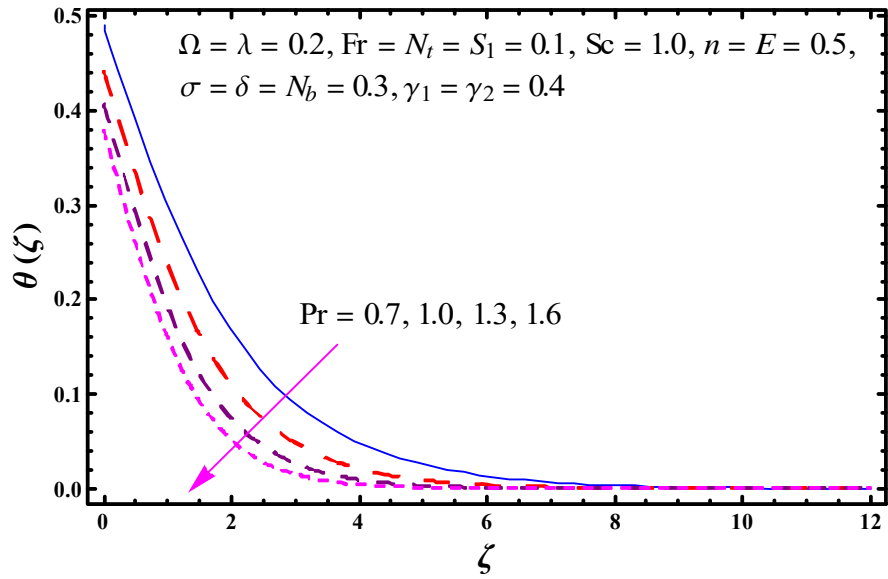
Figure 3.7 : Sketch for $\theta(\zeta)$ against Pr.
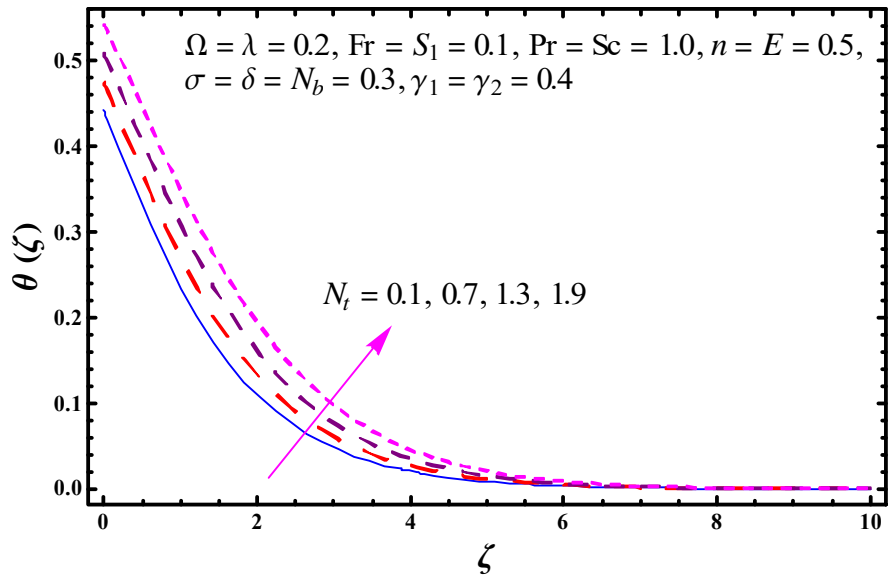
Figure 3.8 : Sketch for $\theta(\zeta)$ against N_t.
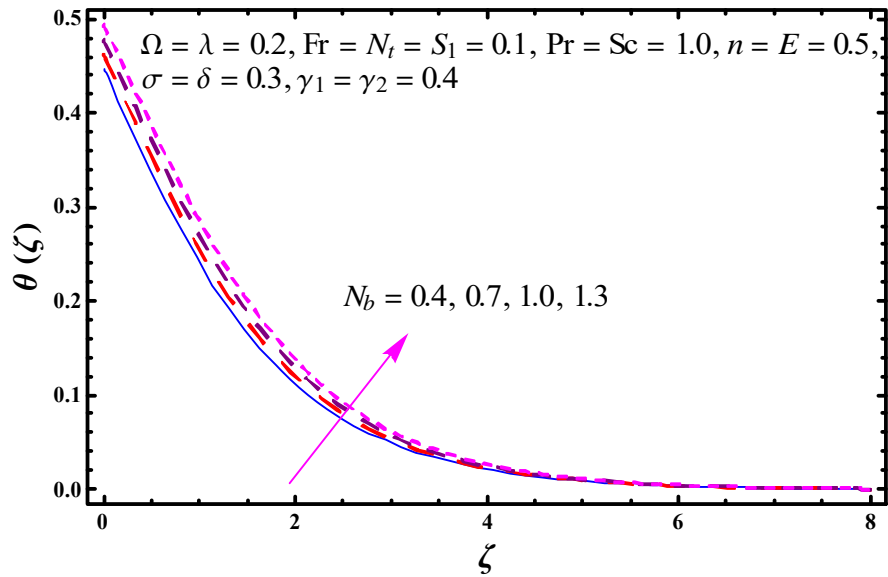
Figure 3.9 : Sketch for $\theta(\zeta)$ against N_b.
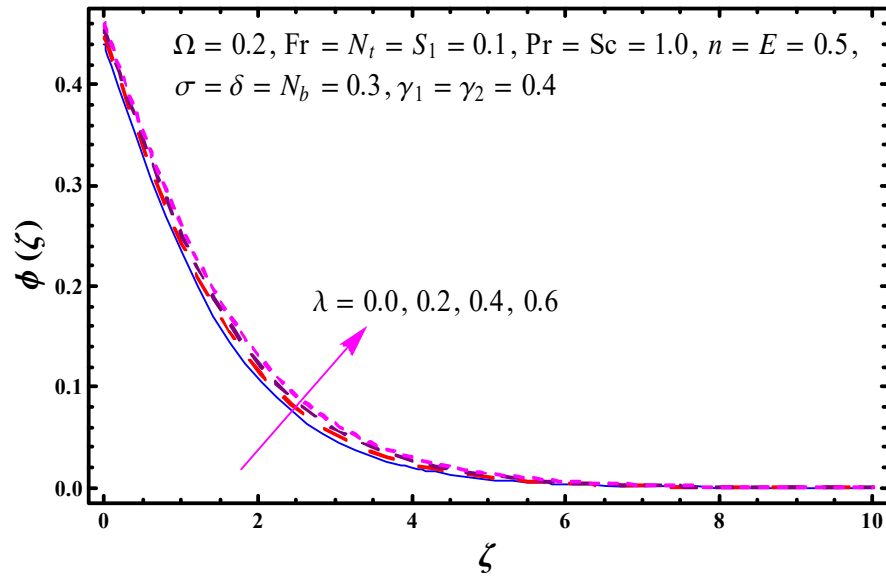
Figure 3.10 : Sketch for $\phi(\zeta)$ against λ.
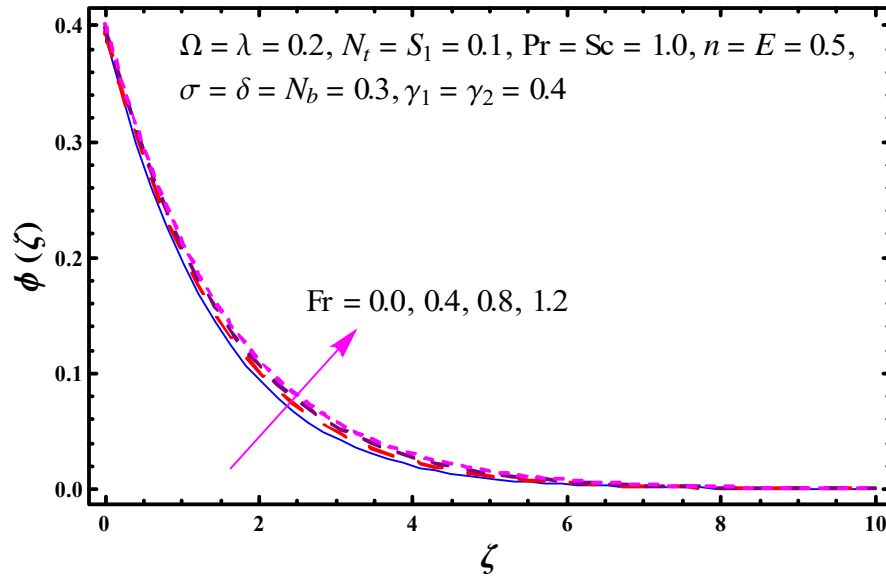
Figure 3.11 : Sketch for $\phi(\zeta)$ against Fr.

Figure 3.12 : Sketch for $\phi(\zeta)$ against Ω.
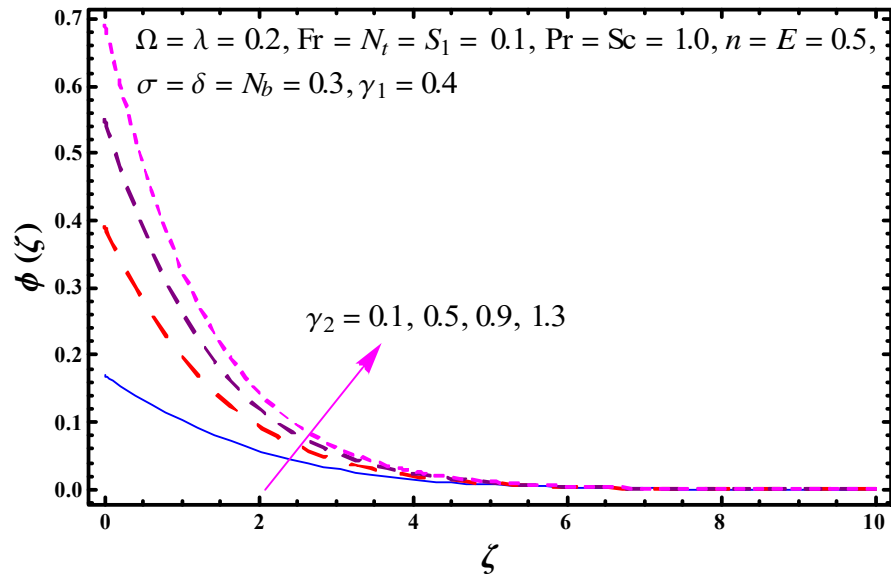
Figure 3.13 : Sketch for $\phi(\zeta)$ against γ_2.
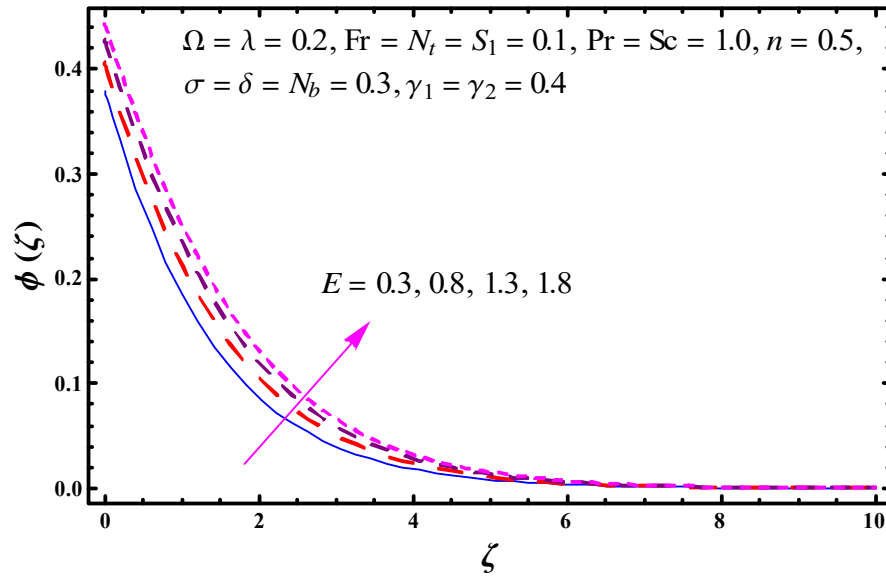
Figure 3.14 : Sketch for $\phi(\zeta)$ against E.
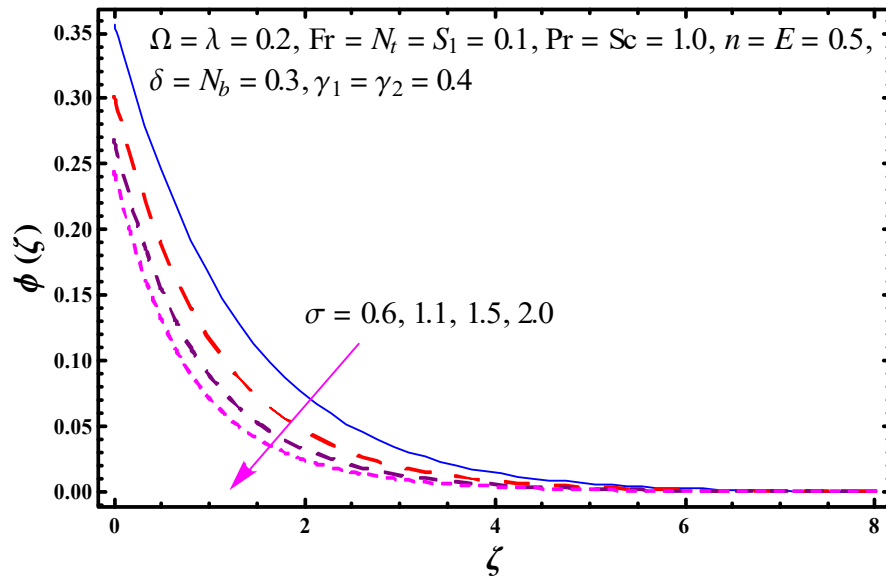
Figure 3.15 : Sketch for $\phi(\zeta)$ against σ.
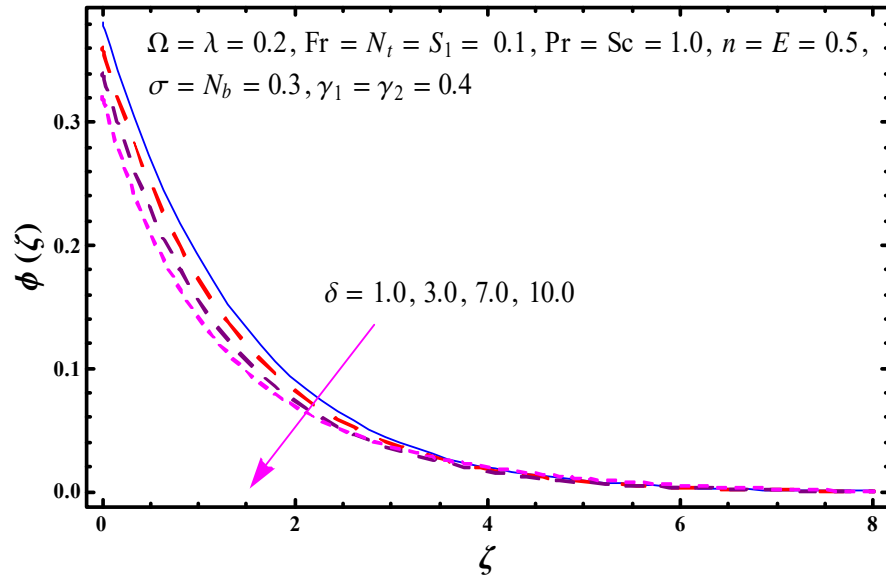
Figure 3.16 : Sketch for $\phi(\zeta)$ against δ.
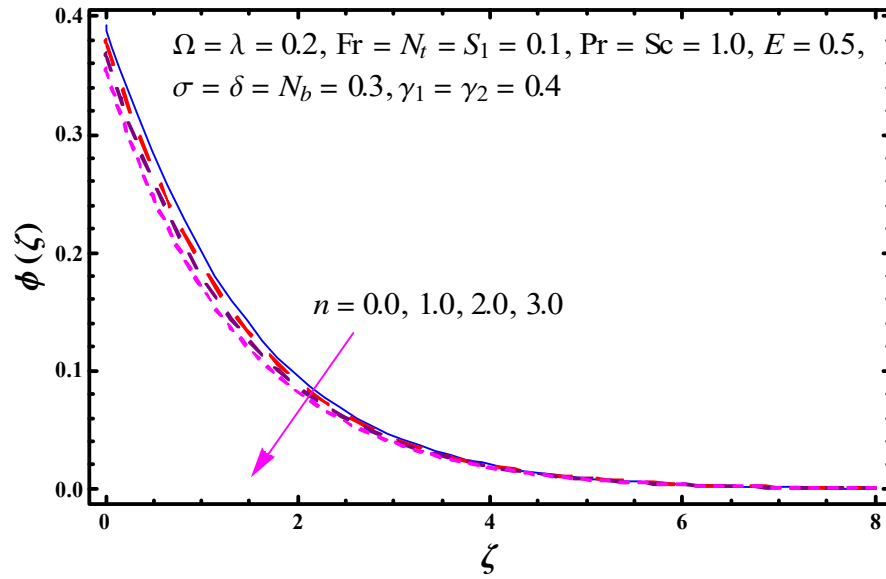
Figure 3.17 : Sketch for $\phi(\zeta)$ against n.
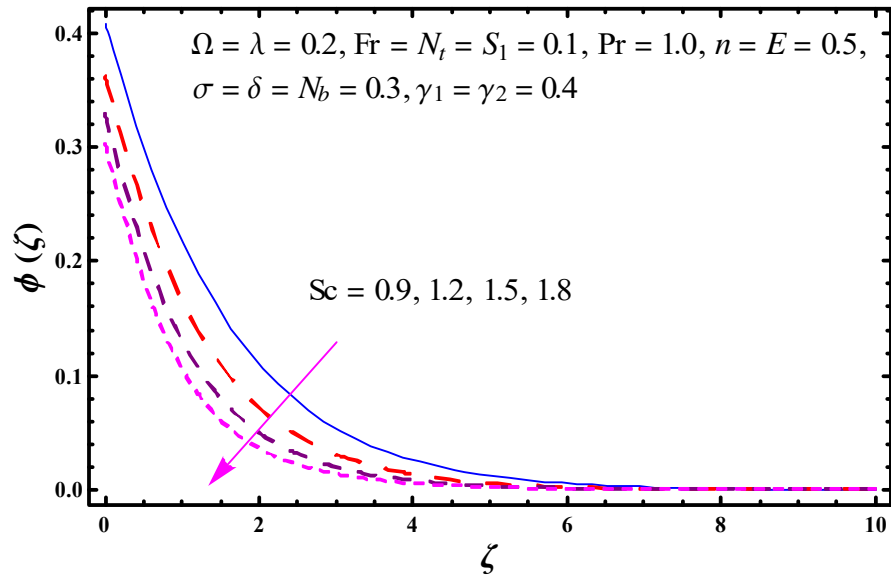
Figure 3.18 : Sketch for $\phi(\zeta)$ against Sc.
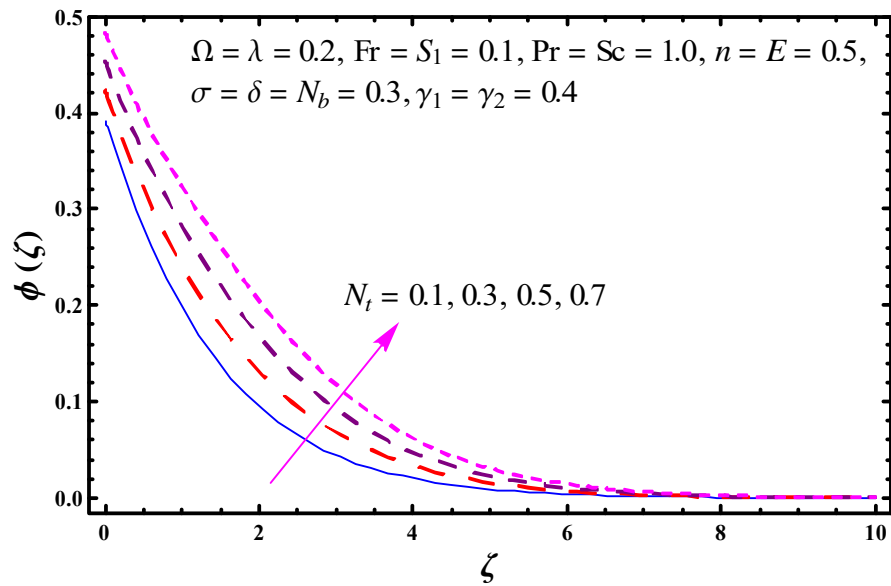
Figure 3.19 : Sketch for $\phi(\zeta)$ against N_t.
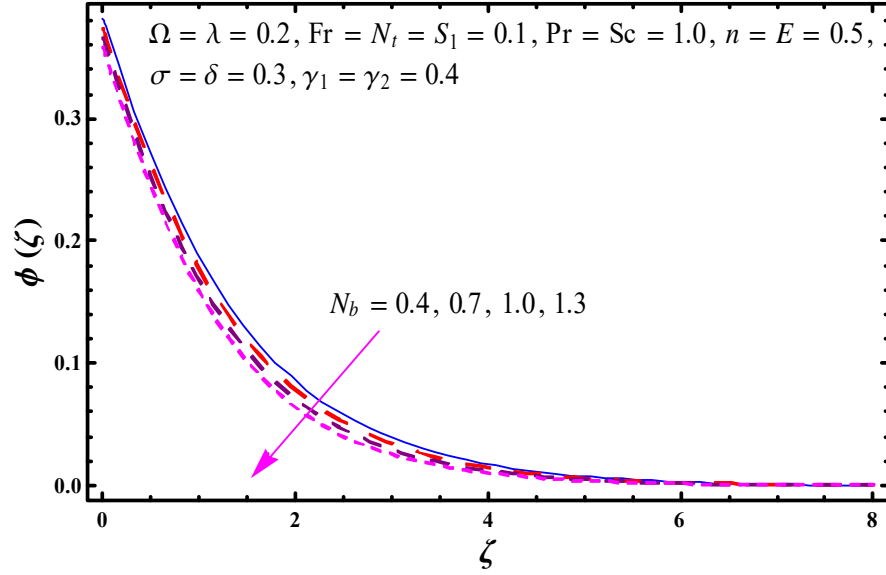
Figure 3.20 : Sketch for $\phi(\zeta)$ against N_b.

Table 3.1: Numerical data for coefficients of skin friction $-(\text{Re}_x)^{-1/2}C_{fy}$ and $-(\text{Re}_x)^{-1/2}C_{fx}$ through various estimations of λ, Ω and Fr.

λ	Fr	Ω	$-(\text{Re}_x)^{-1/2}C_{fx}$	$-(\text{Re}_x)^{-1/2}C_{fy}$
0.0	0.1	0.2	1.06329	0.23769
0.1			1.10532	0.22319
0.2			1.14675	0.21087
0.2	0.1	0.2	1.14675	0.21087
	0.2		1.17424	0.20994
	0.3		1.20121	0.20905
0.2	0.1	0.05	1.12589	0.05425
		0.1	1.13024	0.10786
		0.2	1.14675	0.21087

Table 3.2: Numerical data of local Nusselt number $(\text{Re}_x)^{-1/2}Nu_x$ for various estimations of λ, Fr, Ω, S_1, N_t, γ_1, N_b and $\Pr$.

λ	Fr	S_1	Ω	N_t	γ_1	N_b	$\Pr$	$(\text{Re}_x)^{-1/2}Nu_x$
0.0	0.1	0.1	0.2	0.1	0.4	0.3	1.0	0.20049
0.1								0.19793
0.2								0.19516
0.2	0.1	0.1	0.2	0.1	0.4	0.3	1.0	0.19516
	0.2							0.19395
	0.3							0.19274
0.2	0.1	0.0	0.2	0.1	0.4	0.3	1.0	0.22327
		0.1						0.19516
		0.2						0.10988
0.2	0.1	0.1	0.0	0.1	0.4	0.3	1.0	0.19988
			0.1					0.19867
			0.2					0.19516
0.2	0.1	0.1	0.2	0.1	0.4	0.3	1.0	0.19516
				0.7				0.17634
				1, 3				0.15554
0.2	0.1	0.1	0.2	0.1	0.15	0.3	1.0	0.10803
					0.30			0.16816
					0.45			0.20616
0.2	0.1	0.1	0.2	0.1	0.4	0.1	1.0	0.20031
						0.2		0.19775
						0.3		0.19516
0.2	0.1	0.1	0.2	0.1	0.4	0.3	1.0	0.19516
							1.5	0.22758
							2.0	0.24673

Table 3.3: Numerical data of local Sherwood number (rate of mass transfer) for several estimations of σ, Sc, N_t, E, δ, N_b, n and γ_2.

σ	Sc	N_t	E	δ	N_b	n	γ_2	$(\text{Re}_x)^{-1/2}Sh_x$
0.6	1.0	0.1	0.5	0.3	0.3	0.5	0.4	0.26683
1.4								0.29359
2.2								0.30795
0.3	0.5	0.1	0.5	0.3	0.3	0.5	0.4	0.24795
	1.0							0.27188
	1.5							0.28709
0.3	1.0	0.1	0.5	0.3	0.3	0.5	0.4	0.24795
		0.3						0.23063
		0.5						0.21648
0.3	1.0	0.1	0.15	0.3	0.3	0.5	0.4	0.25606
			0.30					0.25247
			0.45					0.24905
0.3	1.0	0.1	0.5	0.1	0.3	0.5	0.4	0.24649
				0.3				0.24795
				0.5				0.24932
0.3	1.0	0.1	0.5	0.3	0.1	0.5	0.4	0.22599
					0.2			0.24244
					0.3			0.24795
0.3	1.0	0.1	0.5	0.3	0.3	0.0	0.4	0.24679
						0.5		0.24795
						1.0		0.24915
0.3	1.0	0.1	0.5	0.3	0.3	0.5	0.3	0.20394
							0.7	0.34320
							1.0	0.40553

3.3   Major observations

Final points of this chapter are listed below:

- Qualitatively the effects of λ and Fr on temperature $\theta(\zeta)$ and nano-concentration $\phi(\zeta)$ are similar.

- Both temperature $\theta(\zeta)$ and nano-concentration $\phi(\zeta)$ represent increasing behavior for higher rotational parameter Ω.

- Temperature $\theta(\zeta)$ and associated thermal layer thickness are enhanced via $(S_1 > 0)$ while an opposite behavior is noted for $(S_1 < 0)$.

- Temperature and nano-concentration have increasing trend against higher γ_1 and γ_2.

- Higher E give stronger nano-concentration field $\phi(\zeta)$.

- An enhancement in Sc and Pr yields low temperature and nano-concentration.

- Nano-concentration $\phi(\zeta)$ shows decaying trend for higher δ and σ.

- Both Temperature and nano-concentration have similar behavior for N_t.

- Larger Brownian motion parameter N_b exhibit stronger temperature $\theta(\zeta)$ while opposite behavior holds for nano-concentration $\phi(\zeta)$.

Chapter 4

Influence of homogeneous-heterogeneous reactions in three-dimensional rotating flow of nanofluid subject to Darcy-Forchheimer porous medium: An optimal analysis

Non-Darcian three dimensional rotating flow of viscous fluid is analyzed in presence of heterogeneous-homogeneous reactions. A deformable surface generates flow. Surface has constant mass and thermal flux conditions. Novel characteristics of Brownian dispersion and thermophoresis are retained. Optimal homotopic strategy is used to construct the solutions. Roles of influential variables on physical quantities are graphically examined. Our findings reveal that an enhancement in thermophoresis parameter yields stronger thermal and concentration fields while opposite holds via higher Brownian motion parameter.

4.1 Statement

Here impact of homogeneous-heterogeneous reactions in 3D rotating flow of nanoliquid is discussed. Non-Darcian relation characterized permeable space. Constant heat and mass flux conditions are also considered. Buongiorno relation of nanoliquid is employed in mathematical development. Surface in Cartesian coordinate framework is considered. Liquid occupies the space $z \geq 0$. We denote c as the stretching rate. Homogeneous response for cubic catalysis is

$$A + 2B \rightarrow 3B, \ rate = k_c ab^2. \tag{4.1}$$

At surface the heterogeneous response is

$$A \rightarrow B, \ rate = k_s a. \tag{4.2}$$

Here rate constants are symbolized by k_c and k_s and the substance species A and B have concentrations a and b individually. Resulting expressions are

$$\frac{\partial u}{\partial x} + \frac{\partial v}{\partial y} + \frac{\partial w}{\partial z} = 0, \tag{4.3}$$

$$u\frac{\partial u}{\partial x} + v\frac{\partial u}{\partial y} + w\frac{\partial u}{\partial z} - 2\omega v = \nu\frac{\partial^2 u}{\partial z^2} - \frac{\nu}{k^*}u - Fu^2, \tag{4.4}$$

$$u\frac{\partial v}{\partial x} + v\frac{\partial v}{\partial y} + w\frac{\partial v}{\partial z} + 2\omega u = \nu\frac{\partial^2 v}{\partial z^2} - \frac{\nu}{k^*}v - Fv^2, \tag{4.5}$$

$$u\frac{\partial T}{\partial x} + v\frac{\partial T}{\partial y} + w\frac{\partial T}{\partial z} = \alpha^\star\frac{\partial^2 T}{\partial z^2} + \frac{(\rho c)_p}{(\rho c)_f}\left(\frac{D_T}{T_\infty}\left(\frac{\partial T}{\partial z}\right)^2 + D_B\left(\frac{\partial C}{\partial z}\frac{\partial T}{\partial z}\right)\right), \tag{4.6}$$

$$u\frac{\partial C}{\partial x} + v\frac{\partial C}{\partial y} + w\frac{\partial C}{\partial z} = \frac{D_T}{T_\infty}\left(\frac{\partial^2 T}{\partial z^2}\right) + D_B^*\left(\frac{\partial^2 C}{\partial z^2}\right), \tag{4.7}$$

$$u\frac{\partial a}{\partial x} + v\frac{\partial a}{\partial y} + w\frac{\partial a}{\partial z} = -k_c ab^2 + D_A\left(\frac{\partial^2 a}{\partial z^2}\right), \tag{4.8}$$

$$u\frac{\partial b}{\partial x} + v\frac{\partial b}{\partial y} + w\frac{\partial b}{\partial z} = k_c ab^2 + D_B\left(\frac{\partial^2 b}{\partial z^2}\right), \tag{4.9}$$

subject to conditions

$$u = cx = u_w(x), \ v = 0, \ w = 0, \ -k\left(\frac{\partial T}{\partial z}\right) = q_w, \ -D_B\left(\frac{\partial C}{\partial z}\right) = j_w, \left.\begin{array}{c}\\\\\end{array}\right\} \quad (4.10)$$

$$D_A\frac{\partial a}{\partial z} = k_s a, \ D_B\frac{\partial b}{\partial z} = -k_s a \ \text{at} \ z = 0,$$

$$u \to 0, \ v \to 0, \ T \to T_\infty, \ C \to C_\infty, \ a \to a_0, \ b \to 0 \ \text{as} \ z \to \infty. \quad (4.11)$$

Here u, v and w represent velocities in $x-$, $y-$ and $z-$directions, μ the absolute viscosity, k^* the porousness of permeable medium, $F = C_b/xk^{*1/2}$ the variable inertial coefficient of permeable space, C_b the drag coefficient, $\nu = \mu/\rho_f$ the kinematic viscosity, $\alpha^* = k/(\rho c)_f$ the warm diffusivity, $(\rho c)_f$ the warmth capability of the fluid, $(\rho c)_p$ the viable warmth capability of the nanomaterials, T the temperature, D_B^* the Brownian development, C the concentration and D_T thermophoretic dispersion coefficient. Letting

$$u = cxf'(\zeta), \ v = cxg(\zeta), \ w = -(c\nu)^{1/2}f(\zeta), \ \zeta = \left(\frac{c}{\nu}\right)^{1/2}z, \ T = T_\infty + \sqrt{\frac{\nu}{c}}\frac{q_w}{k}\theta(\zeta), \left.\begin{array}{c}\\\\\end{array}\right\} \quad (4.12)$$

$$C = C_\infty + \sqrt{\frac{\nu}{c}}\frac{j_w}{D_B}\phi(\zeta), \ a = a_0 r(\zeta), \ b = a_0 h(\zeta),$$

expression (4.3) is automatically verified and Eqs. $(4.4) - (4.11)$ are reduced to

$$f''' + ff'' - f'^2 + 2\Omega g - \lambda f' - Frf'^2 = 0, \quad (4.13)$$

$$g'' + fg' - f'g - 2\Omega f' - \lambda g - Frg^2 = 0, \quad (4.14)$$

$$\theta'' + \Pr\left(f\theta' + N_b\theta'\phi' + N_t\theta'^2\right) = 0, \quad (4.15)$$

$$\phi'' + Sc_b f\phi' + \frac{N_t}{N_b}\theta'' = 0, \quad (4.16)$$

$$\frac{1}{Sc}r'' + fr' - k_1 rh^2 = 0, \quad (4.17)$$

$$\frac{\delta}{Sc}h'' + fh' + k_1 rh^2 = 0, \quad (4.18)$$

$$f(0) = g(0) = 0, \ f'(0) = 1, \ \theta'(0) = -1, \ \phi'(0) = -1, \left.\begin{array}{c}\\\\\end{array}\right\} \quad (4.19)$$

$$r'(0) = k_2 r(0), \ \delta h'(0) = -k_2 r(0),$$

$$f'(\infty) \to 0, \ g(\infty) \to 0, \ \theta(\infty) \to 0, \ \phi(\infty) \to 0, \ r(\infty) \to 1, \ h(\infty) \to 0. \quad (4.20)$$

Here porosity parameter, Forchheimer number, swirling parameter, Prandtl parameter, Brownian movement parameter, Schmidt number, strength of homogeneous response, ratio of mass dissemination coefficients, thermophoresis parameter, Schmidt number (for heterogeneous-homogeneous responses) and strength of heterogeneous response are symbolized by λ, Fr, Ω, Pr, N_b, Sc_b, k_1, δ, N_t, Sc and k_2 separately. These parameters are characterized by:

$$\left.\begin{array}{c} \lambda = \frac{\nu}{k^* c}, \ Fr = \frac{C_b}{k^{*1/2}}, \ \Omega = \frac{\omega}{c}, \ \mathrm{Pr} = \frac{\nu}{\alpha^*}, \ N_b = \frac{(\rho c)_p D_B^*(C_w - C_\infty)}{(\rho c)_f \nu}, \ Sc_b = \frac{\nu}{D_B^*}, \\ k_1 = \frac{k_c a_0^2}{c}, \ \delta = \frac{D_B}{D_A}, \ N_t = \frac{(\rho c)_p D_T (T_w - T_\infty)}{(\rho c)_f \nu T_\infty}, \ Sc = \frac{\nu}{D_A}, \ k_2 = \frac{k_s}{D_A}\sqrt{\frac{\nu}{c}}. \end{array}\right\}$$ (4.21)

Assuming that $D_A = D_B$ we have $\delta = 1$ and thus

$$r(\zeta) + h(\zeta) = 1.$$ (4.22)

Now Eqs. (4.17) and (4.18) yield

$$\frac{1}{Sc}r'' + fr' - k_1(1-r)^2 r = 0,$$ (4.23)

with the boundary conditions

$$r'(0) = k_2 r(0), \ r(\infty) \to 1.$$ (4.24)

The physical quantities are given by

$$\left.\begin{array}{c} (\mathrm{Re}_x)^{-1/2} C_f = f''(0), \\ (\mathrm{Re}_x)^{-1/2} C_g = g'(0), \\ (\mathrm{Re}_x)^{-1/2} Nu_x = \frac{1}{\theta(0)}, \\ (\mathrm{Re}_x)^{-1/2} Sh_x = \frac{1}{\phi(0)}. \end{array}\right\}$$ (4.25)

In above mentioned expressions, local Reynolds number is $(\mathrm{Re}_x = u_w x / \nu)$.

4.2 Initial guesses

For OHAM solutions construction, the operators and initial guesses satisfy

$$f_0(\zeta) = 1 - e^{-\zeta}, \quad g_0(\zeta) = 0, \quad \theta_0(\zeta) = e^{-\zeta},$$
$$\phi_0(\zeta) = e^{-\zeta}, \quad r_0(\zeta) = 1 - \frac{1}{2}e^{-k_2\zeta}, \tag{4.26}$$

$$\dddot{\mathcal{L}}_f^* = \frac{d^3 f}{d\zeta^3} - \frac{df}{d\zeta}, \quad \dddot{\mathcal{L}}_g^* = \frac{d^2 g}{d\zeta^2} - g, \quad \dddot{\mathcal{L}}_\theta^* = \frac{d^2 \theta}{d\zeta^2} - \theta,$$
$$\dddot{\mathcal{L}}_\phi^* = \frac{d^2 \phi}{d\zeta^2} - \phi, \quad \dddot{\mathcal{L}}_r^* = \frac{d^2 r}{d\zeta^2} - r. \tag{4.27}$$

We have following properties

$$\dddot{\mathcal{L}}_f^\star \left[\tilde{B}_1^{\star\star\star} + \tilde{B}_2^{\star\star\star} e^\zeta + \tilde{B}_3^{\star\star\star} e^{-\zeta} \right] = 0, \quad \dddot{\mathcal{L}}_g^\star \left[\tilde{B}_4^{\star\star\star} e^\zeta + \tilde{B}_5^{\star\star\star} e^{-\zeta} \right] = 0,$$
$$\dddot{\mathcal{L}}_\theta^\star \left[\tilde{B}_6^{\star\star\star} e^\zeta + \tilde{B}_7^{\star\star\star} e^{-\zeta} \right] = 0, \quad \dddot{\mathcal{L}}_\phi^\star \left[\tilde{B}_8^{\star\star\star} e^\zeta + \tilde{B}_9^{\star\star\star} e^{-\zeta} \right] = 0,$$
$$\dddot{\mathcal{L}}_\theta^\star \left[\tilde{B}_{10}^{\star\star\star} e^\zeta + \tilde{B}_{11}^{\star\star\star} e^{-\zeta} \right] = 0, \tag{4.28}$$

in which $\tilde{B}_j^{\star\star\star}$ $(j = 1 - 11)$ indicate arbitrary constants.

4.3 OHAM solutions

The non-zero parameters $\hbar_f$, $\hbar_g$, $\hbar_\theta$, $\hbar_\phi$ and $\hbar_r$ in arrangements direct the combination partition and furthermore rate of homotopic arrangements. For optimal information of $\hbar_f$, $\hbar_g$, $\hbar_\theta$, $\hbar_\phi$ and $\hbar_r$, idea of minimization through average squared errors proposed by Liao [87] is utilized as follows.

$$\varepsilon_{\mathring{m}^\star}^f = \frac{1}{\check{k}^\star + 1} \sum_{j=0}^{\check{k}^\star} \left[\mathcal{N}_f \left(\sum_{\mathring{i}=0}^{\mathring{m}^\star} \tilde{f}(\zeta), \sum_{\mathring{i}=0}^{\mathring{m}^\star} \tilde{g}(\zeta) \right)_{\zeta = j\delta\zeta} \right]^2, \tag{4.29}$$

$$\varepsilon_{\mathring{m}^\star}^g = \frac{1}{\check{k}^\star + 1} \sum_{j=0}^{\check{k}^\star} \left[\mathcal{N}_g \left(\sum_{\mathring{i}=0}^{\mathring{m}^\star} \tilde{f}(\zeta), \sum_{\mathring{i}=0}^{\mathring{m}^\star} \tilde{g}(\zeta) \right)_{\zeta = j\delta\zeta} \right]^2, \tag{4.30}$$

$$\varepsilon_{\mathring{m}^\star}^\theta = \frac{1}{\check{k}^\star + 1} \sum_{j=0}^{\check{k}^\star} \left[\mathcal{N}_\theta \left(\sum_{\mathring{i}=0}^{\mathring{m}^\star} \tilde{f}(\zeta), \sum_{\mathring{i}=0}^{\mathring{m}^\star} \tilde{g}(\zeta), \sum_{\mathring{i}=0}^{\mathring{m}^\star} \tilde{\theta}(\zeta) \right)_{\zeta = j\delta\zeta} \right]^2, \tag{4.31}$$

$$\varepsilon_{\mathring{m}^\star}^\phi = \frac{1}{\check{k}^\star + 1} \sum_{j=0}^{\check{k}^\star} \left[\mathcal{N}_\phi \left(\sum_{\mathring{i}=0}^{\mathring{m}^\star} \tilde{f}(\zeta), \sum_{\mathring{i}=0}^{\mathring{m}^\star} \tilde{g}(\zeta), \sum_{\mathring{i}=0}^{\mathring{m}^\star} \tilde{\phi}(\zeta) \right)_{\zeta = j\delta\zeta} \right]^2, \tag{4.32}$$

$$\varepsilon_{\mathring{m}^\star}^r = \frac{1}{\check{k}^\star + 1} \sum_{j=0}^{\check{k}^\star} \left[\mathcal{N}_r \left(\sum_{\mathring{i}=0}^{\mathring{m}^\star} \tilde{f}(\zeta), \sum_{\mathring{i}=0}^{\mathring{m}^\star} \tilde{g}(\zeta), \sum_{\mathring{i}=0}^{\mathring{m}^\star} \tilde{r}(\zeta) \right)_{\zeta = j\delta\zeta} \right]^2, \tag{4.33}$$

By Liao [87] :

$$\varepsilon_{\mathring{m}^\star}^t = \varepsilon_{\mathring{m}^\star}^f + \varepsilon_{\mathring{m}^\star}^g + \varepsilon_{\mathring{m}^\star}^\theta + \varepsilon_{\mathring{m}^\star}^\phi + \varepsilon_{\mathring{m}^\star}^r, \tag{4.34}$$

where $\varepsilon_{\mathring{m}^\star}^t$ denotes total residual squared error, $\delta\zeta = 0.5$ and $k = 20$. Optimal data for convergence control parameters at 2nd order of approximations is $\hbar_f = -0.57714$, $\hbar_g = -1.35539$, $\hbar_\theta = -1.53886$, $\hbar_\phi = -1.34514$, $\hbar_r = -1.47433$ and $\varepsilon_{\mathring{m}^\star}^t = 2.84 \times 10^{-2}$. Figure 4.1 displays the plot of total residual error. Table 4.1 demonstrates individual normal squared residual errors. It is examined that individual normal squared residual errors decays through order.
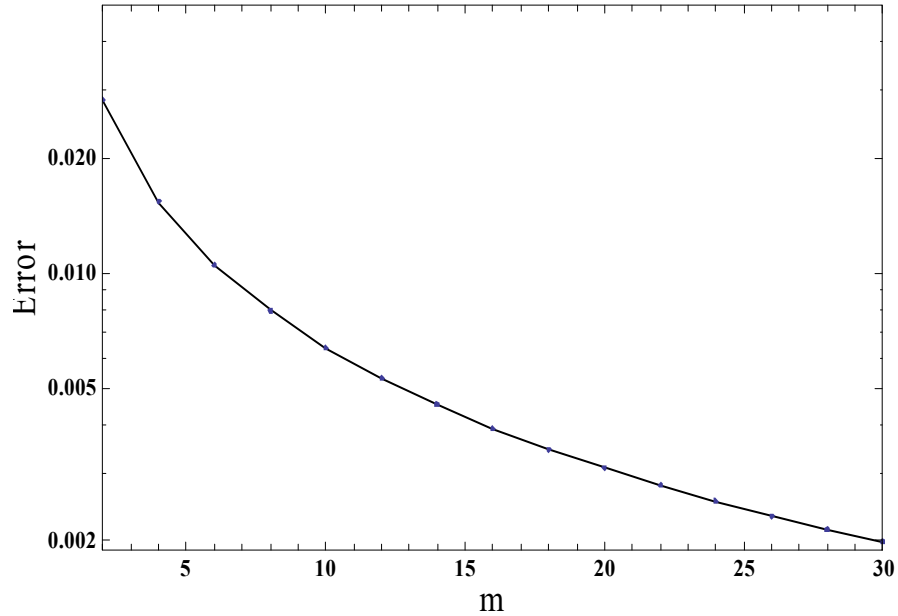
Figure 4.1 : Total residual error sketch.

Table 4.1. Optimal convergence control variables and total average squared residual errors.

$\mathring{m}$	$\varepsilon_{\mathring{m}}^{f}$	$\varepsilon_{\mathring{m}}^{g}$	$\varepsilon_{\mathring{m}}^{\theta}$	$\varepsilon_{\mathring{m}}^{\phi}$	$\varepsilon_{\mathring{m}}^{r}$
2	5.01×10^{-4}	8.19×10^{-5}	1.16×10^{-2}	1.61×10^{-2}	9.78×10^{-5}
6	5.71×10^{-5}	1.10×10^{-5}	3.60×10^{-3}	6.78×10^{-3}	5.36×10^{-5}
10	2.07×10^{-5}	3.95×10^{-6}	1.80×10^{-3}	4.52×10^{-3}	4.11×10^{-5}
16	8.50×10^{-6}	1.43×10^{-6}	8.62×10^{-4}	3.02×10^{-3}	3.10×10^{-5}
20	5.63×10^{-6}	8.66×10^{-7}	5.88×10^{-4}	2.47×10^{-3}	2.68×10^{-5}
24	4.03×10^{-6}	5.68×10^{-7}	4.23×10^{-4}	2.08×10^{-3}	2.35×10^{-5}
30	2.68×10^{-6}	3.34×10^{-7}	2.79×10^{-4}	1.68×10^{-3}	1.99×10^{-5}

4.4 Discussion

This part shows outcomes of physical flow variables like porosity parameter $\lambda(0.1 \leqslant \lambda \leqslant 0.7)$, Forchheimer number $Fr(0.0 \leqslant Fr \leqslant 0.9)$, rotational parameter $\Omega(0.00 \leqslant \Omega \leqslant 0.06)$, Prandtl parameter $\Pr(0.7 \leqslant \Pr \leqslant 1.6)$, Schmidt parameter $Sc_b(0.8 \leqslant Sc_b \leqslant 1.4)$, Brownian movement parameter $N_b(0.1 \leqslant N_b \leqslant 0.4)$, thermophoresis number $N_t(0.00 \leqslant N_t \leqslant 0.45)$, Schmidt number $Sc(0.1 \leqslant Sc \leqslant 1.5)$ (for homogeneous-heterogeneous reactions), homogeneous reaction parameter $k_1(0.00 \leqslant k_1 \leqslant 0.75)$ and heterogeneous reaction parameter $k_2(0.22 \leqslant k_2 \leqslant 0.55)$ on nondimensional temperature $\theta(\zeta)$, concentration $\phi(\zeta)$ and concentration rate $r(\zeta)$. Effect of Forchheimer number Fr on $\theta(\zeta)$ appeared in Figure 4.2. Both $\theta(\zeta)$ and thermal layer are enhanced for Fr. Physically an enhancement in Fr yields generation of higher drag forces (resistive forces) and consequently due to these forces the temperature of fluid enhances. Figure 4.3 explains impact of λ on temperature $\theta(\zeta)$. It is examined that by elevating λ, $\theta(\zeta)$ raises. Figure 4.4 presents the curves of $\theta(\zeta)$ via Ω. Higher Ω improves $\theta(\zeta)$ and thickness of thermal layer. Figure 4.5 demonstrates that $\theta(\zeta)$ is diminished via greater Pr. Figure 4.6 shows that how thermophoresis variable N_t influences temperature field. Higher N_t comprise more temperature field. Figure 4.7 is developed to see the variation in $\theta(\zeta)$ via greater Brownian movement parameter N_b. More N_b offers an improvement in $\theta(\zeta)$. Figure 4.8 presents varieties in nano-concentration $\phi(\zeta)$ for various estimations of Fr. Here $\phi(\zeta)$ becomes less for greater Fr. Figure 4.9 exhibits role of λ on $\phi(\zeta)$. Here λ enhanced $\phi(\zeta)$ and related layer thickness.

Curves of $\phi(\zeta)$ against various estimations of Ω are shown in Figure 4.10. An increase in Ω corresponds to more $\phi(\zeta)$. Figure 4.11 is developed to analyze the variation of $\phi(\zeta)$ against higher Schmidt number Sc_b. This Figure demonstrates that higher Sc_b yields reduction in $\phi(\zeta)$. Figure 4.12 displays nano-concentration $\phi(\zeta)$ via greater estimations of N_t. Greater N_t present more $\phi(\zeta)$. Figure 4.13 clarifies that nano-concentraton $\phi(\zeta)$ decreases for N_b. Figure 4.14 outlines that concentration rate $r(\zeta)$ elevates against higher Forchheimer number Fr. Figure 4.15 is plotted to notice that how porosity λ changes $r(\zeta)$. By expanding λ, $r(\zeta)$ exhibits increasing pattern. Impact of Ω on $r(\zeta)$ is depicted in Figure 4.16. Here $r(\zeta)$ is higher by means of Ω. Figure 4.17 portrays that Schmidt number Sc relate to more $r(\zeta)$. From Figure 4.18 we see that higher homogeneous response parameter k_1 demonstrates a decrease in $r(\zeta)$. Figure 4.19 shows that more heterogeneous response parameter k_2 gives higher concentration rate $r(\zeta)$. Figure 4.20 introduces the effects of Ω and Fr on $C_f \operatorname{Re}_x^{1/2}$. It is seen that $C_f \operatorname{Re}_x^{1/2}$ upgrades for both Ω and Fr. Figure 4.21 indicates effects of Ω and λ on $C_f \operatorname{Re}_x^{1/2}$. Obviously $C_f \operatorname{Re}_x^{1/2}$ demonstrates elevating behavior for Ω and λ. Figure 4.22 elucidates outcome of Ω and Fr on $C_g \operatorname{Re}_y^{1/2}$. Clearly $C_g \operatorname{Re}_y^{1/2}$ elevates against stronger Ω while reduction is observed via higher Fr. Figure 4.23 displays the impacts of Ω and λ on $C_g \operatorname{Re}_y^{1/2}$. Obviously $C_g \operatorname{Re}_y^{1/2}$ shows similar pattern against higher λ and Ω. Highlights of Pr and N_b on $Nu_x \operatorname{Re}_x^{-1/2}$ are revealed by means of Figure 4.24. Strikingly $Nu_x \operatorname{Re}_x^{-1/2}$ decays for both Pr and N_b. Figure 4.25 outlines the effects of Sc_b and N_t on $Sh_x \operatorname{Re}_x^{-1/2}$. From this Figure it is examined that $Sh_x \operatorname{Re}_x^{-1/2}$ decays via higher N_t while inverse outcomes are noticed for Sc_b. Table 4.2 validates the present results with the previous published results in a limiting sense. Here we noticed that the present OHAM solutions have good agreement with the previous solutions by Wang [27].

$\lambda = 0.2, \Omega = N_t = 0.1, k_1 = N_b = 0.3, k_2 = 0.5, \text{Sc} = \text{Pr} = 1.0, \text{Sc}_b = 0.7$

Fr = 0.0, 0.3, 0.6, 0.9
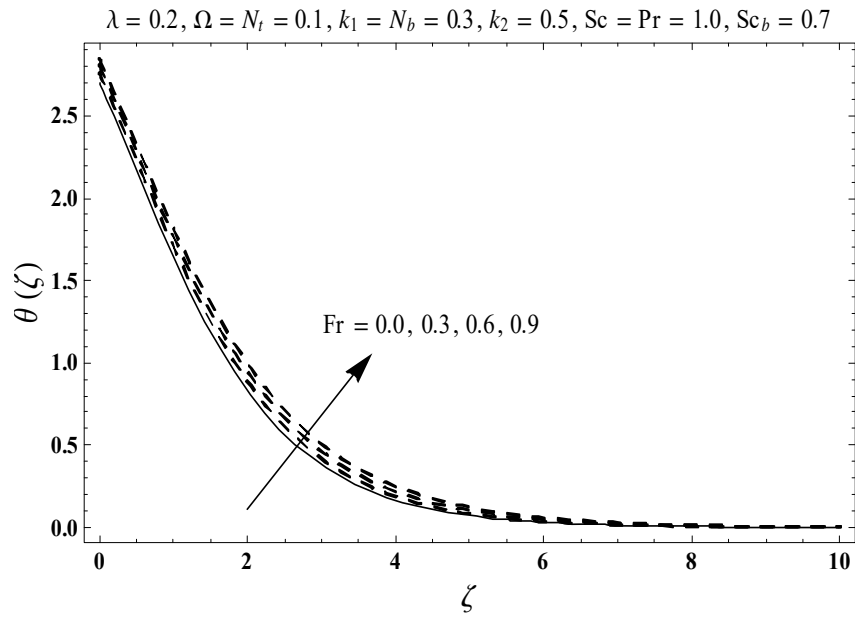
Figure 4.2 : Sketch for $\theta(\zeta)$ against Fr.

$\text{Fr} = \Omega = N_t = 0.1, k_1 = N_b = 0.3, k_2 = 0.5, \text{Sc} = \text{Pr} = 1.0, \text{Sc}_b = 0.7$

$\lambda = 0.1, 0.3, 0.5, 0.7$
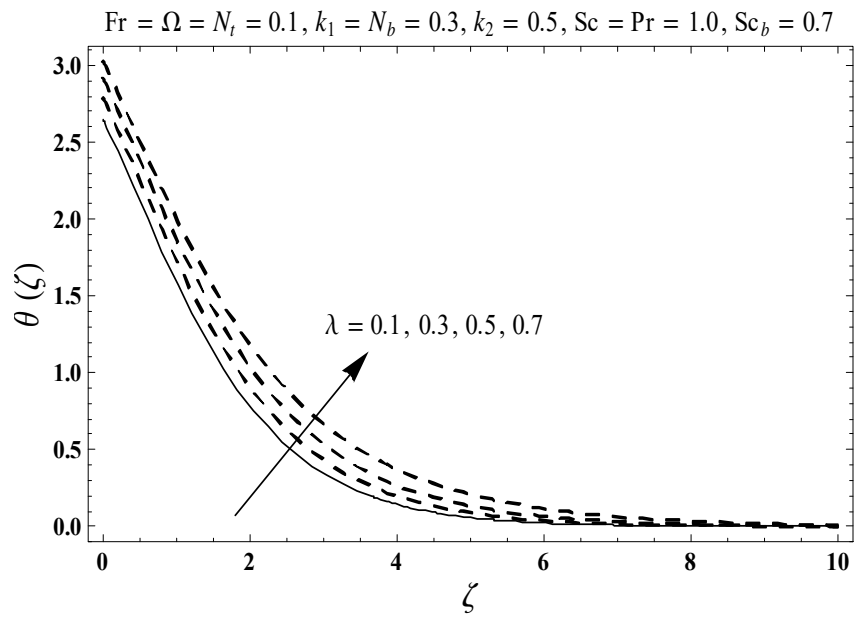
Figure 4.3 : Sketch for $\theta(\zeta)$ against λ.

$\lambda = 0.2$, Fr $= N_t = 0.1$, $k_1 = N_b = 0.3$, $k_2 = 0.5$, Sc $=$ Pr $= 1.0$, Sc$_b = 0.7$

$\Omega = 0.0$, 0.02, 0.04, 0.06
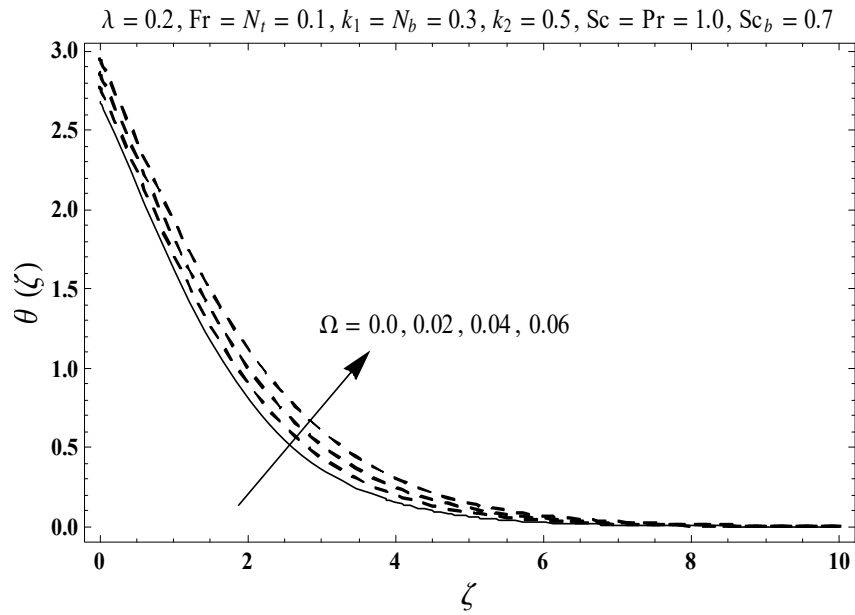
Figure 4.4 : Sketch for $\theta(\zeta)$ against Ω.

$\lambda = 0.2$, Fr $= \Omega = N_t = 0.1$, $k_1 = N_b = 0.3$, $k_2 = 0.5$, Sc $= 1.0$, Sc$_b = 0.7$

Pr $= 0.7$, 1.0, 1.3, 1.6
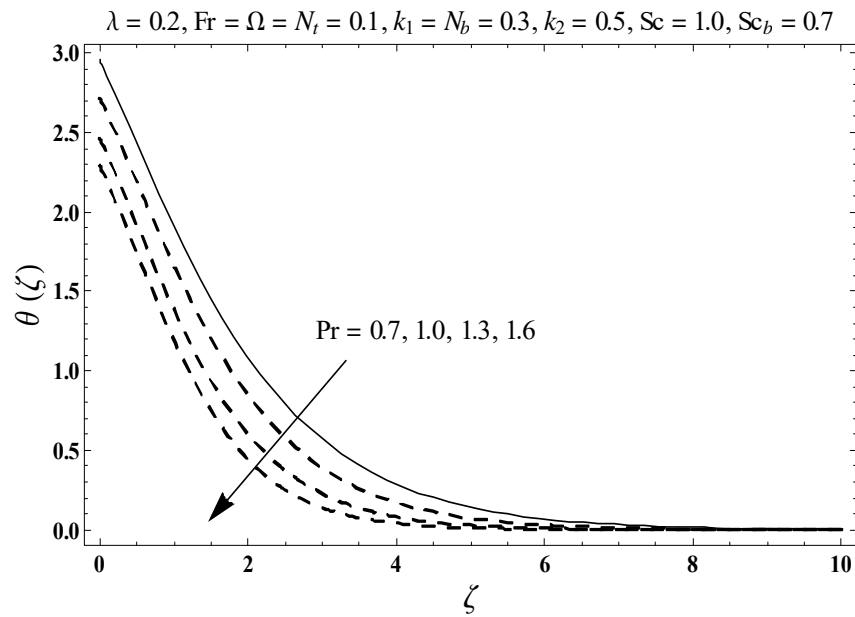
Figure 4.5 : Sketch for $\theta(\zeta)$ against Pr.

$\lambda = 0.2$, Fr $= \Omega = 0.1$, $k_1 = N_b = 0.3$, $k_2 = 0.5$, Sc $=$ Pr $= 1.0$, Sc$_b = 0.7$

$N_t = 0.0, 0.15, 0.30, 0.45$
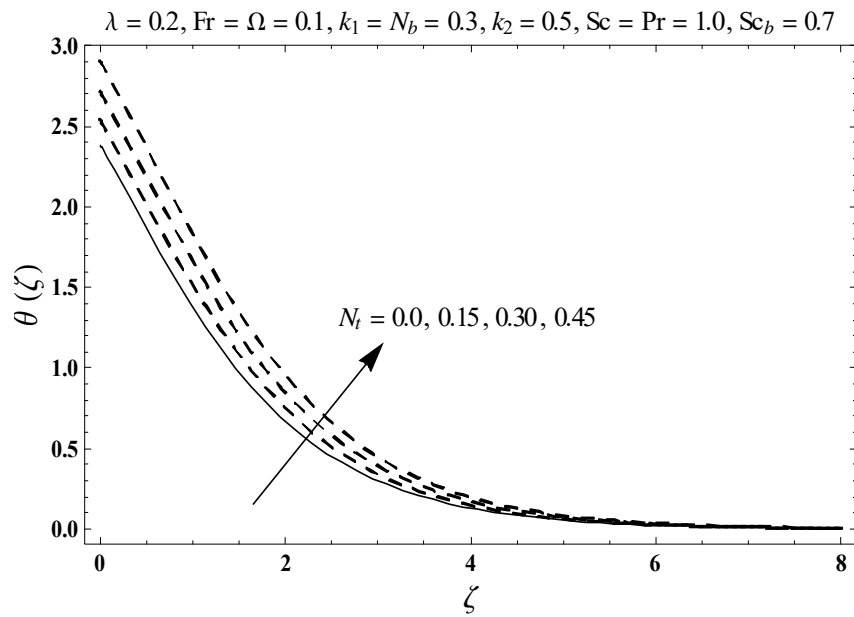
Figure 4.6 : Sketch for $\theta(\zeta)$ against N_t.

$\lambda = 0.2$, Fr $= \Omega = N_t = 0.1$, $k_1 = 0.3$, $k_2 = 0.5$, Sc $=$ Pr $= 1.0$, Sc$_b = 0.7$

$N_b = 0.4, 0.7, 1.0, 1.3$
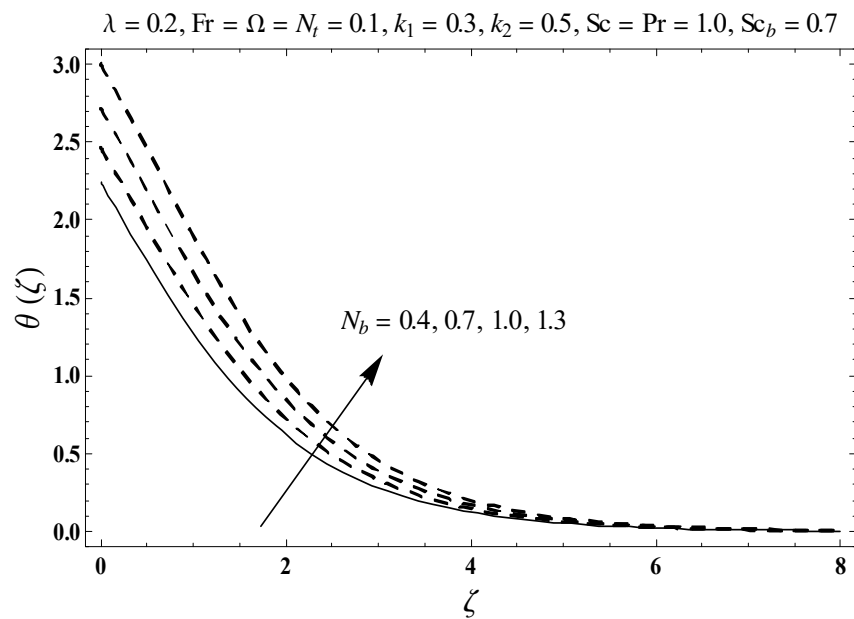
Figure 4.7 : Sketch for $\theta(\zeta)$ against N_b.

63

$\lambda = 0.2, \Omega = N_t = 0.1, k_1 = N_b = 0.3, k_2 = 0.5, \text{Sc} = \text{Pr} = 1.0, \text{Sc}_b = 0.7$

Fr = 0.0, 0.3, 0.6, 0.9
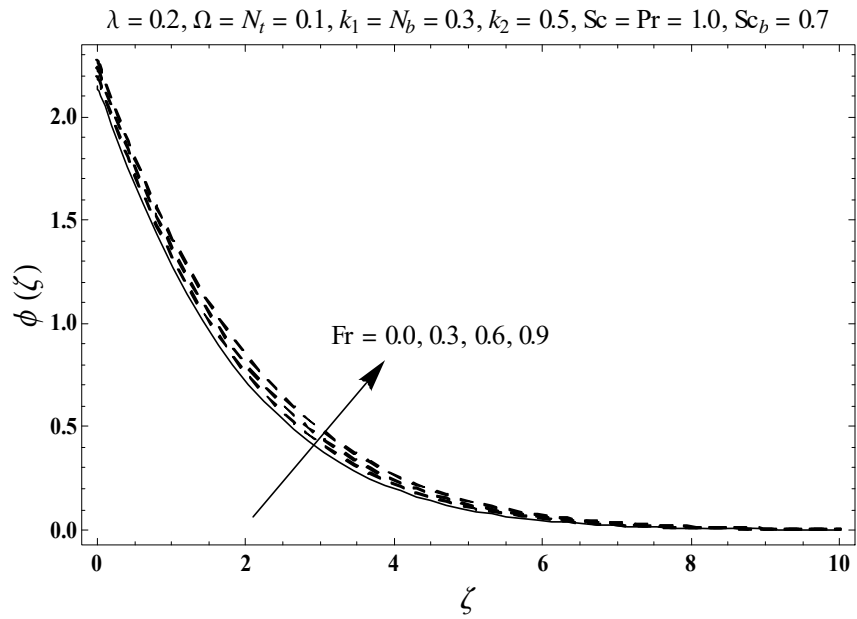
Figure 4.8 : Sketch for $\phi(\zeta)$ against Fr.

$\text{Fr} = \Omega = N_t = 0.1, k_1 = N_b = 0.3, k_2 = 0.5, \text{Sc} = \text{Pr} = 1.0, \text{Sc}_b = 0.7$

$\lambda = 0.1, 0.3, 0.5, 0.7$
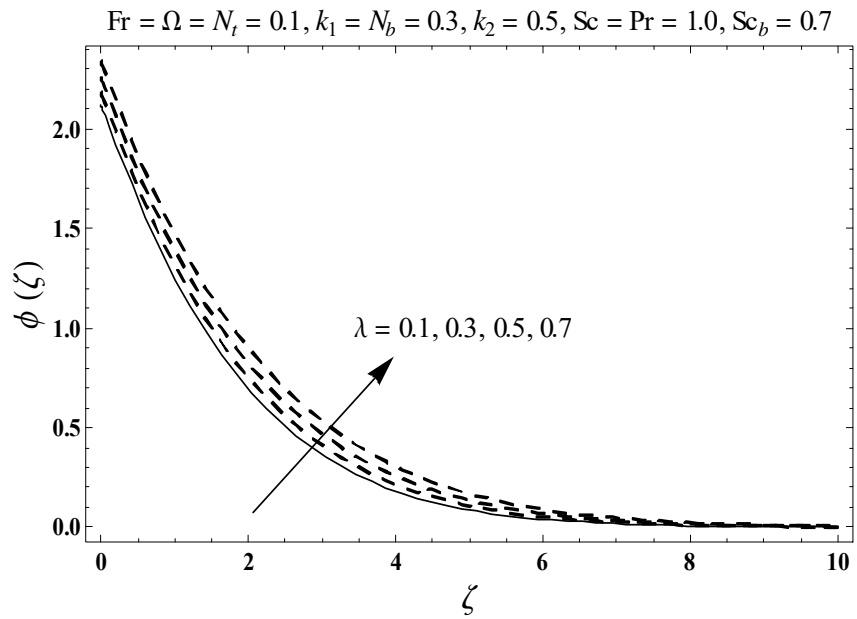
Figure 4.9 : Sketch for $\phi(\zeta)$ against λ.

64

$\lambda = 0.2$, $\mathrm{Fr} = N_t = 0.1$, $k_1 = N_b = 0.3$, $k_2 = 0.5$, $\mathrm{Sc} = \mathrm{Pr} = 1.0$, $\mathrm{Sc}_b = 0.7$

$\Omega = 0.0,\, 0.02,\, 0.04,\, 0.06$
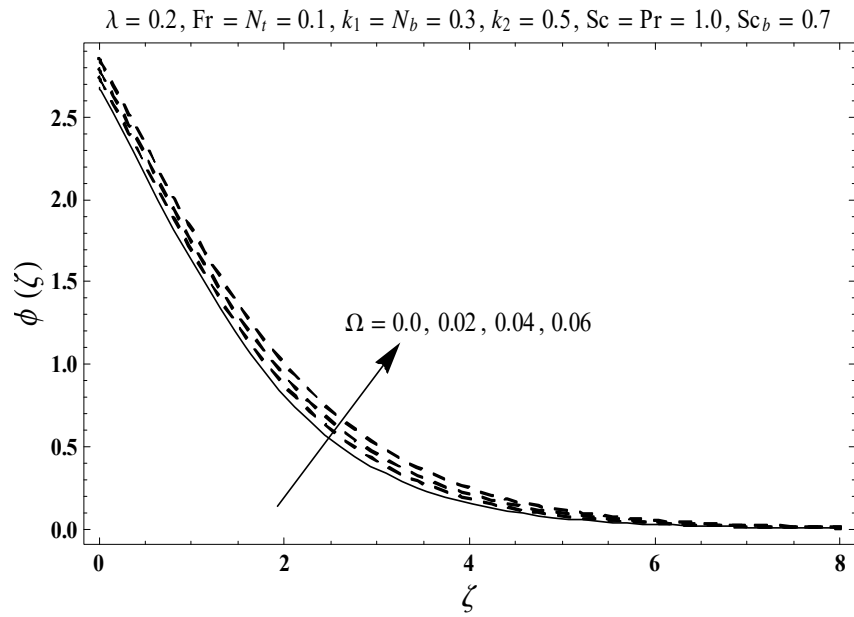
Figure 4.10 : Sketch for $\phi(\zeta)$ against Ω.

$\lambda = 0.2$, $\mathrm{Fr} = \Omega = N_t = 0.1$, $k_1 = N_b = 0.3$, $k_2 = 0.5$, $\mathrm{Sc} = \mathrm{Pr} = 1.0$

$\mathrm{Sc}_b = 0.8,\, 1.0,\, 1.2,\, 1.4$
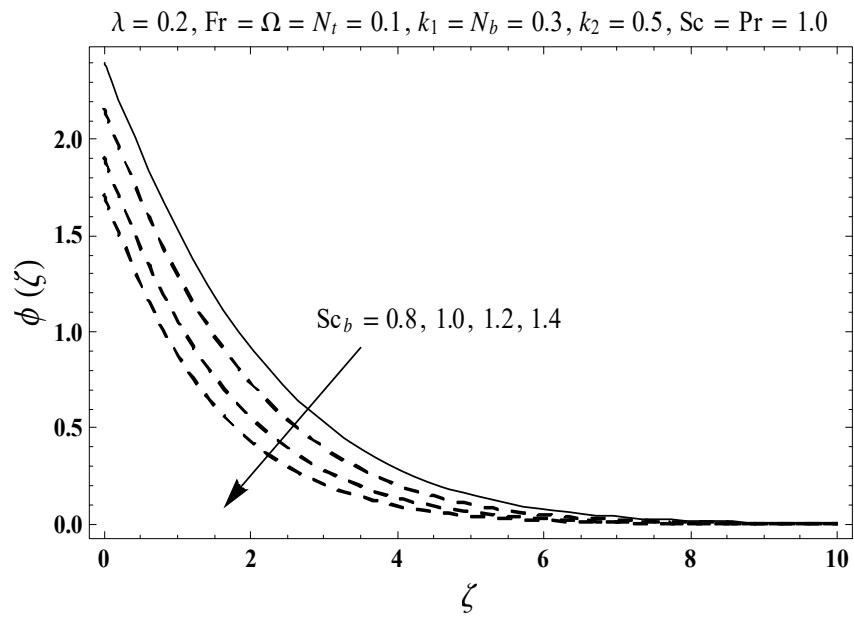
Figure 4.11 : Sketch for $\phi(\zeta)$ against Sc_b.

$\lambda = 0.2$, Fr $= \Omega = 0.1$, $k_1 = N_b = 0.3$, $k_2 = 0.5$, Sc $=$ Pr $= 1.0$, Sc$_b = 0.7$

$N_t = 0.0$, 0.15, 0.30, 0.45
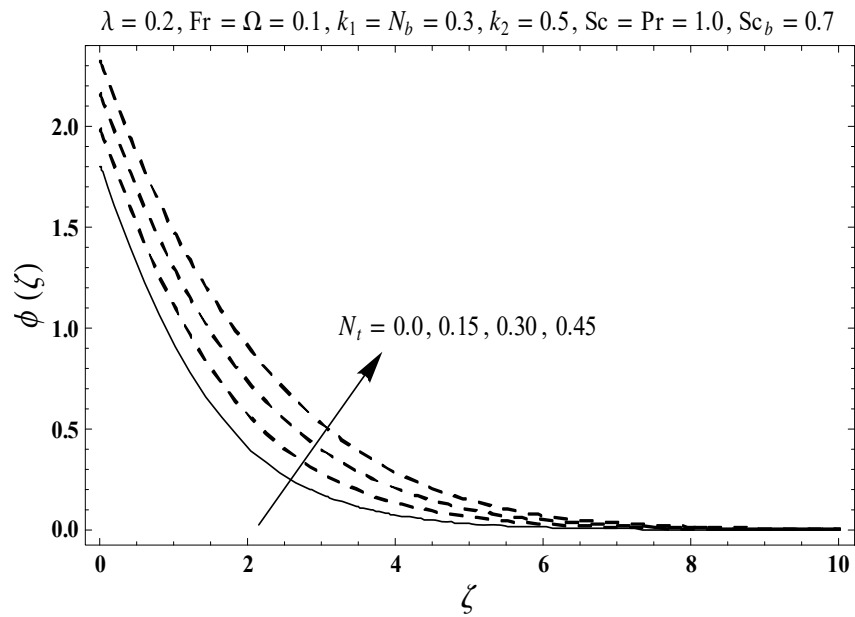
Figure 4.12 : Sketch for $\phi(\zeta)$ against N_t.

$\lambda = 0.2$, Fr $= \Omega = N_t = 0.1$, $k_1 = 0.3$, $k_2 = 0.5$, Sc $=$ Pr $= 1.0$, Sc$_b = 0.7$

$N_b = 0.1$, 0.2, 0.3, 0.4
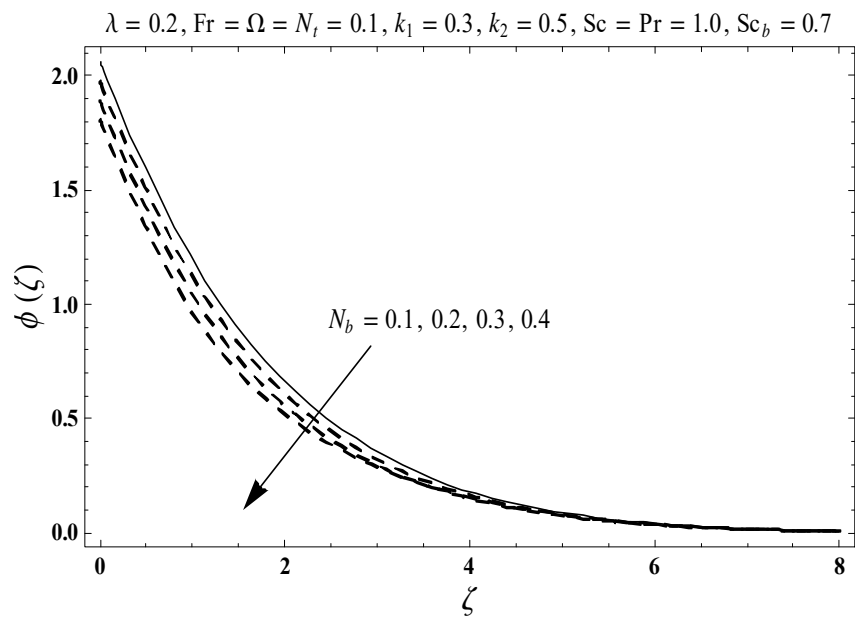
Figure 4.13 : Sketch for $\phi(\zeta)$ against N_b.
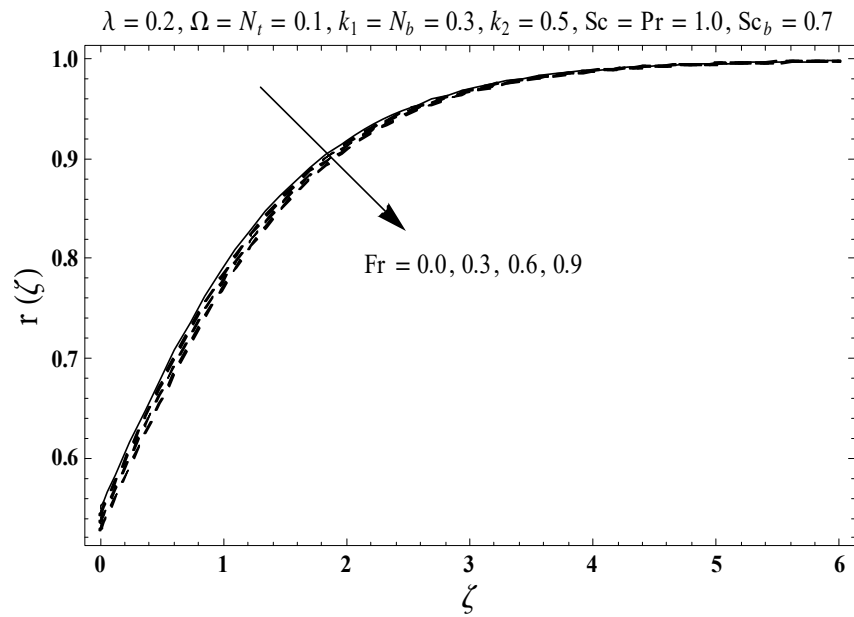
Figure 4.14 : Sketch for $r(\zeta)$ against Fr.
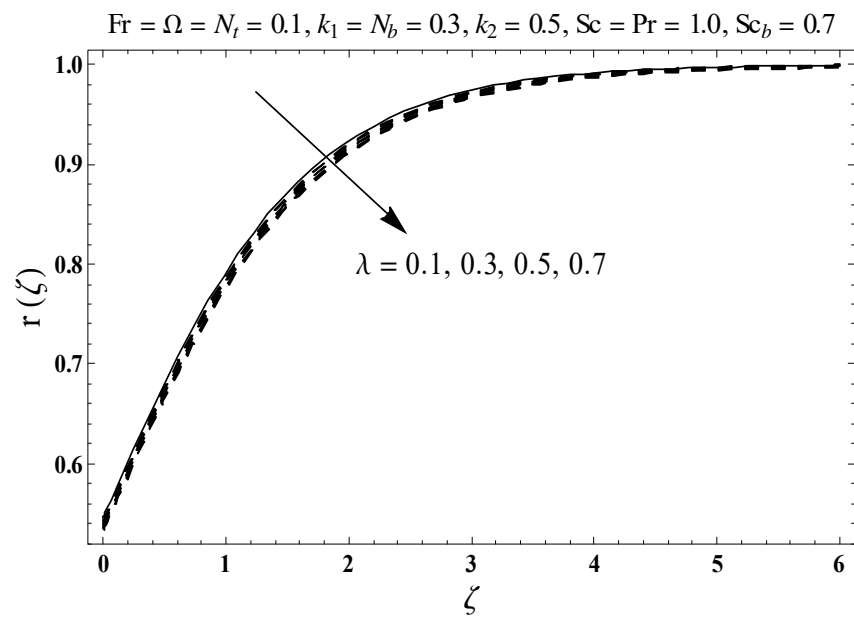
Figure 4.15 : Sketch for $r(\zeta)$ against λ.

$\lambda = 0.2$, Fr $= N_t = 0.1$, $k_1 = N_b = 0.3$, $k_2 = 0.5$, Sc $=$ Pr $= 1.0$, Sc$_b = 0.7$

$\Omega = 0.0, 0.02, 0.04, 0.06$
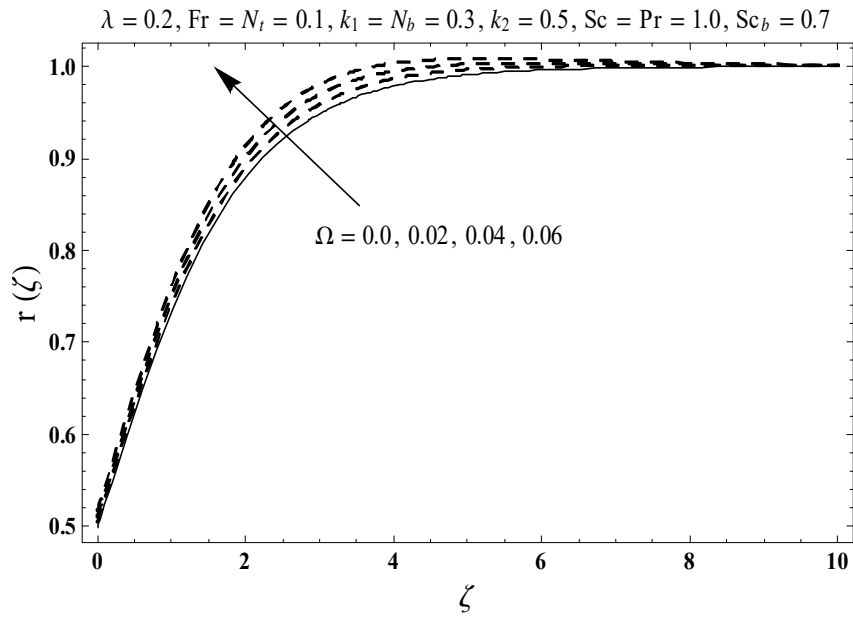
Figure 4.16 : Sketch for $r(\zeta)$ against Ω.

$\lambda = 0.2$, Fr $= \Omega = N_t = 0.1$, $k_1 = N_b = 0.3$, $k_2 = 0.5$, Pr $= 1.0$, Sc$_b = 0.7$

Sc $= 0.1, 0.5, 1.0, 1.5$
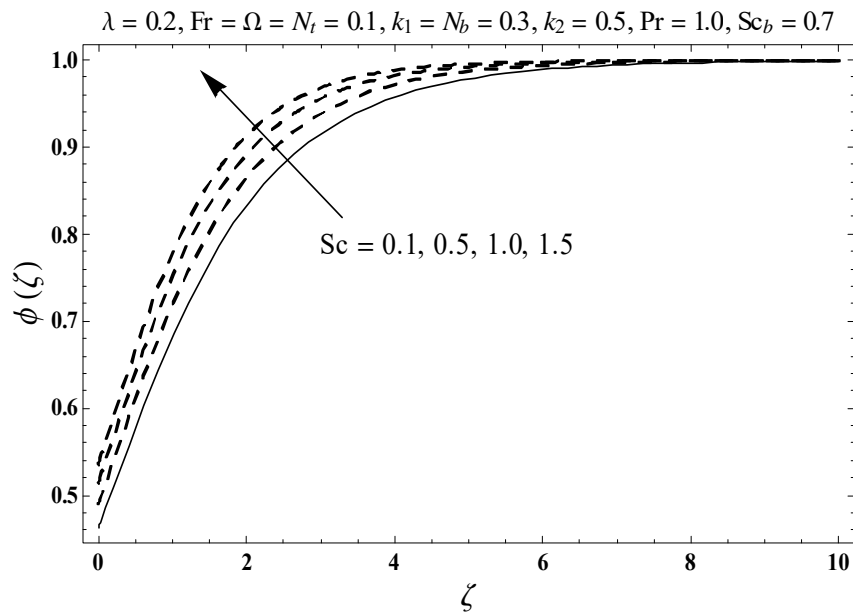
Figure 4.17 : Sketch for $r(\zeta)$ against Sc.

68

$k_1 = 0.0, 0.25, 0.50, 0.75$
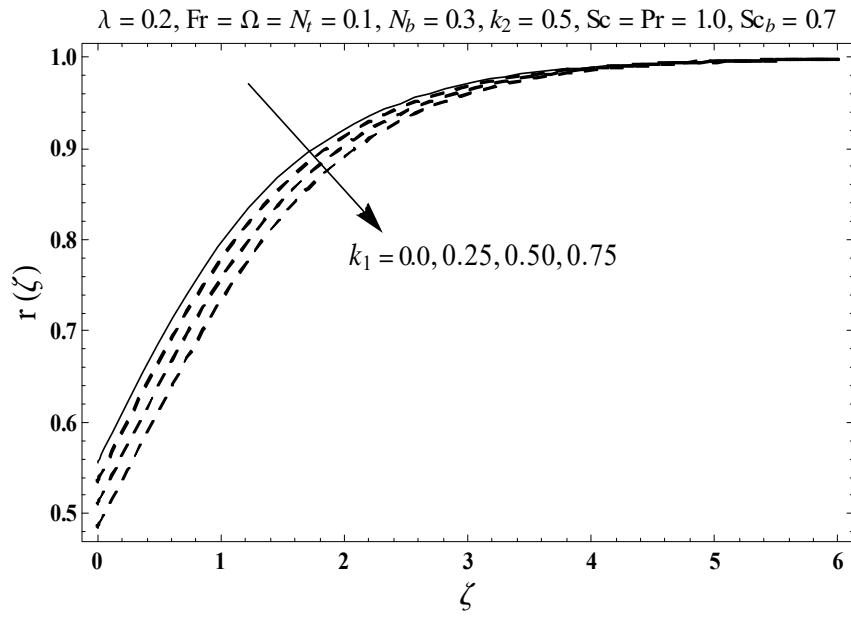
Figure 4.18 : Sketch for $r(\zeta)$ against k_1.

$\lambda = 0.2$, Fr = $\Omega = N_t = 0.1$, $k_1 = N_b = 0.3$, Sc = Pr = 1.0, Sc$_b = 0.7$

$k_2 = 0.22, 0.33, 0.44, 0.55$
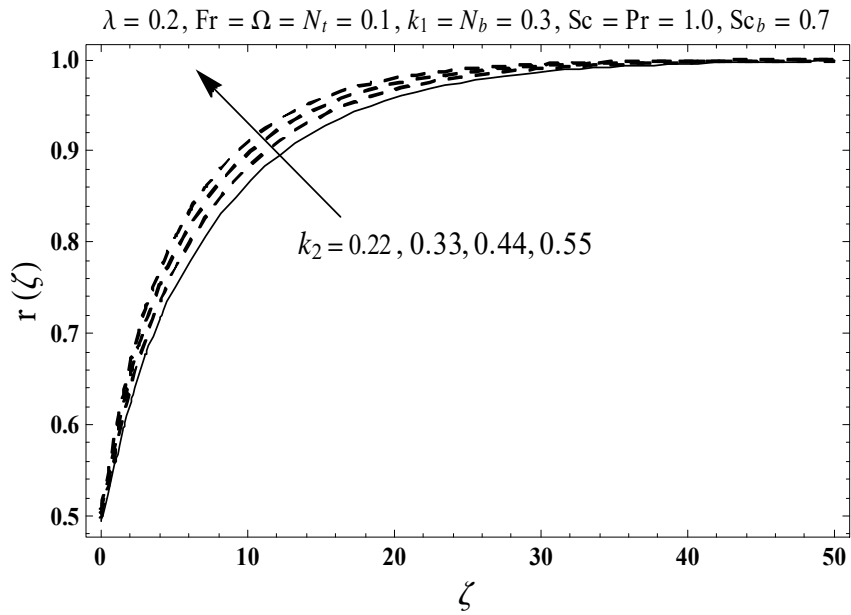
Figure 4.19 : Sketch for $r(\zeta)$ against k_2.
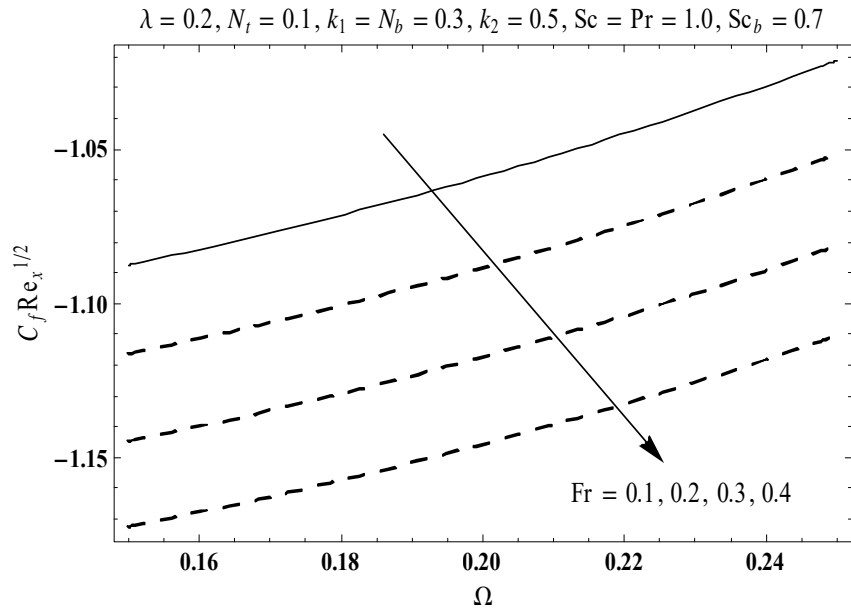
Figure 4.20 : Sketch for $C_f \, \text{Re}_x^{1/2}$ against Ω and Fr.

$\text{Fr} = N_t = 0.1, k_1 = N_b = 0.3, k_2 = 0.5, \text{Sc} = \text{Pr} = 1.0, \text{Sc}_b = 0.7$
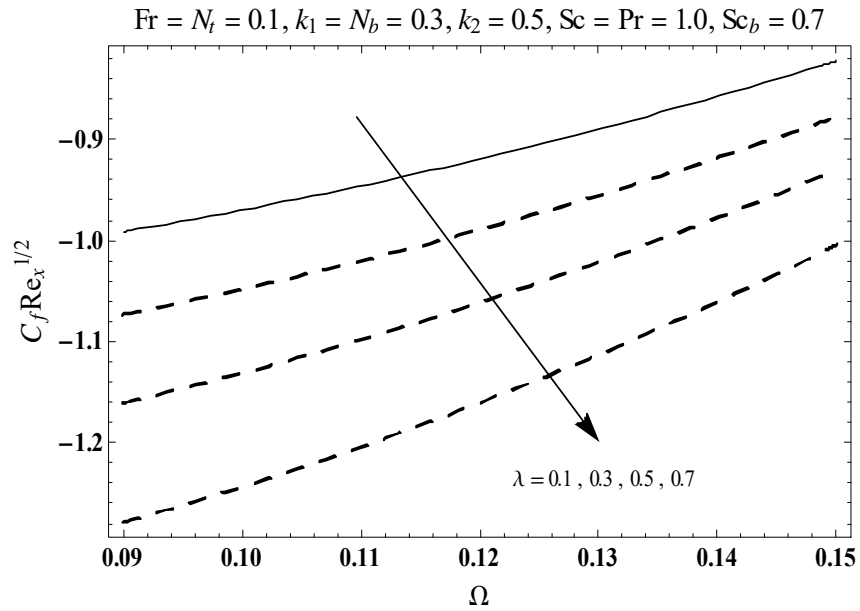
Figure 4.21 : Sketch for $C_f \, \text{Re}_x^{1/2}$ against Ω and λ.

$\lambda = 0.2, N_t = 0.1, k_1 = N_b = 0.3, k_2 = 0.5, \text{Sc} = \text{Pr} = 1.0, \text{Sc}_b = 0.7$

Fr = 0.1, 0.2, 0.3, 0.4
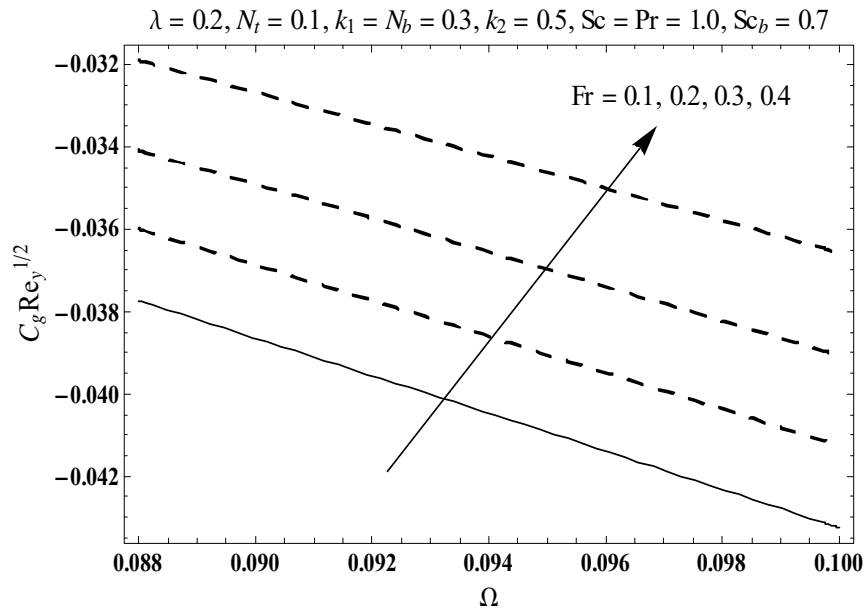
Figure 4.22 : Sketch for $C_g \, \text{Re}_y^{1/2}$ against Ω and Fr.

$Fr = N_t = 0.1, k_1 = N_b = 0.3, k_2 = 0.5, \text{Sc} = \text{Pr} = 1.0, \text{Sc}_b = 0.7$

$\lambda = 0.1, 0.3, 0.5, 0.7$
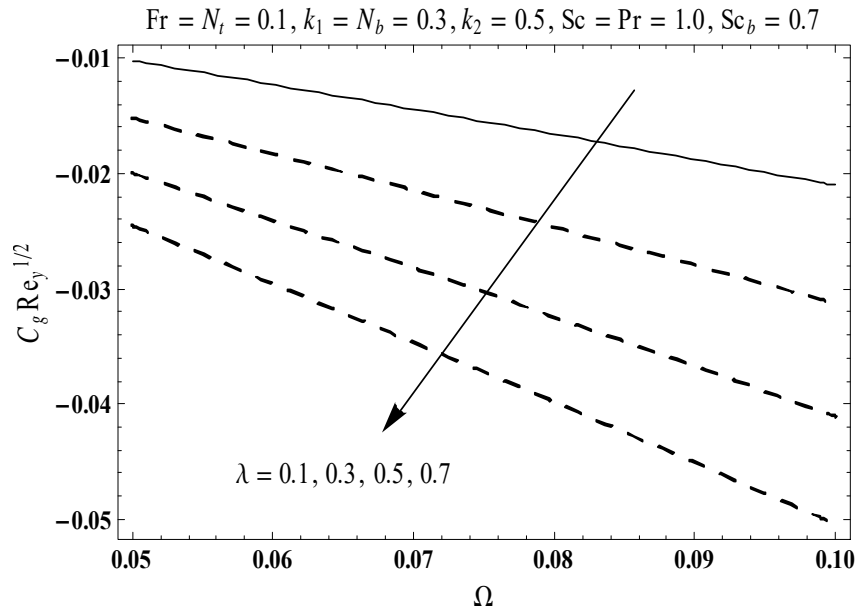
Figure 4.23 : Sketch for $C_g \, \text{Re}_y^{1/2}$ against Ω and λ.

$\lambda = 0.2$, Fr $= \Omega = N_t = 0.1$, $k_1 = 0.3$, $k_2 = 0.5$, Sc $= 1.0$, Sc$_b = 0.7$

Pr $= 0.7$, 1.0, 1.3, 1.6
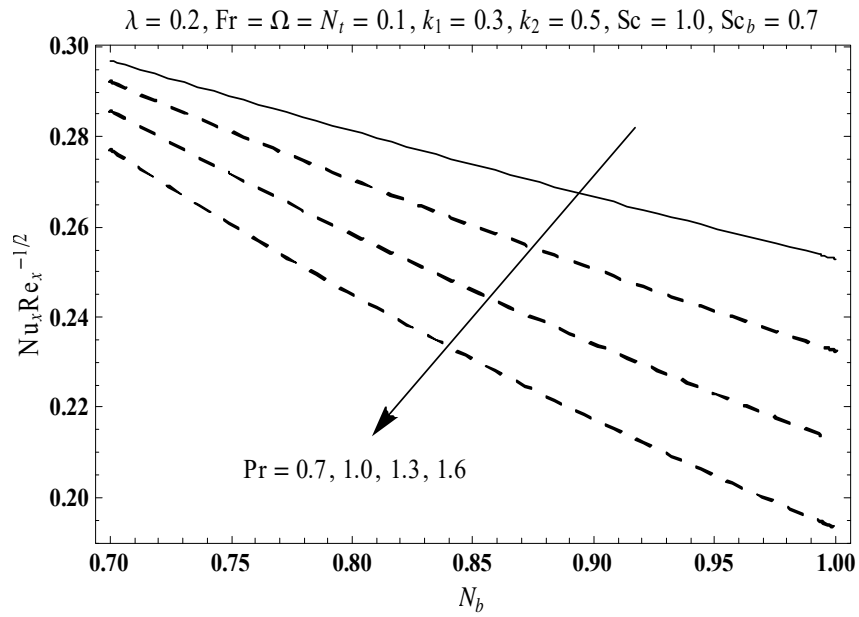
Figure 4.24 : Sketch for $Nu_x \operatorname{Re}_x^{-1/2}$ against Pr and N_b.

$\lambda = 0.2$, Fr $= \Omega = 0.1$, $k_1 = N_b = 0.3$, $k_2 = 0.5$, Sc $=$ Pr $= 1.0$

Sc$_b = 0.5$, 0.7, 0.9, 1.1
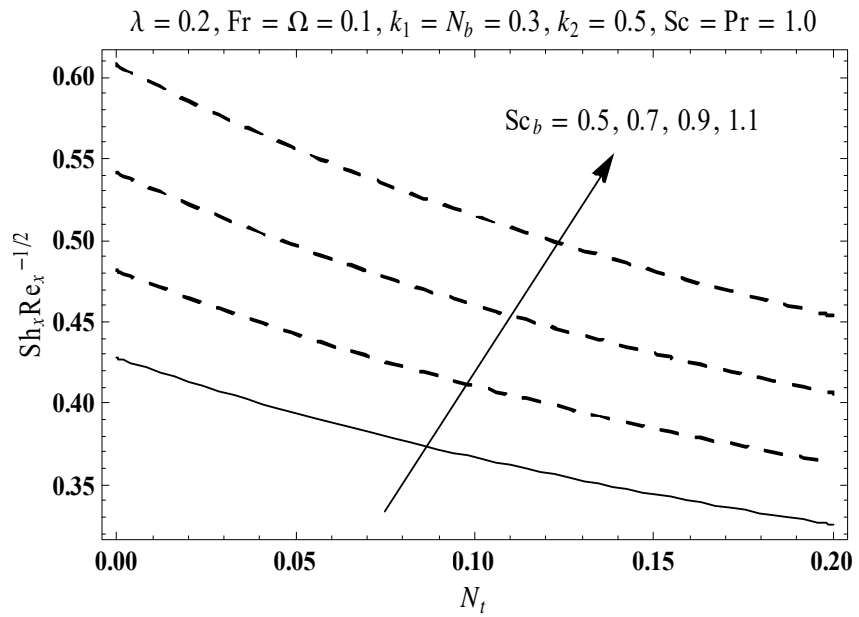
Figure 4.25 : Sketch for $Sh_x \operatorname{Re}_x^{1/2}$ against Sc_b and N_t.

72

Table 4.2. Comparative values of $-f''(0)$ and $-g'(0)$ against Ω when $\lambda = Fr = 0$.

Ω	$-f''(0)$		$-g'(0)$	
	OHAM	Wang [27]	OHAM	Wang [27]
0	1	1	0	0
0.5	1.13844	1.1384	0.51284	0.5128
1	1.32502	1.3250	0.83713	0.8371
2	1.65234	1.6523	1.28732	1.2873

4.5 Major observations

Presented analysis lead to following major results:

- Both temperature $\theta(\zeta)$ and nano-concentration $\phi(\zeta)$ have comparable impacts for λ and Fr while inverse circumstance is seen for concentration rate $r(\zeta)$.

- An addition in Ω demonstrates comparable pattern for temperature $\theta(\zeta)$, nano-concentration $\phi(\zeta)$ and concentration rate $r(\zeta)$.

- Larger Schmidt Sc_b and Prandtl Pr numbers have lower temperature and nano-concentration.

- Temperature and concentration through N_t have similar pattern.

- N_b for temperature and concentration exhibits reverse impacts.

- An augmentation in thermal Biot parameter γ_1 and concentration Biot parameter γ_2 leads to higher $\theta(\zeta)$ and $\phi(\zeta)$.

- Higher Schmidt number Sc (for homogeneous and heterogeneous responses) display more concentration rate $r(\zeta)$.

- An improvement in k_1 relates to reduction of concentration rate while for k_2 the outcomes are reverse.

Chapter 5

Numerical treatment for non-Darcian 3D rotating flow of nanoliquid with prescribed heat and mass fluxes

Non-Darcian three dimensional rotating nanoliquid flow with prescribed mass and thermal fluxes is addressed in this chapter. Flow is developed by an exponentially deformed surface. Thermophoretic dispersion and irregular motion phenomenas are employed. An efficient numerical solver namely NDSolve is used to develop solutions for resulting nonlinear problems. Plots have been displayed in order to scrutinize impact of various sundry variables involved in the solutions. Moreover the coefficients of surface drag, local Nusselt (rate of heat transfer) and Sherwood (rate of mass transfer) numbers are also elaborated graphically.

5.1   Statement

Here we elaborate steady 3D rotating nanoliquid flow induced by an exponentially actuating surface. Non-Darcian permeable space is considered. Random movement and thermophoretic diffusion processes are examined. Cartesian coordinates are taken. Let $u_w(x) = U_0 e^{x/L}$ be sur-

face moving velocity. Further, fluid rotates about $z-$direction with consistent angular velocity ω. Relevant equations and boundary conditions have following forms:

$$\frac{\partial u}{\partial x} + \frac{\partial v}{\partial y} + \frac{\partial w}{\partial z} = 0, \tag{5.1}$$

$$u\frac{\partial u}{\partial x} + v\frac{\partial u}{\partial y} + w\frac{\partial u}{\partial z} - 2\omega v = \nu\frac{\partial^2 u}{\partial z^2} - \frac{\nu}{k^\star}u - Fu^2, \tag{5.2}$$

$$u\frac{\partial v}{\partial x} + v\frac{\partial v}{\partial y} + w\frac{\partial v}{\partial z} + 2\omega u = \nu\frac{\partial^2 v}{\partial z^2} - \frac{\nu}{k^\star}v - Fv^2, \tag{5.3}$$

$$u\frac{\partial T}{\partial x} + v\frac{\partial T}{\partial y} + w\frac{\partial T}{\partial z} = \alpha^\star\frac{\partial^2 T}{\partial z^2} + \frac{(\rho c)_p}{(\rho c)_f}\left(\frac{D_T}{T_\infty}\left(\frac{\partial T}{\partial z}\right)^2 + D_B\left(\frac{\partial T}{\partial z}\frac{\partial C}{\partial z}\right)\right), \tag{5.4}$$

$$u\frac{\partial C}{\partial x} + v\frac{\partial C}{\partial y} + w\frac{\partial C}{\partial z} = \frac{D_T}{T_\infty}\left(\frac{\partial^2 T}{\partial z^2}\right) + D_B\left(\frac{\partial^2 C}{\partial z^2}\right). \tag{5.5}$$

$$\left.\begin{array}{c} u = u_w(x) = U_0 e^{x/L}, \ v = 0, \ w = 0, \ -k\left(\frac{\partial T}{\partial z}\right)_w = T_0 e^{\frac{(A+1)x}{2L}}, \\ -D_B\left(\frac{\partial C}{\partial z}\right)_w = C_0 e^{\frac{(B+1)x}{2L}} \ \text{at} \ z = 0, \end{array}\right\} \tag{5.6}$$

$$u \to 0, \quad v \to 0, \quad T \to T_\infty, \quad C \to C_\infty \quad \text{when} \ z \to \infty. \tag{5.7}$$

Note that u, v and w represent the velocity components in $x-$, $y-$ and $z-$directions while $\nu\left(= \mu/\rho_f\right)$, μ and ρ_f stands for kinematic viscosity, dynamic viscosity and density of base liquid, $k^\star$ for permeability of porous medium, $F = C_b/xk^{\star 1/2}$ for variable inertia coefficient of permeable space, D_B for Brownian diffusivity, C_b for drag coefficient, $\alpha^\star = k/(\rho c)_f$, $(\rho c)_p$, k, $(\rho c)_f$ for thermal diffusivity, effective thermal potential of nanomaterials, thermal efficiency and thermal potential of liquid respectively, D_T for thermophoretic dispersion coefficient, A, L, T_∞, B, C_∞ for temperature exponent, far away temperature of liquid, concentration exponent and far away concentration of liquid respectively. Considering

$$\left.\begin{array}{c} u = U_0 e^{x/L}f'(\zeta), \ v = U_0 e^{x/L}g(\zeta), \ w = -\left(\frac{\nu U_0}{2L}\right)^{1/2}e^{x/2L}\left(f(\zeta) + \zeta f'(\zeta)\right), \\ T = T_\infty + \frac{T_0}{k}\sqrt{\frac{2\nu L}{U_0}}e^{Ax/2L}\theta(\zeta), \ C = C_\infty + \frac{C_0}{D_B}\sqrt{\frac{2\nu L}{U_0}}e^{Bx/2L}\phi(\zeta), \ \zeta = \left(\frac{U_0}{2\nu L}\right)^{1/2}e^{x/2L}z, \end{array}\right\} \tag{5.8}$$

equation (5.1) is trivially justified while Eqs. (5.2) − (5.7) are reduced to

$$f''' + ff'' - 2f'^2 + 4\Omega g - 2\lambda f' - 2Frf'^2 = 0, \tag{5.9}$$

76

$$g'' + fg' - 2f'g - 4\Omega f' - 2\lambda g - 2Frg^2 = 0, \tag{5.10}$$

$$\theta'' + \Pr\left(f\theta' - Af'\theta + N_b\theta'\phi' + N_t\theta'^2\right) = 0, \tag{5.11}$$

$$\phi'' + Sc\left(f\phi' - Bf'\phi\right) + \frac{N_t}{N_b}\theta'' = 0, \tag{5.12}$$

$$f(0) = g(0) = 0, \ f'(0) = 1, \ \theta'(0) = -1, \ \phi'(0) = -1, \tag{5.13}$$

$$f'(\infty) \to 0, \ g(\infty) \to 0, \ \theta(\infty) \to 0, \ \phi(\infty) \to 0. \tag{5.14}$$

Here rotation number, porosity parameter, Forchheimer number, Prandtl number, thermophoresis parameter, Schmidt number and Brownian motion parameter are symbolized by Ω, λ, Fr, Pr, N_t, Sc and N_b respectively. Nondimensional forms of these parameters are given below:

$$\left.\begin{array}{l} \lambda = \frac{\nu L}{k^\star u_w}, \ Fr = \frac{C_b}{k^{\star 1/2}}, \ \Omega = \frac{\omega L}{u_w}, \ \Pr = \frac{\nu}{\alpha^\star}, \ Sc = \frac{\nu}{D_B}, \\ Nb = \frac{(\rho c)_p D_B (C_w - C_\infty)}{(\rho c)_f \nu}, \ Nt = \frac{(\rho c)_p D_T (T_w - T_\infty)}{(\rho c)_f \nu T_\infty}. \end{array}\right\} \tag{5.15}$$

Coefficients of skin friction and local Nusselt and Sherwood numbers satisfy

$$\left.\begin{array}{l} \left(\frac{\mathrm{Re}_x}{2}\right)^{1/2} C_{fx} = f''(0), \\ \left(\frac{\mathrm{Re}_x}{2}\right)^{1/2} C_{fy} = g'(0), \\ \frac{L}{x}\left(\frac{\mathrm{Re}_x}{2}\right)^{-1/2} Nu_x = \frac{1}{\theta(0)}, \\ \frac{L}{x}\left(\frac{\mathrm{Re}_x}{2}\right)^{-1/2} Sh_x = \frac{1}{\phi(0)}. \end{array}\right\} \tag{5.16}$$

5.2 Discussion

This section elaborates the outcomes of Brownian motion parameter N_b, local porosity parameter λ, Forchheimer number Fr, Schmidt number Sc, temperature exponent A, local rotational parameter Ω, Prandtl number $\Pr$, thermophoresis parameter N_t and concentration exponent B on nondimensional temperature $\theta(\zeta)$ and nano-concentration $\phi(\zeta)$. Figure 5.1 displays variation of temperature field $\theta(\zeta)$ for higher λ. An elevation in λ yields stronger temperature $\theta(\zeta)$ and related layer thickness. Figure 5.2 is displayed to observe influence of Fr on $\theta(\zeta)$. Higher Fr exhibit an increasing trend in $\theta(\zeta)$. Figure 5.3 shows impact of Ω on $\theta(\zeta)$. Higher Ω leads to stronger $\theta(\zeta)$. Figure 5.4 elucidates that temperature field $\theta(\zeta)$ exhibits decreasing behavior for

greater A. Figure 5.5 elucidates $\theta(\zeta)$ against Prandtl number Pr. $\theta(\zeta)$ decayed for higher Pr. Figure 5.6 is scrutinized to analyze the influence of N_b on $\theta(\zeta)$. By increasing N_b, $\theta(\zeta)$ shows increasing trend. Figure 5.7 demonstrates the variation of temperature $\theta(\zeta)$ against higher N_t. Temperature $\theta(\zeta)$ is elevated against larger N_t. Figure 5.8 depicts that how temperature $\theta(\zeta)$ is get influenced by higher λ. For higher λ, temperature $\theta(\zeta)$ elevates. Impact of Fr on $\phi(\zeta)$ is presented in Figure 5.9. An increasing impact of $\phi(\zeta)$ is noted for higher Fr. Figure 5.10 is displayed to visualize the behavior of Ω on dimensionless nano-concentration field $\phi(\zeta)$. Non-dimensional nano-concentration field escalates against higher values of Ω. Effect of C on nano-concentration $\phi(\zeta)$ is exhibited in Figure 5.11. Larger concentration exponent yield lower concentration field $\phi(\zeta)$ and related layer thickness. Nano-concentration field $\phi(\zeta)$ curves for higher Sc are illustrated in Figure 5.12. Here concentration field $\phi(\zeta)$ exhibits decreasing trend via larger Schmidt number Sc. Figure 5.13 studied N_b variations on $\phi(\zeta)$. An increment in N_b shows reduction in $\phi(\zeta)$. Figure 5.14 presents the outcome of thermophoresis parameter N_t for concentration field $\phi(\zeta)$. Larger thermophoresis parameter N_t lead to an escalation in $\phi(\zeta)$. Table 5.1 investigates numerical computations of coefficients of surface drag $-f''(0)$ and $-g'(0)$ for several estimations of porosity parameter λ, Forchheimer number Fr and rotation parameter Ω. Surface drag coefficients are increasing functions of Ω while reverse behavior is noticed for larger λ and Fr. Table 5.2 shows numerical computations of local Nusselt number $\frac{1}{\theta(0)}$ and local Sherwood number $\frac{1}{\phi(0)}$ for λ, Fr, Ω, Sc, Pr, N_t and N_b when $A = B = 0.5$. Local Nusselt (rate of heat transfer) decays against λ, Fr, Ω, N_t and N_b. Effects of Sc and Pr on rate of heat transfer are quite similar. Further mass transfer rate (local Sherwood number) has lower and higher values for larger (λ, Fr, Ω, Pr, N_t, N_b) and (Sc) respectively.
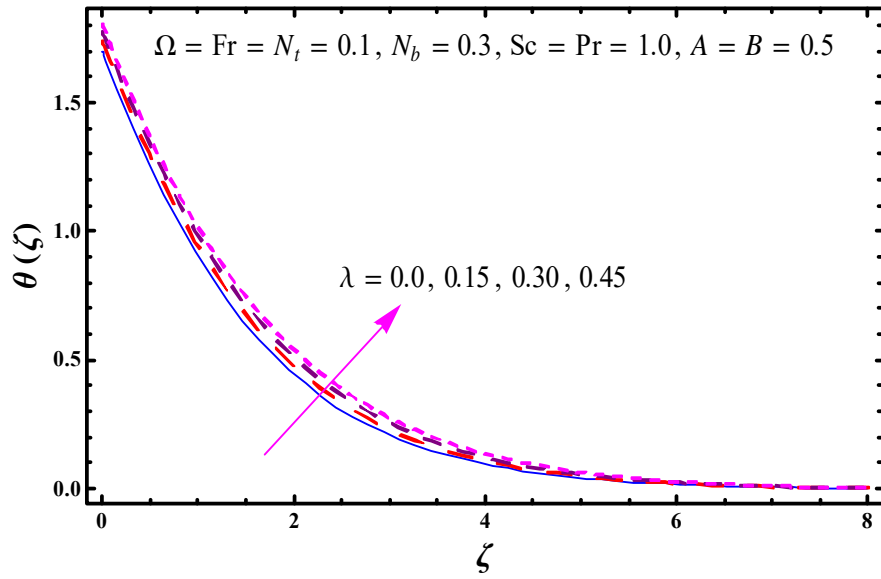
Figure 5.1 : Sketch for $\theta(\zeta)$ against λ.
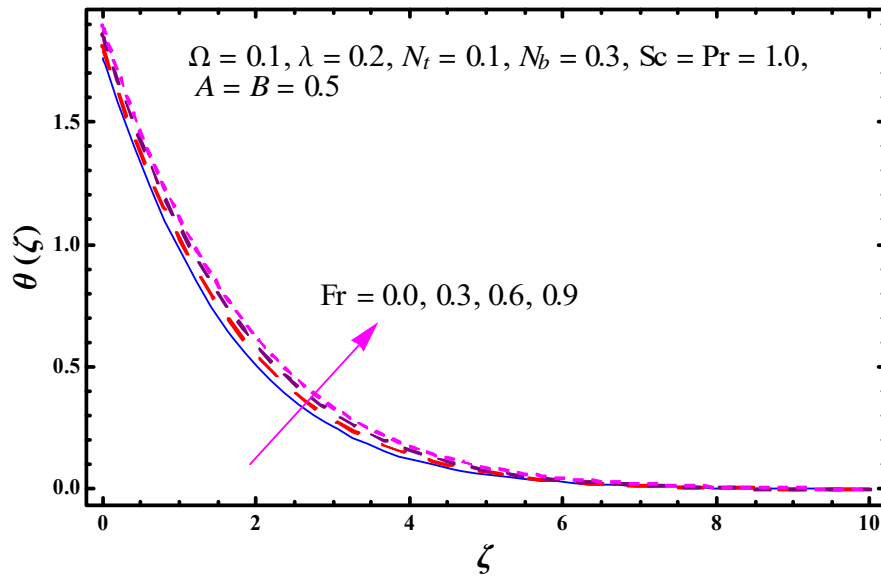
Figure 5.2 : Sketch for $\theta(\zeta)$ against Fr.
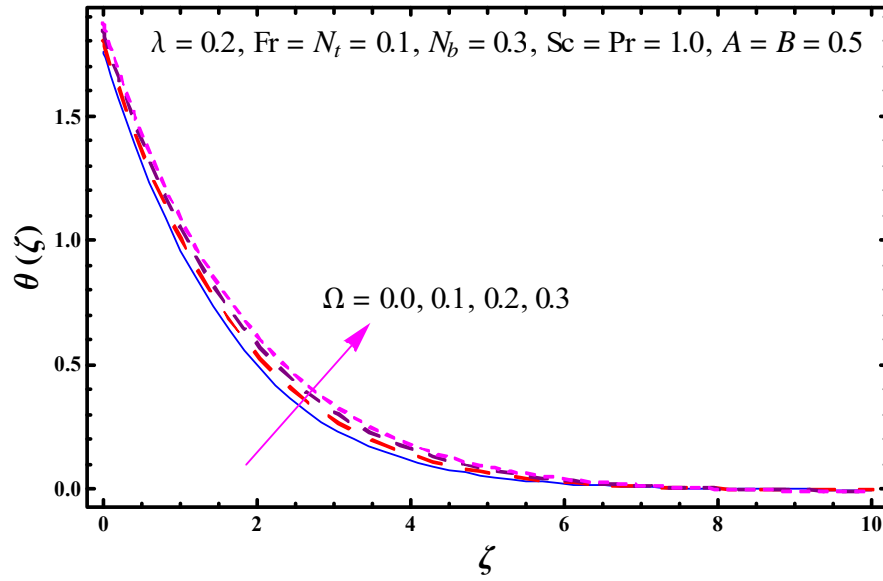
Figure 5.3 : Sketch for $\theta\left(\zeta\right)$ against Ω.
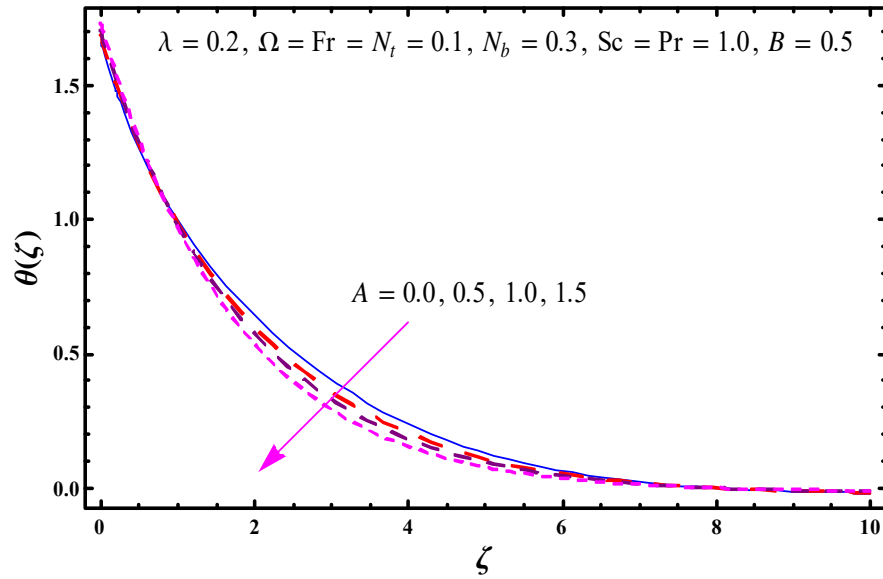
Figure 5.4 : Sketch for $\theta\left(\zeta\right)$ against A.
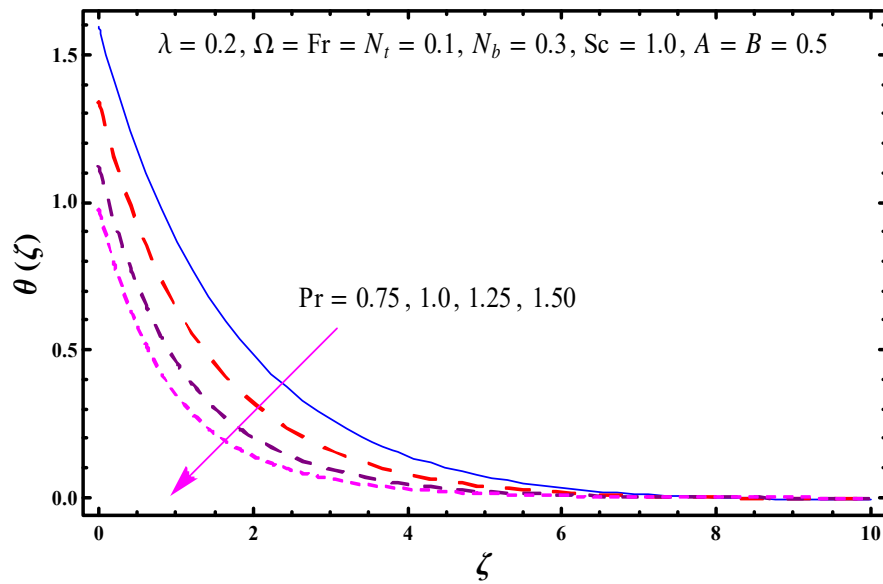
Figure 5.5 : Sketch for $\theta(\zeta)$ against Pr.
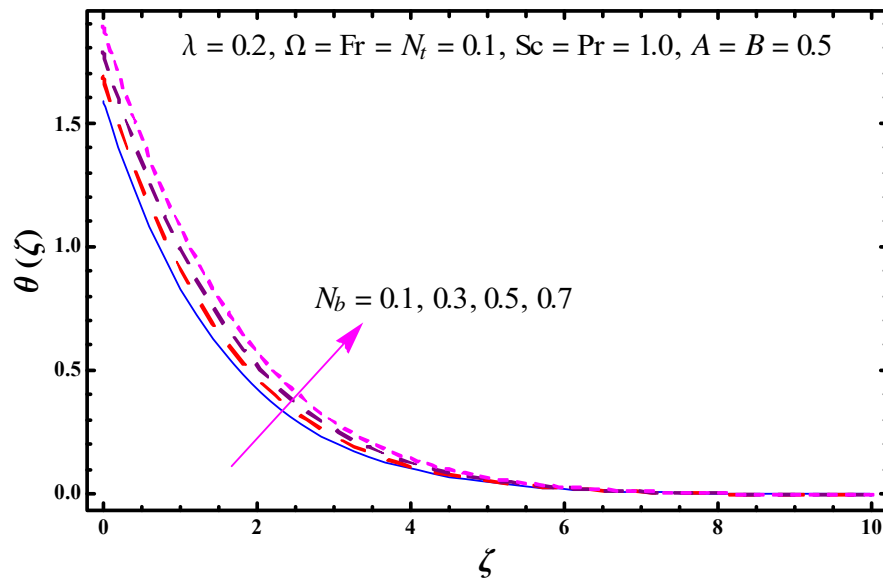
Figure 5.6 : Sketch for $\theta(\zeta)$ against N_b.
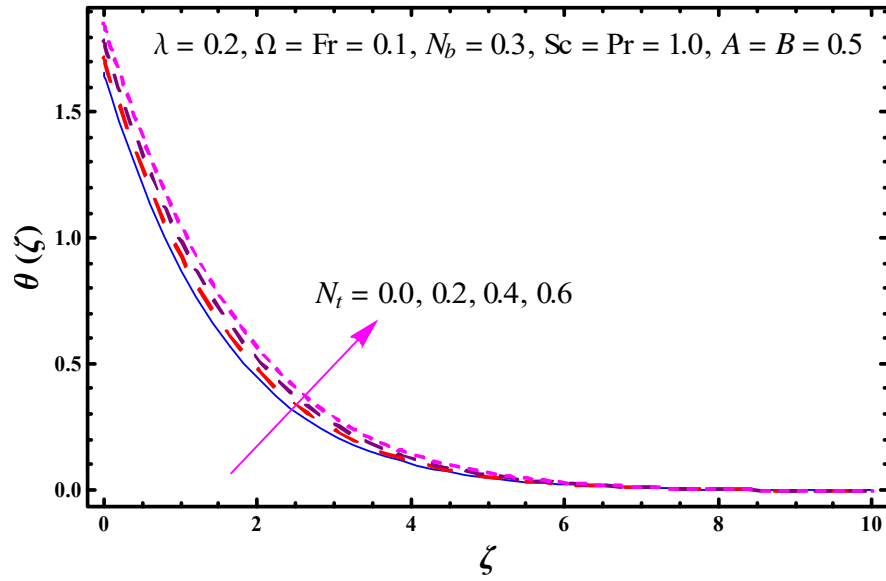
Figure 5.7 : Sketch for $\theta(\zeta)$ against N_t.
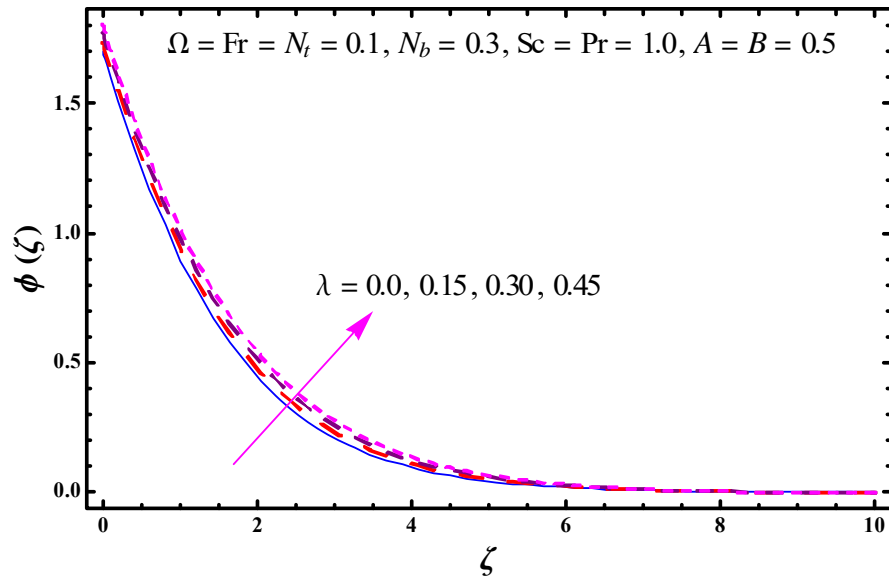
Figure 5.8 : Sketch for $\phi(\zeta)$ against λ.
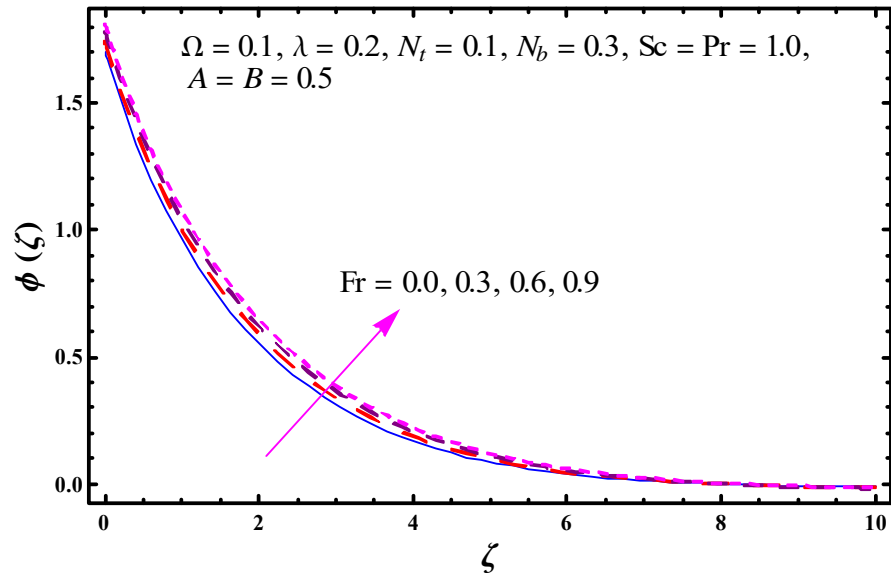
Figure 5.9 : Sketch for $\phi(\zeta)$ against Fr.
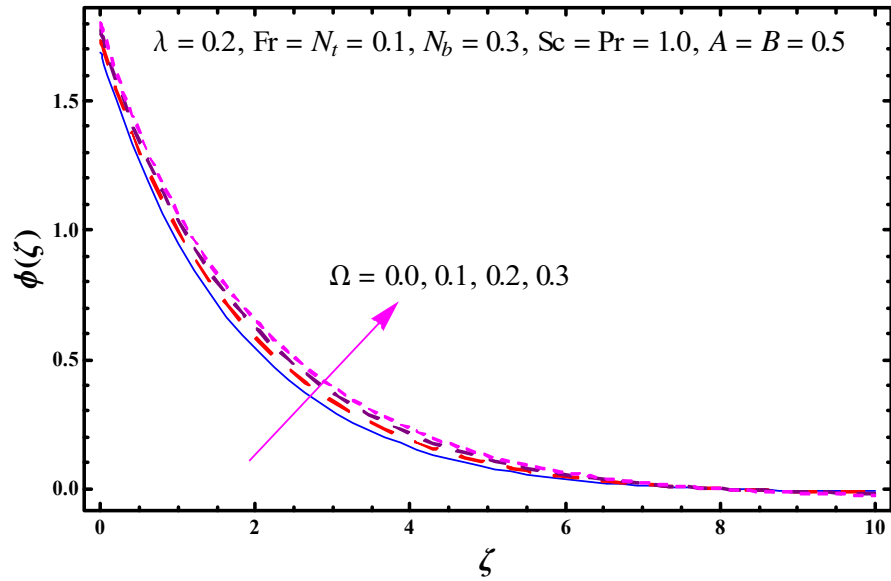
Figure 5.10 : Sketch for $\phi(\zeta)$ against Ω.
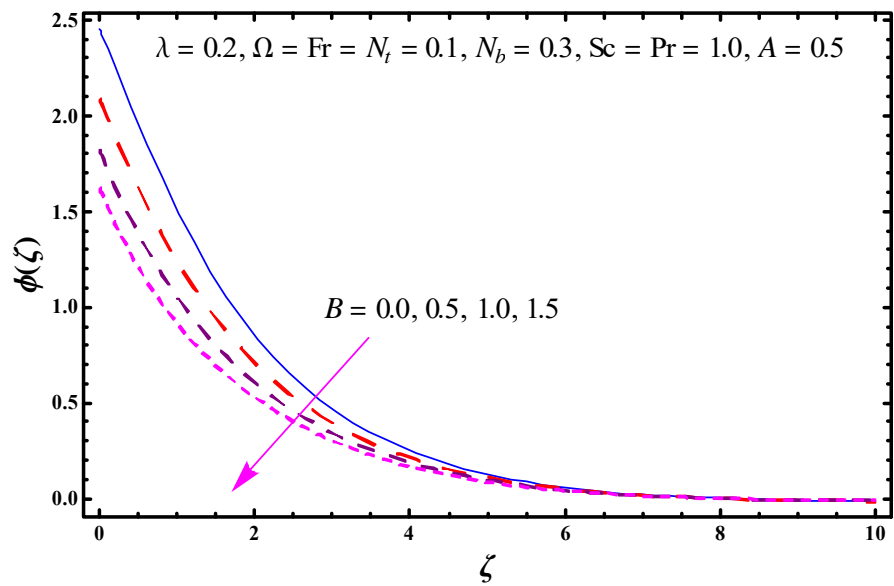
Figure 5.11 : Sketch for $\phi(\zeta)$ against B.
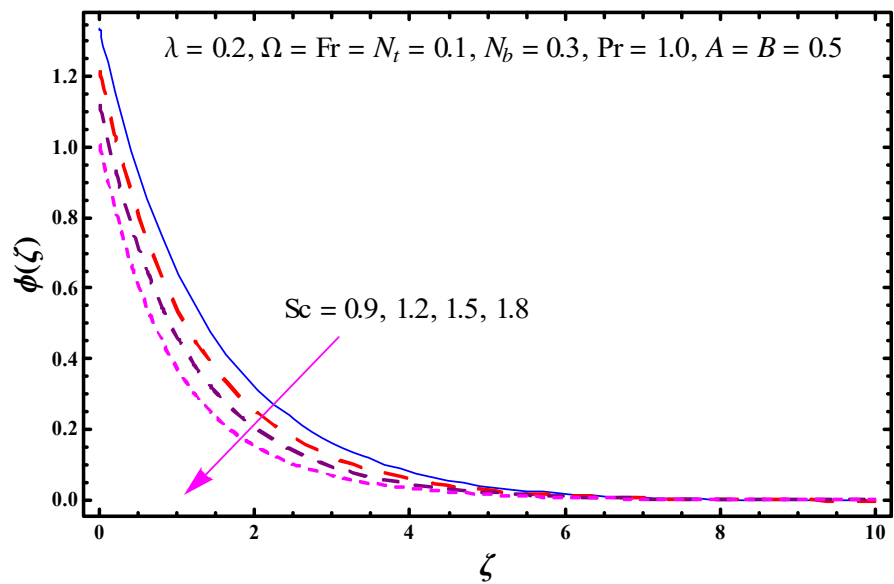
Figure 5.12 : Sketch for $\phi(\zeta)$ against Sc.
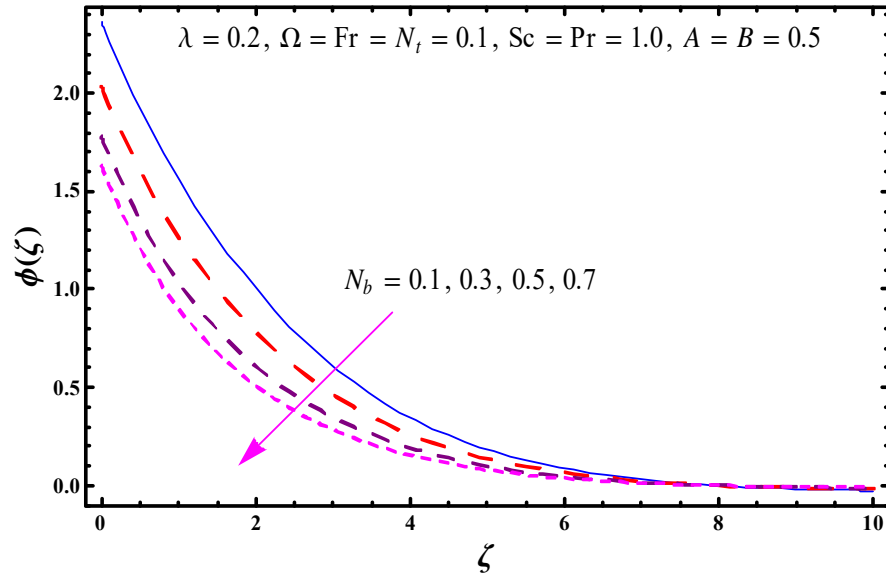
Figure 5.13 : Sketch for $\phi(\zeta)$ against N_b.
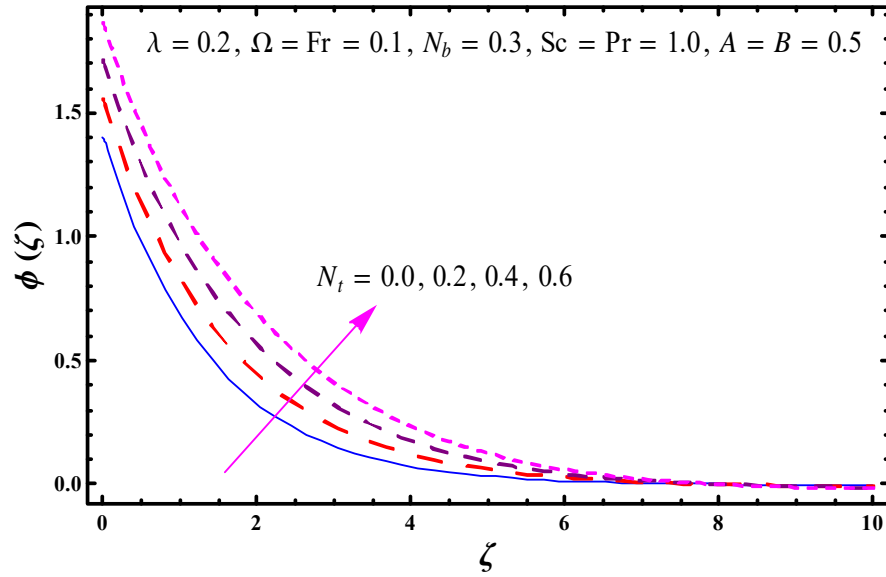
Figure 5.14 : Sketch for $\phi(\zeta)$ against N_t.

Table 5.1: Numeric data of surface drag coefficients $-f''(0)$ and $-g'(0)$ for distinct estimations of λ, Fr and Ω.

λ	Fr	Ω	$-f''(0)$	$-g'(0)$
0.0	0.1	0.2	1.351292	0.197898
0.1			1.420528	0.179629
0.2			1.487723	0.165819
0.2	0.1	0.2	1.487723	0.165819
	0.2		1.531017	0.164732
	0.3		1.573174	0.163694
0.2	0.1	0.05	1.479441	0.083713
		0.1	1.487723	0.165819
		0.2	1.517052	0.320662

Table 5.2: Numerical data of local Sherwood (rate of mass transfer) and local Nusselt (rate of heat transfer) numbers for distinct estimation of λ, Fr, Ω, N_t, Sc, N_b and Pr when $A = B = 0.5$.

λ	Fr	Ω	N_t	Sc	N_b	Pr	$\frac{1}{\theta(0)}$	$\frac{1}{\phi(0)}$
0.0	0.1	0.1	0.1	1.0	0.3	1.0	0.588588	0.611136
0.1							0.574766	0.597735
0.2							0.560822	0.584156
0.2	0.1	0.1	0.1	1.0	0.3	1.0	0.560822	0.584156
	0.2						0.555576	0.579322
	0.3						0.550526	0.564681
0.2	0.1	0.0	0.1	1.0	0.3	1.0	0.567862	0.591813
		0.1					0.560822	0.584156
		0.2					0.542852	0.565183
0.2	0.1	0.1	0.1	1.0	0.3	1.0	0.560822	0.584156
			0.3				0.190363	0.294592
			0.5				0.013188	0.013188
0.2	0.1	0.1	0.1	0.5	0.3	1.0	0.540982	0.350973
				1.0			0.560822	0.584156
				1.5			0.572558	0.785375
0.2	0.1	0.1	0.1	1.0	0.1	1.0	0.628977	0.584156
					0.2		0.593994	0.533559
					0.3		0.560822	0.423571
0.2	0.1	0.1	0.1	1.0	0.3	0.7	0.454659	0.588643
						1.0	0.560822	0.584156
						1.3	0.648453	0.582013

5.3   Major observations

Darcy-Forchheimer three dimensional (3D) rotating flow of nanoliquid due to a linearly stretch-able surface with constant heat and mass flux conditions is discussed. The preeminent findings of current analysis are structured as below:

- Greater values of λ and Fr exhibit similar behavior for both temperature $\theta(\zeta)$ and nano-concentration $\phi(\zeta)$ fields.

- Both temperature $\theta(\zeta)$ and nano-concentration $\phi(\zeta)$ fields represent increasing behavior for higher local rotational parameter Ω.

- An increment in temperature A and concentration B exponents corresponds to diminishment in temperature $\theta(\zeta)$ and nano-concentration $\phi(\zeta)$ fields.

- Higher estimations of Schmidt Sc and Prandtl Pr numbers yields lower temperature and nano-concentration fields.

- Brownian movement parameter N_b for temperature and nano-concentration have quite reverse impacts.

- Both temperature and concentration profiles are increased via thermophoresis parameter N_t.

Chapter 6

Entropy generation optimization for 3D rotating flow of nanoliquid subject to activation energy, porous medium and slip condition

This chapter addresses entropy generation in radiative flow of nanoliquid by considering activation energy and rotating frame. Impacts of viscous dissipation, porous medium and velocity slip condition are considered. Total rate of entropy production is also computed. Buongiorno's model is implemented for nanoliquid transport. Nonlinear ODE's are developed through apposite transformations. The reduced nonlinear ODE's have been handled with the assistance of BVP4c. Graphs are made to predict the influences of several sundry variables on velocities, nano-concentration, entropy generation, temperature, skin-friction, local Nusselt number, Bejan number and local Sherwood number.

6.1 Statement

Here irreversibility analysis in steady radiative swirling flow of nanoliquid is studied. Effects of velocity slip, viscous dissipation, activation energy and porous medium are also discussed.

Transport mechanism for nanofluid has been addressed by Buongiorno model. Stretched surface in Cartesian coordinate variables is chosen at $z = 0$ while fluid occupies $z \geq 0$. The extending velocity in the existence of slip condition is taken as $\left(U_w = ax + L_1 \frac{\partial u}{\partial z}\right)$. Rate of stretching is a. The plate and fluid are in a state of rigid body rotation through angular velocity ω. Using the above mentioned assumptions, the resulting problems can be finally reduced into the forms

$$\frac{\partial u}{\partial x} + \frac{\partial v}{\partial y} + \frac{\partial w}{\partial z} = 0, \tag{6.1}$$

$$u\frac{\partial u}{\partial x} + v\frac{\partial u}{\partial y} + w\frac{\partial u}{\partial z} - 2\omega v = \nu\frac{\partial^2 u}{\partial z^2} - \frac{\nu}{k^\star}u, \tag{6.2}$$

$$u\frac{\partial v}{\partial x} + v\frac{\partial v}{\partial y} + w\frac{\partial v}{\partial z} + 2\omega u = \nu\frac{\partial^2 v}{\partial z^2} - \frac{\nu}{k^\star}v, \tag{6.3}$$

$$\begin{aligned}
u\frac{\partial T}{\partial x} + v\frac{\partial T}{\partial y} + w\frac{\partial T}{\partial z} &= \alpha^\star\frac{\partial^2 T}{\partial z^2} - \frac{1}{(\rho c)_f}\frac{\partial q_r}{\partial z} + \frac{\mu}{(\rho c)_f}\left(\left(\frac{\partial u}{\partial z}\right)^2 + \left(\frac{\partial v}{\partial z}\right)^2\right) + \frac{\mu}{k^\star(\rho c)_f}\left(u^2 + v^2\right) \\
&+ \frac{(\rho c)_p}{(\rho c)_f}\left(\frac{D_T}{T_\infty}\left(\frac{\partial T}{\partial z}\right)^2 + D_B\left(\frac{\partial C}{\partial z}\frac{\partial T}{\partial z}\right)\right),
\end{aligned} \tag{6.4}$$

$$u\frac{\partial C}{\partial x} + v\frac{\partial C}{\partial y} + w\frac{\partial C}{\partial z} = D_B\left(\frac{\partial^2 C}{\partial z^2}\right) - k_r^2\left(C - C_\infty\right)\left(\frac{T}{T_\infty}\right)^n\exp\left(-\frac{E_a}{\kappa T}\right) + \frac{D_T}{T_\infty}\left(\frac{\partial^2 T}{\partial z^2}\right), \tag{6.5}$$

with

$$u = U_w,\ v = 0,\ w = 0,\ T = T_w,\ C = C_w\ \text{at}\ z = 0, \tag{6.6}$$

$$u \to 0,\quad v \to 0,\quad T \to T_\infty,\quad C \to C_\infty\quad \text{when}\ z \to \infty, \tag{6.7}$$

in which $(u,\ v,\ w)$ denote velocities in $(x,\ y,\ z)$ directions respectively, absolute viscosity (μ), kinematic viscosity (ν), (ρ_f) density, $(k^\star)$ permeability of permeable space, thermal diffusivity $(\alpha^\star)$, thermal efficiency (k), heat capacitance of the liquid $(\rho c)_f$, radiative heat flux (q_r), Brownian coefficient (D_B), effective heat capacitance of nanoparticles $(\rho c)_p$, temperature (T), concentration (C), thermophoretic coefficient (D_T), activation energy (E_a), fitted rate constant (n), reaction rate (k_r), Boltzmann constant (κ) and (L_1) velocity slip coefficient. Rosseland's approximation is utilized to develop radiative heat flux (q_r) which can be manifested as:

$$q_r = -\frac{4\sigma_1}{3m_1}\frac{\partial(T^4)}{\partial z}, \tag{6.8}$$

where (σ_1) stands for Stefan-Boltzmann constant and (m_1) for coefficient of mean absorption. We consider that temperature difference inside the flow is such that T^4 can be expanded as a linear combination of temperature. By utilizing Taylor's series and omitting higher order values we get:

$$T^4 = -3T_\infty^4 + 4T_\infty^3 T. \tag{6.9}$$

From Eqs. (6.8) and (6.9) one arrives at

$$\frac{\partial q_r}{\partial z} = -\frac{16\sigma_1 T_\infty^3}{3m_1}\frac{\partial^2 T}{\partial z^2}. \tag{6.10}$$

Substitution of Eq. (6.10) into Eq. (6.4) yields

$$u\frac{\partial T}{\partial x} + v\frac{\partial T}{\partial y} + w\frac{\partial T}{\partial z} = \alpha^\star\frac{\partial^2 T}{\partial z^2} + \frac{16\sigma_1 T_\infty^3}{3m_1(\rho c)_f}\frac{\partial^2 T}{\partial z^2} + \frac{\mu}{(\rho c)_f}\left(\left(\frac{\partial u}{\partial z}\right)^2 + \left(\frac{\partial v}{\partial z}\right)^2\right) + \frac{\mu}{k^\star(\rho c)_f}\left(u^2 + v^2\right)$$
$$+\frac{(\rho c)_p}{(\rho c)_f}\left(\frac{D_T}{T_\infty}\left(\frac{\partial T}{\partial z}\right)^2 + D_B\left(\frac{\partial C}{\partial z}\frac{\partial T}{\partial z}\right)\right). \tag{6.11}$$

Considering

$$\left.\begin{array}{l} u = axf'(\zeta), \ v = axg(\zeta), \ w = -(a\nu)^{1/2}f(\zeta), \\ \zeta = \left(\frac{a}{\nu}\right)^{1/2}z, \ \theta(\zeta) = \frac{T-T_\infty}{T_w-T_\infty}, \ \phi(\zeta) = \frac{C-C_\infty}{C_w-C_\infty}. \end{array}\right\} \tag{6.12}$$

Equation (6.1) is fully satisfied and Eqs. $(6.2) - (6.7)$ and (6.11) are reduced to

$$f''' + ff'' - f'^2 + 2\Omega g - \lambda f' = 0, \tag{6.13}$$

$$g'' + fg' - f'g - 2\Omega f' - \lambda g = 0, \tag{6.14}$$

$$\frac{1}{\Pr}(1 + Tr)\theta'' + Ec(f''^2 + g'^2) + N_b\phi'\theta'$$
$$+\lambda Ec(f'^2 + g^2) + \theta'f + N_t\theta'^2 = 0, \tag{6.15}$$

$$\frac{1}{Sc}\phi'' + f\phi' + \frac{1}{Sc}\frac{N_t}{N_b}\theta'' - \sigma\left(1 + \delta\theta\right)^n\phi\exp\left(-\frac{E}{1 + \delta\theta}\right) = 0, \tag{6.16}$$

$$f(0) = g(0) = 0, \ f'(0) = 1 + \alpha f''(0), \ \theta(0) = 1, \ \phi(0) = 1, \tag{6.17}$$

$$f'(\infty) \to 0, \ g(\infty) \to 0, \ \theta(\infty) \to 0, \ \phi(\infty) \to 0, \tag{6.18}$$

where (λ) denotes porosity parameter, (Ω) rotation parameter, (Tr) thermal radiation parameter, (N_b) Brownian movement parameter, (Pr) Prandtl number, (σ) chemical reaction parameter, (Sc) Schmidt parameter, (E) nondimensional activation energy, (α) velocity slip parameter, thermophoresis diffusion parameter (N_t) and temperature difference parameter (δ). We define

$$
\left.
\begin{aligned}
&\lambda = \frac{\nu}{k^\star a}, \ \Omega = \frac{\omega}{a}, \ Tr = \frac{16\sigma_1 T_\infty^3}{3km_1}, \ Sc = \frac{\nu}{D_B}, \ \sigma = \frac{k_r^2}{a}, \\
&N_b = \frac{(\rho c)_p D_B (C_w - C_\infty)}{(\rho c)_f \nu}, \ E = \frac{E_a}{\kappa T_\infty}, \ N_t = \frac{(\rho c)_p D_T (T_w - T_\infty)}{(\rho c)_f \nu T_\infty}, \\
&\alpha = L_1 \sqrt{\frac{a}{\nu}}, \ Ec = \frac{a^2 x^2}{c_p (T_w - T_\infty)}, \ \Pr = \frac{\nu}{\alpha^\star}, \ \delta = \frac{T_w - T_\infty}{T_\infty}.
\end{aligned}
\right\}
\tag{6.19}
$$

Non-dimensional forms of coefficients of surface drag, local Sherwood and Nusselt (rates of mass and heat transfer) numbers are

$$
\left.
\begin{aligned}
(\mathrm{Re}_x)^{1/2} C_{fx} &= f''(0), \\
(\mathrm{Re}_y)^{1/2} C_{fy} &= g'(0), \\
(\mathrm{Re}_x)^{-1/2} Nu_x &= -(1 + Tr)\theta'(0), \\
(\mathrm{Re}_x)^{-1/2} Sh_x &= -\phi'(0).
\end{aligned}
\right\}
\tag{6.20}
$$

Here local Reynolds number is ($\mathrm{Re}_x = ax^2/\nu$).

6.2 Entropy analysis

Entropy generation equation for the current flow situation can be described as:

$$
S_G = \frac{k}{T_\infty^2}\left(1 + \frac{16\sigma_1 T_\infty^3}{3km_1}\right)\left(\frac{\partial T}{\partial z}\right)^2 + \frac{\mu}{T_\infty}\left(\left(\frac{\partial u}{\partial z}\right)^2 + \left(\frac{\partial v}{\partial z}\right)^2\right)
\tag{6.21}
$$
$$
+ \frac{\mu}{k^\star T_\infty}\left(u^2 + v^2\right) + \frac{RD}{C_\infty}\left(\frac{\partial C}{\partial z}\right)^2 + \frac{RD}{T_\infty}\left(\frac{\partial T}{\partial z}\frac{\partial C}{\partial z}\right).
$$

After transformations (6.12) in Eq. (6.21), one obtains

$$
N_S = \frac{S_G}{S_{G_0}} = \alpha_1(1 + Tr)\theta'^2 + Br(f''^2 + g'^2) + \lambda Br(f'^2 + g^2) + L\theta'\phi' + L\frac{\alpha_2}{\alpha_1}\phi'^2,
\tag{6.22}
$$

where

$$
S_{G_0} = \frac{ka(T_w - T_\infty)}{\nu T_\infty}.
\tag{6.23}
$$

92

Eq. (6.22) represents the dimensionless form of entropy generation equation. Here Br, L, α_1 and α_2 stand for nondimensional Brinkman number, diffusive number, temperature ratio number and concentration ratio number respectively. These variables are defined by

$$Br = \frac{a^2 x^2 \mu}{k(T_w - T_\infty)}, \; L = \frac{RD(C_w - C_\infty)}{k}, \; \alpha_1 = \frac{T_w - T_\infty}{T_\infty}, \; \alpha_2 = \frac{C_w - C_\infty}{C_\infty}. \tag{6.24}$$

Mathematical expression for the Bejan number is

$$Be = \frac{\text{Entropy via heat transfer}}{\text{Total entropy}}, \tag{6.25}$$

$$Be = \frac{\alpha_1(1+Tr)\theta'^2}{\alpha_1(1+Tr)\theta'^2 + Br(f''^2 + g'^2) + \lambda Br(f'^2 + g^2) + L\theta'\phi' + L\frac{\alpha_2}{\alpha_1}\phi'^2}. \tag{6.26}$$

6.3   Discussion

In this portion Figures $(6.1 - 6.38)$ are plotted for the examination of velocity, Bejan number, temperature, entropy production and nano-concentration through involved physical variables. Figure 6.1 depicts the curves of velocity field $f'(\zeta)$ against different values of porosity parameter λ. One an easily see the reduction of $f'(\zeta)$ for higher values of λ. Physically an inverse relation exists between the porosity parameter and permeability. Higher porosity parameter yields lower permeability which decays the fluid motion. Due to this reason the velocity $f'(\zeta)$ decreases. Figure 6.2 delineates the influence of Ω on $f'(\zeta)$. Basically angular velocity to actuating rate ratio is known as rotation parameter. Higher Ω correspond to stronger rotational rate. It causes a decrease in velocity $f'(\zeta)$. Figure 6.3 represents the impact of α on $f'(\zeta)$. Depreciating behavior of $f'(\zeta)$ has been noted via stronger α. Physically by enhancing α, less adhesive strength is developed between the surface and the liquid particles which yields more resistance (opposing force) for migration of moving velocity to the liquid. Figure 6.4 displays impact of porosity parameter on velocity $g(\zeta)$. Reduction occurred in velocity $g(\zeta)$ via higher λ. Figure 6.5 examines effect of Ω on velocity $g(\zeta)$. An increasing trend is observed against higher Ω. Physical argument behind this mechanism is that Ω plays a prime role to boost up the flow along $y-$direction. By enhancing Ω, an oscillatory behavior is noticed in the velocity $g(\zeta)$. Figure 6.6 shows how temperature $\theta(\zeta)$ is influenced by higher λ. It is noticed that by increasing λ,

temperature $\theta(\zeta)$ elevates. Physically presence of permeable medium developes resistance in liquid movement and consequently it shows reduction in liquid velocity. Therefore an elevation is observed in $\theta(\zeta)$. Figure 6.7 depicts a change in $\theta(\zeta)$ for larger Ω. Temperature $\theta(\zeta)$ is elevated via higher Ω. Figure 6.8 has been drawn to visualize the behavior of Tr on $\theta(\zeta)$. $\theta(\zeta)$ upsurged for growing estimations of Tr. Physically coefficient of mean absorption has an inverse association with radiation parameter. Thus when radiation parameter has larger values then mean absorption coefficient reduces which developes more heat and consequently fluid temperature is enhanced. Temperature $\theta(\zeta)$ through higher Ec is presented in Figure 6.9. Eckert number is based on dissipation of heat because of its relation between enthalpy and enthalpy difference so $\theta(\zeta)$ enhances. Influence of Pr on $\theta(\zeta)$ is illustrated in Figure 6.10. Decaying impact of temperature $\theta(\zeta)$ is noticed for higher Pr. By definition, momentum to thermal diffusivity ratio is known as Prandtl number. An increment in Pr yields weaker thermal diffusivity. Such minute thermal diffusivity yields lower $\theta(\zeta)$. Behavior of N_t on $\theta(\zeta)$ is shown in Figure 6.11. Fluid temperature in boundary layer region boosted up for higher N_t. Basically an escalation in N_t means more force exerts on fluid particles and consequently more fluid transfers from the hotter space to the colder space. Therefore an enhancement in N_t leads to boost up the fluid temperature in boundary layer region. Impact of N_b on $\theta(\zeta)$ is highlighted in Figure 6.12. $\theta(\zeta)$ is increased by higher N_b. An escalation in N_b leads to rise the random motion of nanoparticles inside the flow zone. This intensified irregular motion increases the kinetic energy of the particles due to which temperature $\theta(\zeta)$ is enhanced. Figure 6.13 is constructed to see outcome of λ on nano-concentration $\phi(\zeta)$. Nano-concentration is enhanced via higher λ. Figure 6.14 elucidates that nano-concentration field is enhanced via greater values of Ω. $\phi(\zeta)$ behavior for Sc is exhibited in Figure 6.15. One can apparently see that $\phi(\zeta)$ depreciates for greater Sc. Figure 6.16 is developed to see the influence of N_t on the nano-concentration field $\phi(\zeta)$. It is perceived that the nano-concentration field is an increasing function of N_t. Figure 6.17 explores effect of N_b on $\phi(\zeta)$. We noticed that higher N_b lead to reduction of $\phi(\zeta)$. Figure 6.18 is drawn to analyze the behavior of E on $\phi(\zeta)$. Here an elevation in E depreciates modified Arrhenius function $\left(\frac{T}{T_\infty}\right)^n \exp\left(-\frac{E_a}{\kappa T}\right)$. This finally develops the productive chemical reaction which results in nano-concentration $\phi(\zeta)$ enhancement. Figure 6.19 describes the variation of $\phi(\zeta)$ for higher chemical reaction parameter σ on nano-concentration $\phi(\zeta)$. This Figure depicts

94

that an increase in σ yields an enhancement in the relation $(1+\delta\theta)^n \sigma \exp\left(-\frac{E}{1+\delta\theta}\right)$. This ultimately supports the destructive chemical mechanism due to which concentration elevates. Depreciation in ϕ is occurred with a higher nano-concentration gradient at the surface. Impact of δ on $\phi(\zeta)$ has been exhibited in Figure 6.20. Decaying trend of $\phi(\zeta)$ is seen via higher δ. Figure 6.21 explores that nano-concentration field $\phi(\zeta)$ is a decaying function of n. Figure 6.22 presents the effect of λ on entropy production N_G. With increase in values of λ, the viscosity of liquid elevates which developes more resistance (opposing force) within the liquid particles due to which disturbance in the system decreases and hence entropy production also decays. Be also decreases via increasing λ (see Figure 6.23). Figures 6.24 and 6.25 are plotted to evaluate the influence of Tr on $N_G(\zeta)$ and Be. From these Figures it is also observed that entropy of the system elevates against Tr while Be indicates same behavior. Figure 6.26 is developed to investigate the influence of Br on $N_G(\zeta)$. From this Figure it is analyzed that entropy elevates via stronger Br. Since Br is based on viscous dissipation so viscous effects become less prominent for greater Br which yields an entropy enhancement. An opposite impact of Be is seen for greater estimations of Br (See Figure 6.27). Figures 6.28 and 6.29 explain the behavior of diffusive variable L on N_G and Be. We examined that disorderness in system accelerates via greater L while Be exhibit a decaying behavior. Figures 6.30 to 6.32 describe the variations of $C_{fx}(\text{Re}_x)^{1/2}$ via higher λ, Ω and α. From these Figures it can be observed that $C_{fx}(\text{Re}_x)^{1/2}$ elevates against higher λ and Ω while reverse situation is observed for higher α. Figures 6.33 and 6.34 are developed to explore the main impacts of Ω and λ on $(\text{Re}_y)^{1/2}C_{fy}$. These graphs exhibit that $(\text{Re}_y)^{1/2}C_{fy}$ depreciates against stronger λ while increasing behavior is noticed against higher Ω. Influences of N_t and N_b on rate of heat transfer are disclosed through Figures 6.35 and 6.36. From these Figures it can be analyzed that $(\text{Re}_x)^{-1/2}Nu_x$ decreases via larger estimations of N_t and N_b. Figures 6.37 and 6.38 indicate that impacts of E and σ on mass transfer rate (local Sherwood number) $(\text{Re}_x)^{-1/2}Sh_x$ respectively. From these Figures one can easily analyze that $(\text{Re}_x)^{-1/2}Sh_x$ displays opposite role for higher σ and E.
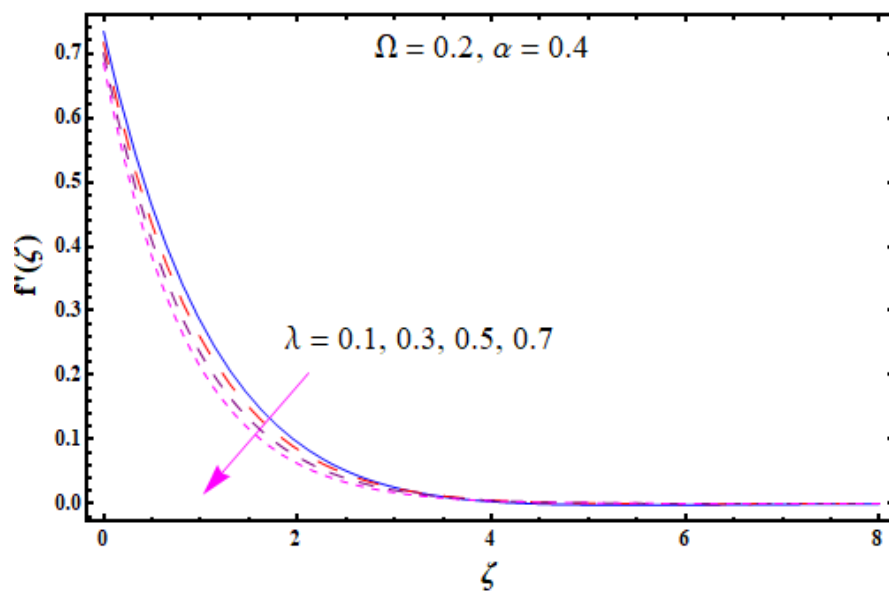
Figure 6.1 : Sketch for $f'(\zeta)$ against λ.
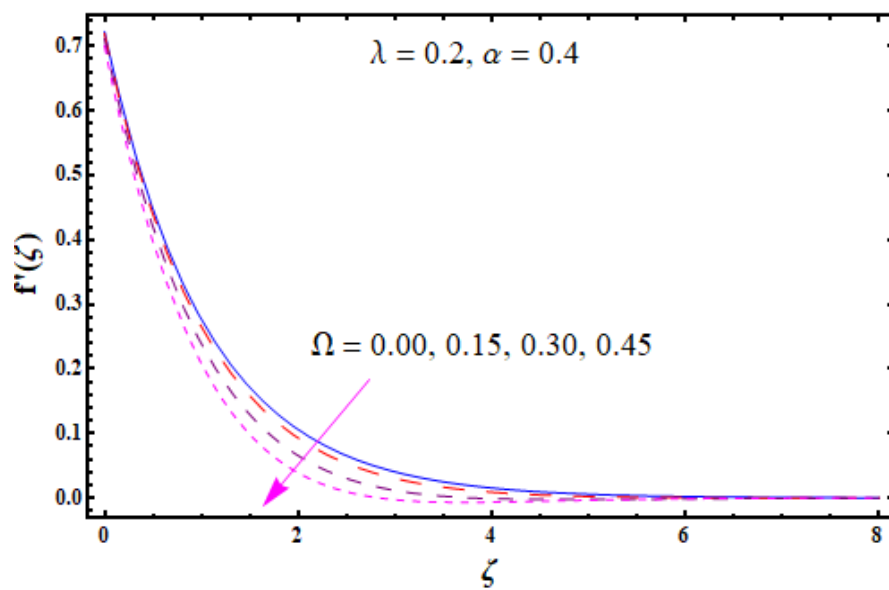
Figure 6.2 : Sketch for $f'(\zeta)$ against Ω.
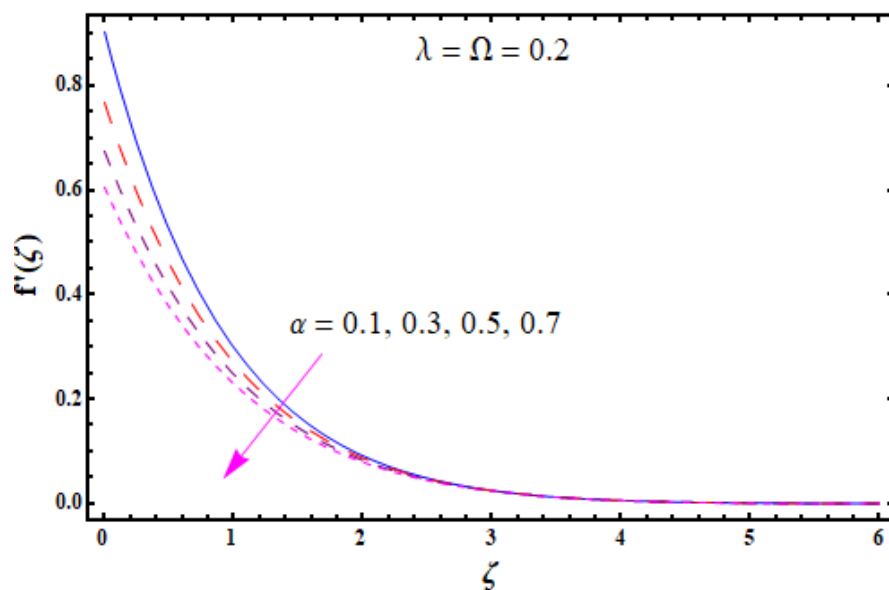
Figure 6.3 : Sketch for $f'(\zeta)$ against α.
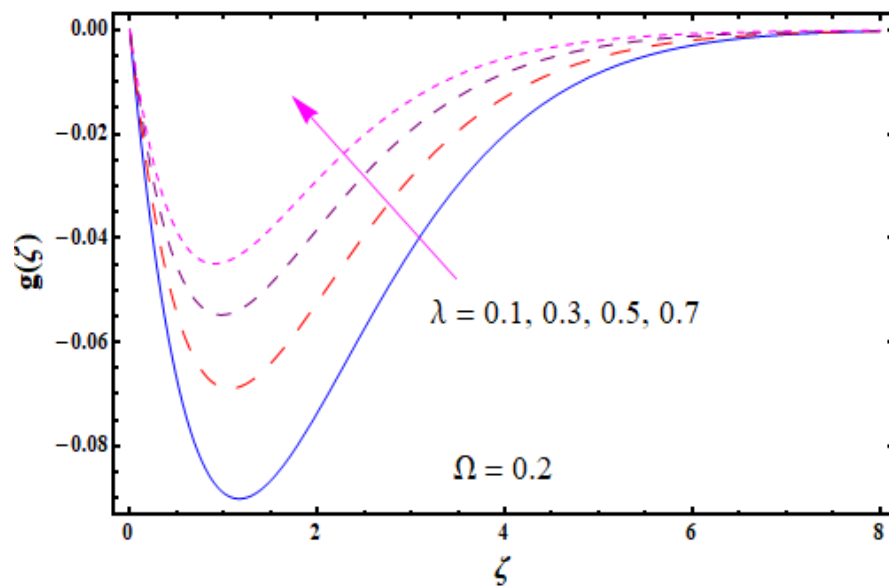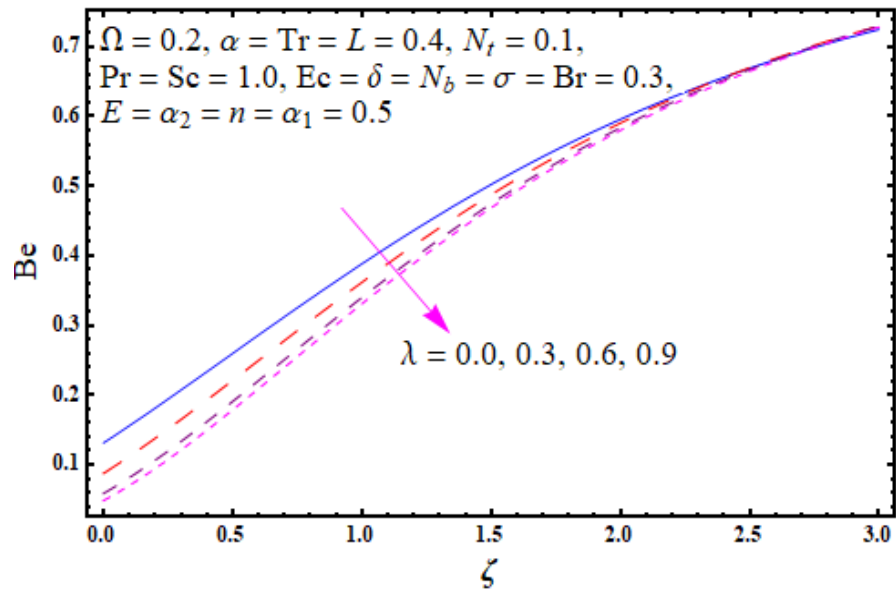

Figure 6.4 : Sketch for $g(\zeta)$ against λ.

97
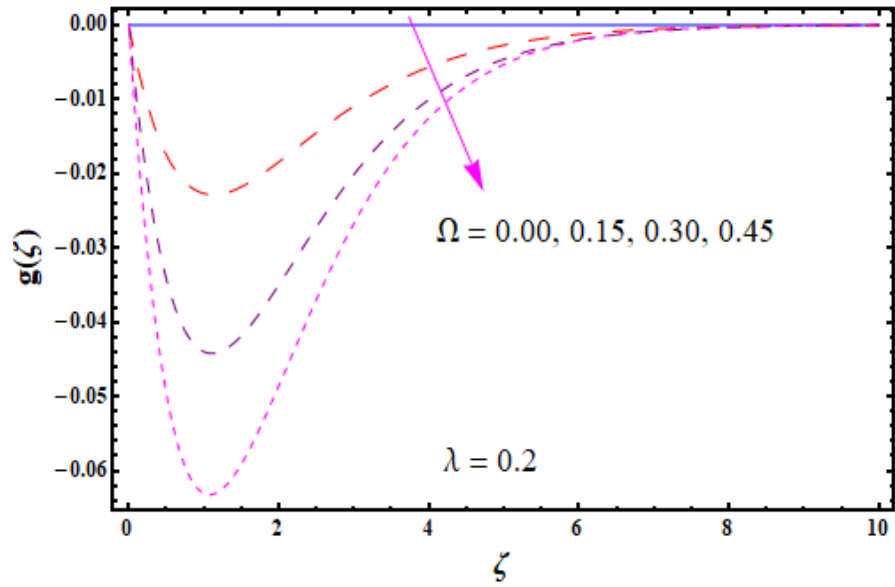
Figure 6.5 : Sketch for $g(\zeta)$ against Ω.
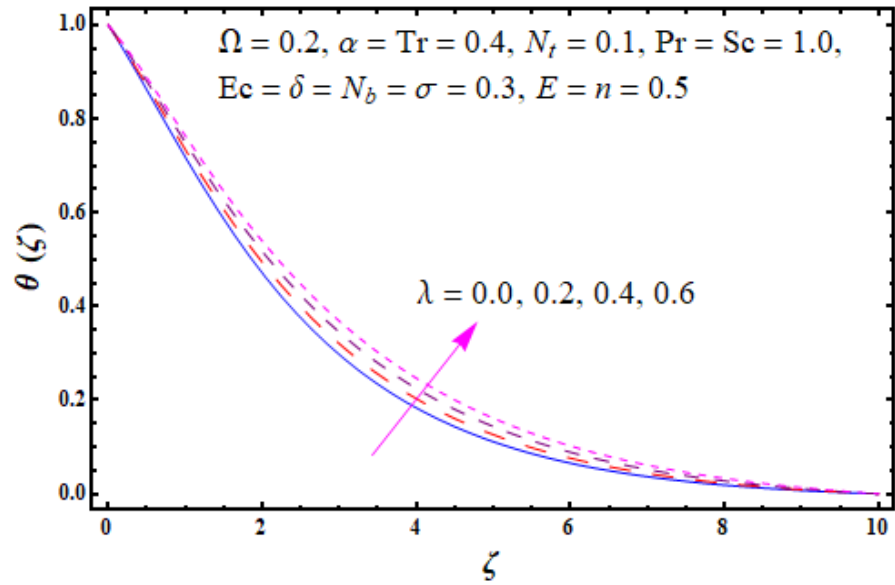
Figure 6.6 : Sketch for $\theta(\zeta)$ against λ.
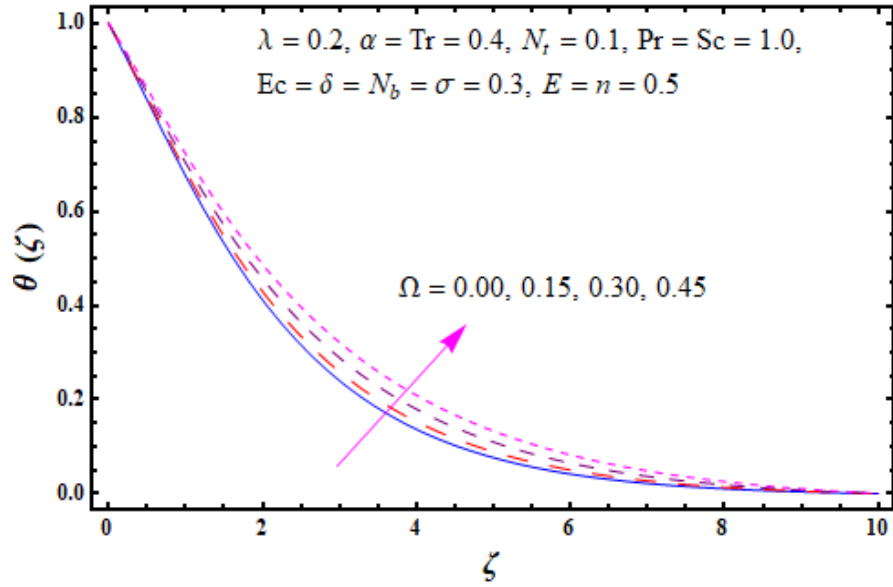
Figure 6.7 : Sketch for $\theta(\zeta)$ against Ω.
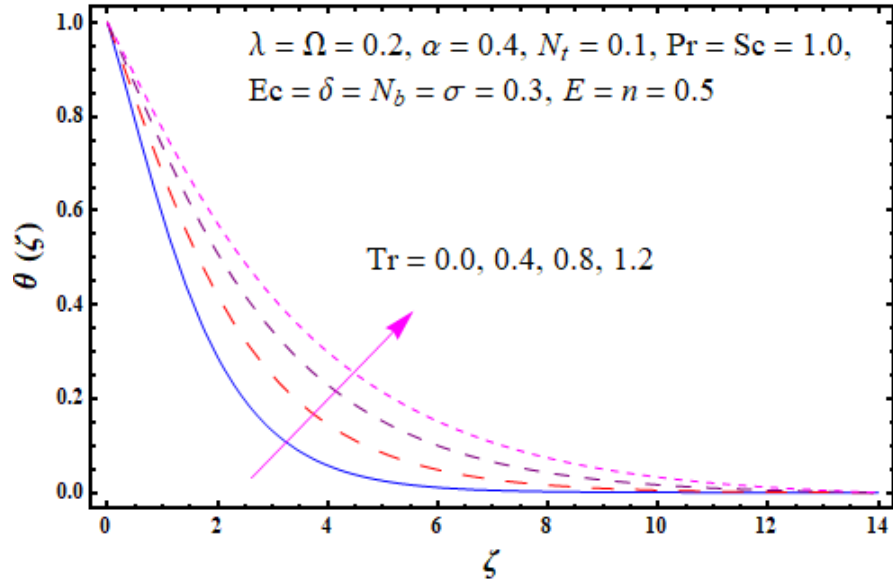
Figure 6.8 : Sketch for $\theta(\zeta)$ against Tr.
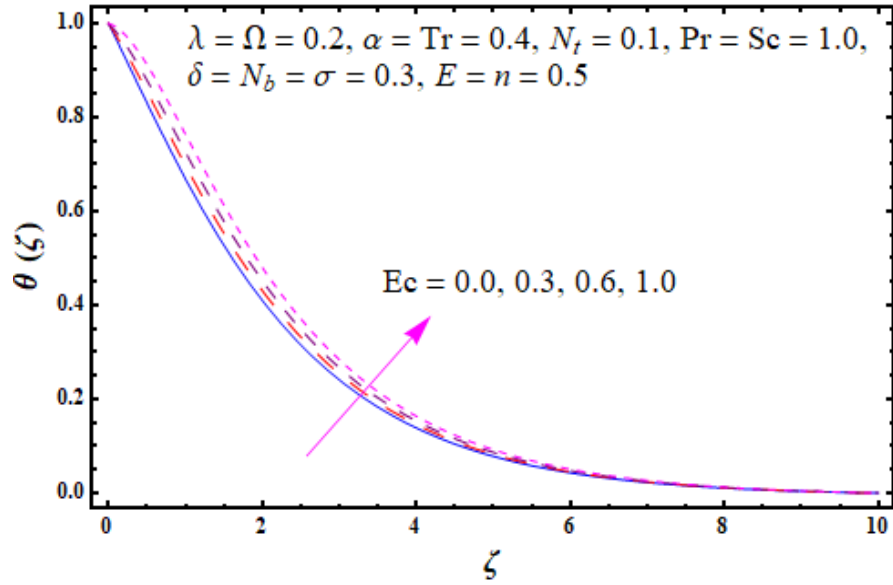
Figure 6.9 : Sketch for $\theta(\zeta)$ against Ec.
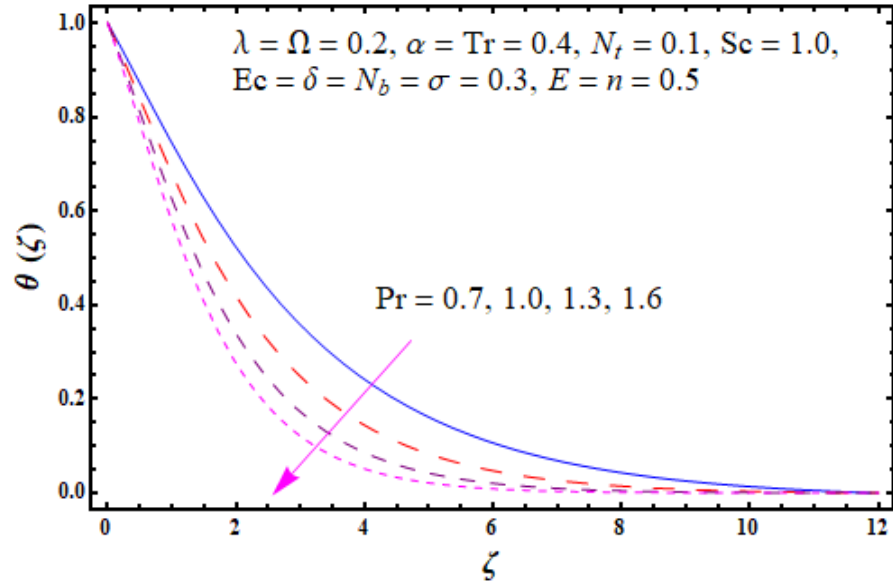
Figure 6.10 : Sketch for $\theta(\zeta)$ against Pr.
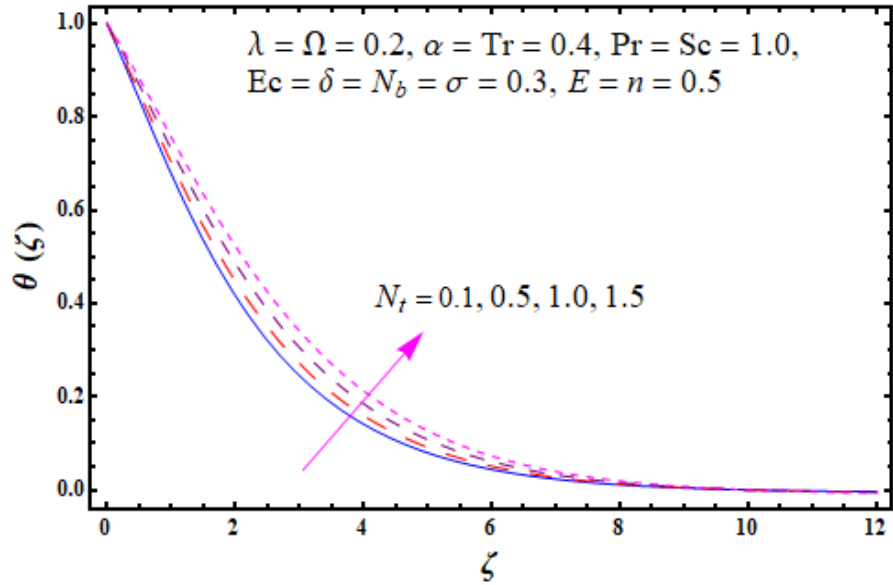
Figure 6.11 : Sketch for $\theta(\zeta)$ against N_t.
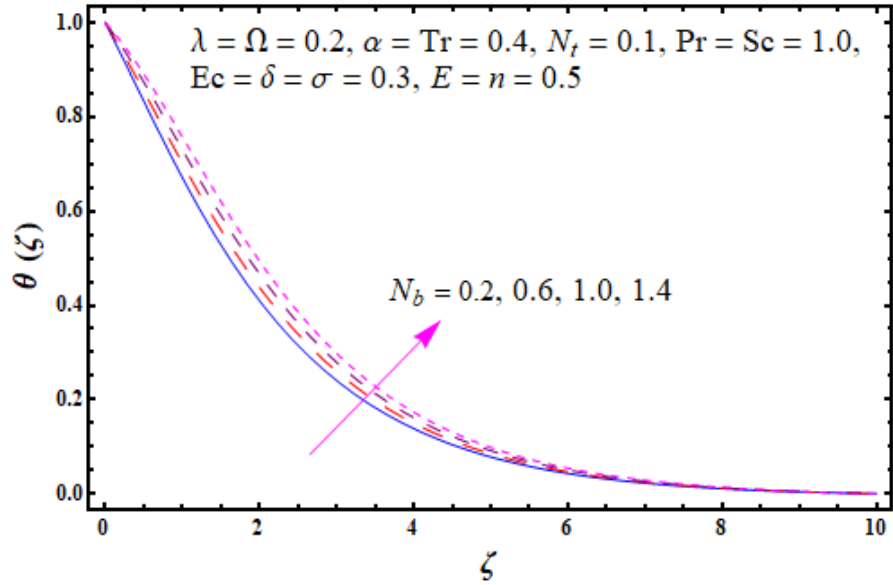
Figure 6.12 : Sketch for $\theta(\zeta)$ against N_b.
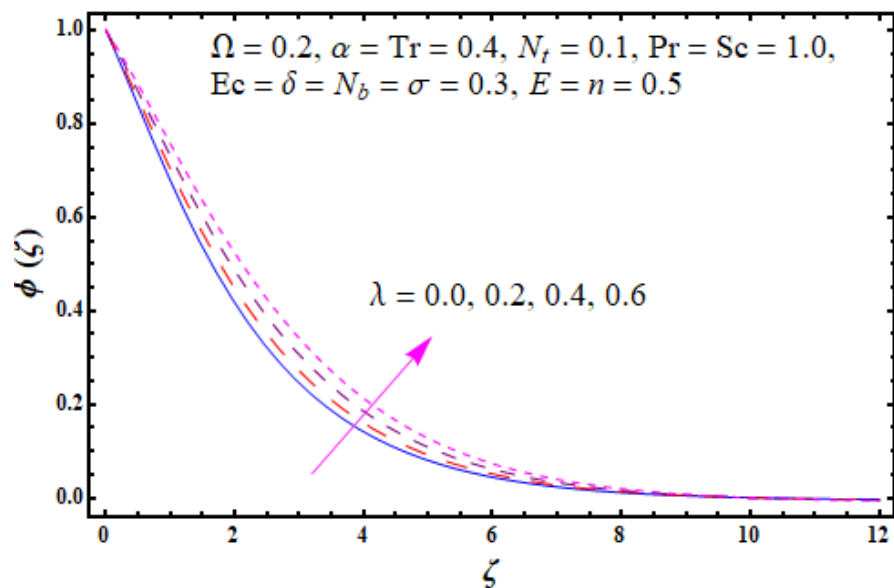
Figure 6.13 : Sketch for $\phi(\zeta)$ against λ.
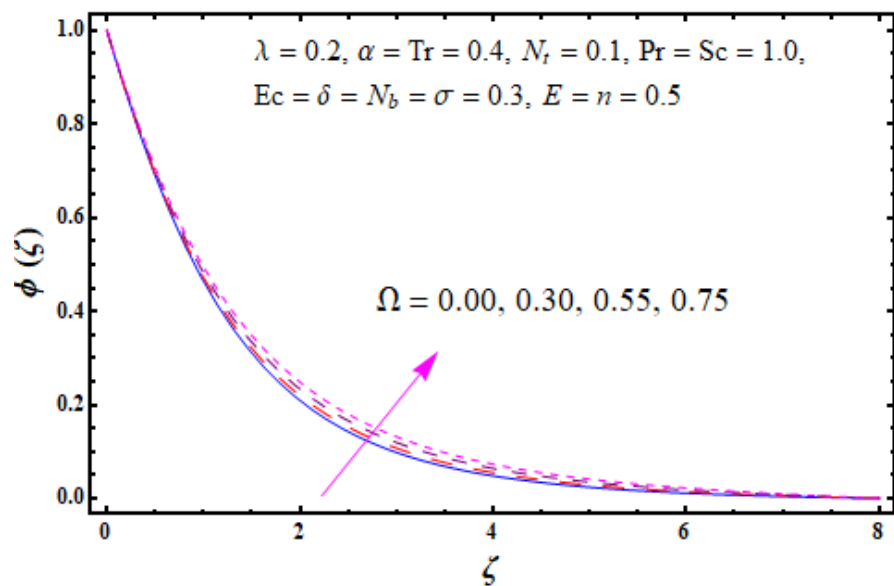
Figure 6.14 : Sketch for $\phi(\zeta)$ against Ω.

102
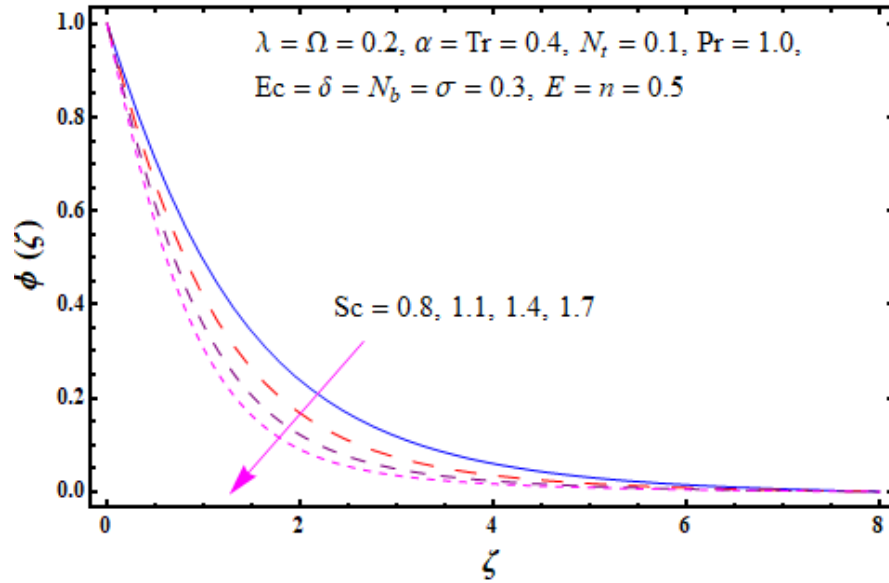
Figure 6.15 : Sketch for $\phi(\zeta)$ against Sc.
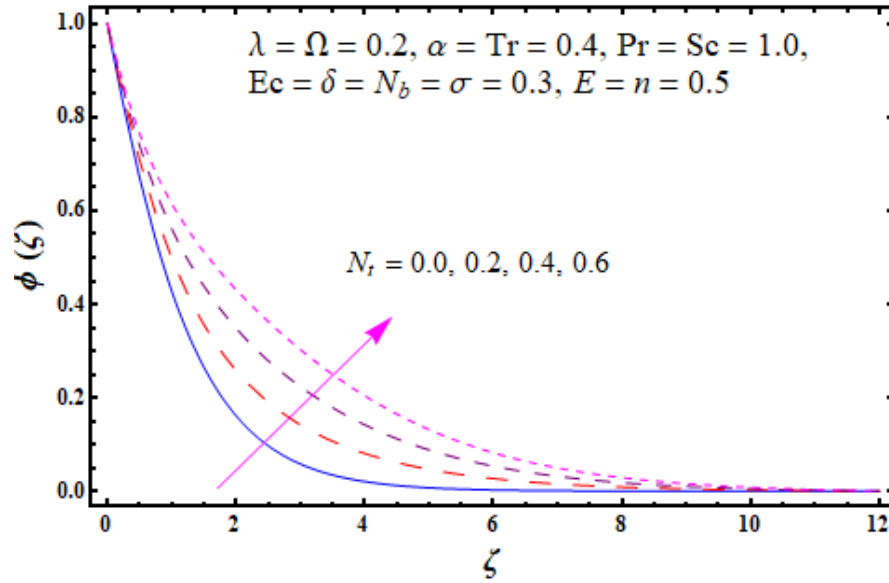
Figure 6.16 : Sketch for $\phi(\zeta)$ against N_t.
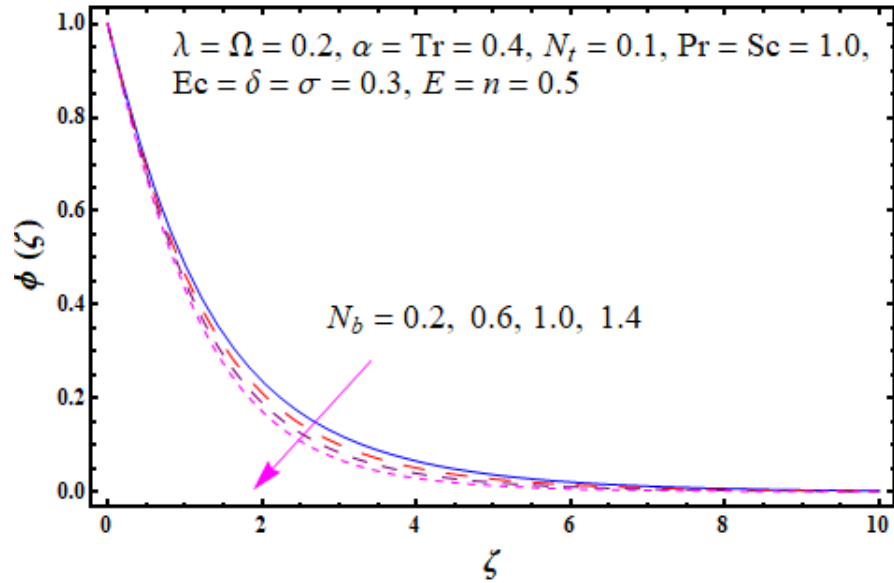
Figure 6.17 : Sketch for $\phi(\zeta)$ against N_b.
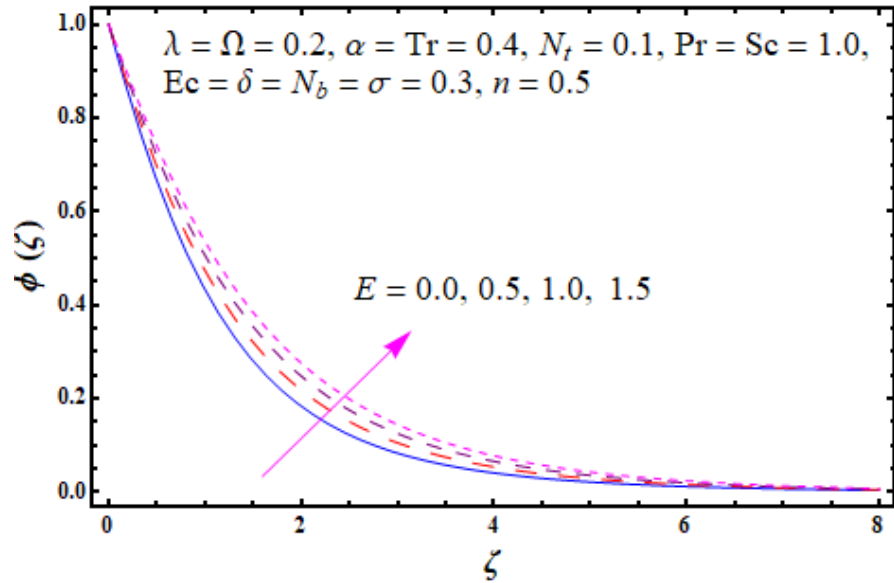
Figure 6.18 : Sketch for $\phi(\zeta)$ against E.

104
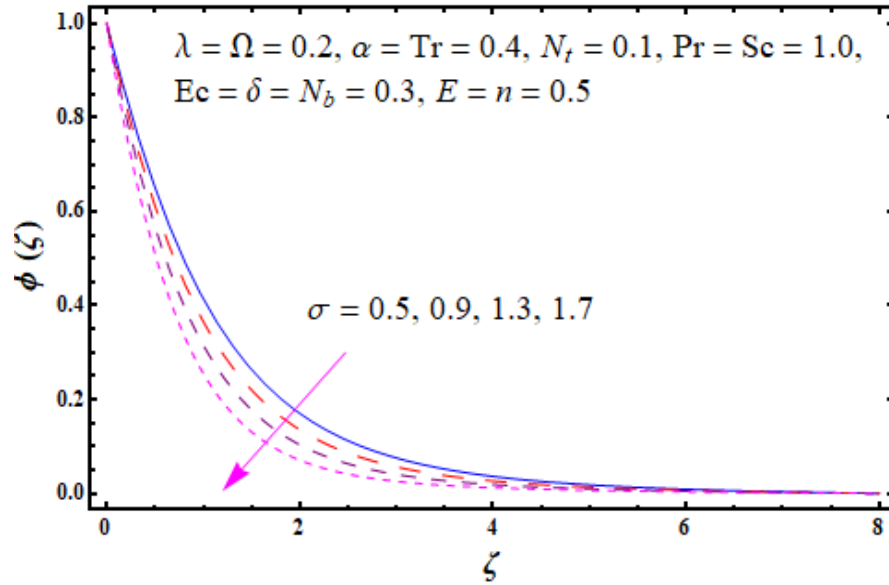
Figure 6.19 : Sketch for $\phi(\zeta)$ against σ.
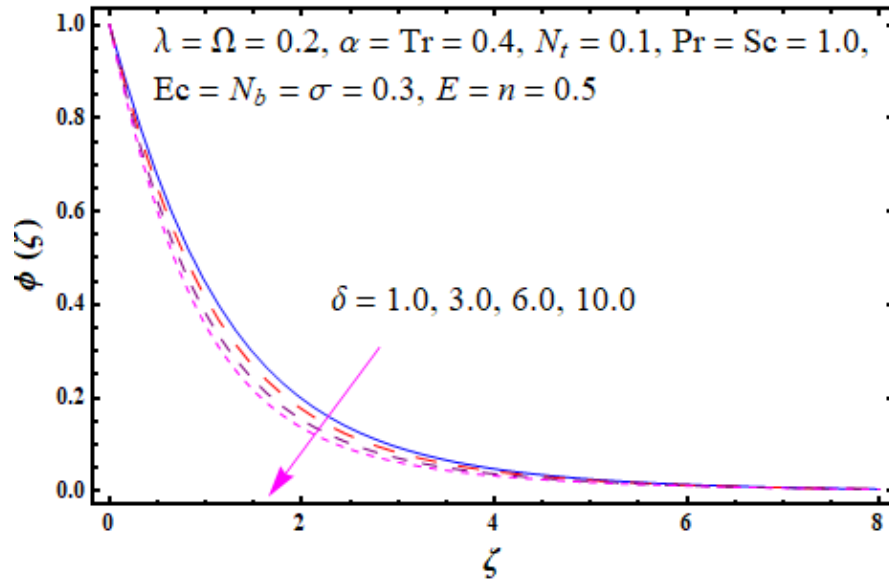
Figure 6.20 : Sketch for $\phi(\zeta)$ against δ.

105
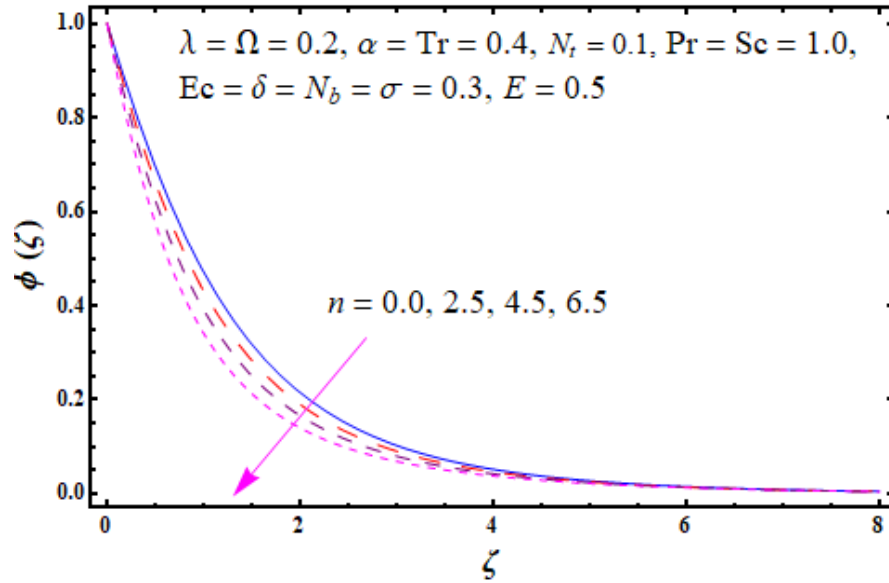
Figure 6.21 : Sketch for $\phi(\zeta)$ against n.
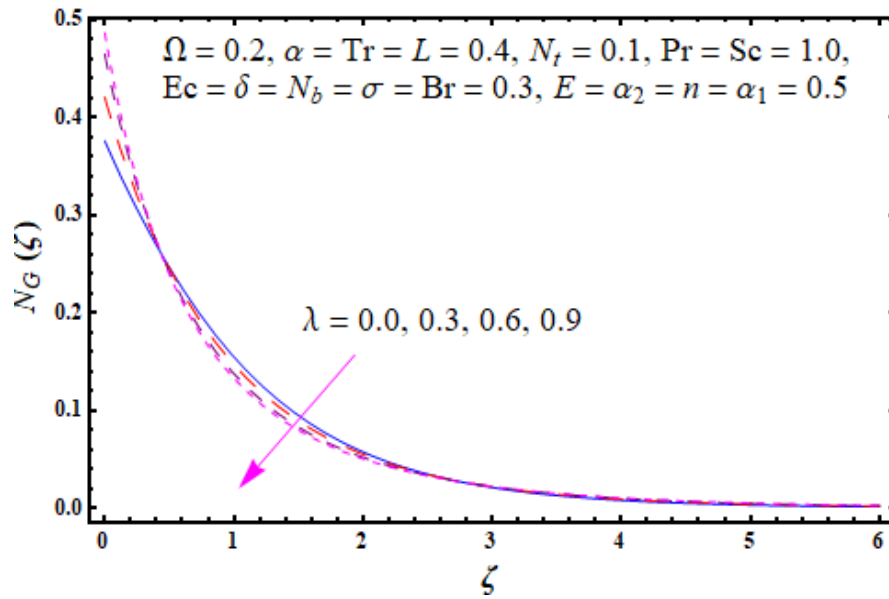
Figure 6.22 : Sketch for $N_G(\zeta)$ against λ.

Figure 6.23 : Sketch for Be against λ.
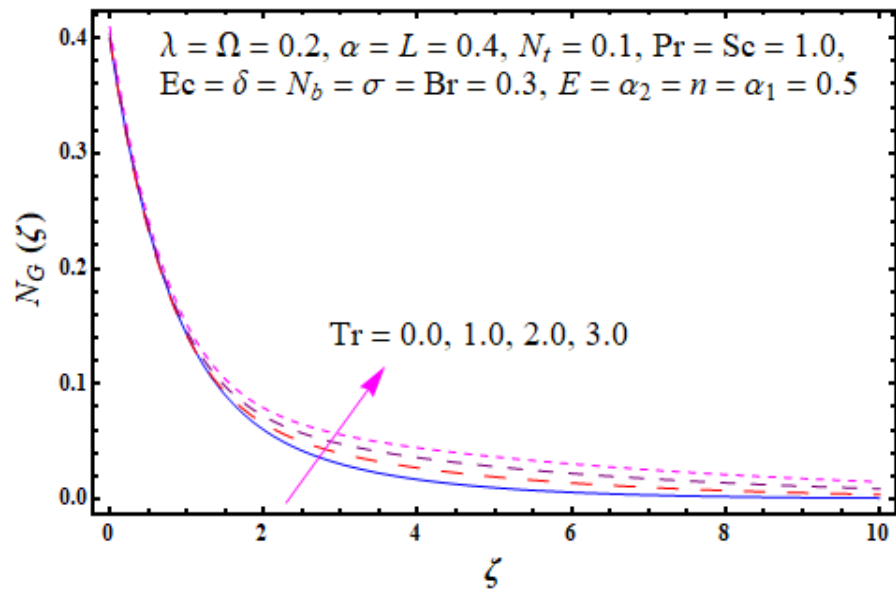
Figure 6.24 : Sketch for $N_G(\zeta)$ against Tr.
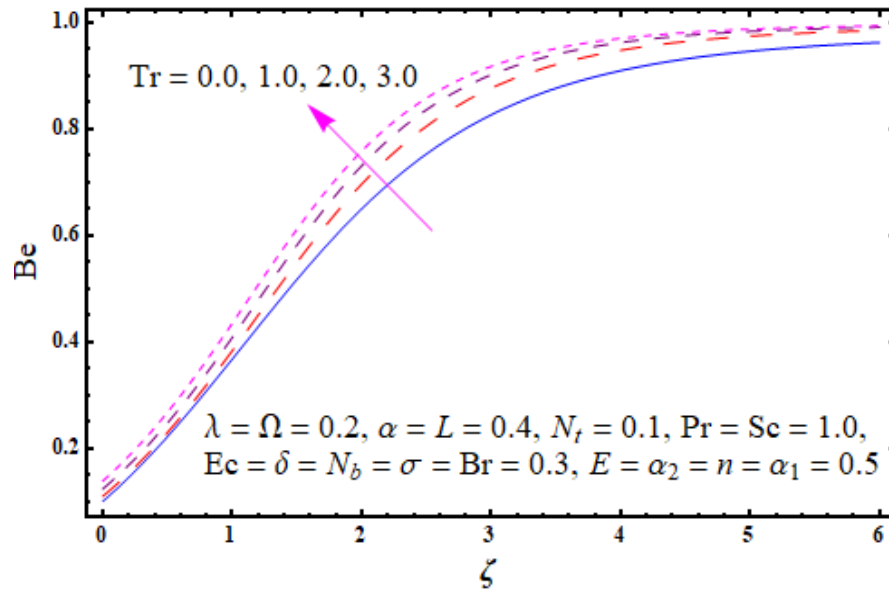
Figure 6.25 : Sketch for Be against Tr.
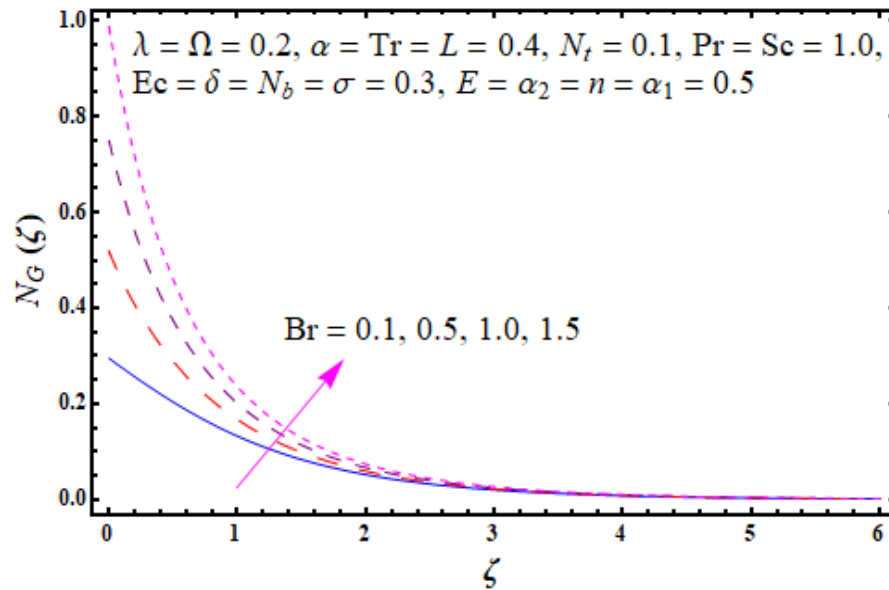
Figure 6.26 : Sketch for $N_G(\zeta)$ against Br.
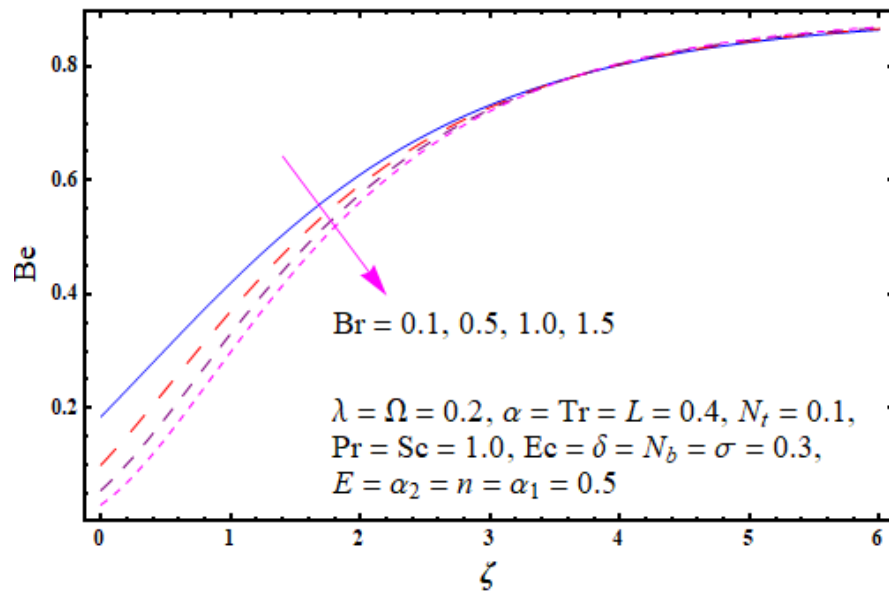
Figure 6.27 : Sketch for Be against Br.
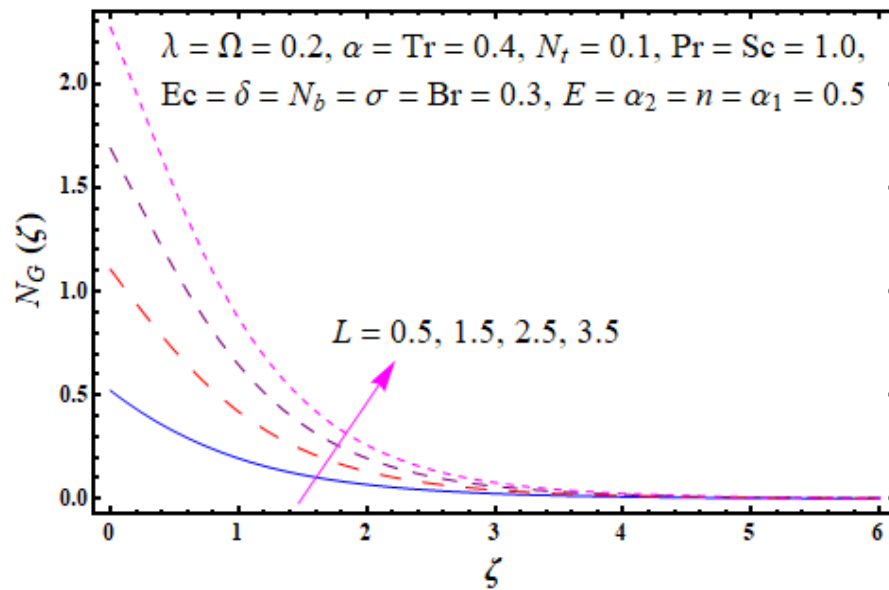
Figure 6.28 : Sketch for $N_G(\zeta)$ against L.
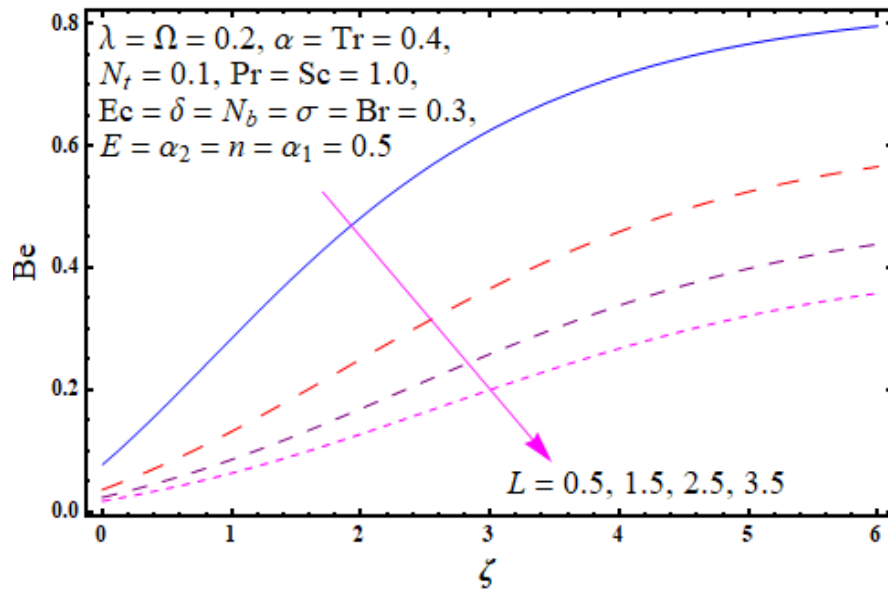
Figure 6.29 : Sketch for Be against L.
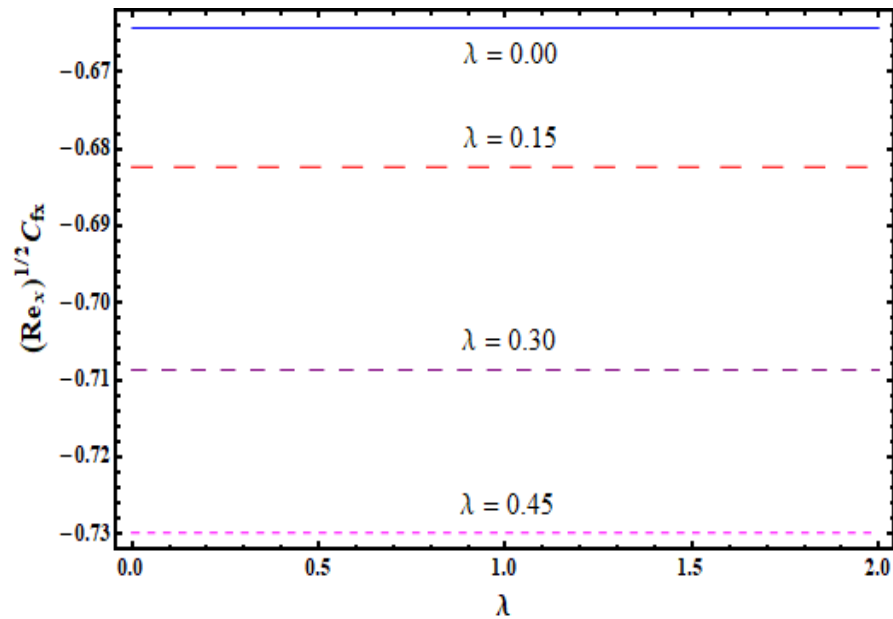
Figure 6.30 : Sketch for $C_{fx}(\text{Re}_x)^{1/2}$ against λ.
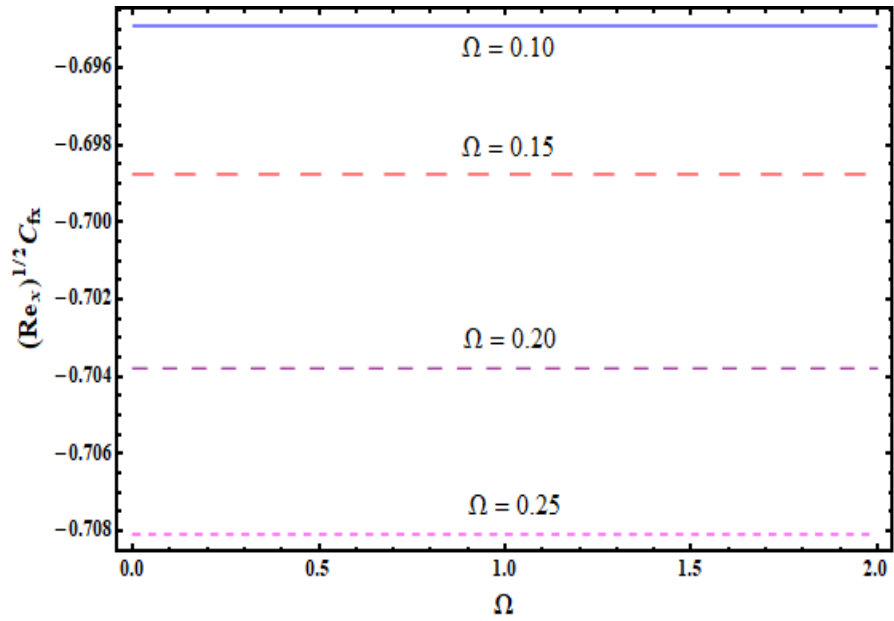
Figure 6.31 : Sketch for $C_{fx}(\mathrm{Re}_x)^{1/2}$ against Ω.
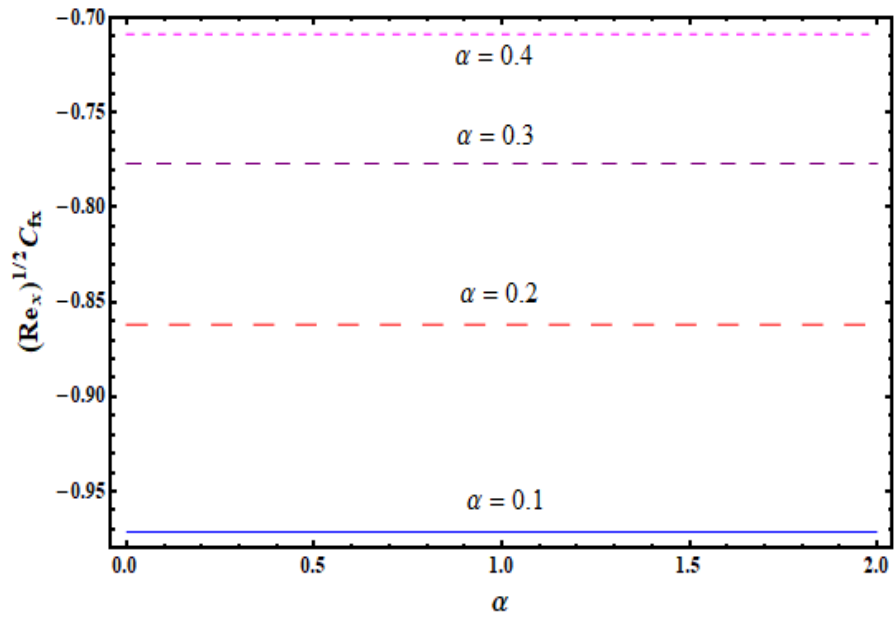
Figure 6.32 : Sketch for $C_{fx}(\mathrm{Re}_x)^{1/2}$ against α.

111
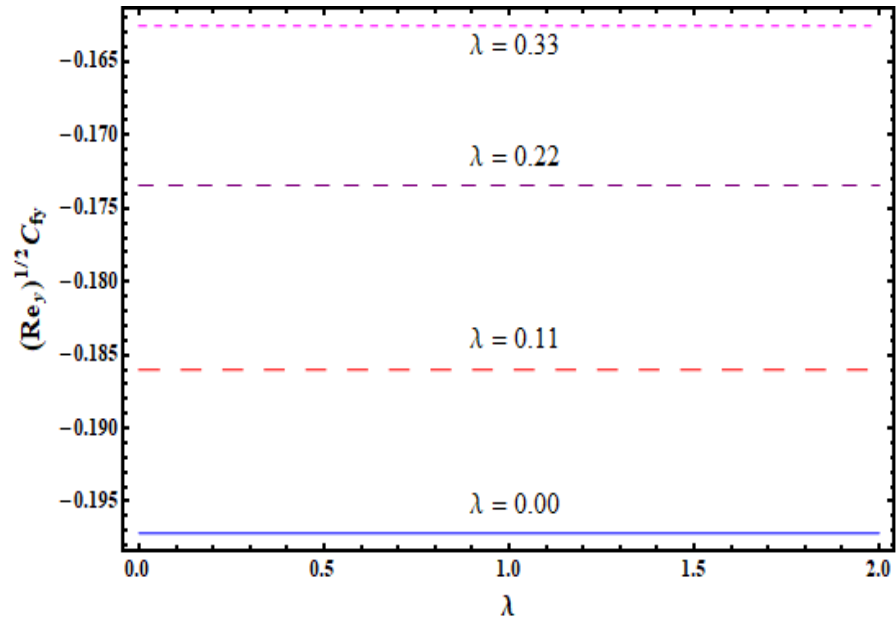
Figure 6.33 : Sketch for $C_{fy}(\mathrm{Re}_y)^{1/2}$ against λ.
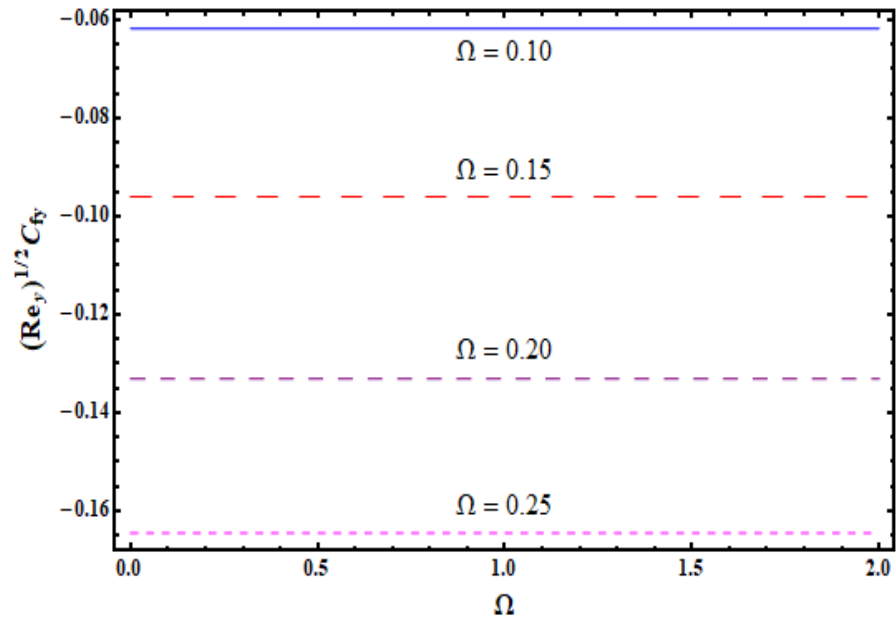
Figure 6.34 : Sketch for $C_{fy}(\mathrm{Re}_y)^{1/2}$ against Ω.

112
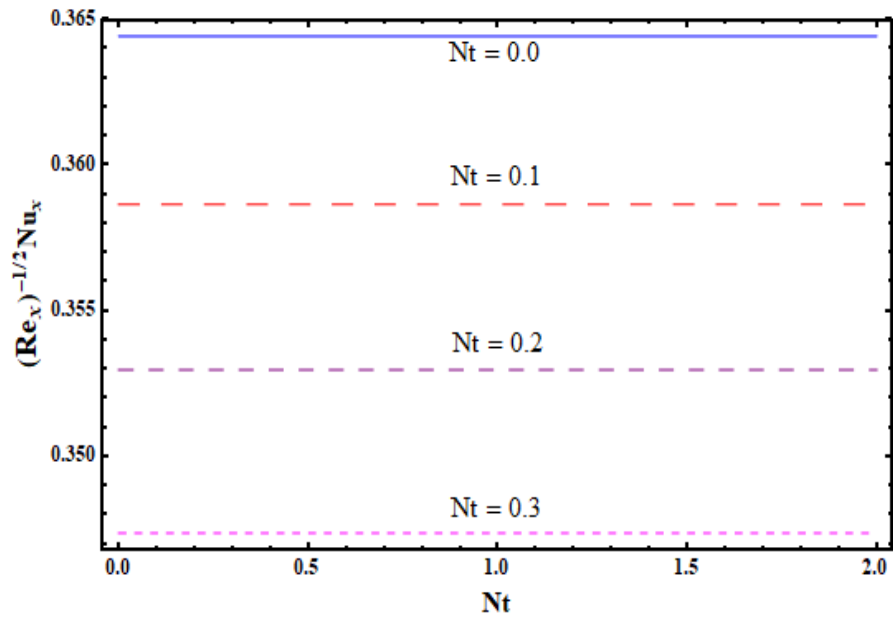
Figure 6.35 : Sketch for $(Re_x)^{-1/2}Nu_x$ against N_t.
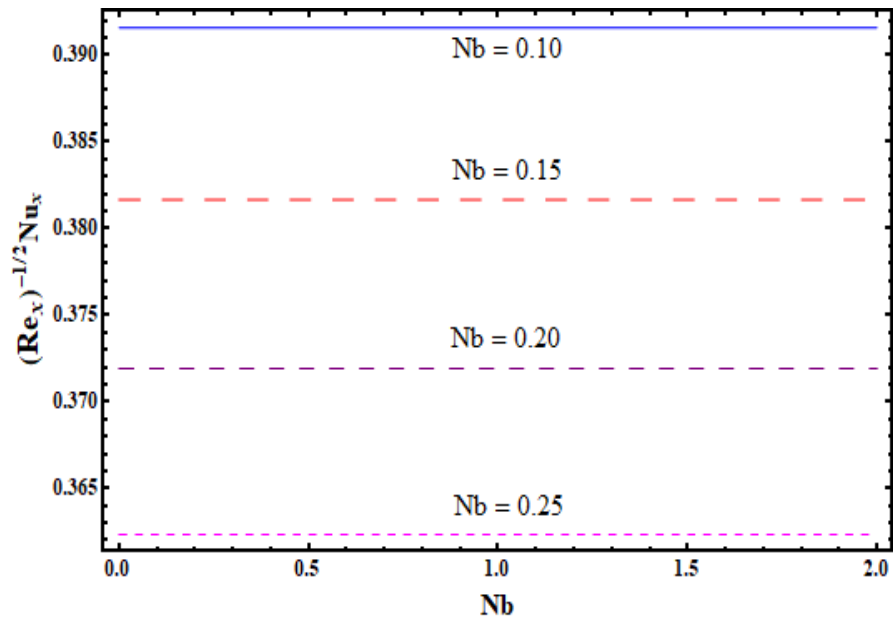
Figure 6.36 : Sketch for $(Re_x)^{-1/2}Nu_x$ against N_b.
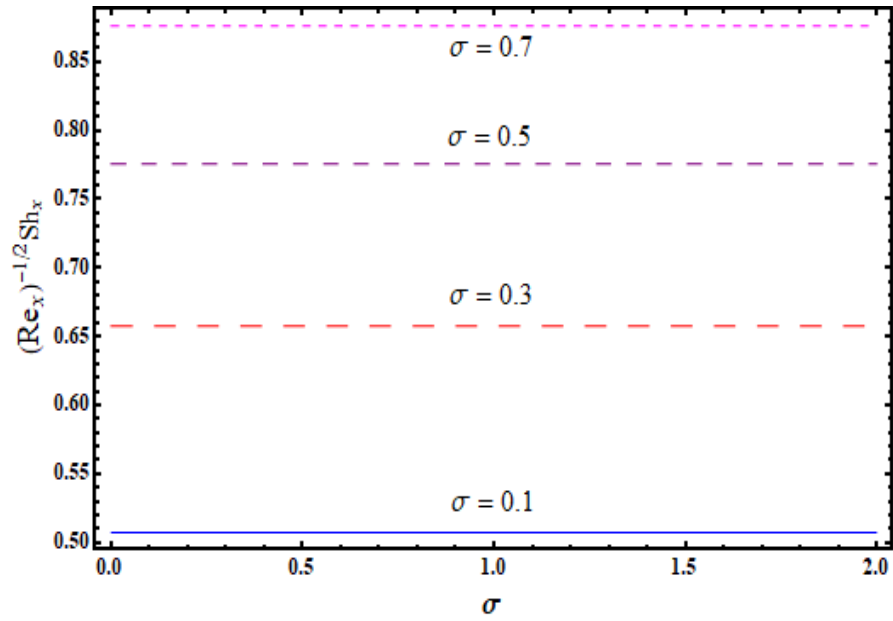
Figure 6.37 : Sketch for $(\mathrm{Re}_x)^{-1/2}Sh_x$ against σ.
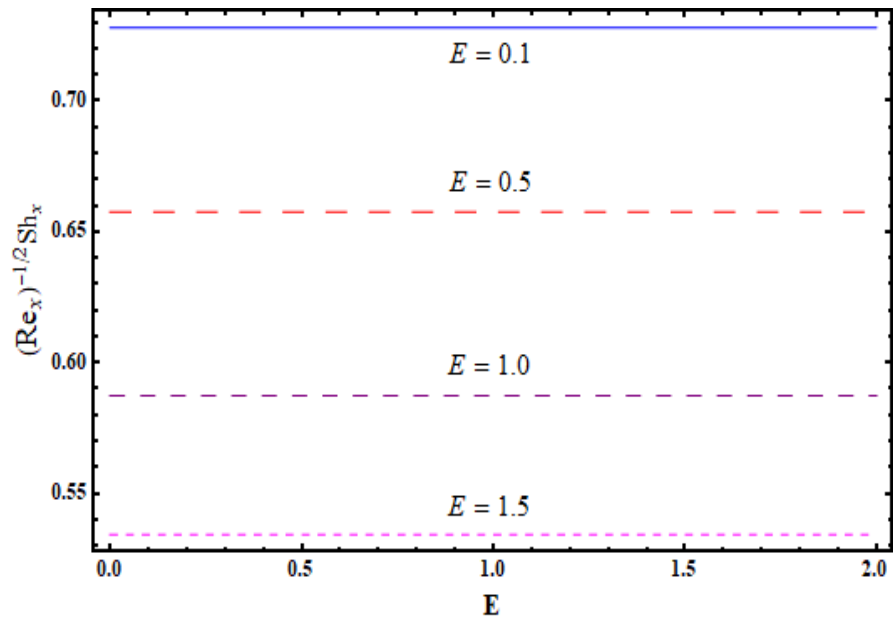
Figure 6.38 : Sketch for $(\mathrm{Re}_x)^{-1/2}Sh_x$ against E.

114

6.4   Major observations

Major observations of the problem considered in this chapter are given below:

- Higher porosity parameter λ exhibit similar behavior for both velocities $f'(\zeta)$ and $g(\zeta)$ while reverse situation is observed against Ω.

- Both $\theta(\zeta)$ and $\phi(\zeta)$ depict increasing trend against stronger λ and Ω.

- Temperature enhances for larger radiation parameter Tr, Brownian movement parameter N_b, Eckert number Ec and thermophoresis parameter N_t.

- Prandtl Pr and Schmidt Sc numbers for $\theta(\zeta)$ and $\phi(\zeta)$ have similar effects.

- Higher N_t and E correspond to stronger nano-concentration field $\phi(\zeta)$ while inverse trend is seen for higher N_b, σ, δ and n.

- Entropy production $N_G(\zeta)$ is maximum for greater Tr, Br and L.

- Bejan number enhances for Tr while it decays for higher λ, Br and L.

- Coefficients of surface drag $(\mathrm{Re}_x)^{1/2}C_{fx}$ and $(\mathrm{Re}_x)^{1/2}C_{fy}$ have similar trend for higher porosity parameter λ.

- Higher N_t and N_b give rise to reduction of heat transfer rate.

- Mass transfer rate reduces for higher E while reverse pattern is noticed for σ.

Chapter 7

Analysis of entropy production and activation energy in hydromagnetic rotating flow of nanoliquid with velocity slip and convective conditions

This chapter investigates entropy production in three dimensional hydromagnetic swirling flow of nanoliquid with binary chemical mechanism and activation energy. Entropy production and Bejan number have been demonstrated through the existence of porous medium, viscous dissipation, magnetic field, thermal radiation and heat source/sink. Velocity slip, convective heat and mass conditions are imposed at the surface. The nonlinear equations are developed through transformation scheme. Shooting method is employed for solutions of resulting nonlinear expressions. Salient behaviors of several pertinent variables on velocities, nano-concentration, entropy production, Bejan number and temperature distributions are examined graphically. Further rates of mass transfer and coefficients of surface drag and rate of heat transfer are graphically analyzed via different variables.

116

7.1 Statement

Here steady 3D hydromagnetic flow of nanoliquid subject to radiative heat transfer is under consideration. Both fluid and stretched surface are in a rotating frame. The total rate of entropy production is computed. A uniform magnetic field of strength B_0 is imposed perpendicular to stretched surface. Effect of activation energy and binary chemical mechanism is studied. Thermophoresis and Brownian motion impacts are also taken for current analysis. Velocity slip and convective conditions are also implemented at surface. The viscous fluid filling space $z \geq 0$ rotates uniformly with constant rate ω. The considered surface is assumed to have velocity $U_w(x) = ax + L_1 \frac{\partial u}{\partial z}$. L_1 being slip coefficient. Resulting boundary-layer expressions under the above mentioned assumptions are

$$\frac{\partial u}{\partial x} + \frac{\partial v}{\partial y} + \frac{\partial w}{\partial z} = 0, \tag{7.1}$$

$$u\frac{\partial u}{\partial x} + v\frac{\partial u}{\partial y} + w\frac{\partial u}{\partial z} - 2\omega v = \nu\frac{\partial^2 u}{\partial z^2} - \frac{\sigma B_0^2}{\rho_f}u - \frac{\nu}{k^\star}u, \tag{7.2}$$

$$u\frac{\partial v}{\partial x} + v\frac{\partial v}{\partial y} + w\frac{\partial v}{\partial z} + 2\omega u = \nu\frac{\partial^2 v}{\partial z^2} - \frac{\sigma B_0^2}{\rho_f}u - \frac{\nu}{k^\star}v, \tag{7.3}$$

$$\begin{aligned} u\frac{\partial T}{\partial x} + v\frac{\partial T}{\partial y} + w\frac{\partial T}{\partial z} &= \left(\alpha^\star + \frac{16\sigma_1 T_\infty^3}{3m_1(\rho c)_f}\right)\frac{\partial^2 T}{\partial z^2} + \frac{(\rho c)_p}{(\rho c)_f}\left(D_B\left(\frac{\partial T}{\partial z}\frac{\partial C}{\partial z}\right) + \frac{D_T}{T_\infty}\left(\frac{\partial T}{\partial z}\right)^2\right) \\ &+ \frac{\mu}{(\rho c)_f}\left(\left(\frac{\partial u}{\partial z}\right)^2 + \left(\frac{\partial v}{\partial z}\right)^2\right) + \frac{\mu}{k^\star(\rho c)_f}\left(u^2 + v^2\right) + \frac{\sigma B_0^2}{(\rho c)_f}\left(u^2 + v^2\right) + \frac{Q_0}{(\rho c)_f}(T - T_\infty), \end{aligned} \tag{7.4}$$

$$u\frac{\partial C}{\partial x} + v\frac{\partial C}{\partial y} + w\frac{\partial C}{\partial z} = D_B\left(\frac{\partial^2 C}{\partial z^2}\right) - k_r^2\left(\frac{T}{T_\infty}\right)^n (C - C_\infty)\exp\left(-\frac{E_a}{\kappa T}\right) + \frac{D_T}{T_\infty}\left(\frac{\partial^2 T}{\partial z^2}\right), \tag{7.5}$$

with

$$u = U_w(x) = ax + L_1\frac{\partial u}{\partial z}, \; v = 0, \; w = 0, \; -k\frac{\partial T}{\partial z} = h_1(T_f - T),$$
$$-D_B\frac{\partial C}{\partial z} = h_2(C_f - C) \text{ at } z = 0, \tag{7.6}$$

$$u \to 0, \quad v \to 0, \quad T \to T_\infty, \quad C \to C_\infty \quad \text{when } z \to \infty, \tag{7.7}$$

in which (u, v, w) express velocities in (x, y, z) directions respectively, absolute viscosity (μ), (σ) electrical conductivity, (B_0) strength of uniform magnetic field, $(k^\star)$ permeability of porous medium, thermal diffusivity $(\alpha^\star)$, thermal efficiency (k), heat capacitance of the liquid $(\rho c)_f$, Stefan-Boltzmann constant (σ_1), mean absorption coefficient (m_1), Brownian coefficient

(D_B), effective heat capacitance of nanoparticles $(\rho c)_p$, temperature (T), (Q_0) heat generation/absorption coefficient, concentration (C), thermophoretic coefficient (D_T), activation energy (E_a), fitted rate constant (n), reaction rate (k_r), Boltzmann constant (κ), (L_1) velocity slip coefficient and coefficients of mass and heat transfer (h_2) and (h_1) respectively.

Writing

$$u = axf'(\zeta), \ v = axg(\zeta), \ w = -(a\nu)^{1/2}f(\zeta), \\ \left. \zeta = \left(\frac{a}{\nu}\right)^{1/2}z, \ \theta(\zeta) = \frac{T-T_\infty}{T_f-T_\infty}, \ \phi(\zeta) = \frac{C-C_\infty}{C_f-C_\infty}. \right\}$$ (7.8)

Equation (7.1) is fully satisfied and Eqs. $(7.2) - (7.7)$ are reduced to

$$f''' + ff'' - f'^2 + 2\Omega g - (Ha)^2 f' - \lambda f' = 0,$$ (7.9)

$$g'' + fg' - f'g - 2\Omega f' - (Ha)^2 g - \lambda g = 0,$$ (7.10)

$$\frac{1}{\text{Pr}}(1+Tr)\theta'' + \theta'f + Ec(Ha)^2(f'^2 + g^2) + N_b\theta'\phi' \\ +Ec(f''^2 + g'^2) + Ec\lambda(f'^2 + g^2) + S_1\theta + N_t\theta'^2 = 0,$$ (7.11)

$$\frac{1}{Sc}\phi'' + f\phi' + \frac{1}{Sc}\frac{N_t}{N_b}\theta'' - \sigma(1+\delta\theta)^n\phi\exp\left(-\frac{E}{1+\delta\theta}\right) = 0,$$ (7.12)

$$f(0) = g(0) = 0, \ f'(0) = 1 + \alpha f''(0), \ \theta'(0) = -\gamma_1(1 - \theta(0)), \ \phi'(0) = -\gamma_2(1 - \phi(0)),$$ (7.13)

$$f'(\infty) \to 0, \ g(\infty) \to 0, \ \theta(\infty) \to 0, \ \phi(\infty) \to 0.$$ (7.14)

Where (λ) denotes porosity parameter, (Ha) Hartman parameter, (Sc) Schmidt number, (Ω) rotation parameter, (Tr) thermal radiation parameter, (Pr) Prandtl number, (σ) chemical reaction parameter, (N_b) Brownian movement parameter, (Ec) Eckert number, (S_1) heat source/sink parameter, (α) velocity slip parameter, (E) nondimensional activation energy, thermal Biot number γ_1, thermophoresis diffusion parameter (N_t), temperature difference parameter (δ) and concentration Biot number γ_1. We define

$$\lambda = \frac{\nu}{k^\star a}, \ Tr = \frac{16\sigma_1 T_\infty^3}{3km_1}, \ \text{Pr} = \frac{\nu}{\alpha^\star}, \ Sc = \frac{\nu}{D_B}, \ Ec = \frac{a^2x^2}{c_p(T_f-T_\infty)}, \ (Ha)^2 = \frac{\sigma B_0^2}{a\rho_f}, \\ \left. \Omega = \frac{\omega}{a}, \ N_b = \frac{(\rho c)_p D_B(C_f-C_\infty)}{(\rho c)_f\nu}, \ \gamma_1 = \frac{h_1}{k}\sqrt{\frac{\nu}{a}}, \ \alpha = L_1\sqrt{\frac{a}{\nu}}, \ E = \frac{E_a}{\kappa T_\infty}, \right\} \\ \left. \sigma = \frac{k_r^2}{a}, \ S_1 = \frac{Q_0}{a(\rho c)_f}, \ N_t = \frac{(\rho c)_p D_T(T_f-T_\infty)}{(\rho c)_f\nu T_\infty}, \ \gamma_2 = \frac{h_2}{D_B}\sqrt{\frac{\nu}{a}}, \ \delta = \frac{T_w-T_\infty}{T_\infty}. \right\}$$ (7.15)

Skin friction coefficients and heat and mass transfer rates are

$$
\left.
\begin{aligned}
(\mathrm{Re}_x)^{1/2} C_{fx} &= f''(0), \\
(\mathrm{Re}_y)^{1/2} C_{fy} &= g'(0), \\
(\mathrm{Re}_y)^{1/2} Nu_x &= -(1 + Tr)\theta'(0), \\
(\mathrm{Re}_y)^{1/2} Sh_x &= -\phi'(0),
\end{aligned}
\right\}
\tag{7.16}
$$

where $(\mathrm{Re}_x = ax^2/\nu)$ depicts local Reynolds number.

7.2 Entropy analysis

The entropy production in hydromagnetic rotating flow of nanofluid can be expressed as:

$$
\begin{aligned}
S_G = {} & \frac{k}{T_\infty^2}\left(1 + \frac{16\sigma_1 T_\infty^3}{3km_1}\right)\left(\frac{\partial T}{\partial z}\right)^2 + \frac{\mu}{T_\infty}\left(\left(\frac{\partial u}{\partial z}\right)^2 + \left(\frac{\partial v}{\partial z}\right)^2\right) + \frac{\mu}{k^\star T_\infty}\left(u^2 + v^2\right) \\
& + \frac{\sigma B_0^2}{T_\infty}\left(u^2 + v^2\right) + \frac{Q_0}{T_\infty}(T - T_\infty) + \frac{RD}{C_\infty}\left(\frac{\partial C}{\partial z}\right)^2 + \frac{RD}{T_\infty}\left(\frac{\partial T}{\partial z}\frac{\partial C}{\partial z}\right).
\end{aligned}
\tag{7.17}
$$

Eq. (7.17) exhibits fours factors by which entropy is generated. The 1st, 2nd, 3rd , 4th, 5th and 6th terms on right hand side of Eq. (7.17) indicate heat transfer, fluid friction, permeable space, Joule heating, heat source/sink and mass transfer or diffusion irreversibilities respectively. After employing transformations (7.8) on Eq. (7.17), one obtains

$$
\begin{aligned}
N_S = \frac{S_G}{S_{G_0}} = {} & \alpha_1(1 + Tr)\theta'^2 + Br(f''^2 + g'^2) + \lambda Br(f'^2 + g^2) \\
& + (Ha)^2 Br(f'^2 + g^2) + \Pr S_1\theta + L\theta'\phi' + L\frac{\alpha_2}{\alpha_1}\phi'^2,
\end{aligned}
\tag{7.18}
$$

where

$$
S_{G_0} = \frac{ka(T_f - T_\infty)}{\nu T_\infty}.
\tag{7.19}
$$

Eq. (7.18) represents the dimensionless form of entropy generation equation. Where Br, L, α_1 and α_2 stand for nondimensional Brinkman number, diffusive number, temperature ratio number and concentration ratio number respectively. These variables are defined as:

$$
Br = \frac{a^2 x^2 \mu}{k(T_f - T_\infty)}, \; L = \frac{RD(C_f - C_\infty)}{k}, \; \alpha_1 = \frac{T_f - T_\infty}{T_\infty}, \; \alpha_2 = \frac{C_f - C_\infty}{C_\infty}.
\tag{7.20}
$$

Mathematical expression for the Bejan number is

$$Be = \frac{\text{Entropy via heat transfer}}{\text{Total entropy}},$$ (7.21)

$$Be = \frac{\alpha_1(1+Tr)\theta'^2}{\begin{array}{c} \alpha_1(1+Tr)\theta'^2 + Br(f''^2 + g'^2) + \lambda Br(f'^2 + g^2) \\ + (Ha)^2 Br(f'^2 + g^2) + \Pr S_1\theta + L\theta'\phi' + L\frac{\alpha_2}{\alpha_1}\phi'^2, \end{array}}.$$ (7.22)

7.3 Discussion

In this section Figures $(7.1 - 7.44)$ are plotted for the inspection of velocity, Bejan number, temperature, entropy production and concentration against different emerging flow variables. Figure 7.1 describes influence of porosity parameter λ on velocity $f'(\zeta)$. Velocity decays against greater estimations of λ. Figure 7.2 exhibits the curves of velocity field $f'(\zeta)$ against different values of rotation parameter Ω. One can easily notice the reduction in $f'(\zeta)$ via higher values of Ω. Figure 7.3 delineates the influence of Hartman number Ha on velocity $f'(\zeta)$. For higher Ha, the velocity $f'(\zeta)$ decays. Figure 7.4 exhibits the impact of α on $f'(\zeta)$. Depreciating behavior of $f'(\zeta)$ is noted via higher estimations of α. Figure 7.5 depicts influential impact of λ on $g(\zeta)$. Reduction is noticed in velocity $g(\zeta)$ via higher λ. Influence of Ω on $g(\zeta)$ is delineated in Figure 7.6. An increasing behavior is seen against higher Ω. Figure 7.7 shows how velocity $g(\zeta)$ varied by Hartman number Ha. An elevation is observed in the velocity $g(\zeta)$ against stronger Ha. Figure 7.8 demonstrates the variation in temperature $\theta(\zeta)$ for higher porosity parameter λ. Temperature $\theta(\zeta)$ is elevated via higher λ. Figure 7.9 depicts how temperature $\theta(\zeta)$ varied by higher Ω. It is noticed that by increasing Ω, temperature $\theta(\zeta)$ enhanced. Figure 7.10 is drawn to visualize impact of Hartman number Ha on dimensionless temperature $\theta(\zeta)$. Clearly $\theta(\zeta)$ upsurged for growing estimations of Ha. Physically when Ha elevates then Lorentz force (opposing force) developes more friction between liquid particles. On the basis of this frictional force, $\theta(\zeta)$ elevates. Figure 7.11 analyzed the behavior of Biot number γ_1 on $\theta(\zeta)$. An enhancement is observed in temperature via higher estimations of γ_1. Influence of Tr on $\theta(\zeta)$ is presented in Figure 7.12. An elevating impact of $\theta(\zeta)$ is analyzed via higher Tr. Temperature $\theta(\zeta)$ for variation of Ec is presented in Figure 7.13. An increment in

Ec leads to an elevation of $\theta(\zeta)$. Figures 7.14 and 7.15 are developed to analyze the behaviors of heat generation ($S_1 > 0$) and absorption ($S_1 < 0$) parameters. It is examined that temperature shows opposite trend while considering ($S_1 > 0$) and ($S_1 < 0$). Impact of N_t on $\theta(\zeta)$ is displayed in Figure 7.16. Clearly temperature $\theta(\zeta)$ is elevated via higher N_t. Curves of $\theta(\zeta)$ via N_b are developed in Figure 7.17. Here temperature for higher N_b is enhanced. Concentration field $\phi(\zeta)$ behavior for porosity parameter λ is depicted in Figure 7.18. One can apparently observe that $\phi(\zeta)$ elevates for larger λ. Figure 7.19 shows Ω effect on $\phi(\zeta)$. Nano-concentration field and corresponding layer thickness are enhanced via higher Ω. Figure 7.20 explains the impact of Ha on Nano-concentration field $\phi(\zeta)$. Nano-concentration field $\phi(\zeta)$ enhances against higher values of Ha. Figure 7.21 elucidates that nano-concentration field is enhanced via greater values of γ_2. Influence of Sc on $\phi(\zeta)$ is displayed in Figure 7.22. One can apparently notice that $\phi(\zeta)$ depreciates for greater Sc. Figure 7.23 is developed to see the influence of E on the nano-concentration field $\phi(\zeta)$. It is perceived that the nano-concentration field is an increasing function of E. Figure 7.24 displayed outcome of σ on $\phi(\zeta)$. We noticed that higher values of σ cause a depreciation in $\phi(\zeta)$. Figure 7.25 explores that $\phi(\zeta)$ is a depreciating function of δ. Figure 7.26 is developed to analyze the behavior of N_t on $\phi(\zeta)$. Here an elevation in N_t corresponds to stronger $\phi(\zeta)$. Influence of N_b on nano-concentration field $\phi(\zeta)$ is exhibited in Figure 7.27. Decaying trend of $\phi(\zeta)$ is seen via higher N_b. Figure 7.28 presents the behavior of Brinkman number Br on entropy generation N_G. It is observed that entropy elevates when Br augmented. This elevation is due to more intensification of kinetic energy of fluid particles in the boundary layer area. Bejan number also depreciates for incrementing values of Br (See Figure 7.29). Figure 7.30 is portrayed to analyze impact of Ha on entropy generation $N_G(\zeta)$. From this Figure it can be seen that entropy of the system enhances for larger Ha. This happens because an increment of strength of magnetic field induces resistance of flow and as a result fluid friction significantly increases then entropy production rate enhances. Decaying trend is seen in Bejan number via higher estimations of Ha (See Figure 7.31). To visualize the behavior of thermal radiation parameter Tr on entropy production $N_G(\zeta)$, Fig. 7.32 is plotted. An elevation in Tr corresponds to higher entropy generation rate. Physically more heat is generated due to thermal radiation process for which entropy is significantly enhanced. An opposite impact of Bejan number is noted for growing estimations of Tr (See Figure 7.33).

Figures 7.34 and 7.35 elucidate the effect of diffusive variable L on N_G and Be. From these Figures, We can see that entropy increases for larger L while Bejan number exhibits reversing trend. Figures 7.36, 7.37 and 7.38 displayed the variations in $C_{fx}(\text{Re}_x)^{1/2}$ via higher λ, Ha and α. From these Figures it can be observed that $C_{fx}(\text{Re}_x)^{1/2}$ elevates against higher λ and Ha while an opposite situation is observed for higher α. Figures 7.39 and 7.40 are developed to explore the main impacts of λ and Ha on $(\text{Re}_y)^{1/2}C_{fy}$. These graphs exhibit that $C_{fy}(\text{Re}_y)^{1/2}$ decreases for greater estimations of λ and Ha. Influences of γ_1 and N_t on rate of heat transfer are disclosed via Figures 7.41 and 7.42. These Figures exhibit reversing trend in $(\text{Re}_x)^{-1/2}Nu_x$ via growing estimations of γ_1 and N_t. Figures 7.43 and 7.44 demonstrate the impact of γ_2 and N_b on rate of mass transfer respectively. It is recognized that $(\text{Re}_x)^{-1/2}Sh_x$ displays opposite role for higher γ_2 and N_b.
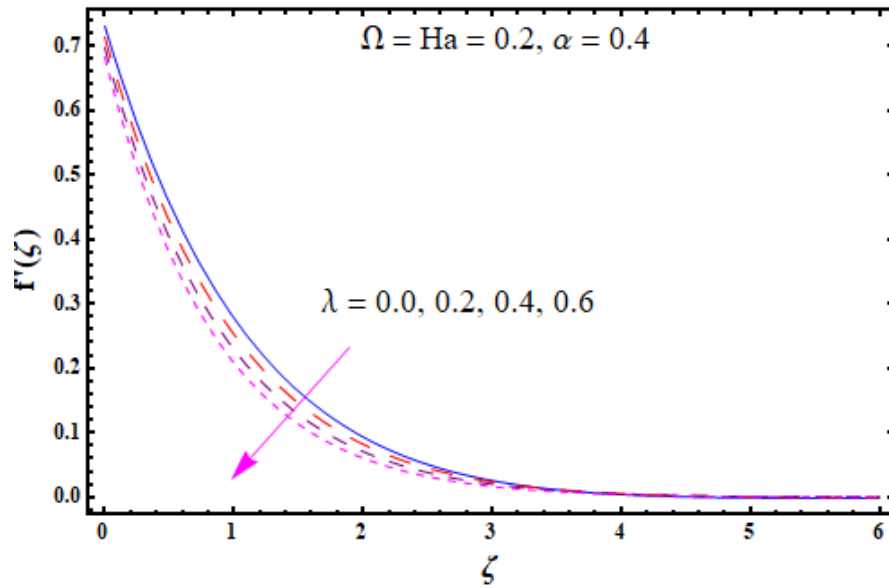
Figure 7.1 : Sketch for $f'(\zeta)$ against λ.
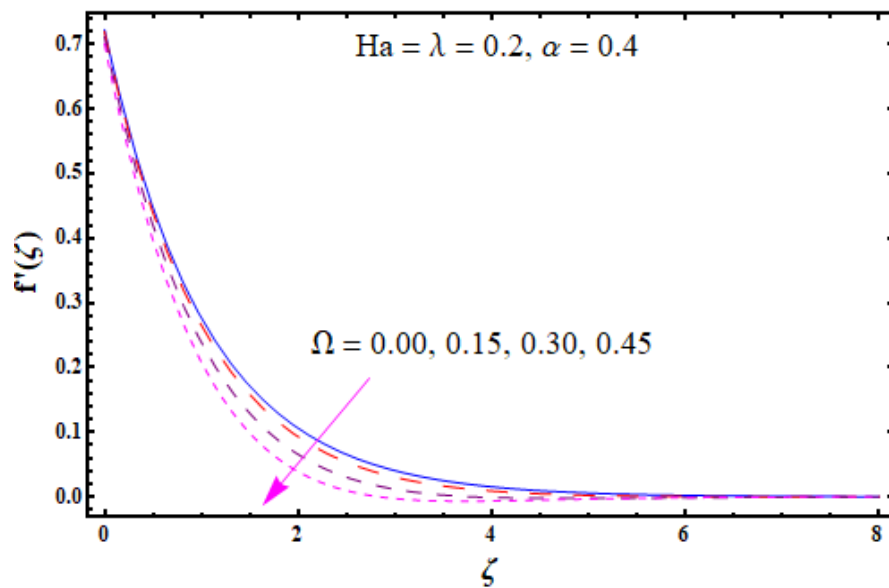
Figure 7.2 : Sketch for $f'(\zeta)$ against Ω.
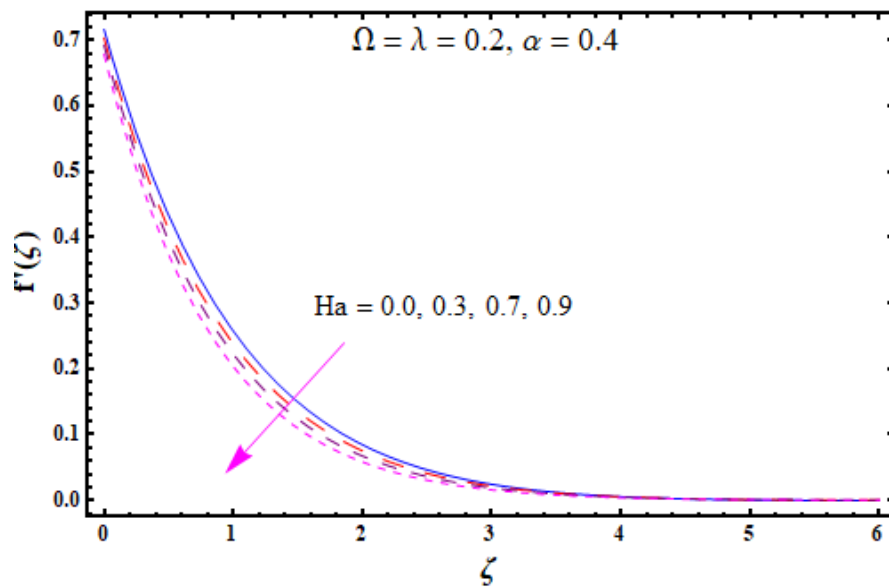
Figure 7.3 : Sketch for $f'(\zeta)$ against Ha.
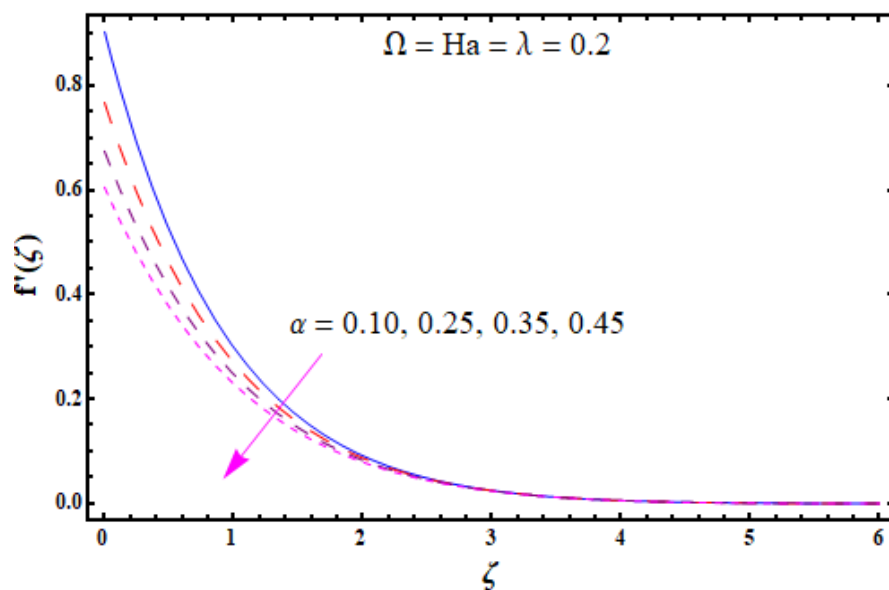
Figure 7.4 : Sketch for $f'(\zeta)$ against α.
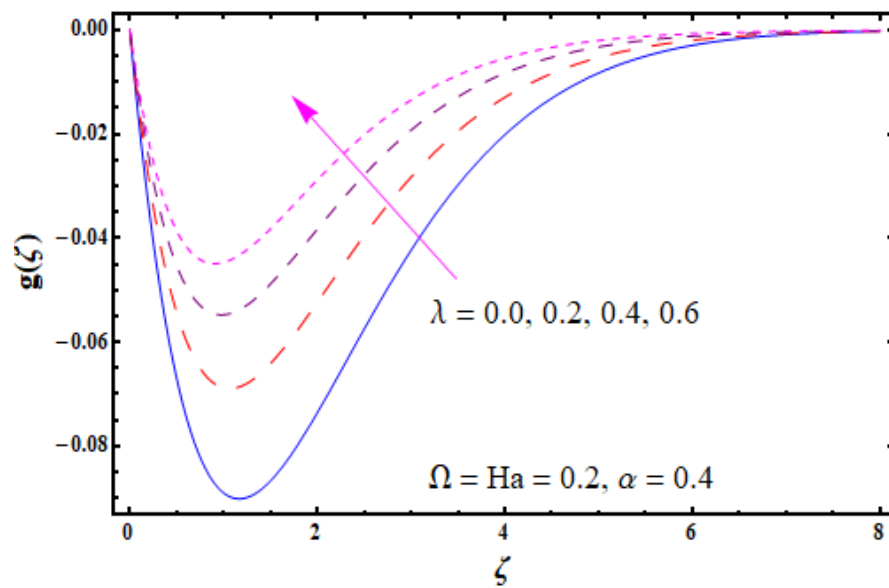
Figure 7.5 : Sketch for $g(\zeta)$ against λ.
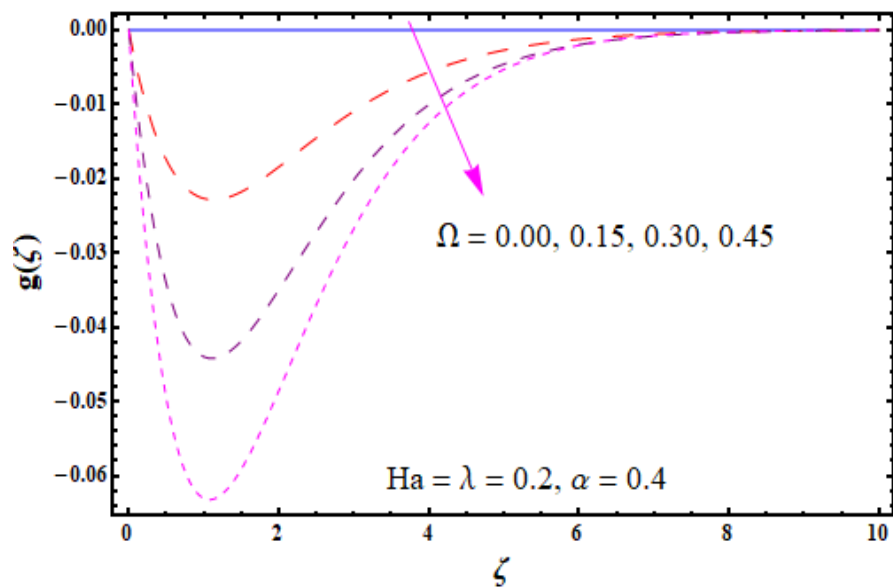
Figure 7.6 : Sketch for $g(\zeta)$ against Ω.
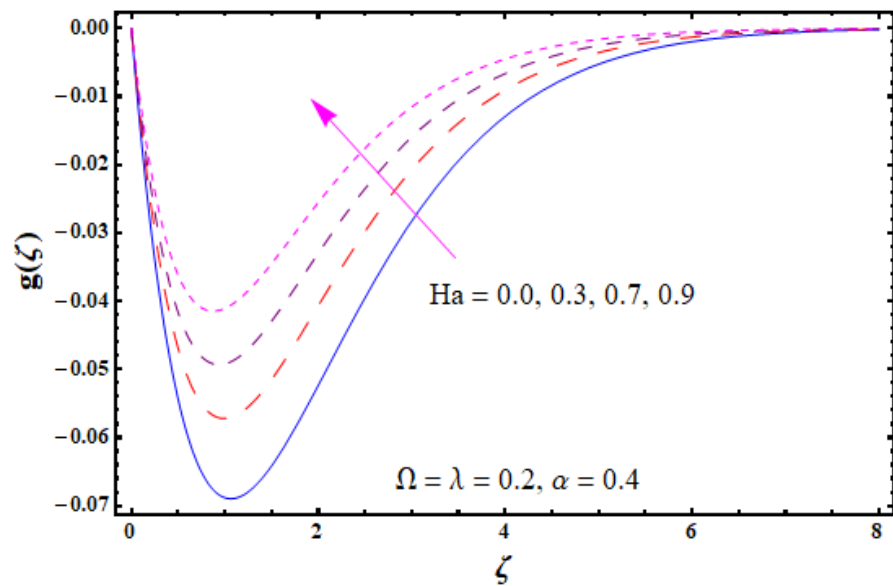
Figure 7.7 : Sketch for $g(\zeta)$ against Ha.
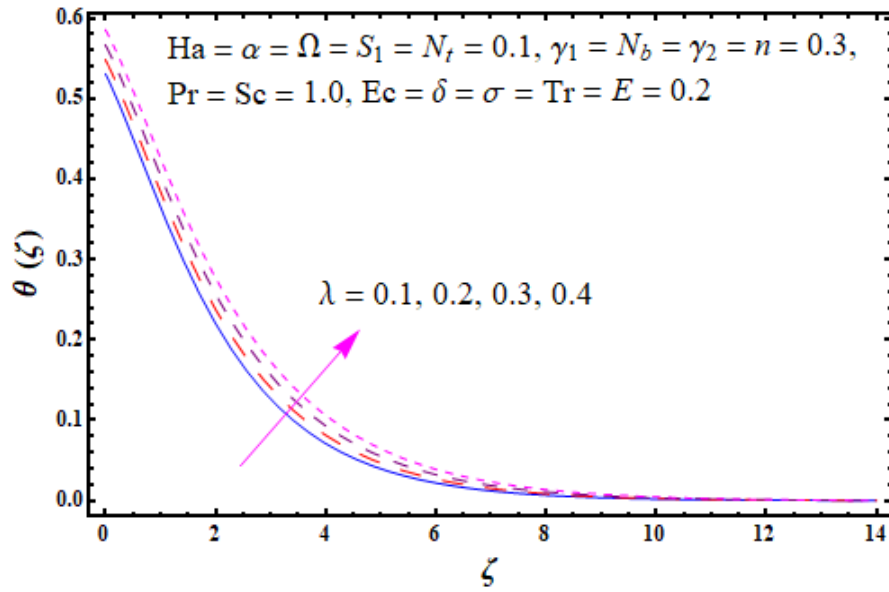
Figure 7.8 : Sketch for $\theta(\zeta)$ against λ.
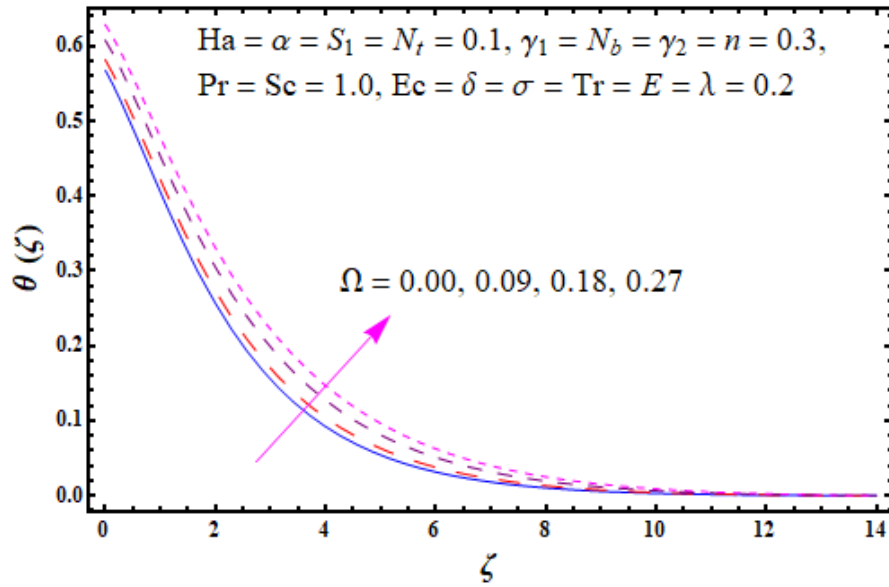
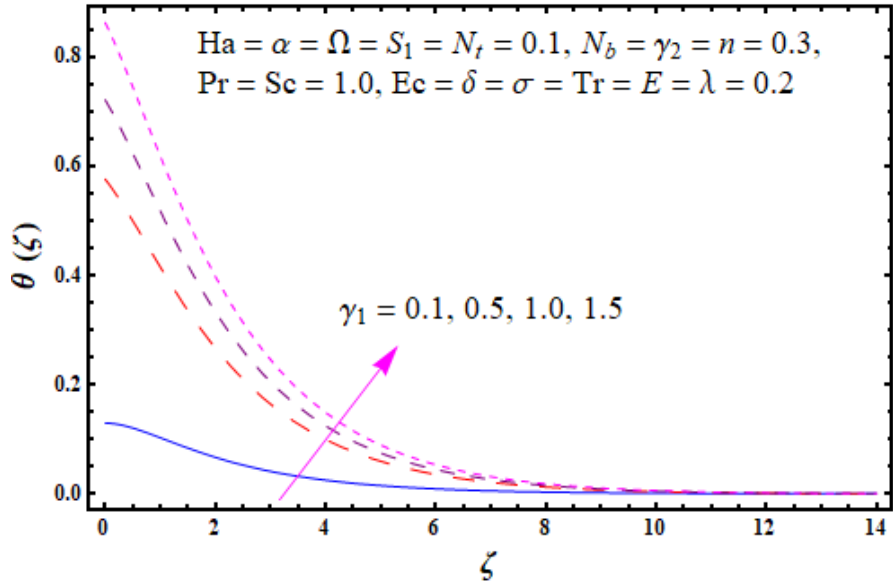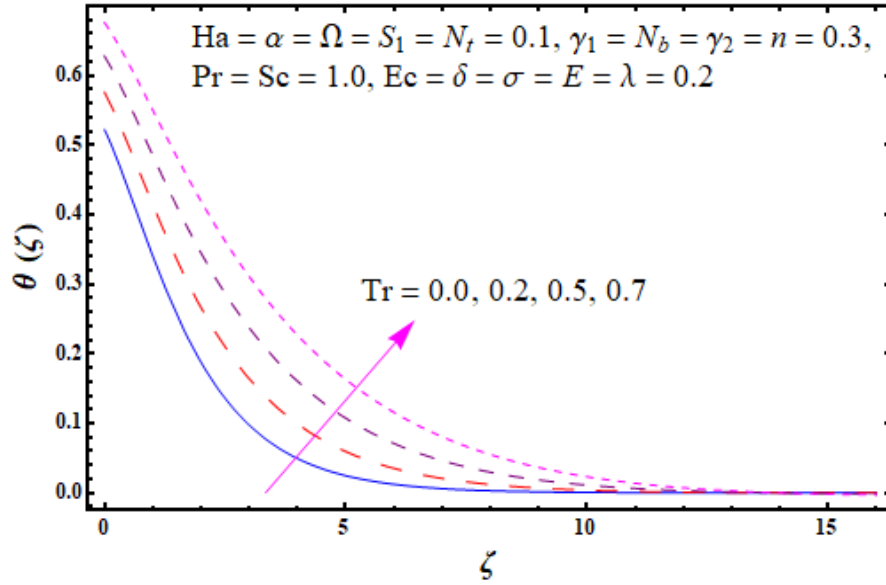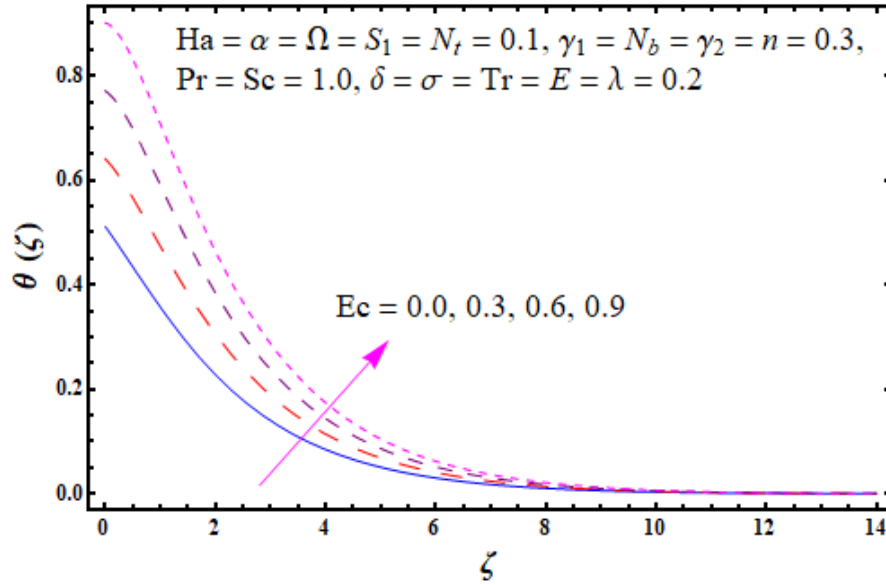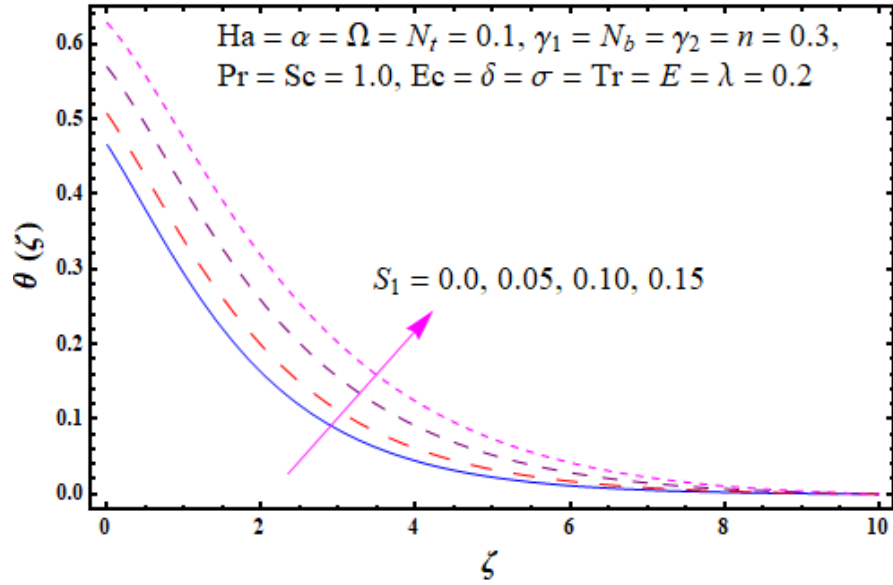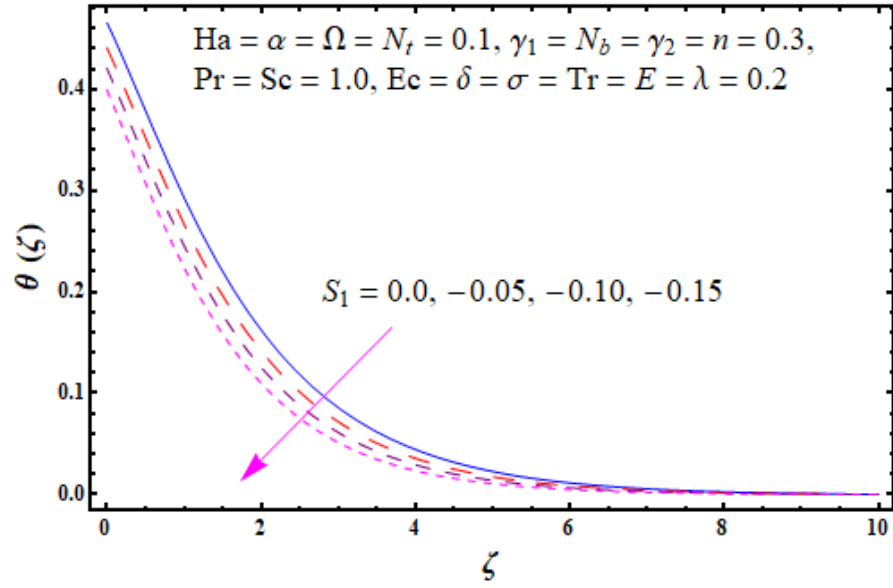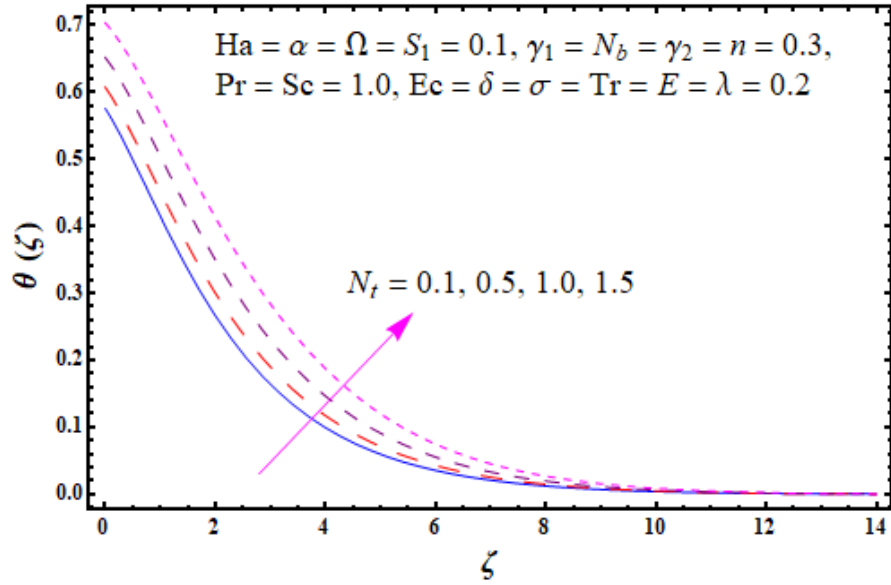Figure 7.9 : Sketch for $\theta(\zeta)$ against Ω.
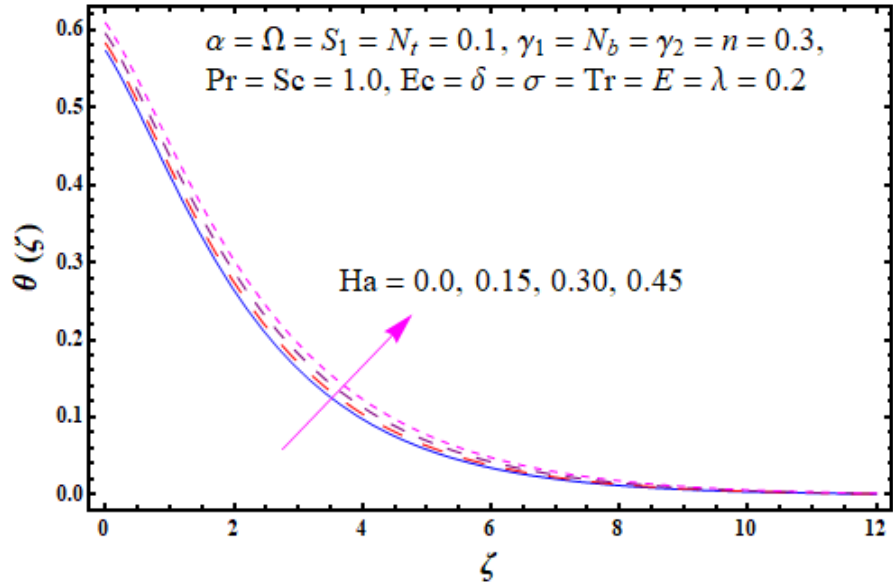
Figure 7.10 : Sketch for $\theta(\zeta)$ against Ha.
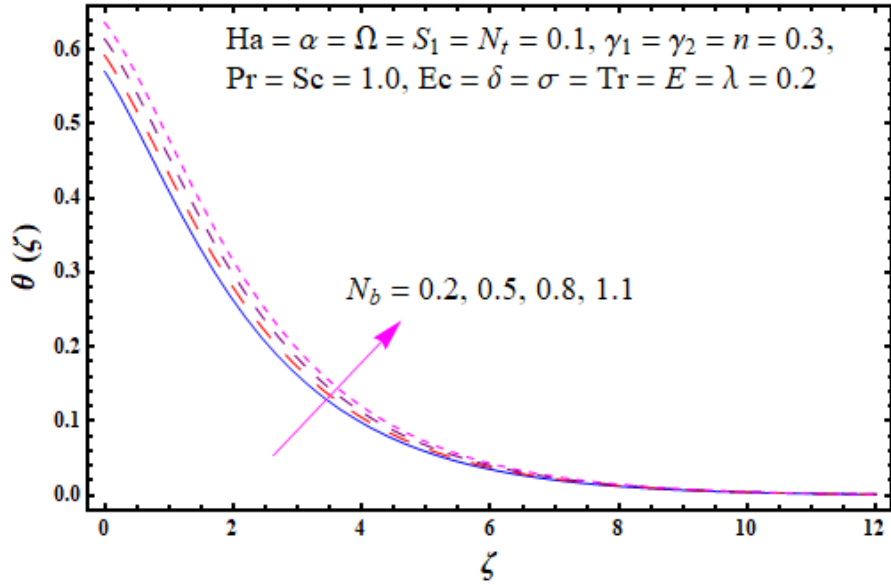

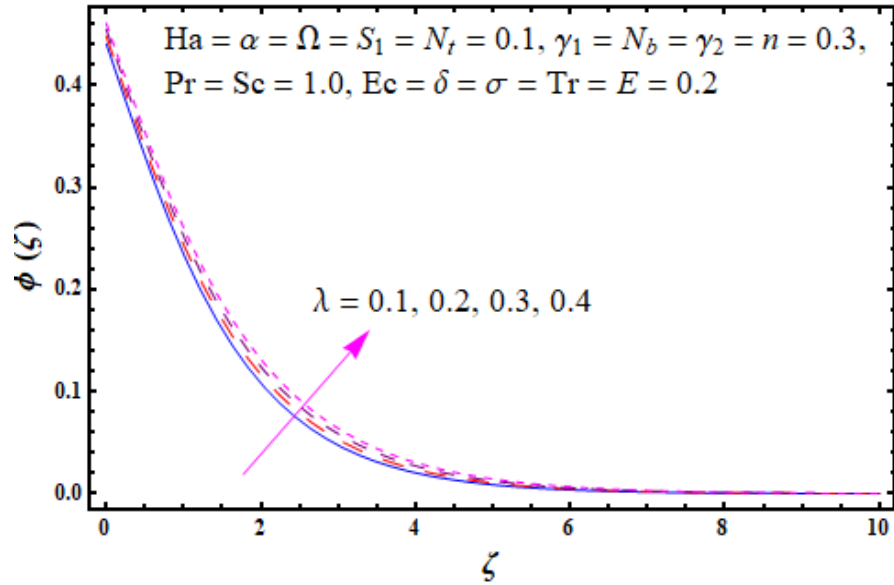Figure 7.11 : Sketch for $\theta(\zeta)$ against γ_1.

127

Figure 7.12 : Sketch for $\theta(\zeta)$ against Tr.

Figure 7.13 : Sketch for $\theta(\zeta)$ against Ec.

128

Figure 7.14 : Sketch for $\theta(\zeta)$ against $(S_1 > 0)$.

Figure 7.15 : Sketch for $\theta(\zeta)$ against $(S_1 < 0)$.

Figure 7.16 : Sketch for $\theta(\zeta)$ against N_t.

Figure 7.17 : Sketch for $\theta(\zeta)$ against N_b.

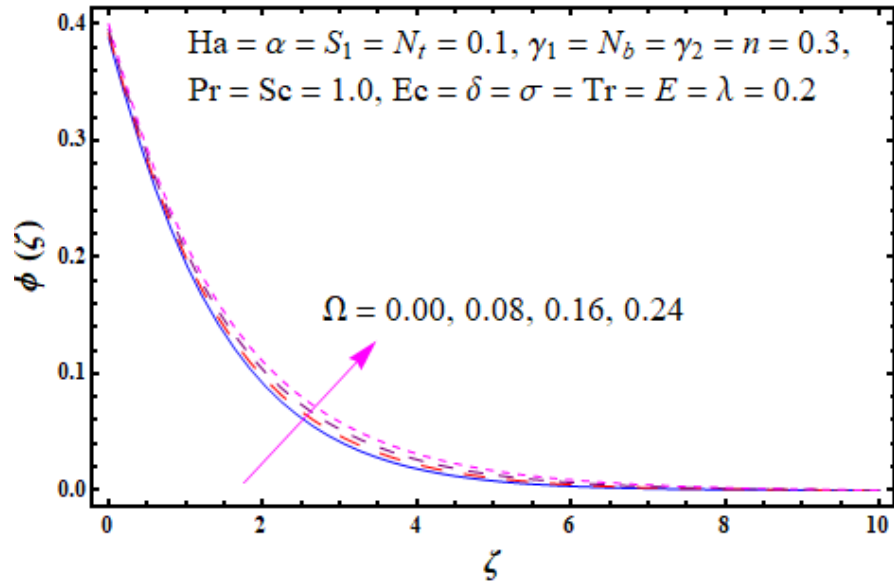Figure 7.18 : Sketch for $\phi(\zeta)$ against λ.
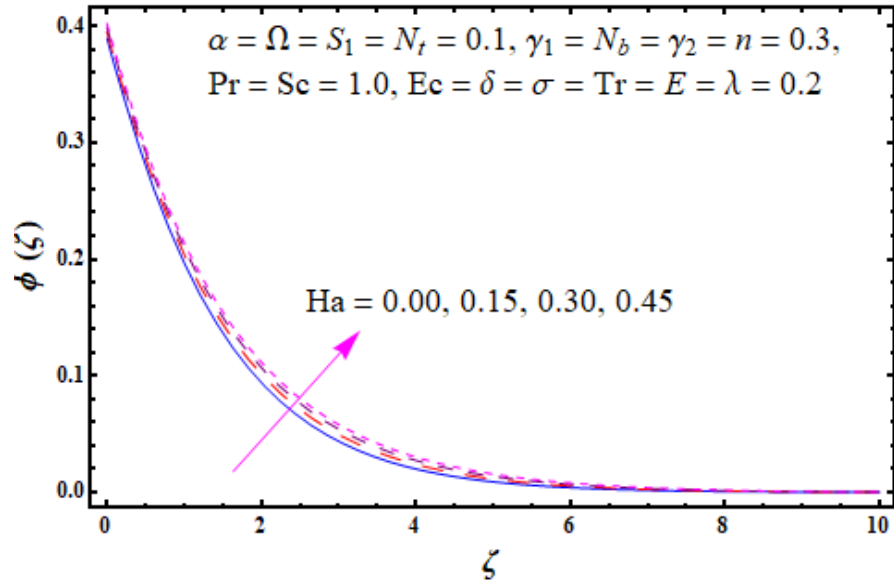

Figure 7.19 : Sketch for $\phi(\zeta)$ against Ω.

131

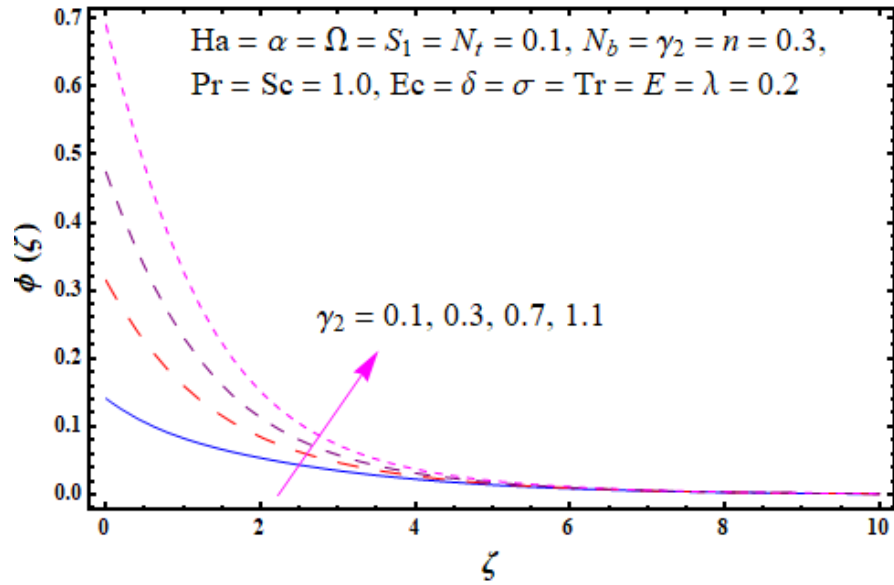Figure 7.20 : Sketch for $\phi(\zeta)$ against Ha.

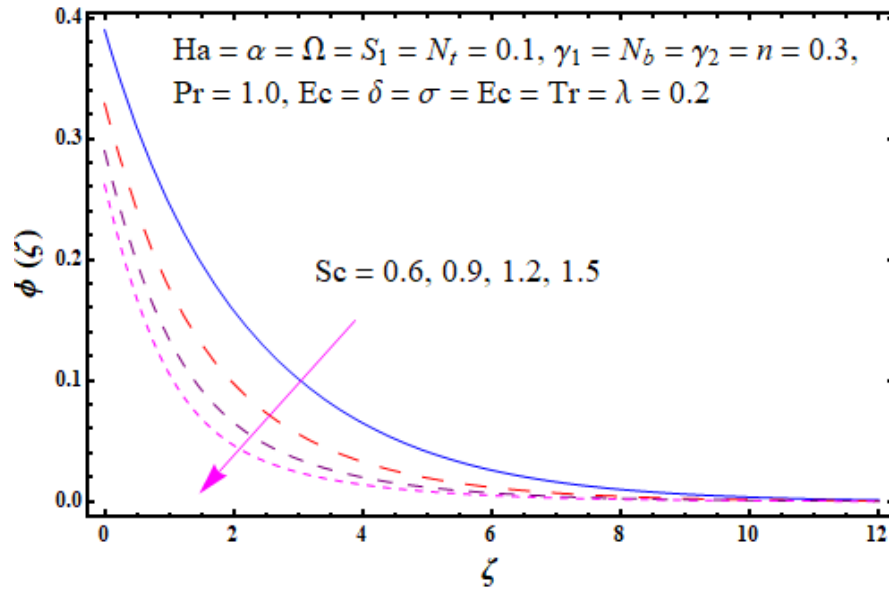Figure 7.21 : Sketch for $\phi(\zeta)$ against γ_2.

132

Figure 7.22 : Sketch for $\phi(\zeta)$ against Sc.

Figure 7.23 : Sketch for $\phi(\zeta)$ against E.

133

Figure 7.24 : Sketch for $\phi(\zeta)$ against σ.

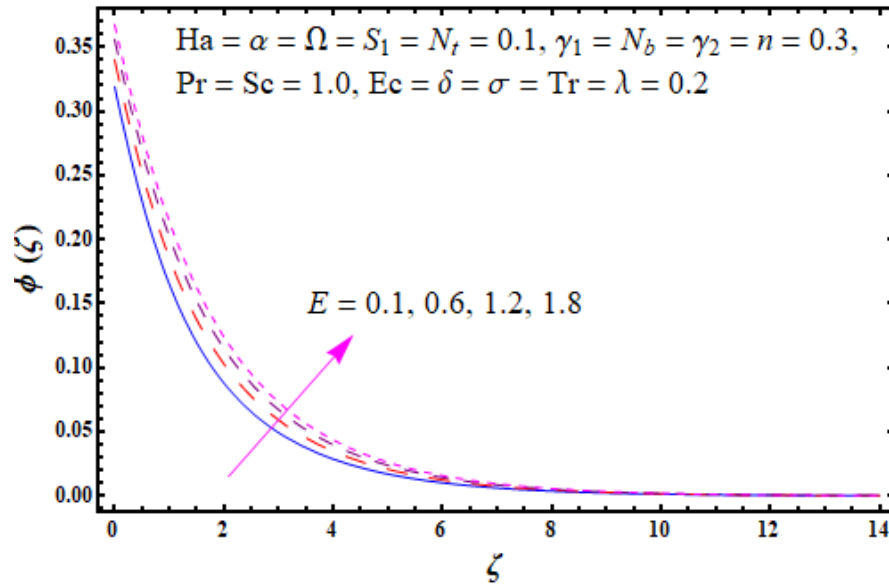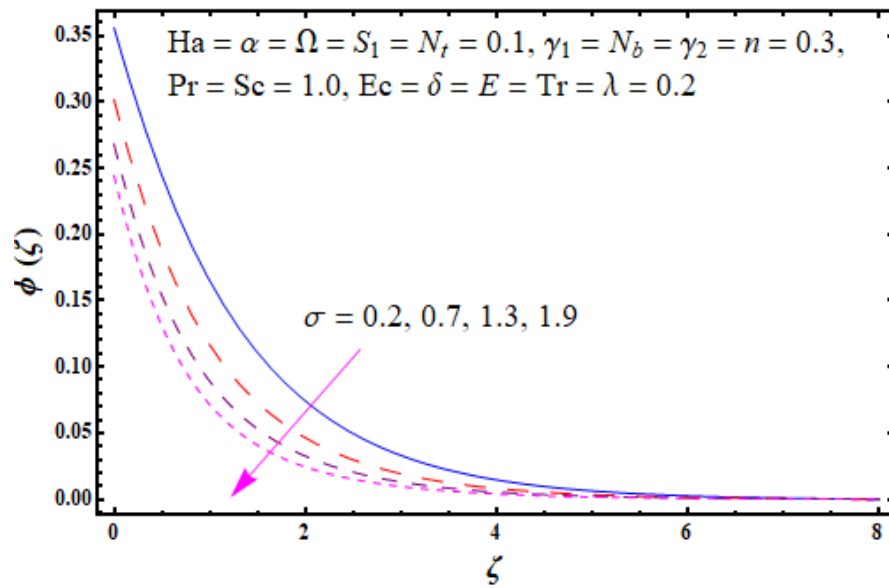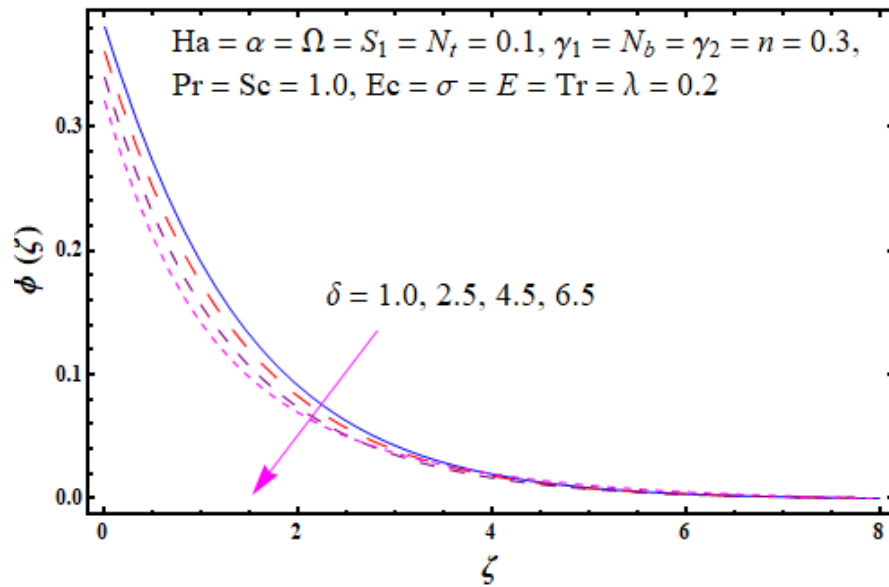Figure 7.25 : Sketch for $\phi(\zeta)$ against δ.

134

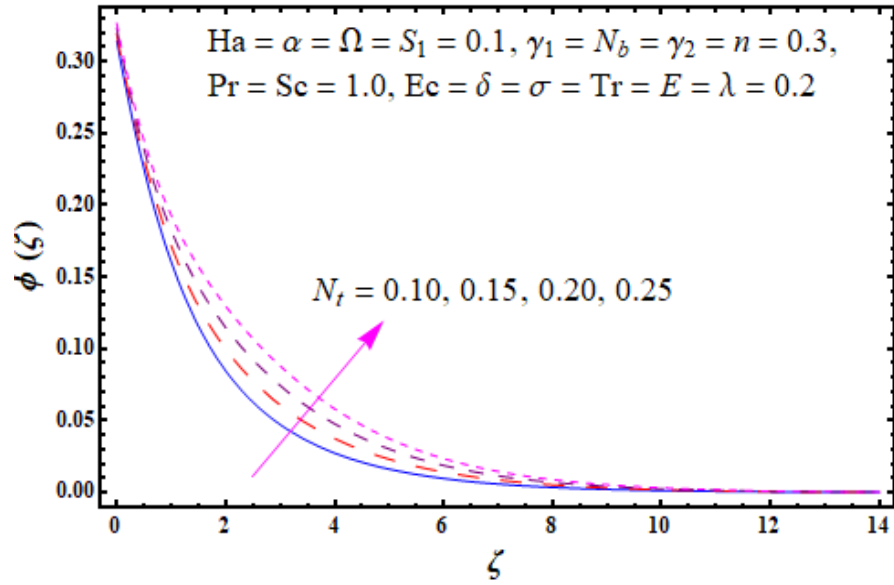Figure 7.26 : Sketch for $\phi(\zeta)$ against N_t.

Figure 7.27 : Sketch for $\phi(\zeta)$ against N_b.
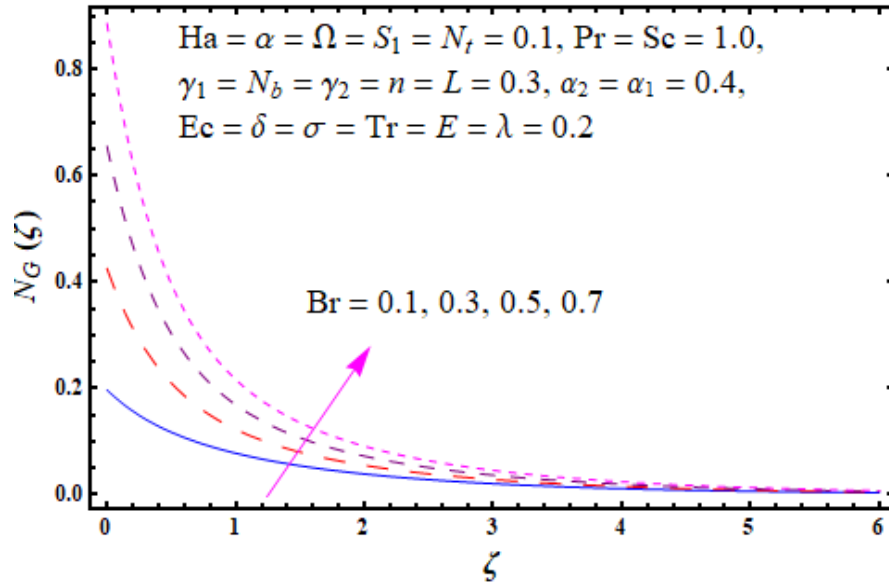
Figure 7.28 : Sketch for $N_G(\zeta)$ against Br.
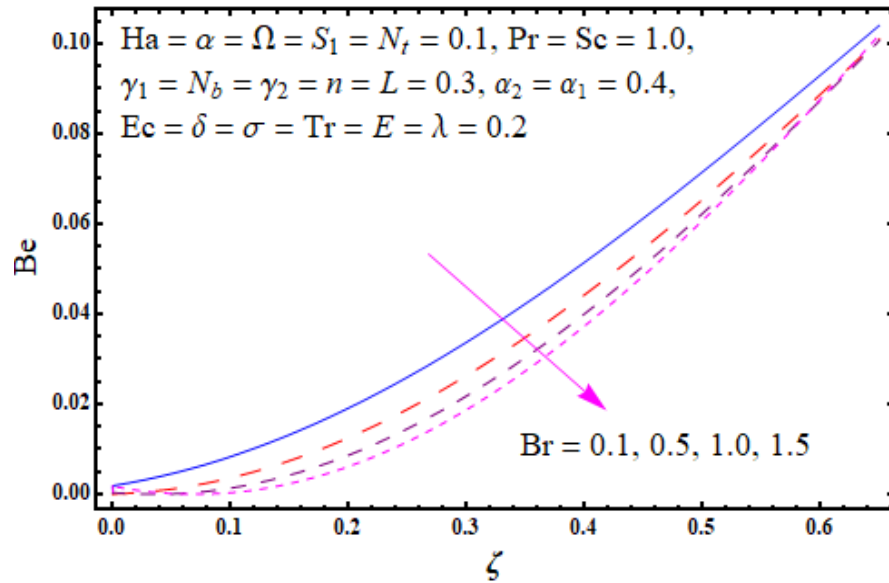
Figure 7.29 : Sketch for Be against Br.
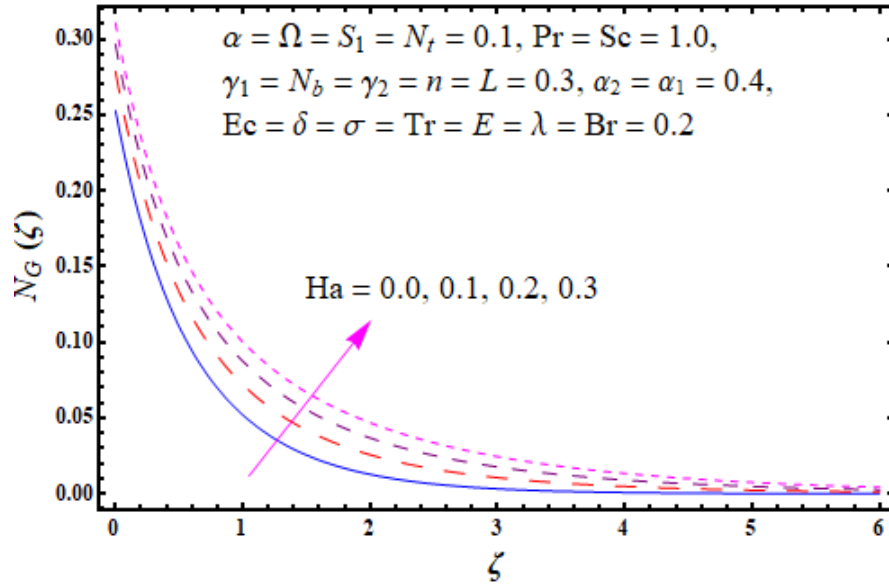
Figure 7.30 : Sketch for $N_G(\zeta)$ against Ha.
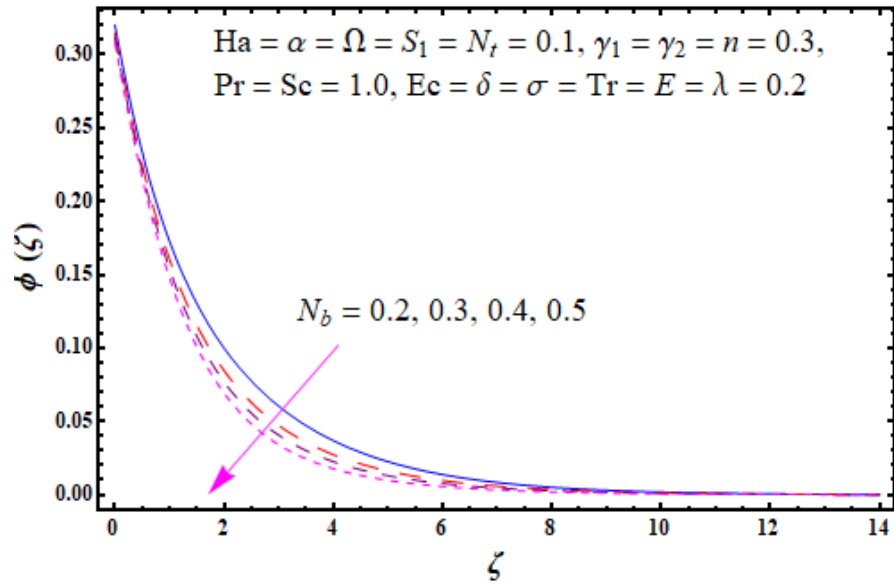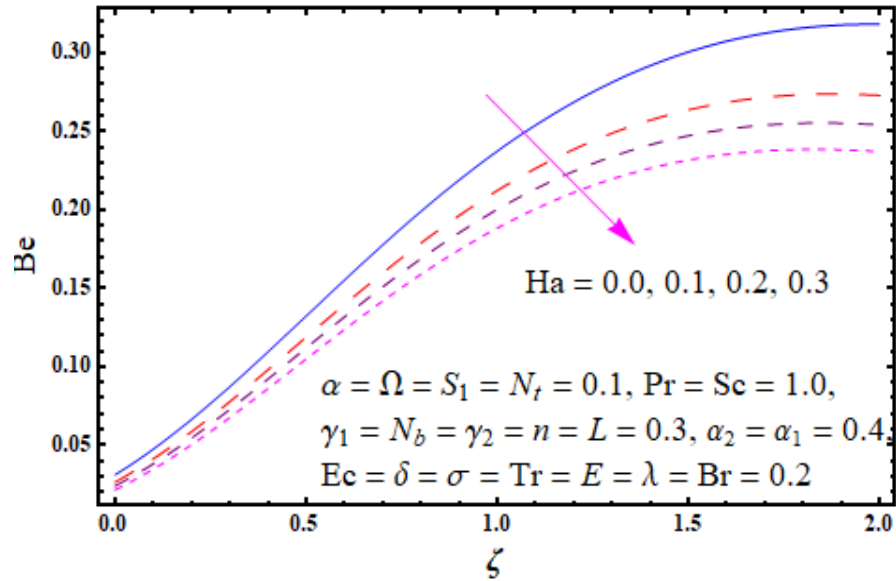

Figure 7.31 : Sketch for Be against Ha.
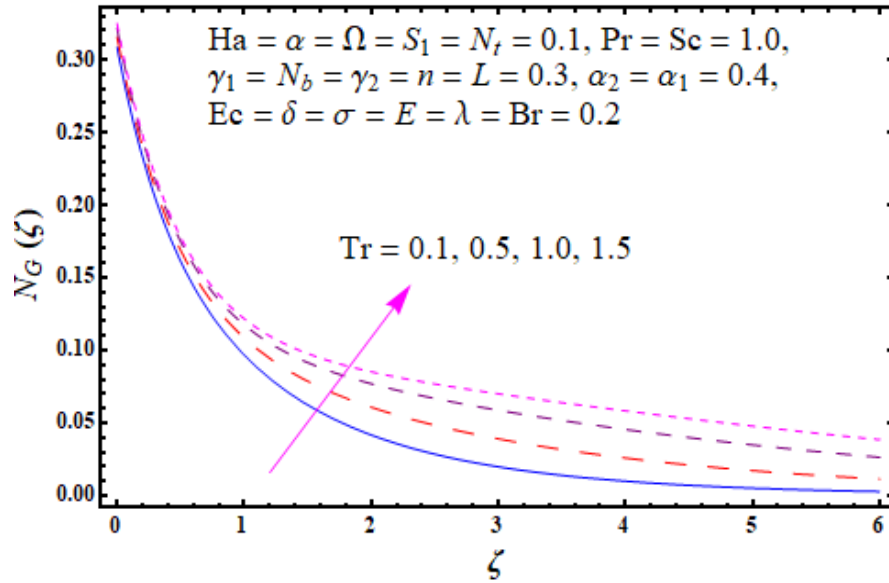
Figure 7.32 : Sketch for $N_G(\zeta)$ against Tr.
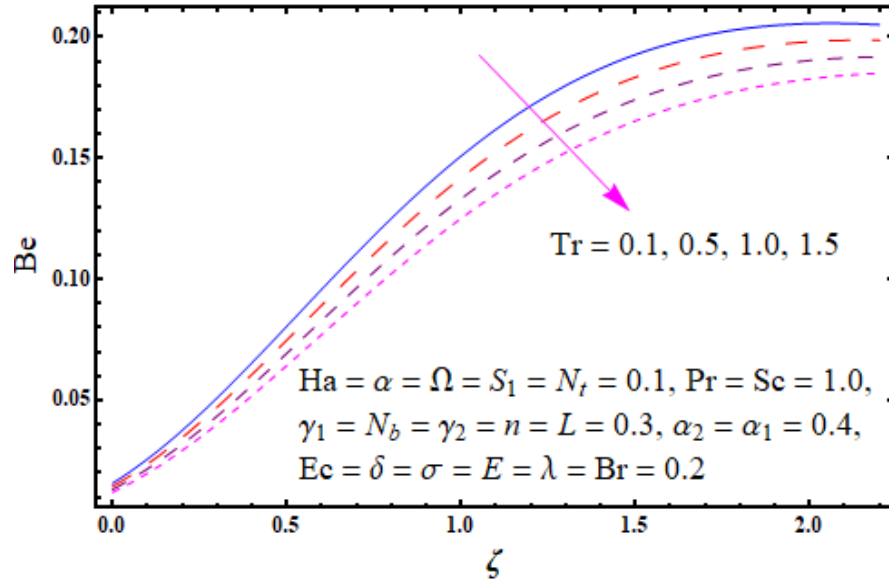
Figure 7.33 : Sketch for Be against Tr.
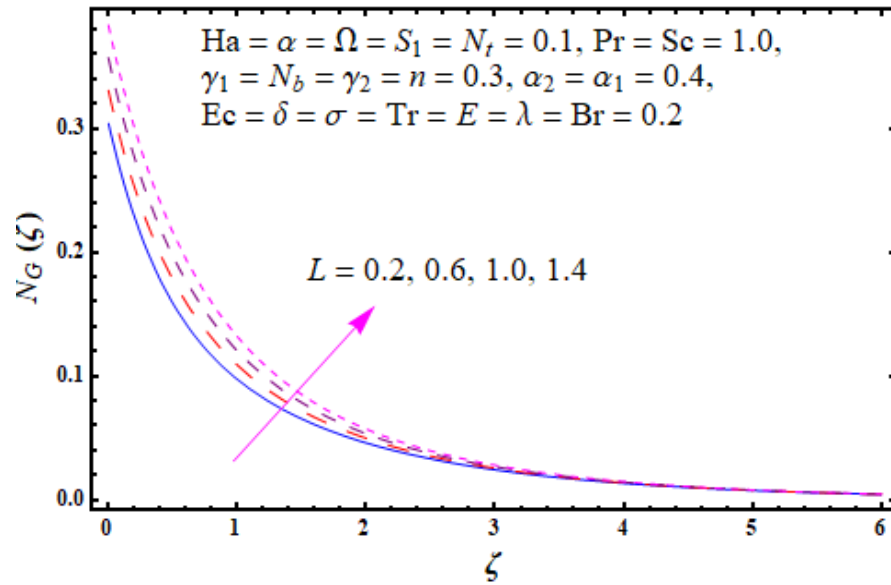
Figure 7.34 : Sketch for $N_G(\zeta)$ against L.
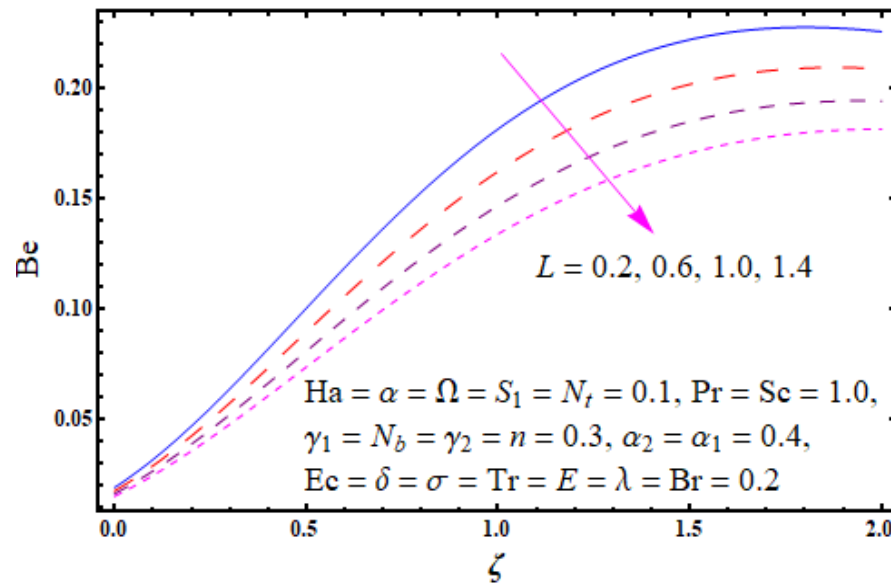
Figure 7.35 : Sketch for Be against L.
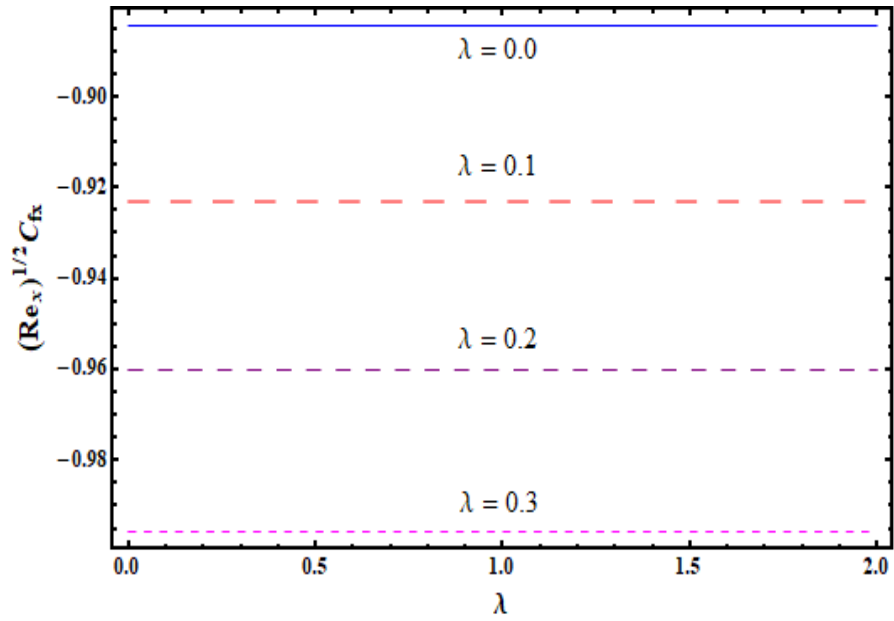
Figure 7.36 : Sketch for $(\text{Re}_x)^{1/2}C_{fx}$ against λ.
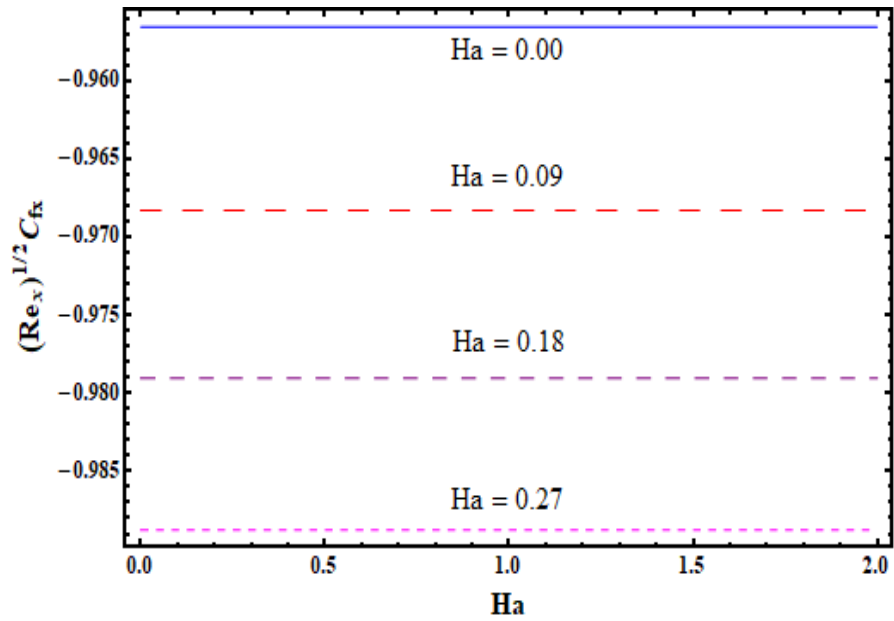
Figure 7.37 : Sketch for $(\text{Re}_x)^{1/2}C_{fx}$ against Ha.
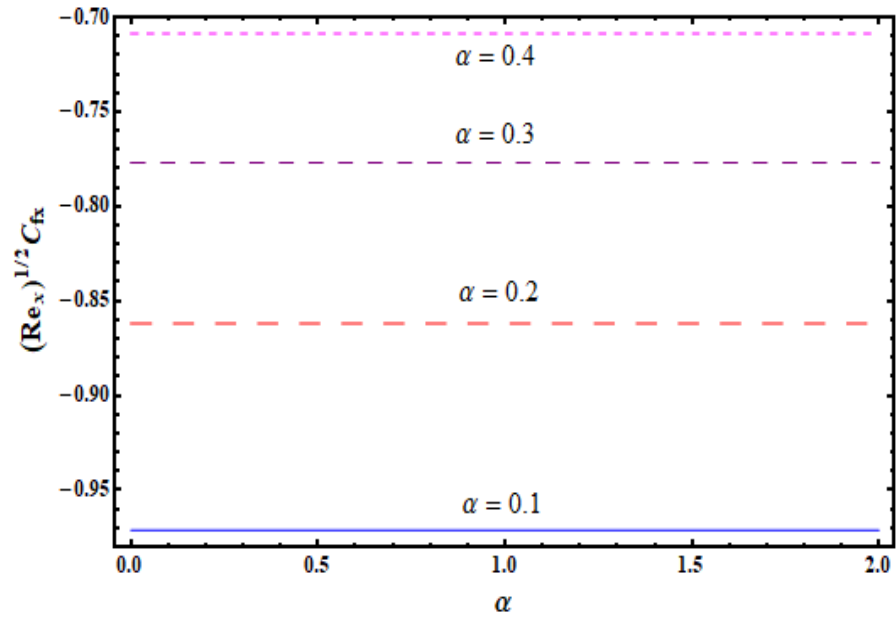
Figure 7.38 : Sketch for $(\mathrm{Re}_x)^{1/2}C_{fx}$ against α.
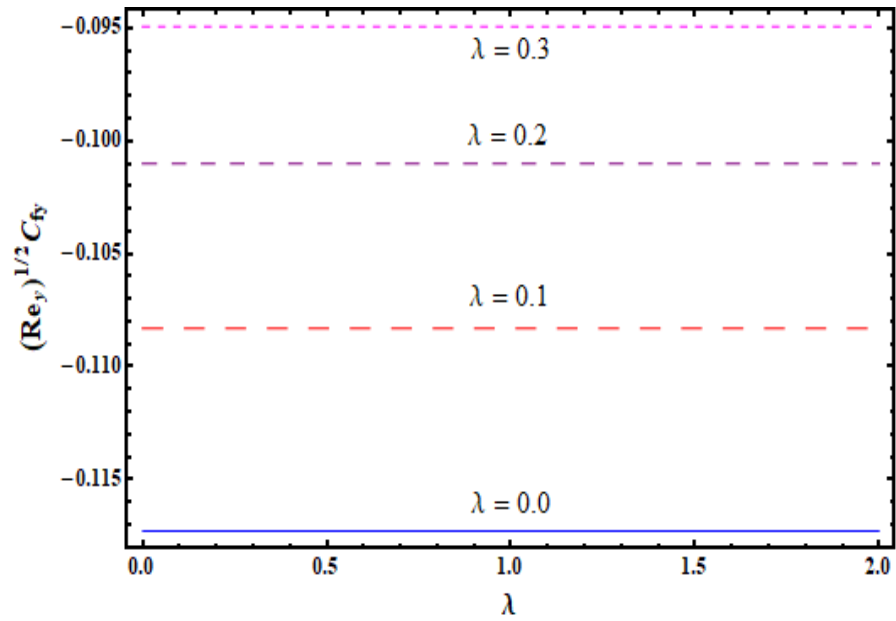
Figure 7.39 : Sketch for $(\mathrm{Re}_y)^{1/2}C_{fy}$ against λ.

141
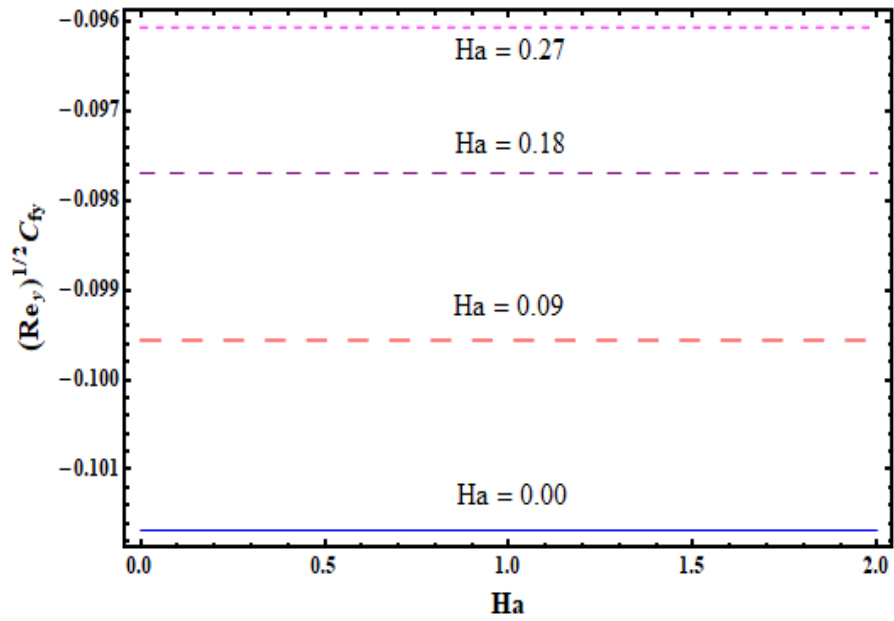
Figure 7.40 : Sketch for $(\mathrm{Re}_y)^{1/2}C_f$ against Ha.
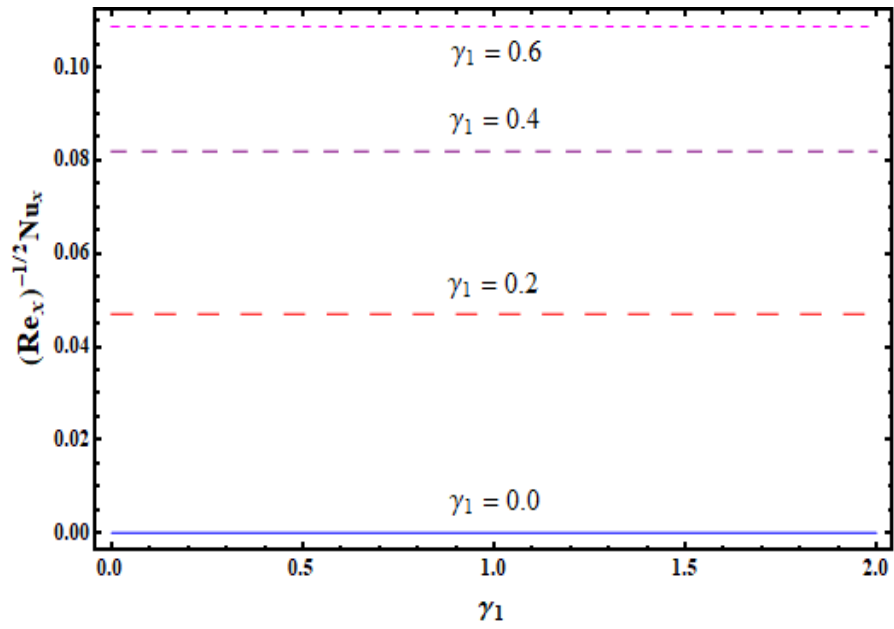
Figure 7.41 : Sketch for $(\mathrm{Re}_x)^{-1/2}Nu_x$ against γ_1.
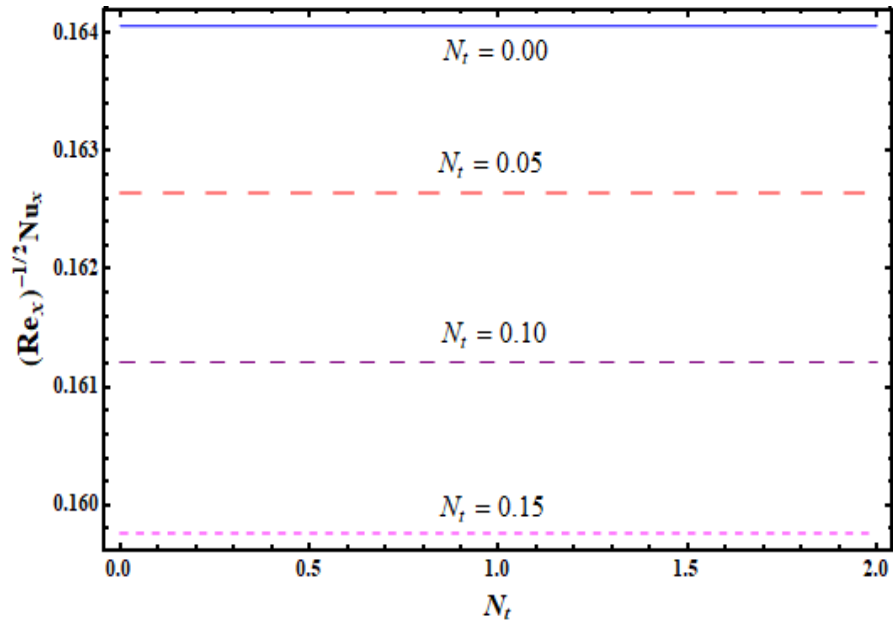
Figure 7.42 :Sketch for $(\mathrm{Re}_x)^{-1/2}Nu_x$ against N_t.
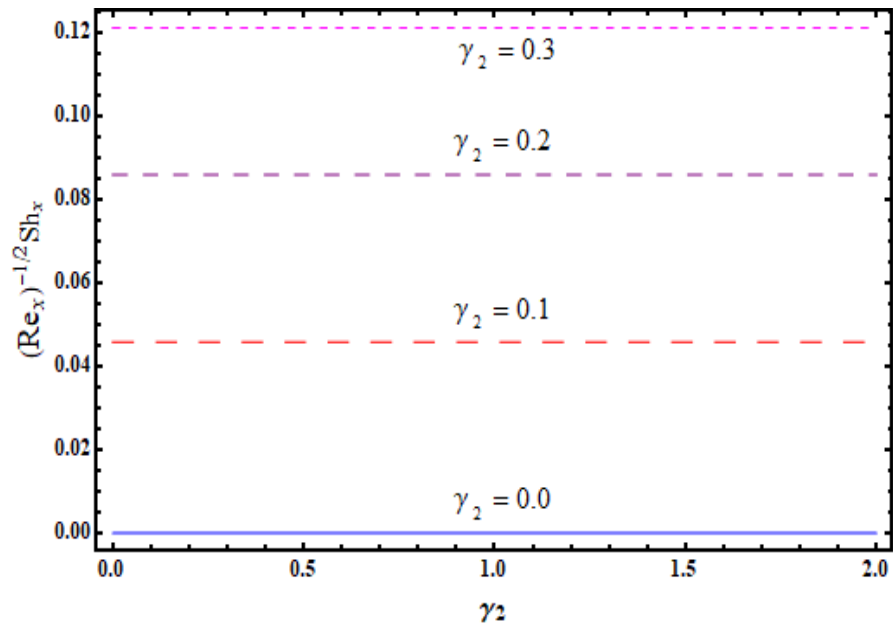
Figure 7.43 : Sketch for $(\mathrm{Re}_x)^{-1/2}Sh_x$ against γ_2.
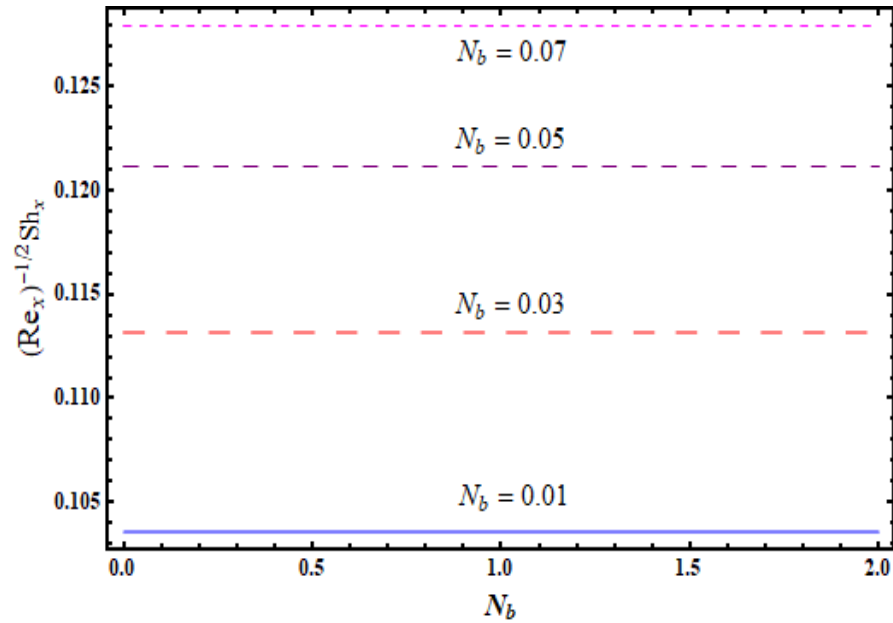
Figure 7.44 : Sketch for $(\mathrm{Re}_x)^{-1/2}Sh_x$ against N_b.

7.4   Major observations

Major findings of the current analysis are described as under:

- Both velocities $f'(\zeta)$ and $g(\zeta)$ depict decaying trend against stronger porosity parameter λ and Hartman number Ha while reverse situation is noticed for rotation parameter Ω.

- An increment in porosity parameter λ, Hartman number Ha, rotation parameter Ω, thermal radiation parameter Tr and Eckert number Ec corresponds to stronger temperature $\theta(\zeta)$.

- Temperature enhances via $(S_1 > 0)$ while decaying trend is observed against $(S_1 < 0)$.

- γ_1 and γ_2 have similar effects for temperature and nano-concentration.

- Higher thermophoresis N_t for $\theta(\zeta)$ and $\phi(\zeta)$ has similar trends while reverse situation is noticed against Brownian diffusion parameter N_b.

144

- Higher E corresponds to stronger nano-concentration field $\phi(\zeta)$ while decaying trend is noted via higher Sc, σ and δ.

- Entropy generation $N_G(\zeta)$ is maximum for higher Ha, Tr, L and Br while Bejan number decays.

- $(\text{Re}_x)^{1/2} C_{fx}$ and $(\text{Re}_y)^{1/2} C_{fy}$ exhibit opposite trend via higher λ and Ha.

- Heat transfer rate elevates for higher γ_1 while it reduces via N_t.

- Mass transfer rate shows similar pattern against γ_2 and N_t.

Chapter 8

Impacts of nonlinear radiative heat flux and activation energy on 3D rotating flow of Maxwell nanoliquid with convective conditions: A numerical study

Activation energy impact on 3D Maxwell nanoliquid flow with heat source/sink is discussed. A system consisting of surface and fluid are in solid body rotation. Mathematical modelling is developed through nonlinear thermal radiation. An irregular motion and thermophoretic diffusion aspects are also retained. Convective boundary conditions for heat and mass transfer are adopted. Nonlinear partial differential equations (PDEs) are transformed into ordinary ones by utilizing appropriate relations. Shooting method is used to generate the solutions for resulting nonlinear expressions. Plots have been constructed to scrutinize impact of physical flow parameters on temperature and nano-concentration. Further rates of mass and heat transfer are graphically examined.

8.1 Statement

Here we illustrate 3D rotating thermally radiative flow of Maxwell nanoliquid under the impact of binary chemical mechanism with activation energy. Brownian motion and thermophoresis impacts are taken in this nanofluid model. Convective boundary conditions for heat and mass transfer are considered. Let $U_w(x) = ax$ denotes the sheet stretching velocity. Further liquid rotates about $z-$axis with velocity ω. Resulting relations are

$$\frac{\partial u}{\partial x} + \frac{\partial v}{\partial y} + \frac{\partial w}{\partial z} = 0, \tag{8.1}$$

$$u\frac{\partial u}{\partial x} + v\frac{\partial u}{\partial y} + w\frac{\partial u}{\partial z} - 2\omega v = \nu\frac{\partial^2 u}{\partial z^2} - \lambda_1 \left(\begin{array}{c} u^2\frac{\partial^2 u}{\partial x^2} + v^2\frac{\partial^2 u}{\partial y^2} + w^2\frac{\partial^2 u}{\partial z^2} \\ +2uv\frac{\partial^2 u}{\partial x \partial y} + 2vw\frac{\partial^2 u}{\partial y \partial z} + 2uw\frac{\partial^2 u}{\partial x \partial z} \\ -2\omega\left(u\frac{\partial v}{\partial x} + v\frac{\partial v}{\partial y} + w\frac{\partial v}{\partial z}\right) + 2\omega\left(v\frac{\partial u}{\partial x} - u\frac{\partial u}{\partial y}\right) \end{array} \right), \tag{8.2}$$

$$u\frac{\partial v}{\partial x} + v\frac{\partial v}{\partial y} + w\frac{\partial v}{\partial z} + 2\omega u = \nu\frac{\partial^2 v}{\partial z^2} - \lambda_1 \left(\begin{array}{c} u^2\frac{\partial^2 v}{\partial x^2} + v^2\frac{\partial^2 v}{\partial y^2} + w^2\frac{\partial^2 v}{\partial z^2} \\ +2uv\frac{\partial^2 v}{\partial x \partial y} + 2vw\frac{\partial^2 v}{\partial y \partial z} + 2uw\frac{\partial^2 v}{\partial x \partial z} \\ +2\omega\left(u\frac{\partial u}{\partial x} + v\frac{\partial u}{\partial y} + w\frac{\partial u}{\partial z}\right) + 2\omega\left(v\frac{\partial v}{\partial x} - u\frac{\partial v}{\partial y}\right) \end{array} \right), \tag{8.3}$$

$$u\frac{\partial T}{\partial x} + v\frac{\partial T}{\partial y} + w\frac{\partial T}{\partial z} = \alpha^\star\frac{\partial^2 T}{\partial z^2} + \frac{Q_0}{(\rho c)_f}(T - T_\infty) - \frac{1}{(\rho c)_f}\frac{\partial q_r}{\partial z}$$
$$+ \frac{(\rho c)_p}{(\rho c)_f}\left(D_B\left(\frac{\partial T}{\partial z}\frac{\partial C}{\partial z}\right) + \frac{D_T}{T_\infty}\left(\frac{\partial T}{\partial z}\right)^2\right), \tag{8.4}$$

$$u\frac{\partial C}{\partial x} + v\frac{\partial C}{\partial y} + w\frac{\partial C}{\partial z} = D_B\left(\frac{\partial^2 C}{\partial z^2}\right) - k_r^2\left(\frac{T}{T_\infty}\right)^n (C - C_\infty)\exp\left(-\frac{E_a}{\kappa T}\right) + \frac{D_T}{T_\infty}\left(\frac{\partial^2 T}{\partial z^2}\right), \tag{8.5}$$

with

$$u = U_w(x) = ax, \ v = 0, \ w = 0, \ -k\frac{\partial T}{\partial z} = h_1\left(T_f - T\right),$$
$$-D_B\frac{\partial C}{\partial z} = h_2(C_f - C) \text{ at } z = 0, \tag{8.6}$$

$$u \to 0, \quad v \to 0, \quad T \to T_\infty, \quad C \to C_\infty \quad \text{when } z \to \infty, \tag{8.7}$$

in which (u, v, w) express velocities in (x, y, z) directions respectively, dynamic viscosity (μ), kinematic viscosity (ν), (ρ_f) density of fluid, liquid relaxation time (λ_1), thermal efficiency (k), heat capacitance of the liquid $(\rho c)_f$, Brownian coefficient (D_B), effective heat capacitance of nanoparticles $(\rho c)_p$, temperature (T), (Q_0) heat generation/absorption coefficient, concentration (C), thermophoretic coefficient (D_T), activation energy (E_a), fitted rate constant (n),

147

reaction rate (k_r), Boltzmann constant (κ) and coefficients of heat and mass transfer (h_1) and (h_2). The nonlinear radiation flux term (q_r) by Rosseland's approximation is expressed as

$$q_r = -\frac{4\sigma_1}{3m_1}\frac{\partial(T^4)}{\partial z} = -\frac{16\sigma_1}{3m_1}T^3\frac{\partial(T)}{\partial z}, \tag{8.8}$$

where Stefan-Boltzmann constant and coefficient of mean absorption are symbolized by (σ_1) and (m_1). Energy expression yields

$$\begin{aligned}
u\frac{\partial T}{\partial x} + v\frac{\partial T}{\partial y} + w\frac{\partial T}{\partial z} &= \frac{\partial}{\partial z}\left(\left(\alpha^\star + \frac{16\sigma_1}{3m_1(\rho c)_f}T^3\right)\frac{\partial(T)}{\partial z}\right) + \frac{Q_0}{(\rho c)_f}(T-T_\infty) \\
&+ \frac{(\rho c)_p}{(\rho c)_f}\left(D_B\left(\frac{\partial T}{\partial z}\frac{\partial C}{\partial z}\right) + \frac{D_T}{T_\infty}\left(\frac{\partial T}{\partial z}\right)^2\right).
\end{aligned} \tag{8.9}$$

We write

$$\left.\begin{aligned}
u &= axf'(\zeta), \ v = axg(\zeta), \ w = -(a\nu)^{1/2}f(\zeta), \\
\zeta &= \left(\frac{a}{\nu}\right)^{1/2}z, \ \theta(\zeta) = \frac{T-T_\infty}{T_f-T_\infty}, \ \phi(\zeta) = \frac{C-C_\infty}{C_f-C_\infty}.
\end{aligned}\right\} \tag{8.10}$$

with $T = T_\infty(1+(\theta_w-1)\theta)$ and $\theta_w = T_f/T_\theta$ (temperature ratio parameter). Equation (8.1) is trivially fulfilled and Eqs. $(8.2)-(8.7)$ and (8.9) take the following forms

$$f''' + ff'' - f'^2 + 2\Omega\left(g - \beta fg'\right) + \beta\left(2ff'f'' - f^2f'''\right) = 0, \tag{8.11}$$

$$g'' + fg' - f'g - 2\Omega\left(\beta(f'^2 + g^2 - ff'') + f'\right) + \beta\left(2ff'g' - g''f^2\right) = 0, \tag{8.12}$$

$$((1+Tr(1+(\theta_w-1)\theta)^3)\theta')' + \Pr N_t\theta'^2 + + \Pr\theta'f + \Pr S_1\theta + \Pr N_b\theta'\phi' = 0, \tag{8.13}$$

$$\frac{1}{Sc}\phi'' + f\phi' + \frac{1}{Sc}\frac{N_t}{N_b}\theta'' - \sigma\left(1+\delta\theta\right)^n\phi\exp\left(-\frac{E}{1+\delta\theta}\right) = 0, \tag{8.14}$$

$$f(0) = g(0) = 0, \ f'(0) = 1, \ \theta'(0) = -\gamma_1(1-\theta(0)), \ \phi'(0) = -\gamma_2(1-\phi(0)), \tag{8.15}$$

$$f'(\infty) \to 0, \ g(\infty) \to 0, \ \theta(\infty) \to 0, \ \phi(\infty) \to 0. \tag{8.16}$$

Here Ω depicts rotation parameter, β Deborah number, Pr Prandtl number, γ_1 thermal Biot number, γ_2 concentrated Biot number, Tr thermal radiation parameter, N_b Brownian motion parameter, N_t thermophoresis parameter, Sc Schmidt number, E nondimensional activation energy, σ chemical reaction parameter, S_1 heat source/sink parameter and δ temperature dif-

ference parameter. We can write these definitions as:

$$\left.\begin{array}{l} \Omega = \frac{\omega}{a}, \ \beta = \lambda_1 a, \ \mathrm{Pr} = \frac{\nu}{\alpha^\star}, \ \gamma_1 = \frac{h_1}{k}\sqrt{\frac{\nu}{a}}, \ \gamma_2 = \frac{h_2}{D_B}\sqrt{\frac{\nu}{a}}, \\[2mm] Tr = \frac{16\sigma_1 T_\infty^3}{3km_1}, \ N_t = \frac{(\rho c)_p D_T(T_f - T_\infty)}{(\rho c)_f \nu T_\infty}, \ E = \frac{E_a}{\kappa T_\infty}, \ \sigma = \frac{k_r^2}{a}, \\[2mm] N_b = \frac{(\rho c)_p D_B(C_f - C_\infty)}{(\rho c)_f \nu}, \ Sc = \frac{\nu}{D_B}, \ S_1 = \frac{Q_0}{a(\rho c)_f}, \ \delta = \frac{T_f - T_\infty}{T_\infty}. \end{array}\right\} \quad (8.17)$$

Non-dimensional forms of local Nusselt (heat transfer rate) Nu_x and Sherwood (mass transfer rate) Sh_x numbers are

$$\left.\begin{array}{l} (\mathrm{Re}_x)^{-1/2} Nu_x = -(1 + Tr\theta_w^3)\theta'(0), \\[2mm] (\mathrm{Re}_x)^{-1/2} Sh_x = -\phi'(0), \end{array}\right\} \quad (8.18)$$

in which local Reynolds number is symbolized by $\mathrm{Re}_x = U_w x/\nu$.

8.2   Discussion

Here effects of emerging flow parameters viz Deborah number β, rotation parameter Ω, thermal Biot parameter γ_1, Prandtl parameter Pr, concentration Biot number γ_2, heat source/sink parameter S_1, thermal radiation parameter Tr, thermophoretic diffusion parameter N_t, temperature difference parameter θ_w, random movement parameter N_b, Schmidt number Sc, nondimensional activation energy E, chemical reaction parameter σ and temperature difference parameter δ on nondimensional temperature $\theta(\zeta)$ and nano-concentration $\phi(\zeta)$. Figure 8.1 presents the outcome of Deborah number β for temperature $\theta(\zeta)$. Temperature field shows elevating trend for higher β. Figure 8.2 scrutinizes the change of temperature $\theta(\zeta)$ for varying Ω. It is analyzed that growing estimation of Ω yields an elevation of temperature $\theta(\zeta)$. Figure 8.3 delineates the role of γ_1 on $\theta(\zeta)$. Here $\theta(\zeta)$ elevates against greater γ_1. Figure 8.4 indicates the influence of $\theta(\zeta)$ against distinct estimations of Tr. One can easily notice the elevation of $\theta(\zeta)$ via higher Tr. Figure 8.5 is portrayed to characterize the consequences of θ_w on $\theta(\zeta)$. An elevating impact of temperature $\theta(\zeta)$ is noted via greater θ_w. Figures 8.6 and 8.7 depict the behaviors of heat production ($S_1 > 0$) and absorption ($S_1 < 0$) parameters on temperature $\theta(\zeta)$. Here temperature depicts reversing trend while considering ($S_1 > 0$) and ($S_1 < 0$). Temperature $\theta(\zeta)$ against higher Pr is depicted in Figure 8.8. Greater Pr indicates decay of $\theta(\zeta)$. Figure 8.9 demonstrates

the variation of temperature $\theta(\zeta)$ for higher N_b. Temperature $\theta(\zeta)$ is elevated via higher N_b. Figure 8.10 displayed the behavior of N_t on $\theta(\zeta)$. An enhancement is observed in temperature via higher estimations of N_t. Figure 8.11 explains the impact of β on nano-concentration field $\phi(\zeta)$. Nano-concentration field $\phi(\zeta)$ enhance via larger β. Figure 8.12 exhibits the effect of Ω on nano-concentration field $\phi(\zeta)$. An elevating impact of $\phi(\zeta)$ is seen for higher Ω. Effect of γ_2 on nano-concentration field $\phi(\zeta)$ is displayed in Figure 8.13. Clearly $\phi(\zeta)$ is increased via greater γ_2. Figure 8.14 portrayed the impact of Sc on dimensionless nano-concentration field $\phi(\zeta)$. Dimensionless nano-concentration field $\phi(\zeta)$ is depreciated for larger Sc. Figure 8.15 is constructed to illustrate the role of E on $\phi(\zeta)$. Here $\phi(\zeta)$ is enhanced via higher E. Figure 8.16 explains the effect of σ on nano-concentration field $\phi(\zeta)$. Nano-concentration field $\phi(\zeta)$ decreases against higher values of σ. Nano-concentration field $\phi(\zeta)$ behavior for δ is expressed in Figure 8.17. One can conveniently see that $\phi(\zeta)$ depreciates via growing δ. Figure 8.18 is developed to deliberate the impact of Brownian movement N_b on $\phi(\zeta)$. We noticed that growing values of N_b causes a depreciation in $\phi(\zeta)$. Figure 8.19 is displayed to examine the role of N_t on $\phi(\zeta)$. Nano-concentration field and corresponding layer thickness are enhanced via higher N_t. Figures 8.20 and 8.21 displayed the variations in $(\mathrm{Re}_x)^{-1/2}Nu_x$ via higher θ_w and N_t. From these sketches. it can be observed that $(\mathrm{Re}_x)^{-1/2}Nu_x$ elevates against larger θ_w while an opposite situation is observed for higher N_t. Figures 8.22 and 8.23 are developed to explore the main impacts of E and N_b on $(\mathrm{Re}_x)^{-1/2}Sh_x$. Clearly $(\mathrm{Re}_x)^{-1/2}Sh_x$ displays opposite role for higher E and N_b.
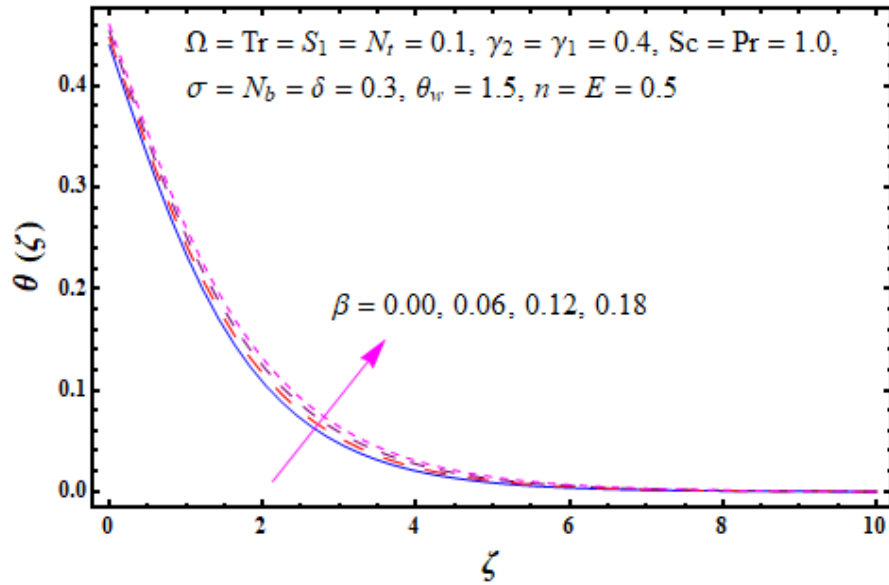
Figure 8.1 : Sketch for $\theta(\zeta)$ against β.
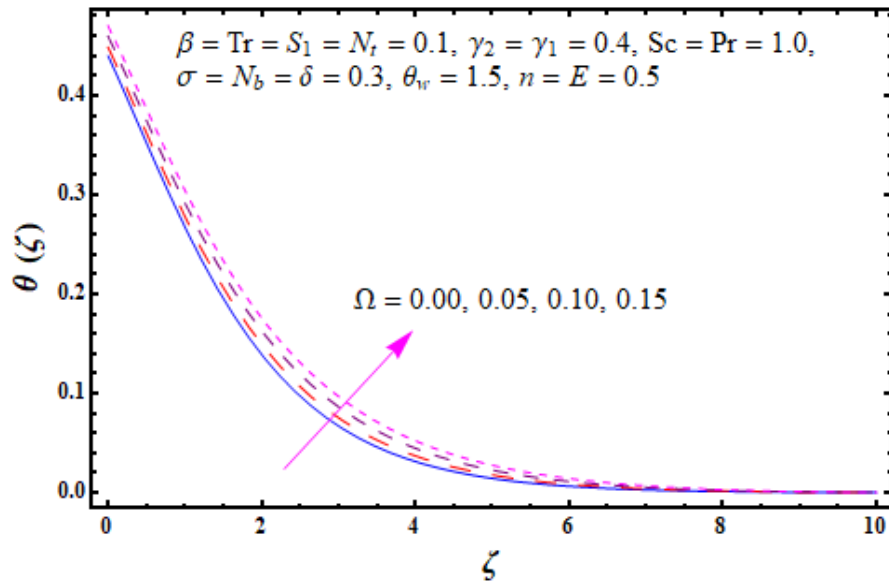
Figure 8.2 : Sketch for $\theta(\zeta)$ against Ω.

151
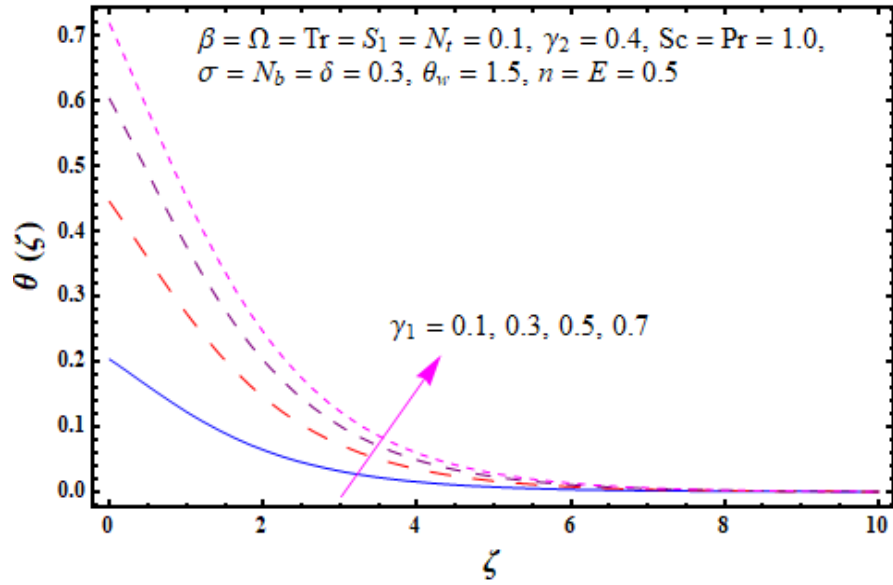
Figure 8.3 : Sketch for $\theta(\zeta)$ agianst γ_1.
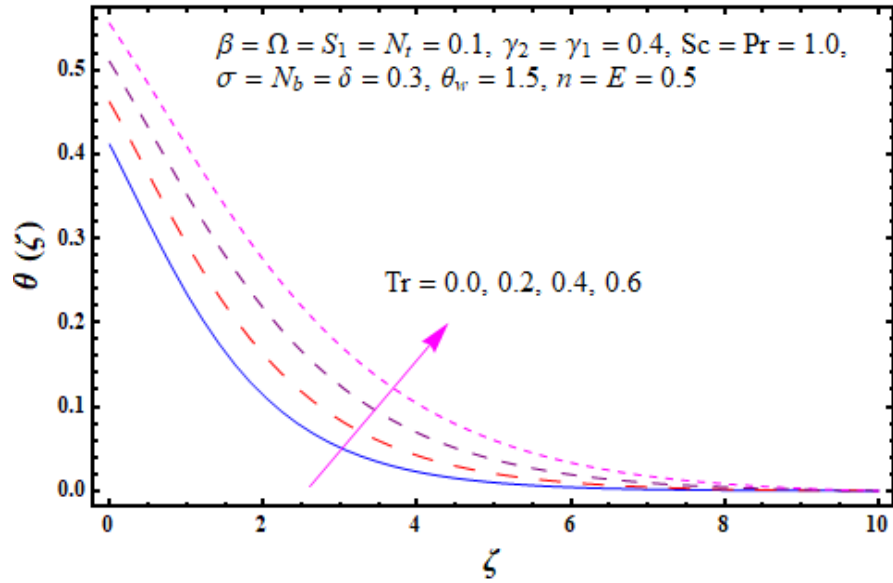
Figure 8.4 : Sketch for $\theta(\zeta)$ against Tr.
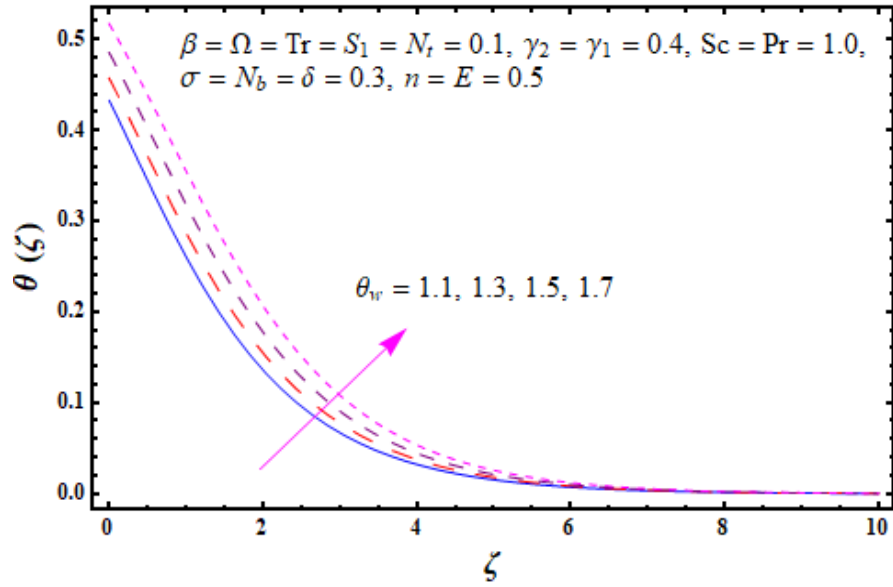
Figure 8.5 : Sketch for $\theta(\zeta)$ against θ_w.
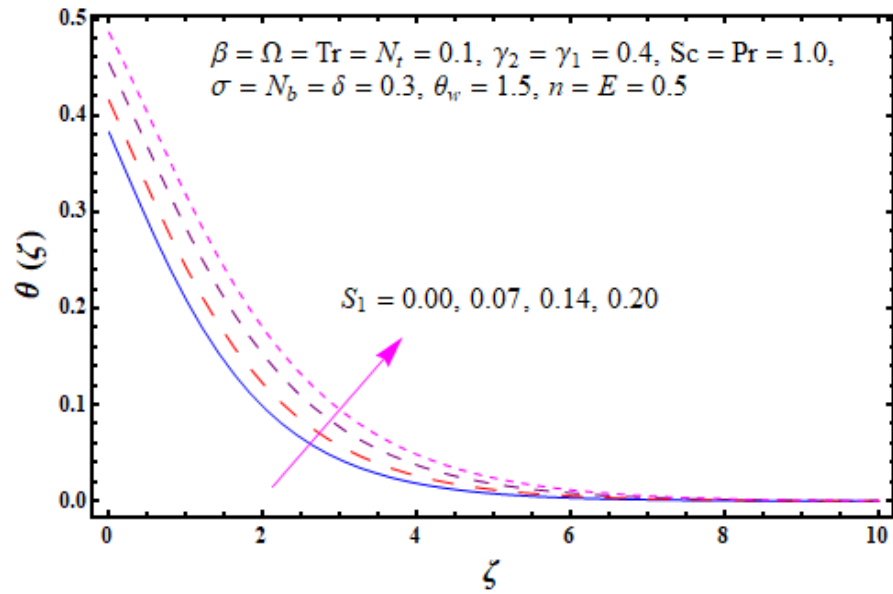
Figure 8.6 : Sketch for $\theta(\zeta)$ against $(S_1 > 0)$.

153
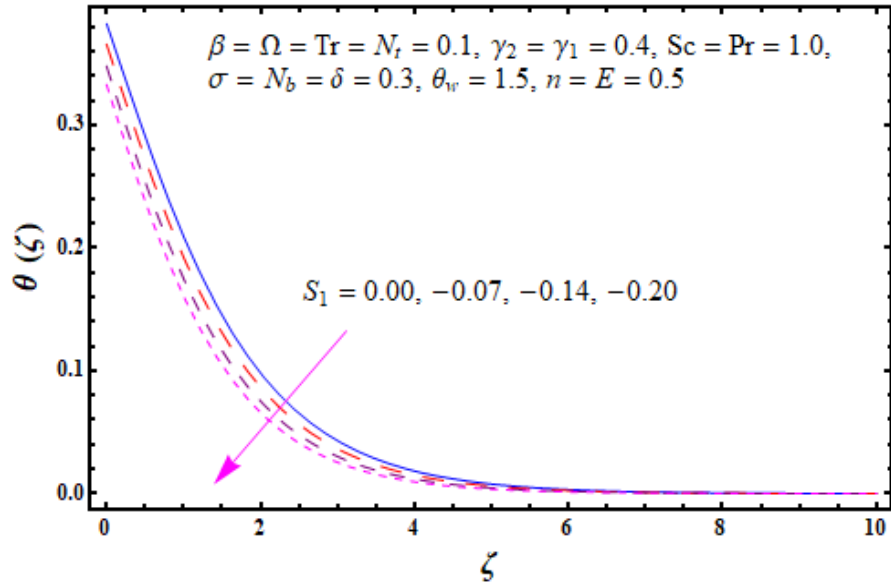
Figure 8.7 : Sketch for $\theta(\zeta)$ against $(S_1 < 0)$.
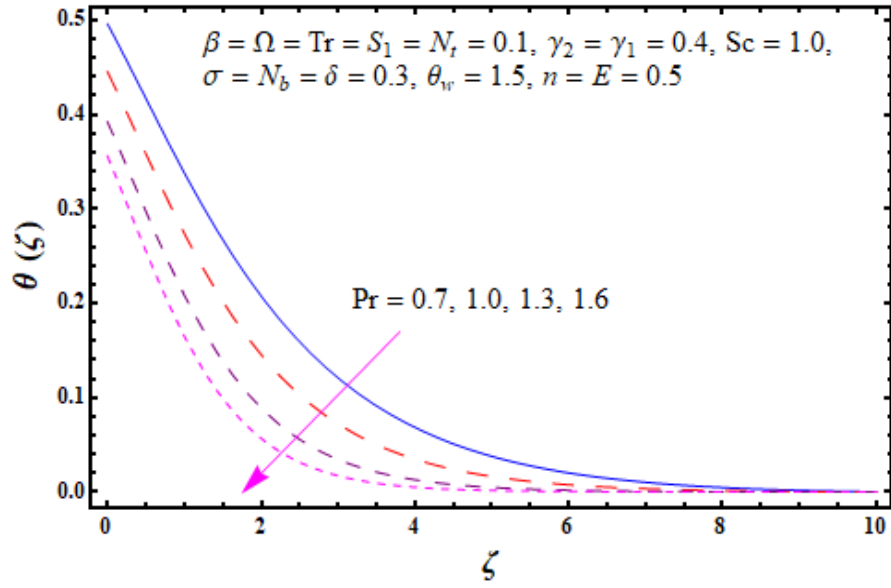
Figure 8.8 : Sketch for $\theta(\zeta)$ against Pr.
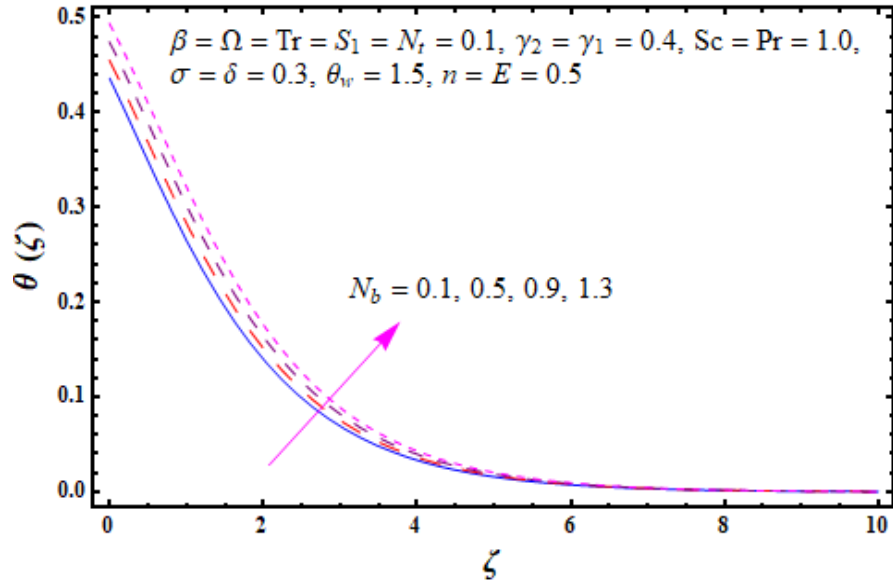
Figure 8.9 : Sketch for $\theta(\zeta)$ against N_b.
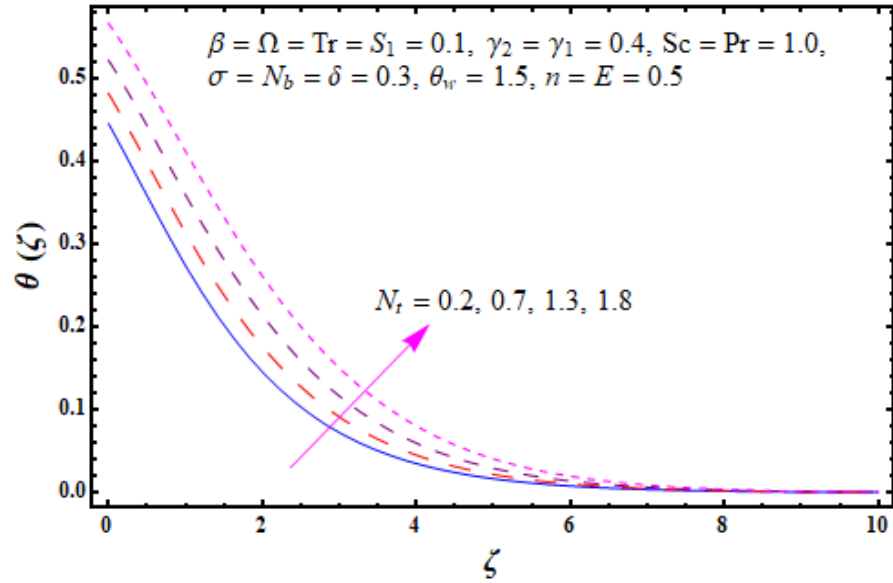
Figure 8.10 : Sketch for $\theta(\zeta)$ against N_t.

155
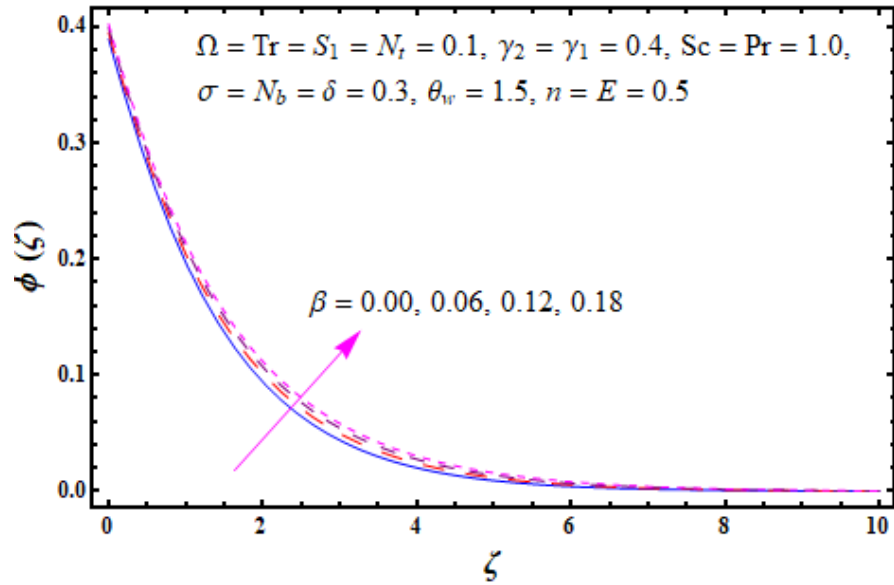
Figure 8.11 : Sketch for $\phi(\zeta)$ against β.
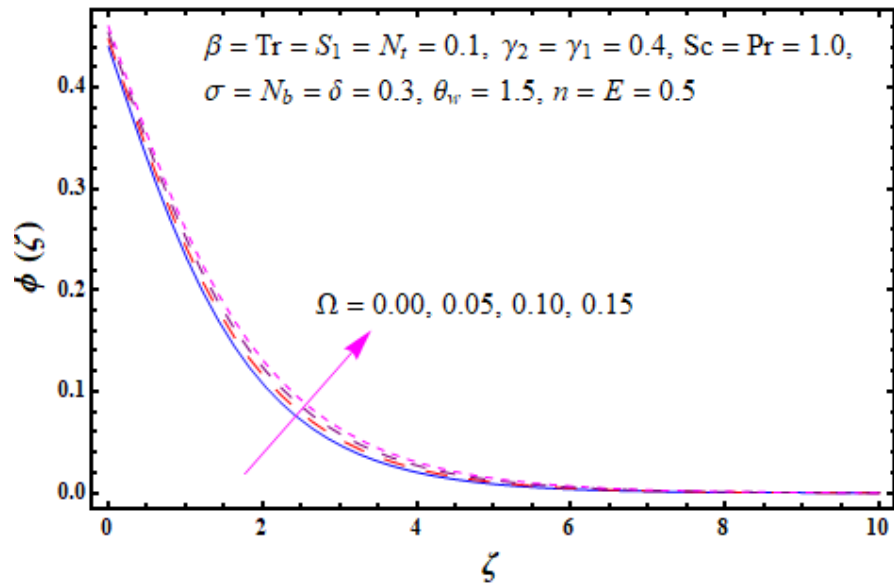
Figure 8.12 : Sketch for $\phi(\zeta)$ against Ω.
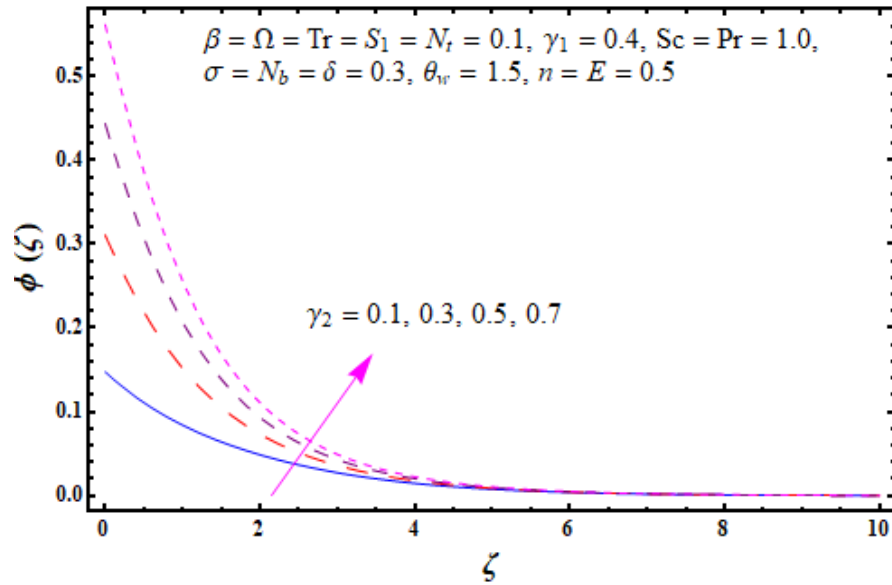
Figure 8.13 : Sketch for $\phi(\zeta)$ against γ_2.
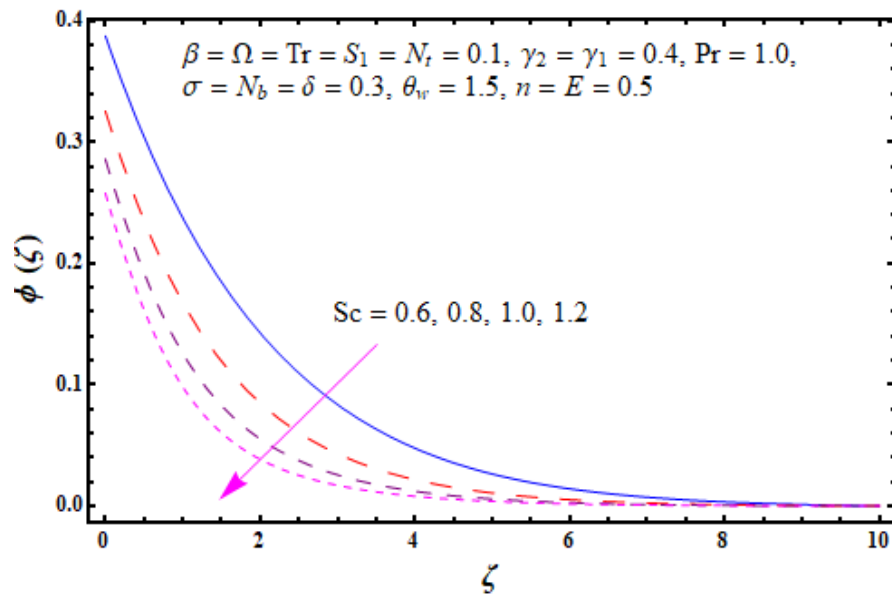
Figure 8.14 : Sketch for $\phi(\zeta)$ against Sc.

157
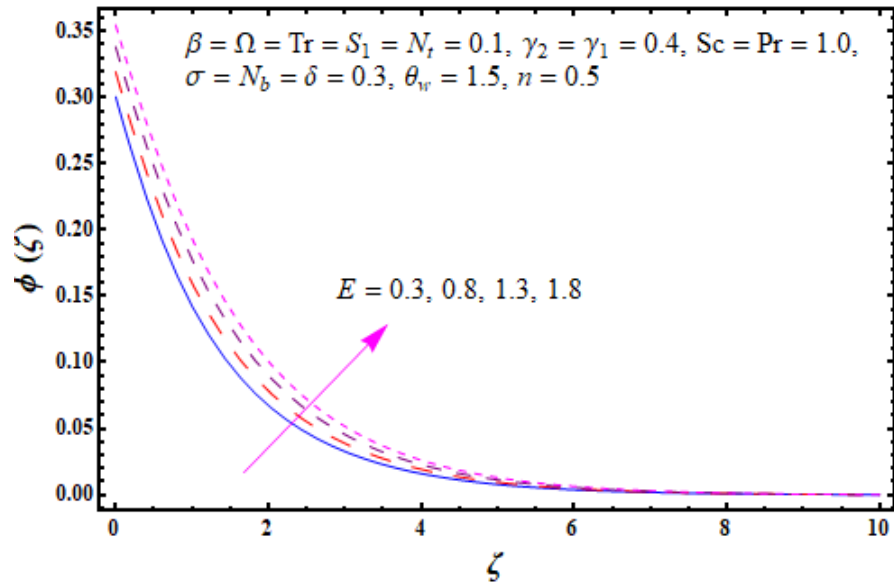
Figure 8.15 : Sketch for $\phi(\zeta)$ against E.
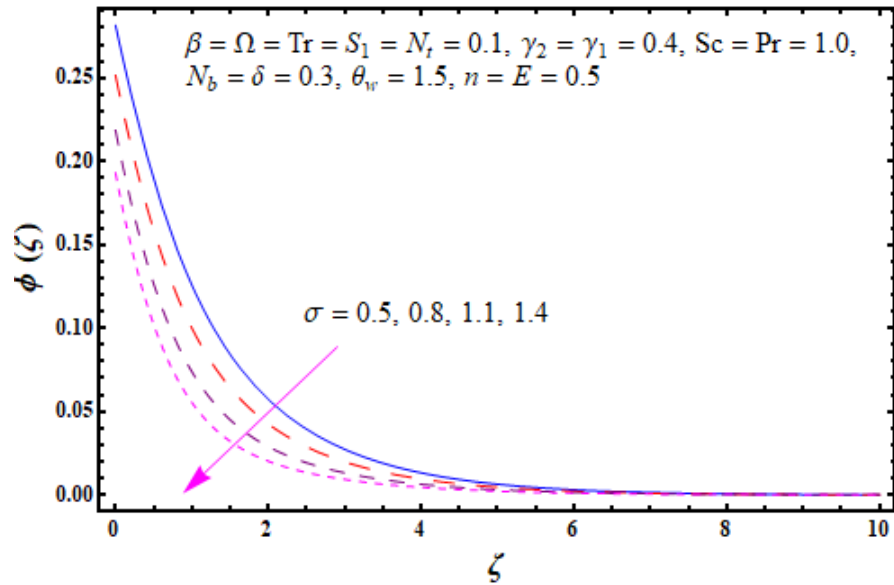
Figure 8.16 : Sketch for $\phi(\zeta)$ against σ.
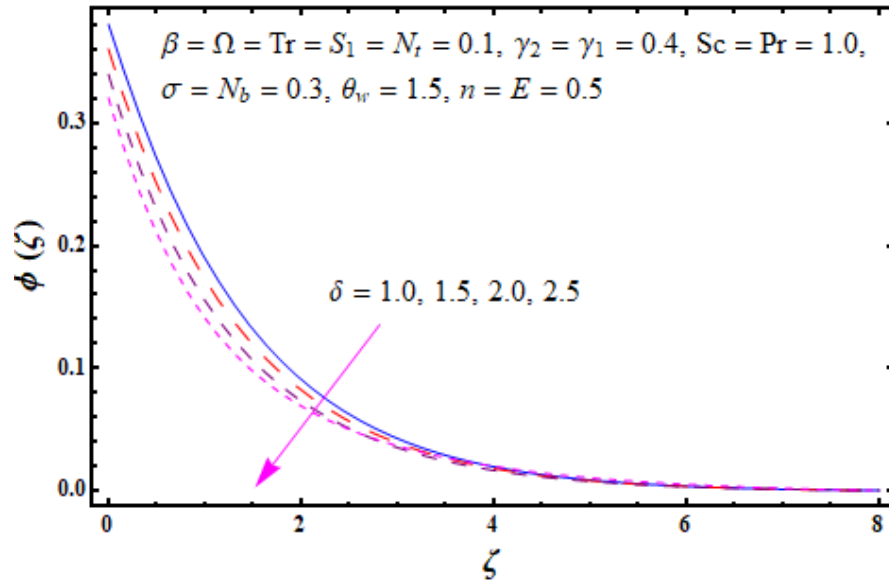
Figure 8.17 : Sketch for $\phi(\zeta)$ against δ.
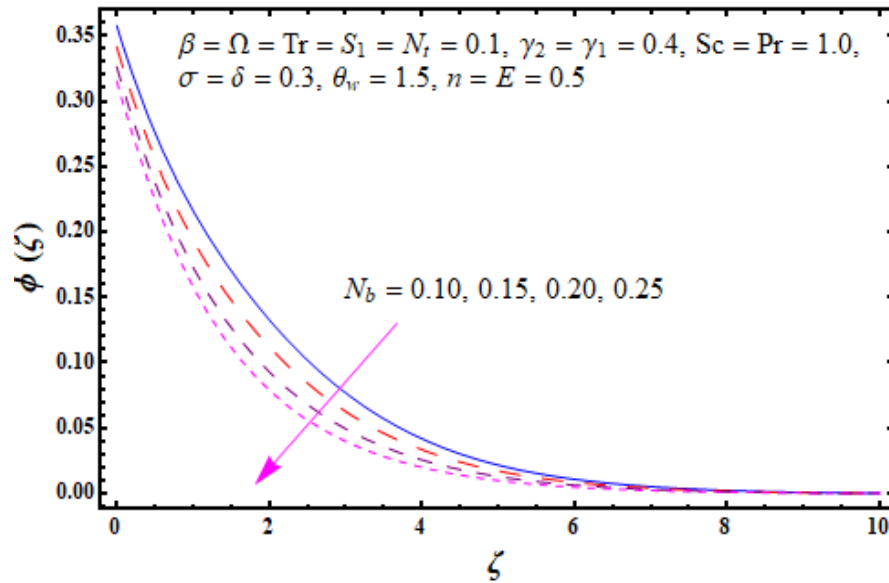
Figure 8.18 : Sketch for $\phi(\zeta)$ against N_b.

159
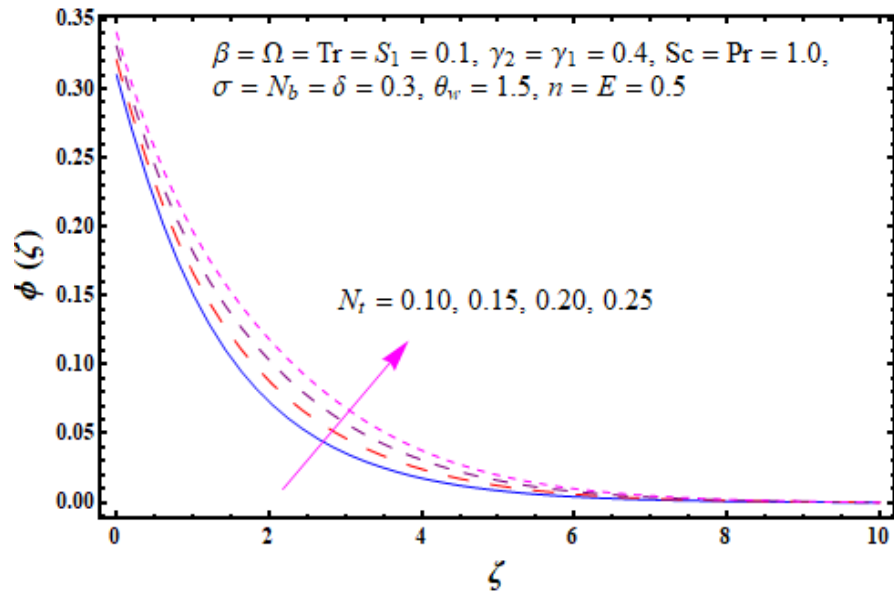
Figure 8.19 : Sketch for $\phi(\zeta)$ against N_t.
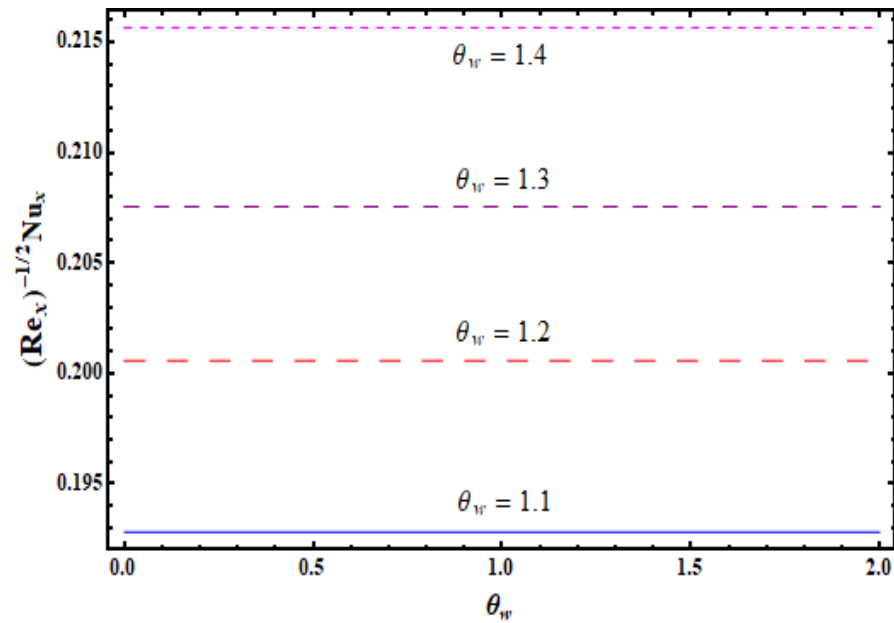
Figure 8.20 : Sketch for $(\mathrm{Re}_x)^{-1/2} Nu_x$ against θ_w.
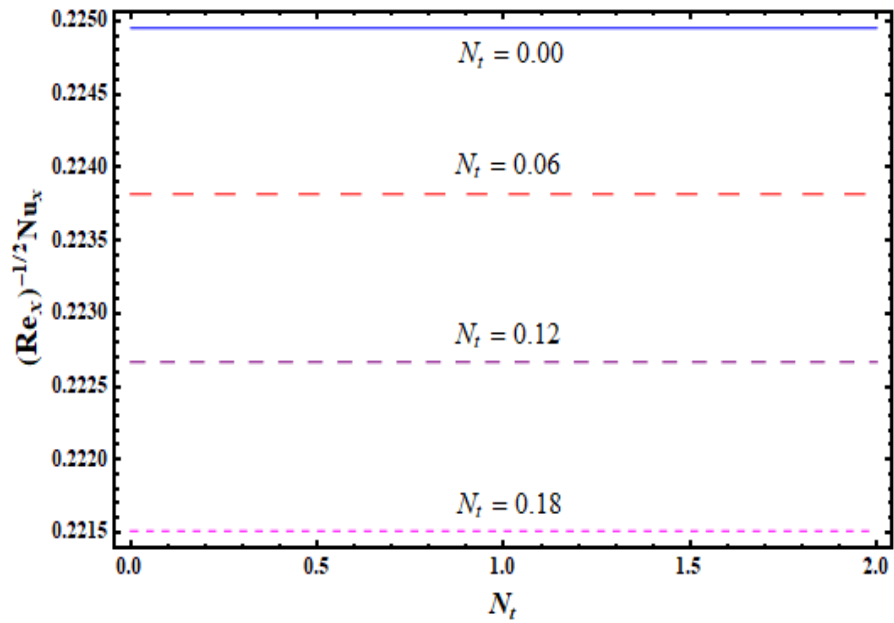
Figure 8.21 : Sketch for $(\text{Re}_x)^{-1/2}Nu_x$ against N_t.
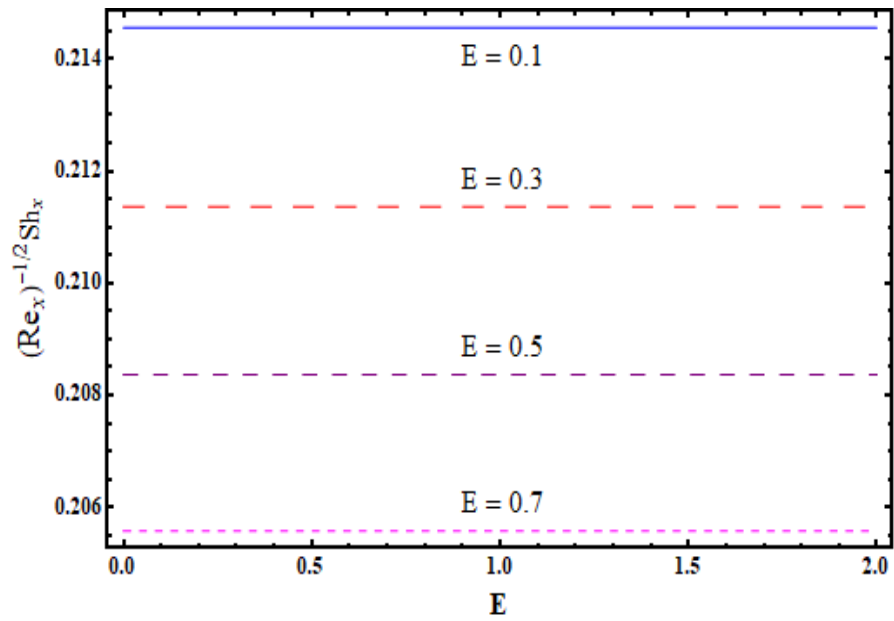
Figure 8.22 : Sketch for $(\text{Re}_x)^{-1/2}Sh_x$ against E.

161
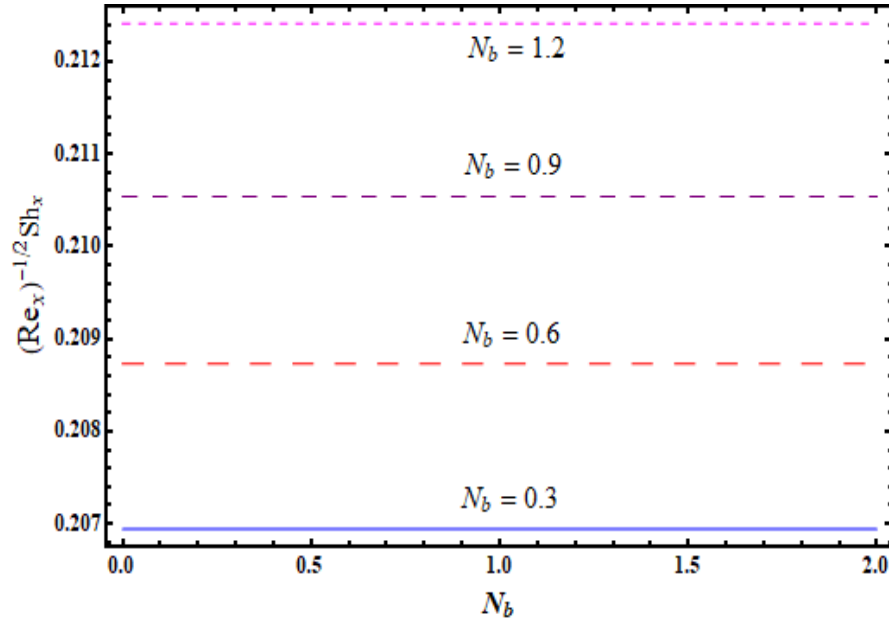
Figure 8.23 : Sketch for $(\text{Re}_x)^{-1/2} Sh_x$ against N_b.

8.3 Major observations

Main findings of present communication are as follows.

- Both temperature $\theta(\zeta)$ and nano-concentration $\phi(\zeta)$ depict similar trend against Deborah number β and rotation parameter Ω.

- An increment in thermal Biot number γ_1 and concentration Biot number γ_2 corresponds to stronger temperature $\theta(\zeta)$ and nano-concentration $\phi(\zeta)$ fields respectively.

- Temperature enhances for $(S_1 > 0)$ while it reduces against $(S_1 < 0)$.

- Temperature $\theta(\zeta)$ is enhanced against larger estimations of temperature ratio parameter θ_w and thermal radiation parameter Tr.

- Higher Pr and Sc correspond to weaker temperature $\theta(\zeta)$ and nano-concentration $\phi(\zeta)$.

- An enhancement in N_t depicts identical trend for temperature $\theta(\zeta)$ and nano-concentration $\phi(\zeta)$ while reverse behavior is noted via higher N_b.

- Nano-concentration $\phi(\zeta)$ field enhances for E while it reduces against σ and δ.

162

- Heat transfer rate elevates via higher θ_w while it decays against N_t.

- Mass transfer rate depreciates against higher E while opposite holds for N_b.

Chapter 9

Three-dimensional rotating flow of Oldroyd-B nanoliquid with convective effect: OHAM analysis

This chapter addresses (3D) rotating flow of an Oldroyd-B fluid flow in the presence of nano-materials. Thermophoresis and Brownian motion are studied. Convective condition for heat transfer is considered. Ordinary differential systems are obtained by reduction process from partial differential expressions. Optimal homotopy analysis method (OHAM) yields solutions development. Impact of emerging variables on flow quantities of interest like velocities, nano-concentration, temperature and rate of heat transfer are examined graphically and in tabular form, and salient features are comprehensively elaborated.

9.1 Statement

We intend to examine steady 3D rotating flow of Oldroyd-B nanoliquid caused by stretched sheet. Thermal convective condition and newly developed constraint about zero nanomaterials flux at sheet are imposed. Besides this sheet is heated by hot liquid with temperature T_f which provides heat transport coefficient h_f. An incompressible Oldroyd-B liquid occupies a space $z \geq 0$. Let $(u_w = ax)$ be surface moving velocity and liquid rotates along $z-$axis with constant

angular velocity ω. The governing problems are defined by

$$\frac{\partial u}{\partial x} + \frac{\partial v}{\partial y} + \frac{\partial w}{\partial z} = 0, \tag{9.1}$$

$$u\frac{\partial u}{\partial x} + v\frac{\partial u}{\partial y} + w\frac{\partial u}{\partial z} - 2\omega v + \lambda_1 \left(\begin{array}{c} u^2\frac{\partial^2 u}{\partial x^2} + v^2\frac{\partial^2 u}{\partial y^2} + w^2\frac{\partial^2 u}{\partial z^2} \\ +2uv\frac{\partial^2 u}{\partial x\partial y} + 2vw\frac{\partial^2 u}{\partial y\partial z} + 2uw\frac{\partial^2 u}{\partial x\partial z} \\ -2\omega\left(u\frac{\partial v}{\partial x} + v\frac{\partial v}{\partial y} + w\frac{\partial v}{\partial z}\right) + 2\omega\left(v\frac{\partial u}{\partial x} - u\frac{\partial u}{\partial y}\right) \end{array} \right)$$

$$= \nu\frac{\partial^2 u}{\partial z^2} + \lambda_2 \left(\begin{array}{c} u\frac{\partial^3 u}{\partial x\partial z^2} + v\frac{\partial^3 u}{\partial y\partial z^2} + w\frac{\partial^3 u}{\partial z^3} \\ -\frac{\partial u}{\partial x}\frac{\partial^2 u}{\partial z^2} - \frac{\partial u}{\partial y}\frac{\partial^2 v}{\partial z^2} - \frac{\partial u}{\partial z}\frac{\partial^2 w}{\partial z^2} \end{array} \right), \tag{9.2}$$

$$u\frac{\partial v}{\partial x} + v\frac{\partial v}{\partial y} + w\frac{\partial v}{\partial z} + 2\omega u + \lambda_1 \left(\begin{array}{c} u^2\frac{\partial^2 v}{\partial x^2} + v^2\frac{\partial^2 v}{\partial y^2} + w^2\frac{\partial^2 v}{\partial z^2} \\ +2uv\frac{\partial^2 v}{\partial x\partial y} + 2vw\frac{\partial^2 v}{\partial y\partial z} + 2uw\frac{\partial^2 v}{\partial x\partial z} \\ +2\omega\left(u\frac{\partial u}{\partial x} + v\frac{\partial u}{\partial y} + w\frac{\partial u}{\partial z}\right) + 2\omega\left(v\frac{\partial v}{\partial x} - u\frac{\partial v}{\partial y}\right) \end{array} \right)$$

$$= \nu\frac{\partial^2 v}{\partial z^2} + \lambda_2 \left(\begin{array}{c} u\frac{\partial^3 v}{\partial x\partial z^2} + v\frac{\partial^3 v}{\partial y\partial z^2} + w\frac{\partial^3 v}{\partial z^3} \\ -\frac{\partial v}{\partial x}\frac{\partial^2 u}{\partial z^2} - \frac{\partial v}{\partial y}\frac{\partial^2 v}{\partial z^2} - \frac{\partial v}{\partial z}\frac{\partial^2 w}{\partial z^2} \end{array} \right), \tag{9.3}$$

$$u\frac{\partial T}{\partial x} + v\frac{\partial T}{\partial y} + w\frac{\partial T}{\partial z} = \alpha^\star\frac{\partial^2 T}{\partial z^2} + \frac{(\rho c)_p}{(\rho c)_f}\left(\frac{D_T}{T_\infty}\left(\frac{\partial T}{\partial z}\right)^2 + D_B\left(\frac{\partial T}{\partial z}\frac{\partial C}{\partial z}\right)\right), \tag{9.4}$$

$$u\frac{\partial C}{\partial x} + v\frac{\partial C}{\partial y} + w\frac{\partial C}{\partial z} = \frac{D_T}{T_\infty}\left(\frac{\partial^2 T}{\partial z^2}\right) + D_B\left(\frac{\partial^2 C}{\partial z^2}\right), \tag{9.5}$$

$$u = u_w = ax,\ v = 0,\ w = 0,\ -k\frac{\partial T}{\partial z} = h_f\left(T_f - T\right),\ \frac{D_T}{T_\infty}\frac{\partial T}{\partial z} + D_B\frac{\partial C}{\partial z} = 0 \text{ at } z = 0, \tag{9.6}$$

$$u \to 0,\ v \to 0,\ T \to T_\infty,\ C \to C_\infty \text{ when } z \to \infty, \tag{9.7}$$

where (μ) represents the absolute viscosity, $\nu\left(= \mu/\rho_f\right)$ the kinematic viscosity which is the ratio of absolute viscosity to density of liquid, k the thermal efficiency, ρ_f the density, $\alpha^\star = k/(\rho c)_f$ the thermal diffusivity, λ_1 the liquid relaxation time, $(\rho c)_f$ the thermal capacity of liquid, λ_2 the liquid retardation time, $(\rho c)_p$ the specific thermal potential of nanomaterials, D_B, C_∞, D_T and T_∞ the Brownian movement, concentration of liquid far away from surface, thermophoretic

dispersion coefficient and temperature of liquid far away from surface respectively. Selecting

$$
\left.\begin{array}{l}
u = axf'(\zeta), \ w = -(a\nu)^{1/2} f(\zeta), \ v = axg(\zeta), \\
\theta(\zeta) = \frac{T-T_\infty}{T_f-T_\infty}, \ \zeta = \left(\frac{a}{\nu}\right)^{1/2} z, \ \phi(\zeta) = \frac{C-C_\infty}{C_\infty}.
\end{array}\right\}
\tag{9.8}
$$

Equation (9.1) is is fully justified and Exps. $(9.2) - (9.7)$ are reduced to

$$
f''' + ff'' - f'^2 + 2\Omega\left(g - \beta_1 fg'\right) + \beta_1\left(2ff'f'' - f^2 f'''\right) + \beta_2\left(f''^2 - ff^{iv}\right) = 0,
\tag{9.9}
$$

$$
g'' + fg' - f'g - 2\Omega\left(f' + \beta_1\left(f'^2 - ff'' + g^2\right)\right) + \beta_1(2ff'g' - f^2 g'')
$$
$$
+\beta_2\left(f'g'' - fg''' - gf''' + g'f''\right) = 0,
\tag{9.10}
$$

$$
\theta'' + \Pr\left(f\theta' + N_b\theta'\phi' + N_t\theta'^2\right) = 0,
\tag{9.11}
$$

$$
\phi'' + Scf\phi' + \frac{N_t}{N_b}\theta'' = 0,
\tag{9.12}
$$

$$
f(0) = g(0) = 0, \ f'(0) = 1, \ \theta'(0) = -\gamma(1 - \theta(0)), \ N_b\phi'(0) + N_t\theta'(0) = 0,
\tag{9.13}
$$

$$
f'(\infty) \to 0, \ g(\infty) \to 0, \ \theta(\infty) \to 0, \ \phi(\infty) \to 0.
\tag{9.14}
$$

Here rotation parameter, fluid relaxation time number, fluid retardation time number, thermal Biot parameter, Prandtl parameter, Brownian movement parameter, Schmidt parameter and thermophoresis parameter are denoted by Ω, β_1, β_2, γ, $\Pr$, N_b, Sc and N_t. We have following definitions

$$
\left.\begin{array}{l}
\Omega = \frac{\omega}{a}, \ \beta_1 = \lambda_1 a, \ \beta_2 = \lambda_2 a, \ \Pr = \frac{\nu}{\alpha^\star}, \ \gamma = \frac{h_f}{k}\sqrt{\frac{\nu}{a}} \\
N_b = \frac{(\rho c)_p D_B C_\infty}{(\rho c)_f \nu}, \ N_t = \frac{(\rho c)_p D_T \left(T_f - T_\infty\right)}{(\rho c)_f \nu T_\infty}, \ Sc = \frac{\nu}{D_B}.
\end{array}\right\}
\tag{9.15}
$$

Non-dimensional form of local Nusselt (rate of heat transfer) number Nu_x is

$$
\mathrm{Re}_x^{-1/2} Nu_x = -\theta'(0).
\tag{9.16}
$$

Here mass flux exhibited through Sherwood number (rate of mass transfer) disappears and $(\mathrm{Re}_x = u_w x/\nu)$ depicts local Reynolds number.

9.2 Initial guesses

The apposite primary assumptions and linear operators are

$$f_0(\zeta) = 1 - e^{-\zeta}, \quad g_0(\zeta) = 0, \quad \theta_0(\zeta) = \frac{\gamma}{1+\gamma}e^{-\zeta}, \quad \phi_0(\zeta) = -\frac{\gamma}{1+\gamma}\frac{N_t}{N_b}e^{-\zeta}, \tag{9.17}$$

$$\dddot{\mathcal{L}}_f^{\star} = \frac{d^3 f}{d\zeta^3} - \frac{df}{d\zeta}, \quad \dddot{\mathcal{L}}_g^{\star} = \frac{d^2 g}{d\zeta^2} - g, \quad \dddot{\mathcal{L}}_\theta^{\star} = \frac{d^2 \theta}{d\zeta^2} - \theta, \quad \dddot{\mathcal{L}}_\phi^{\star} = \frac{d^2 \phi}{d\zeta^2} - \phi, \tag{9.18}$$

subject to

$$\left.\begin{array}{c} \dddot{\mathcal{L}}_f^{\star}\left[\tilde{B}_1^{\star\star\star} + \tilde{B}_2^{\star\star\star}e^{\zeta} + \tilde{B}_3^{\star\star\star}e^{-\zeta}\right] = 0, \quad \dddot{\mathcal{L}}_g^{\star}\left[\tilde{B}_4^{\star\star\star}e^{\zeta} + \tilde{B}_5^{\star\star\star}e^{-\zeta}\right] = 0, \\[2mm] \dddot{\mathcal{L}}_\theta^{\star}\left[\tilde{B}_6^{\star\star\star}e^{\zeta} + \tilde{B}_7^{\star\star\star}e^{-\zeta}\right] = 0, \quad \dddot{\mathcal{L}}_\phi^{\star}\left[\tilde{B}_8^{\star\star\star}e^{\zeta} + \tilde{B}_9^{\star\star\star}e^{-\zeta}\right] = 0, \end{array}\right\} \tag{9.19}$$

in which $\tilde{B}_j^{\star\star\star}$ $(j = 1 - 9)$ exhibits the arbitrary constants.

9.3 OHAM solutions

It is examined that Eqs. $(9.9 - 9.12)$ represent system of nonlinear expressions. Series arrangement of the system is obtained by employing optimal homotopic algorithm. These arrangements contain $\hbar_f$, $\hbar_g$, $\hbar_\theta$ and $\hbar_\phi$ which have prime role in homotopic solutions. The optimal data of $\hbar_f$, $\hbar_g$, $\hbar_\theta$ and $\hbar_\phi$ can be acquired by taking small error. In order to save CPU time, average residual errors at mth-order of approximation i.e.

$$\varepsilon_{\mathring{m}^{\star}}^{f} = \frac{1}{\check{k}^{\star}+1}\sum_{j=0}^{\check{k}^{\star}}\left[\mathcal{N}_f\left(\sum_{\mathring{i}=0}^{\mathring{m}^{\star}}\tilde{f}(\zeta), \sum_{\mathring{i}=0}^{\mathring{m}^{\star}}\tilde{g}(\zeta)\right)_{\zeta=j\delta\zeta}\right]^2, \tag{9.20}$$

$$\varepsilon_{\mathring{m}^{\star}}^{g} = \frac{1}{\check{k}^{\star}+1}\sum_{j=0}^{\check{k}^{\star}}\left[\mathcal{N}_g\left(\sum_{\mathring{i}=0}^{\mathring{m}^{\star}}\tilde{f}(\zeta), \sum_{\mathring{i}=0}^{\mathring{m}^{\star}}\tilde{g}(\zeta)\right)_{\zeta=j\delta\zeta}\right]^2, \tag{9.21}$$

$$\varepsilon_{\mathring{m}^{\star}}^{\theta} = \frac{1}{\check{k}^{\star}+1}\sum_{j=0}^{\check{k}^{\star}}\left[\mathcal{N}_\theta\left(\sum_{\mathring{i}=0}^{\mathring{m}^{\star}}\tilde{f}(\zeta), \sum_{\mathring{i}=0}^{\mathring{m}^{\star}}\tilde{g}(\zeta), \sum_{\mathring{i}=0}^{\mathring{m}^{\star}}\tilde{\theta}(\zeta), \sum_{\mathring{i}=0}^{\mathring{m}^{\star}}\tilde{\phi}(\zeta)\right)_{\zeta=j\delta\zeta}\right]^2, \tag{9.22}$$

$$\varepsilon_{\mathring{m}^\star}^\phi = \frac{1}{\check{k}^\star + 1} \sum_{j=0}^{\check{k}^\star} \left[\mathcal{N}_\phi \left(\sum_{\mathring{i}=0}^{\mathring{m}^\star} \tilde{f}(\zeta), \sum_{\mathring{i}=0}^{\mathring{m}^\star} \tilde{g}(\zeta), \sum_{\mathring{i}=0}^{\mathring{m}^\star} \tilde{\theta}(\zeta), \sum_{\mathring{i}=0}^{\mathring{m}^\star} \tilde{\phi}(\zeta) \right)_{\zeta=j\delta\zeta} \right]^2. \tag{9.23}$$

By Liao [87]:

$$\varepsilon_{\mathring{m}^\star}^t = \varepsilon_{\mathring{m}^\star}^f + \varepsilon_{\mathring{m}^\star}^g + \varepsilon_{\mathring{m}^\star}^\theta + \varepsilon_{\mathring{m}^\star}^\phi, \tag{9.24}$$

in which $\varepsilon_{\mathring{m}^\star}^t$ illustrates total squared residual error, $\delta\zeta = 0.5$ and $k = 20$. At 2nd order of approximations, the optimal data of convergence control variables is $\hbar_f = -1.18623$, $\hbar_g = -1.07468$, $\hbar_\theta = -1.46495$, $\hbar_\phi = -1.03994$ and total averaged squared residual error is $\varepsilon_{\mathring{m}^\star}^t = 9.25 \times 10^{-4}$. Figure 9.1 represents plot of total residual error. Table 9.1 expresses individual average residual error at $\mathring{m}^\star = 2$. It can be seen that average residual errors decay via higher order deformations.
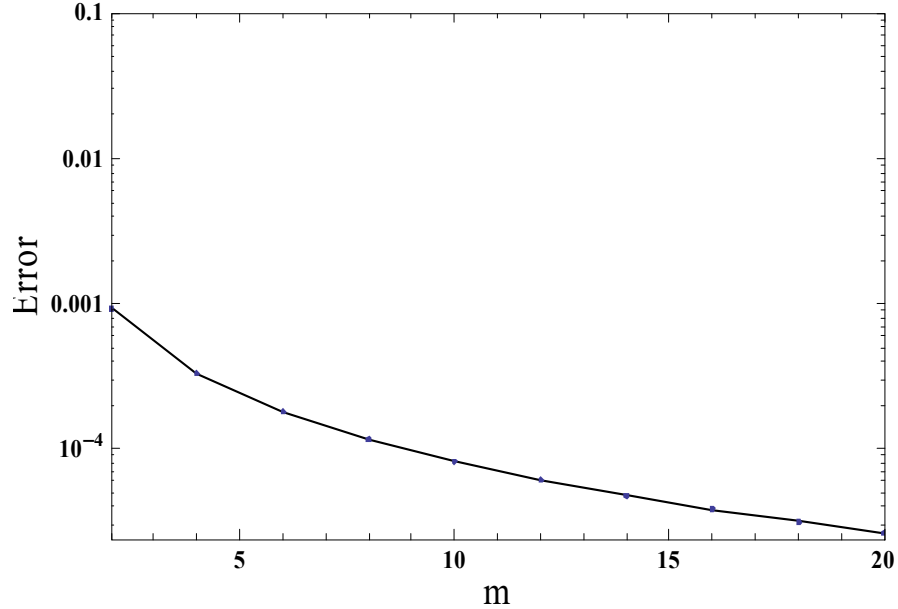
Figure 9.1 : Total residual error sketch.

Table 9.1. Optimal convergence control variables and total average squared residual errors.

$\mathring{m}^\star$	$\varepsilon^f_{\mathring{m}^\star}$	$\varepsilon^g_{\mathring{m}^\star}$	$\varepsilon^\theta_{\mathring{m}^\star}$	$\varepsilon^\phi_{\mathring{m}^\star}$
2	4.79×10^{-5}	7.53×10^{-4}	6.91×10^{-5}	5.51×10^{-5}
6	2.58×10^{-5}	1.29×10^{-4}	6.06×10^{-6}	2.06×10^{-5}
10	1.70×10^{-5}	5.09×10^{-5}	1.84×10^{-6}	1.25×10^{-5}
16	1.08×10^{-5}	1.99×10^{-5}	6.69×10^{-7}	7.04×10^{-6}
20	8.50×10^{-6}	1.23×10^{-5}	4.29×10^{-7}	5.19×10^{-6}

9.4 Discussion

This portion displays influences of physical flow variables like fluid relaxation time number β_1, Schmidt parameter Sc, fluid retardation time number β_2, rotation parameter Ω, Brownian movement parameter N_b, Biot parameter γ, Prandtl parameter Pr and thermophoresis parameter N_t on nondimensional velocities $f'(\zeta)$ and $g(\zeta)$, temperature $\theta(\zeta)$ and nano-concentration $\phi(\zeta)$ fields. Figures 9.2 and 9.3 depict that how fluid relaxation β_1 and retardation β_2 time numbers affect the velocity distribution $f'(\zeta)$. From these Figures it is examined that $f'(\zeta)$ shows opposite behavior against β_1 and β_2. Physically β_1 and β_2 are directly proportional to relaxation and retardation times respectively. Both relaxation and retardation times enhance for higher β_1 and β_2. In fact an increment in relaxation time reduces the fluid velocity while velocity of fluid elevates for greater retardation time. Due to this reason, a decreasing behavior is noticed in velocity $f'(\zeta)$ via β_1 while an increasing trend is noted when β_2 enhances. Figure 9.4 is portrayed to illustrate the influence of Ω on $f'(\zeta)$. Greater values of rotation parameter lead to lower velocity distribution. Physically rotation parameter is the ratio of rotation to extending rates. Higher values of rotation parameter Ω yield more rotational rate which yields reduction in velocity distribution $f'(\zeta)$. Figures 9.5 and 9.6 display variations of β_1 and β_2 on velocity distribution $g(\zeta)$. From these Figures we analyzed that magnitude of velocity distribution $g(\zeta)$ is negative which shows that flow is only in negative $y-$direction. It is interesting to observe that both β_1 and β_2 have different effects near and away from the stretching surface. Figure 9.7 is displayed to examine the variation of $g(\zeta)$ via higher Ω. Reduction is noted in $g(\zeta)$ against higher Ω. Figure 9.8 illustrates impact of β_1 on $\theta(\zeta)$. Here $\theta(\zeta)$ is escalated via higher

β_1. Figure 9.9 depicts that an improvement in β_2 shows decrease of $\theta(\zeta)$. Further under discussion analysis reduces to Maxwell model when $(\beta_2 = 0)$. Figure 9.10 is portrayed to characterize the consequences of β on $\theta(\zeta)$. It is analyzed that distinct estimations of β yields an increase of $\theta(\zeta)$. Figure 9.11 demonstrates the variation of temperature $\theta(\zeta)$ for higher γ. Temperature $\theta(\zeta)$ is incremented via higher γ. Figure 9.12 sketched influential impact of Pr on $\theta(\zeta)$. Clearly growing estimations of Pr causes a depreciation in $\theta(\zeta)$. Figure 9.13 demonstrates the change in $\theta(\zeta)$ for varying N_t. It has been analyzed that growing estimation of Ω yields an elevation in $\theta(\zeta)$. Figure 9.14 presents that bigger β_1 creates an improvement in nano-concentration $\phi(\zeta)$. Figure 9.15 depicts variations of nano-concentration $\phi(\zeta)$ via greater β_2. It is apparently observed that an expansion in β_2 exhibits decay of nano-concentration $\phi(\zeta)$. Figure 9.16 examined impact of N_t on $\phi(\zeta)$. Nano-concentration field is accelerated via higher N_t. Figure 9.17 explains the impact of Sc on nano-concentration field $\phi(\zeta)$. Nano-concentration field $\phi(\zeta)$ decays via stronger Sc. Influence of N_b on nano-concentration $\phi(\zeta)$ is appeared in Figure 9.18. Decaying trend in $\phi(\zeta)$ is noted via higher N_b. Figure 9.19 explained nano-concentration $\phi(\zeta)$ against N_t. An increment is analyzed in $\phi(\zeta)$ via greater N_t. Table 9.2 constructed variation in rate of heat transfer (local Nusselt number) $\mathrm{Re}_x^{-1/2} Nu_x$ via λ, β_1, β_2, γ, N_t, Sc, N_b and Pr. Local Nusselt (rate of heat transfer) number has been decayed via larger λ, β_1 and N_t while reverse behavior is noticed for higher β_2, γ and Pr. Furthermore, the contribution of N_b and Sc on heat transfer rate is quite comparable.

$$\beta_2 = 0.25 \, , \, \Omega = 0.2$$

$$\beta_1 = 0.0, \, 0.3, \, 0.6, \, 1.0$$
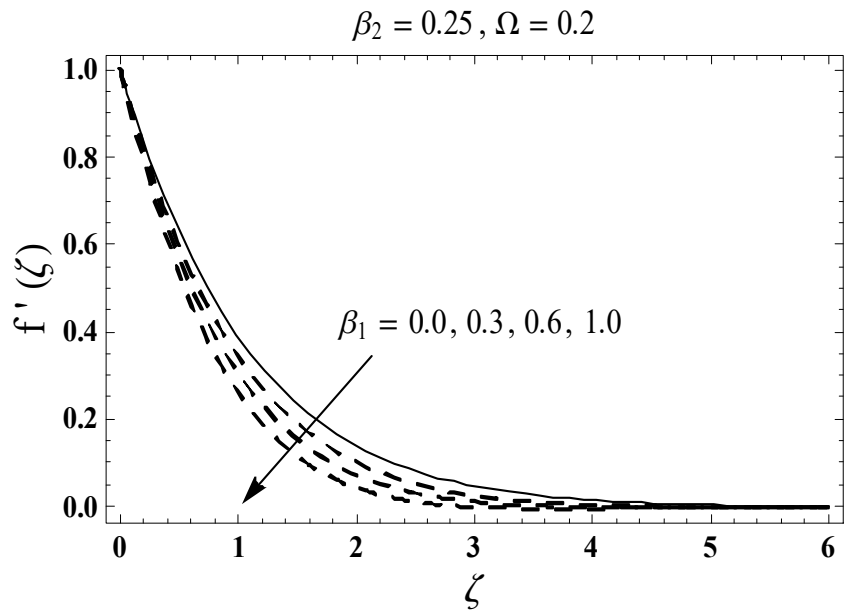
Figure 9.2 : Sketch for $f'(\zeta)$ against β_1.

$$\beta_1 = 0.25 \, , \, \Omega = 0.2$$

$$\beta_2 = 0.0, \, 0.2, \, 0.4, \, 0.6$$
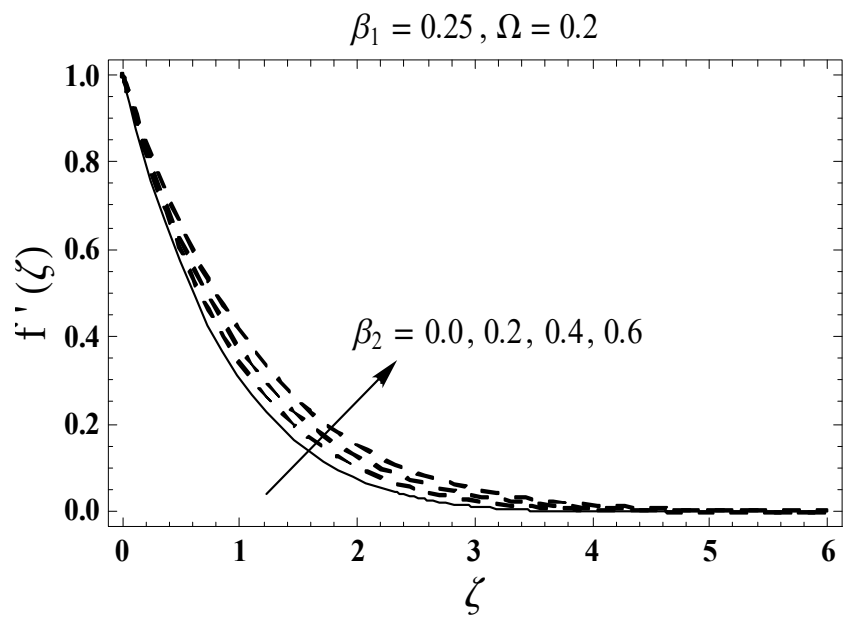
Figure 9.3 : Sketch for $f'(\zeta)$ against β_2.

171
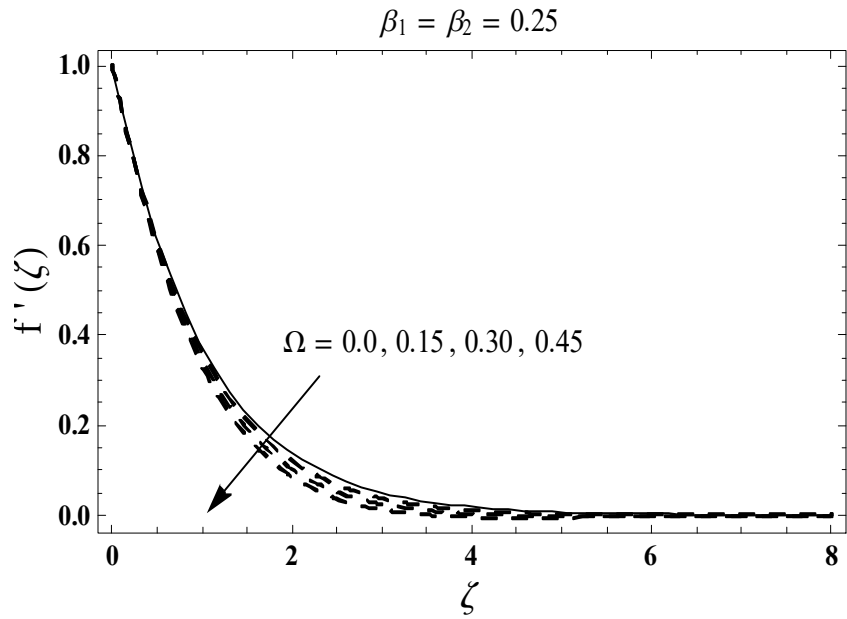
Figure 9.4 : Sketch for $f'(\zeta)$ against Ω.
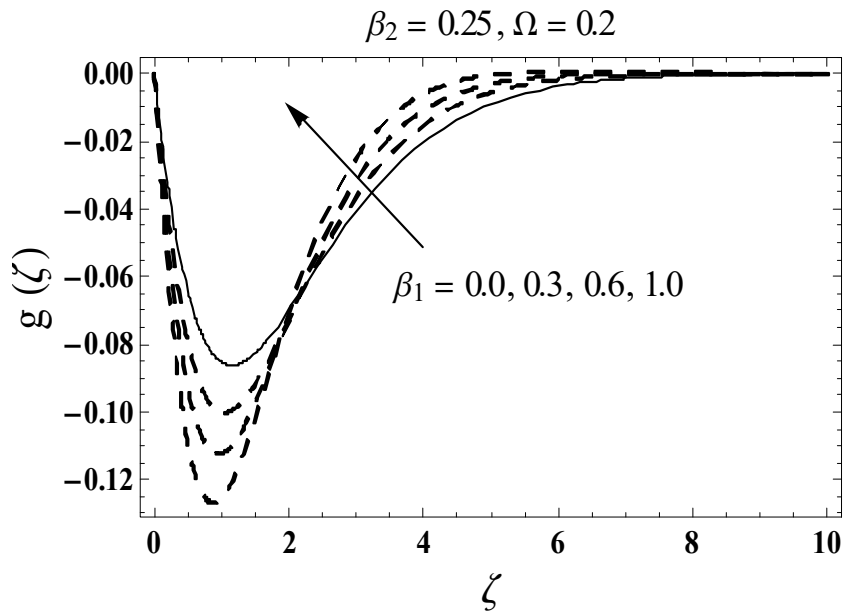
Figure 9.5 : Sketch for $g(\zeta)$ against β_1.

$\beta_1 = 0.25$, $\Omega = 0.2$

$\beta_2 = 0.0, 0.2, 0.4, 0.6$
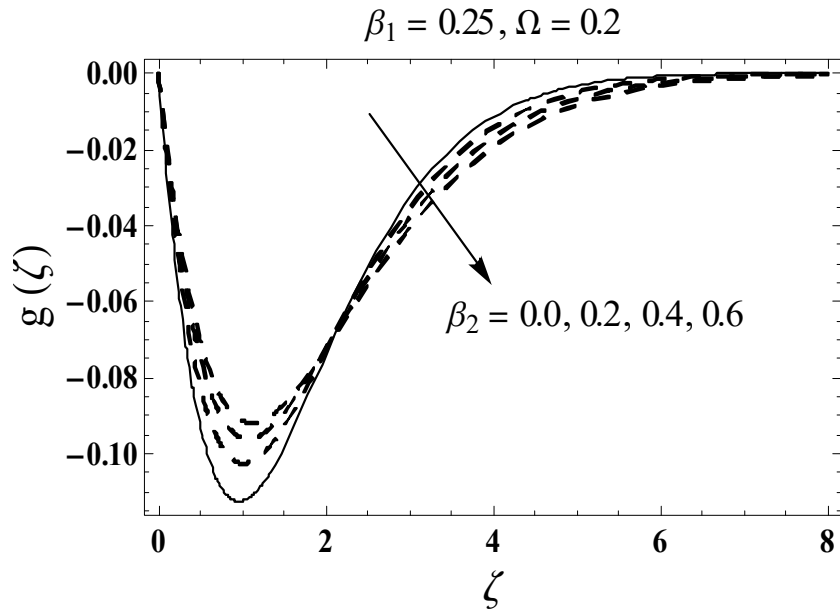
Figure 9.6 : Sketch for $g(\zeta)$ against β_2.

$\beta_1 = \beta_2 = 0.25$

$\Omega = 0.0, 0.15, 0.30, 0.45$
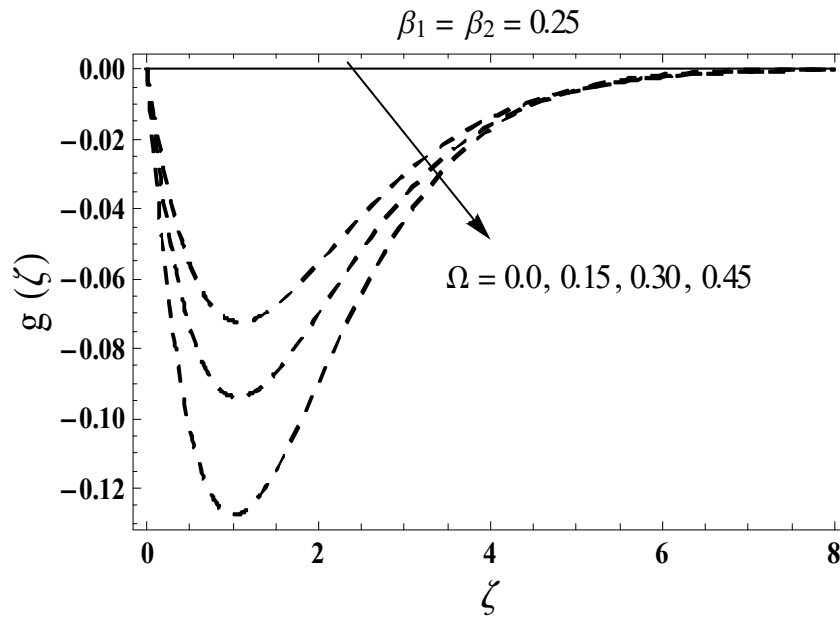
Figure 9.7 : Sketch for $g(\zeta)$ against λ.

$\beta_2 = 0.25, \Omega = 0.2, \gamma = N_b = 0.3, N_t = 0.1, \text{Sc} = \text{Pr} = 1.0$

$\beta_1 = 0.0, 0.3, 0.6, 1.0$
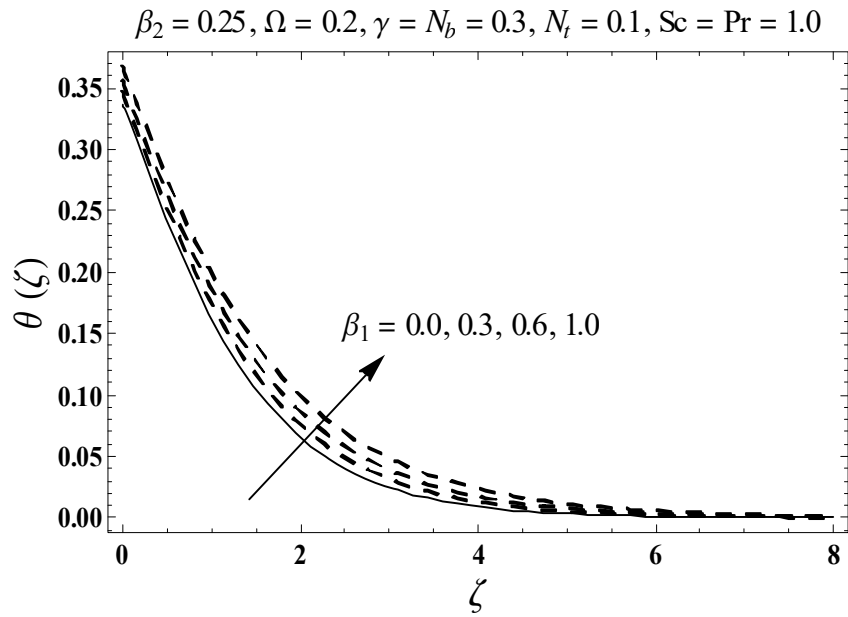
Figure 9.8 : Sketch for $\theta(\zeta)$ against β_1.

$\beta_1 = 0.25, \Omega = 0.2, \gamma = N_b = 0.3, N_t = 0.1, \text{Sc} = \text{Pr} = 1.0$

$\beta_2 = 0.0, 0.2, 0.4, 0.6$
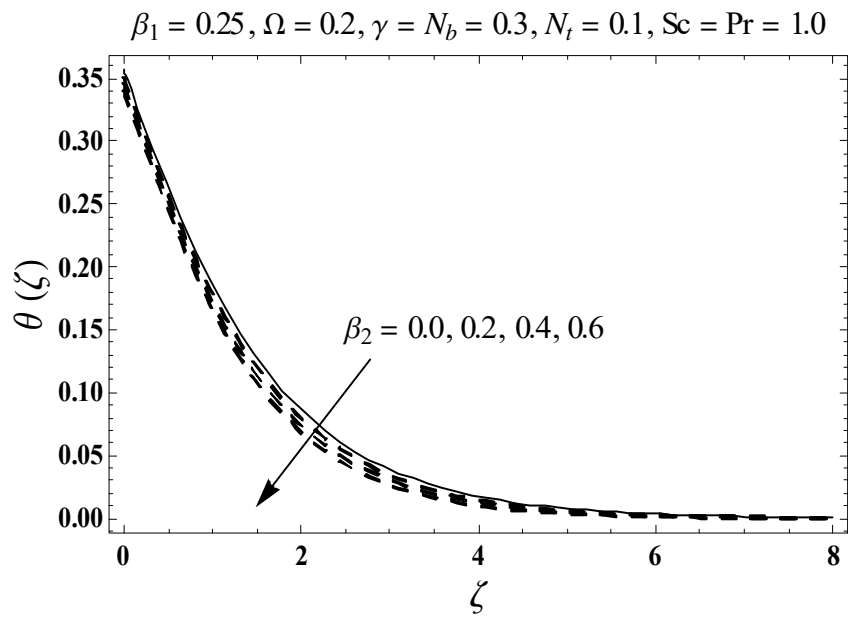
Figure 9.9 : Sketch for $\theta(\zeta)$ against β_2.

174
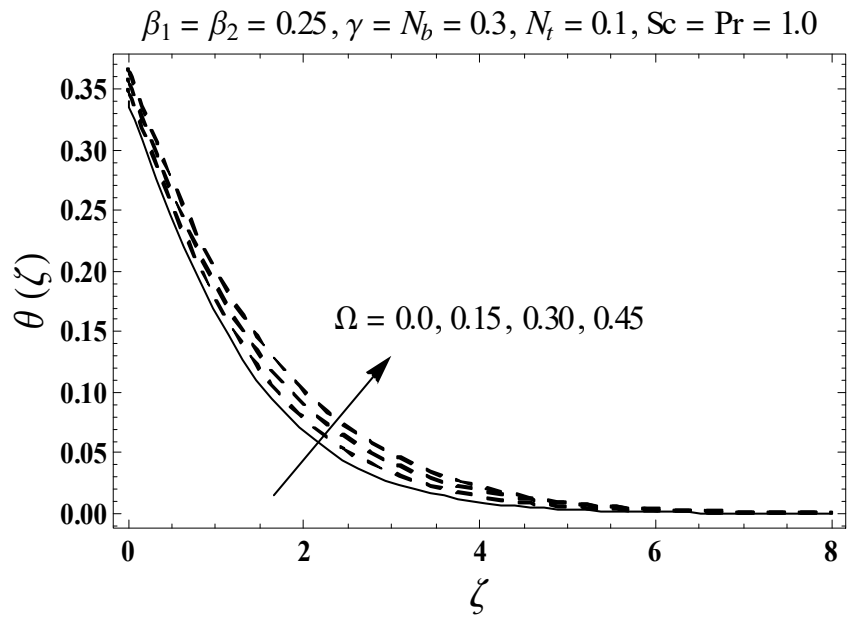
Figure 9.10 : Sketch for $\theta(\zeta)$ against Ω.
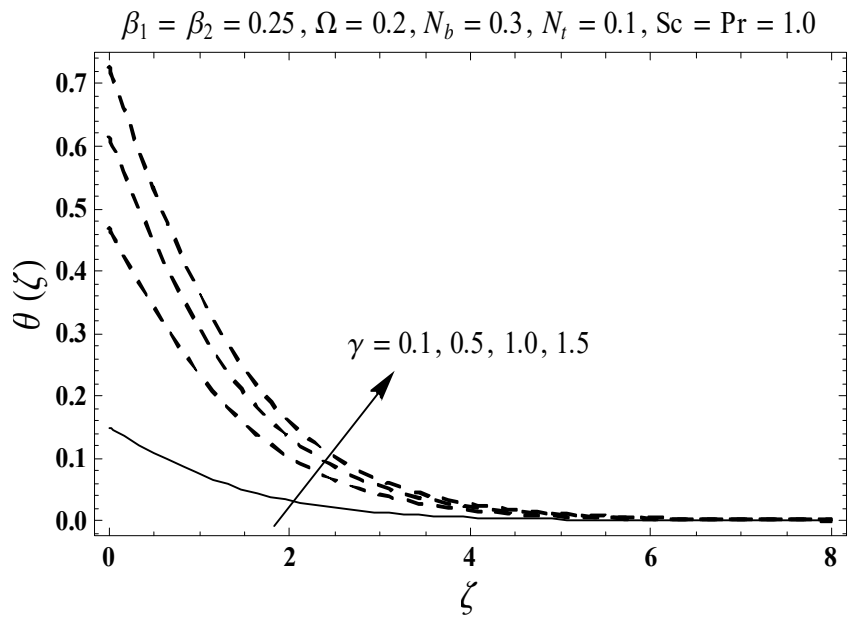
Figure 9.11 : Sketch for $\theta(\zeta)$ against γ.

$\beta_1 = \beta_2 = 0.25$, $\Omega = 0.2$, $\gamma = N_b = 0.3$, $N_t = 0.1$, Sc = 1.0

Pr = 0.7, 1.0, 1.3, 1.6
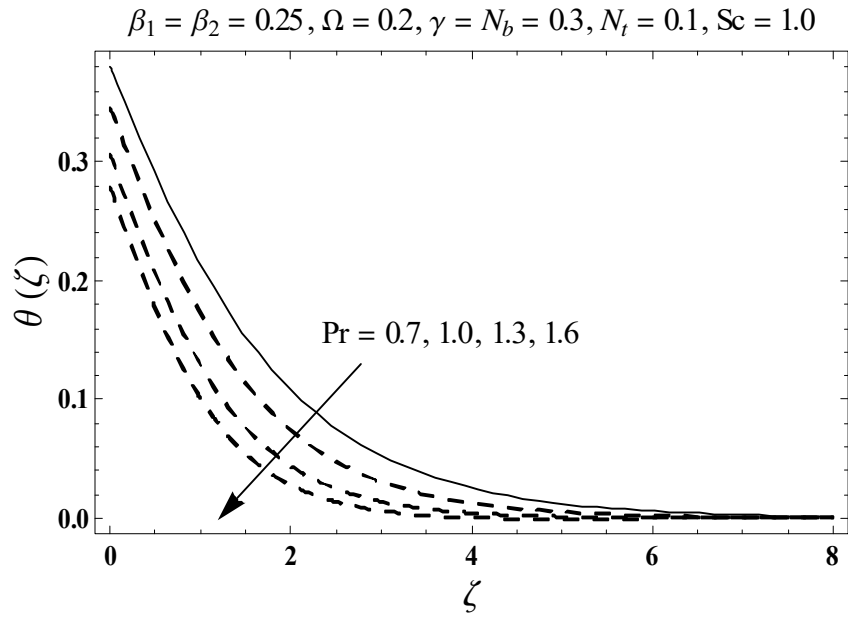
Figure 9.12 : Sketch for $\theta(\zeta)$ against Pr.

$\beta_1 = \beta_2 = 0.25$, $\Omega = 0.2$, $\gamma = N_b = 0.3$, Sc = Pr = 1.0

$N_t = 0.1, 0.7, 1.2, 1.9$
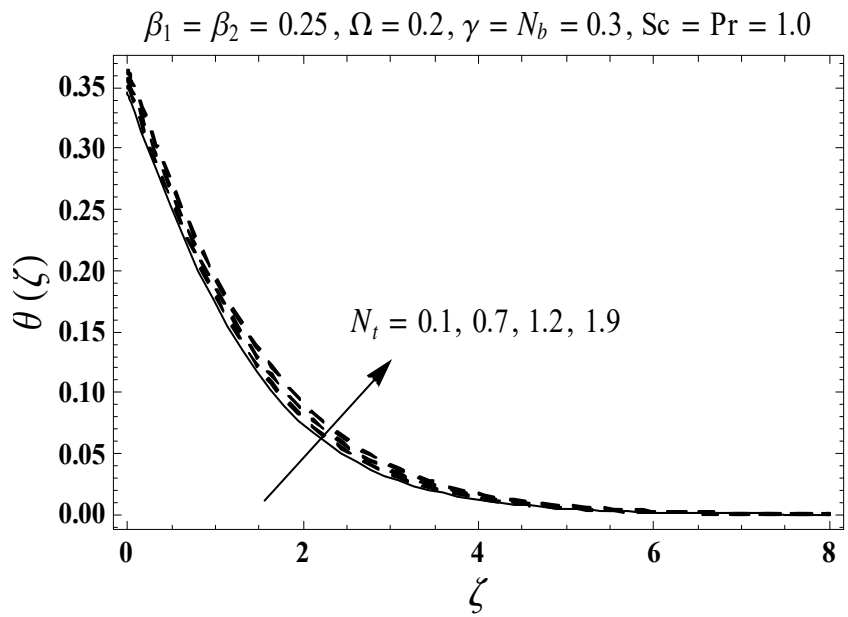
Figure 9.13 : Sketch for $\theta(\zeta)$ against N_t.

176

$$\beta_2 = 0.25, \, \Omega = 0.2, \, \gamma = N_b = 0.3, \, N_t = 0.1, \, \text{Sc} = \text{Pr} = 1.0$$

$\beta_1 = 0.0, \, 0.3, \, 0.6, \, 1.0$
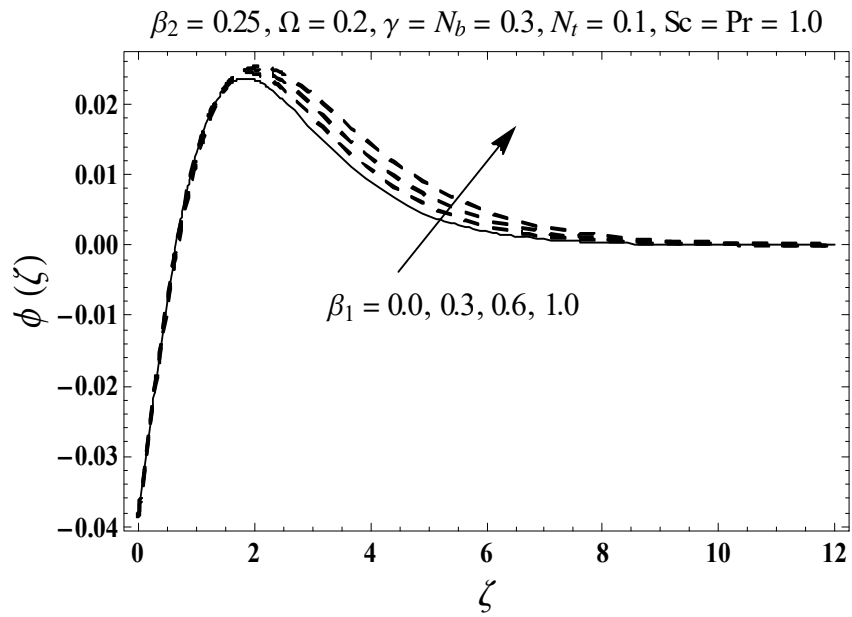
Figure 9.14 : Sketch for $\phi(\zeta)$ against β_1.

$$\beta_1 = 0.25, \, \Omega = 0.2, \, \gamma = N_b = 0.3, \, N_t = 0.1, \, \text{Sc} = \text{Pr} = 1.0$$

$\beta_2 = 0.0, \, 0.2, \, 0.4, \, 0.6$
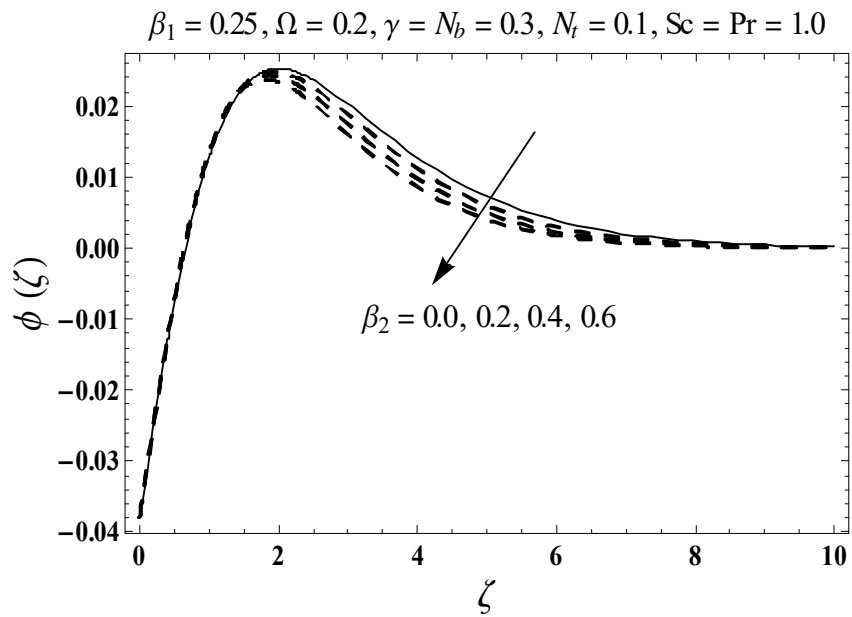
Figure 9.15 : Sketch for $\phi(\zeta)$ against β_2.

177

$\beta_1 = \beta_2 = 0.25$, $\gamma = N_b = 0.3$, $N_t = 0.1$, Sc = Pr = 1.0

$\Omega = 0.0$, 0.15, 0.30, 0.45
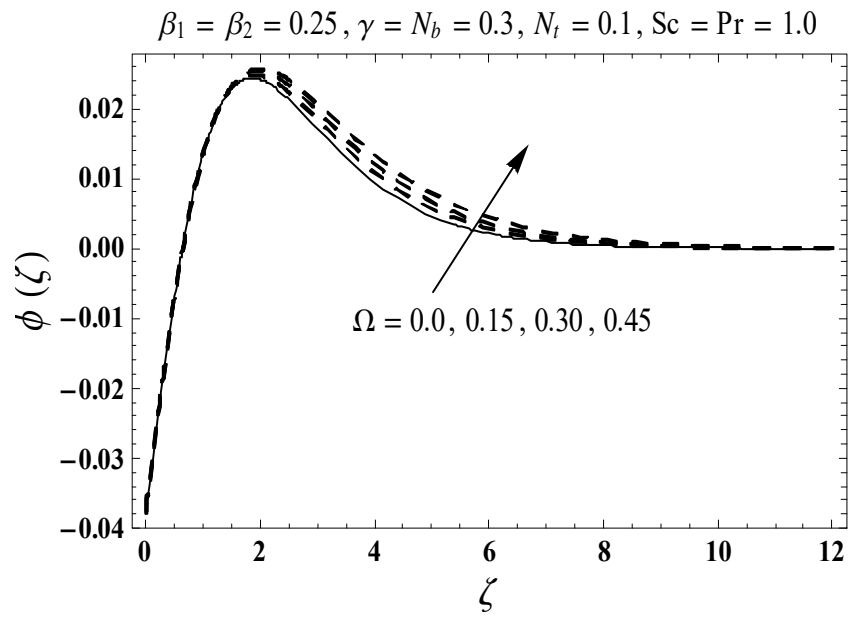
Figure 9.16 : Sketch for $\phi(\zeta)$ against Ω.

$\beta_1 = \beta_2 = 0.25$, $\Omega = 0.2$, $\gamma = N_b = 0.3$, $N_t = 0.1$, Pr = 1.0

Sc = 0.6, 0.9, 1.2, 1.5
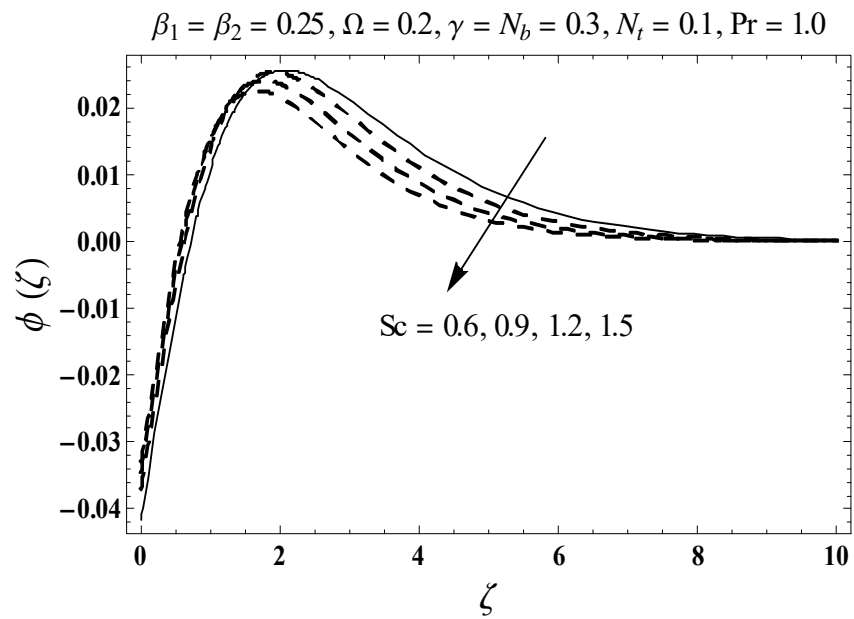
Figure 9.17 : Sketch for $\phi(\zeta)$ against Sc.

178

$\beta_1 = \beta_2 = 0.25, \, \Omega = 0.2, \, \gamma = 0.3, \, N_t = 0.1, \, \text{Sc} = \text{Pr} = 1.0$

$N_b = 0.4, \, 0.7, \, 1.0, \, 1.3$
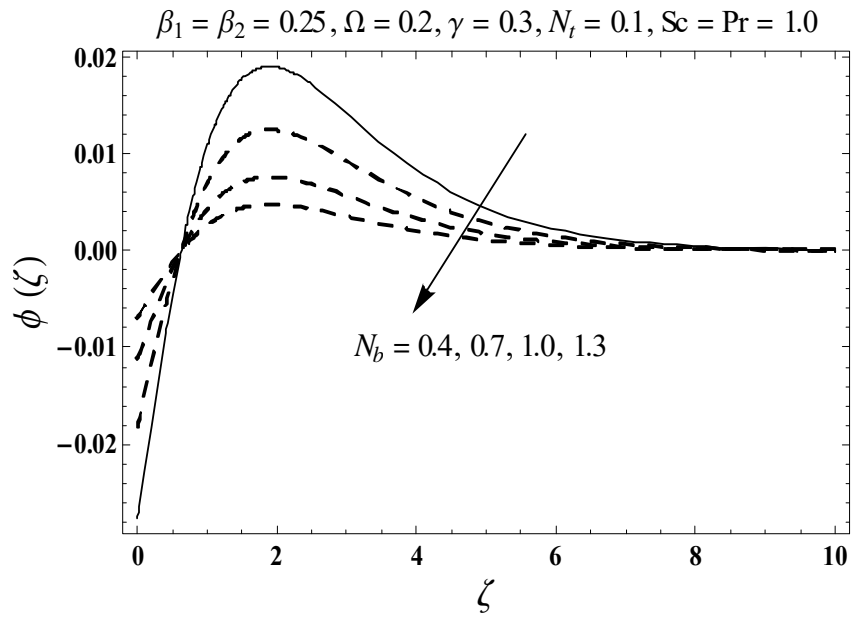
Figure 9.18 : Sketch for $\phi(\zeta)$ against N_b.

$\beta_1 = \beta_2 = 0.25, \, \Omega = 0.2, \, \gamma = N_b = 0.3, \, \text{Sc} = \text{Pr} = 1.0$

$N_t = 0.1, \, 0.7, \, 1.2, \, 1.9$
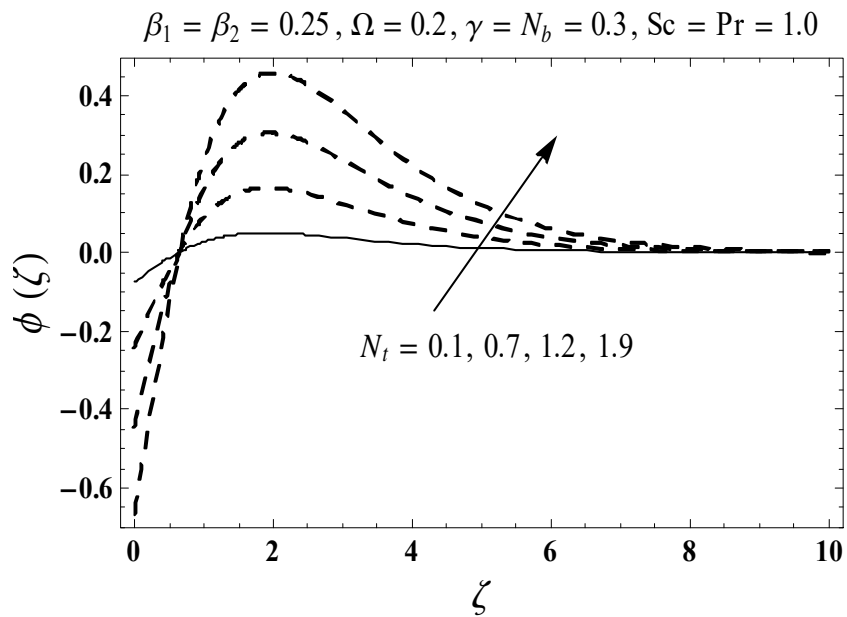
Figure 9.19 : Sketch for $\phi(\zeta)$ against N_t.

Table 9.2: Numerical data of local Nusselt (rate of heat transfer) number via λ, β_1, β_2, γ, N_t, Sc, N_b and Pr.

λ	β_1	β_2	γ	N_t	Sc	N_b	Pr	$\mathrm{Re}_x^{-1/2} Nu_x$
0.1	0.25	0.25	0.3	0.1	1.0	0.3	1.0	0.1977
0.2								0.1964
0.3								0.1951
0.1	0.0	0.25	0.3	0.1	1.0	0.3	1.0	0.1988
	0.3							0.1961
	0.6							0.1932
0.1	0.25	0.0	0.3	0.1	1.0	0.3	1.0	0.1930
		0.2						0.1958
		0.4						0.1979
0.1	0.25	0.25	0.1	0.1	1.0	0.3	1.0	0.0851
			0.7					0.3134
			1.3					0.3943
0.1	0.25	0.25	0.3	0.0	1.0	0.3	1.0	0.1968
				0.5				0.1952
				1.0				0.1935
0.1	0.25	0.25	0.3	0.1	0.5	0.3	1.0	0.1964
					1.0			0.1964
					1.5			0.1964
0.1	0.25	0.25	0.3	0.1	1.0	0.3	1.0	0.1964
						0.7		0.1964
						1.0		0.1964
0.1	0.25	0.25	0.3	0.1	1.0	0.3	0.5	0.1605
							1.0	0.1964
							1.5	0.2143

9.5   Major observations

Key results of this chapter includes:

- Higher fluid relaxation time number β_1 show opposite behavior for both velocities $f'(\zeta)$ and $g(\zeta)$ while similar trend is noticed for temperature $\theta(\zeta)$ and nano-concentration $\phi(\zeta)$ profiles.

- Both velocities $f'(\zeta)$ and $g(\zeta)$ have reverse behavior for higher fluid retardation time number β_2 while decreasing trend is observed for temperature $\theta(\zeta)$ and nano-concentration $\phi(\zeta)$.

- Temperature $\theta(\zeta)$ and nano-concentration $\phi(\zeta)$ are augmented for higher rotation parameter λ while reverse behavior is noticed for velocities $f'(\zeta)$ and $g(\zeta)$.

- Higher Biot parameter γ shows stronger temperature $\theta(\zeta)$ field.

- When N_t enlarges, both nano-concentration $\phi(\zeta)$ and temperature $\theta(\zeta)$ are increased.

- Both Sc and Pr serve to reduce $\phi(\zeta)$ and $\theta(\zeta)$.

- Nano-concentration $\phi(\zeta)$ is decreased against N_b.

- Heat transfer rate decays for higher N_t while it behaves constant for N_b.

Chapter 10

Three-dimensional rotating flow of Jeffrey nanofluid with heat generation/absorption and Arrhenius activation energy: OHAM solutions

Influence of activation energy in three dimensional rotating flow of Jeffrey nanoliquid is addressed. Mathematical modelling is developed by considering heat generation/absorption. Brownian motion and thermophoretic diffusion are considered. Convergent series solutions of the involved nonlinear problems are obtained. Optimal homotopy analysis method (OHAM) is employed for the construction of series solutions. Salient behaviors of several pertinent variables on velocities, nano-concentration and temperature are examined graphically. Further local Nusselt number (heat transfer rate) is graphically described via different flow variables.

10.1 Statement

Here we examine steady 3D rotating flow of Jeffrey nanofluid with heat source/sink. An irregular motion and thermophoretic diffusion impacts are considered for present analysis. Effect of activation energy is also studied. Convective heat and zero mass flux conditions are implemented. Here liquid occupies the domain $z \geq 0$ and the actuating surface is aligned in $x-$direction. Assuming the considered surface is extended in longitudinal direction with velocity $U_w(x) = ax$. In addition, fluid rotates about $z-$axis with constant angular velocity ω. Resulting boundary-layer problems are

$$\frac{\partial u}{\partial x} + \frac{\partial v}{\partial y} + \frac{\partial w}{\partial z} = 0, \tag{10.1}$$

$$u\frac{\partial u}{\partial x} + v\frac{\partial u}{\partial y} + w\frac{\partial u}{\partial z} - 2\omega v = \frac{\nu}{1+\lambda_1}\left(\frac{\partial^2 u}{\partial z^2} + \lambda_2\left(\begin{array}{c} u\frac{\partial^3 u}{\partial x\partial z^2} + v\frac{\partial^3 u}{\partial y\partial z^2} + w\frac{\partial^3 u}{\partial z^3} \\ +\frac{\partial u}{\partial z}\frac{\partial^2 u}{\partial x\partial z} + \frac{\partial v}{\partial z}\frac{\partial^2 u}{\partial y\partial z} + \frac{\partial w}{\partial z}\frac{\partial^2 u}{\partial z^2} \end{array}\right)\right), \tag{10.2}$$

$$u\frac{\partial v}{\partial x} + v\frac{\partial v}{\partial y} + w\frac{\partial v}{\partial z} + 2\omega u = \frac{\nu}{1+\lambda_1}\left(\frac{\partial^2 v}{\partial z^2} + \lambda_2\left(\begin{array}{c} u\frac{\partial^3 v}{\partial x\partial z^2} + v\frac{\partial^3 v}{\partial y\partial z^2} + w\frac{\partial^3 v}{\partial z^3} \\ +\frac{\partial u}{\partial z}\frac{\partial^2 v}{\partial x\partial z} + \frac{\partial v}{\partial z}\frac{\partial^2 v}{\partial y\partial z} + \frac{\partial w}{\partial z}\frac{\partial^2 v}{\partial z^2} \end{array}\right)\right), \tag{10.3}$$

$$\begin{aligned} u\frac{\partial T}{\partial x} + v\frac{\partial T}{\partial y} + w\frac{\partial T}{\partial z} &= \alpha^\star\frac{\partial^2 T}{\partial z^2} + \frac{Q_0}{(\rho c)_f}(T - T_\infty) \\ &+ \frac{(\rho c)_p}{(\rho c)_f}\left(D_B\left(\frac{\partial T}{\partial z}\frac{\partial C}{\partial z}\right) + \frac{D_T}{T_\infty}\left(\frac{\partial T}{\partial z}\right)^2\right), \end{aligned} \tag{10.4}$$

$$u\frac{\partial C}{\partial x} + v\frac{\partial C}{\partial y} + w\frac{\partial C}{\partial z} = D_B\left(\frac{\partial^2 C}{\partial z^2}\right) - k_r^2\left(\frac{T}{T_\infty}\right)^n(C - C_\infty)\exp\left(-\frac{E_a}{\kappa T}\right) + \frac{D_T}{T_\infty}\left(\frac{\partial^2 T}{\partial z^2}\right), \tag{10.5}$$

$$u = U_w(x) = ax, \ v = 0, \ w = 0, \ -k\frac{\partial T}{\partial z} = h_f(T_f - T), \\ D_B\frac{\partial C}{\partial z} + \frac{D_T}{T_\infty}\frac{\partial T}{\partial z} = 0 \text{ at } z = 0, \tag{10.6}$$

$$u \to 0, \quad v \to 0, \quad T \to T_\infty, \quad C \to C_\infty \quad \text{when } z \to \infty, \tag{10.7}$$

in which (u, v, w) express velocities in (x, y, z) directions respectively, absolute viscosity (μ), kinematic viscosity (ν), (ρ_f) density of fluid, ratio of relaxation and retardation times (λ_1), (λ_2) retardation time, $(\alpha^\star)$ thermal diffusivity, thermal efficiency (k), heat capacitance of the liquid $(\rho c)_f$, Brownian coefficient (D_B), temperature (T), effective heat capacitance of nanoparticles $(\rho c)_p$, (Q_0) heat generation/absorption coefficient, concentration (C), thermophoretic coefficient

(D_T), activation energy (E_a), fitted rate constant (n), reaction rate (k_r), Boltzmann constant (κ) and coefficient of heat transfer (h_f).

Letting

$$
\left.\begin{array}{l}
u = axf'(\zeta), \ v = axg(\zeta), \ w = -(a\nu)^{1/2}f(\zeta), \\
\phi(\zeta) = \frac{C-C_\infty}{C_\infty}, \ \theta(\zeta) = \frac{T-T_\infty}{T_f-T_\infty}, \ \zeta = \left(\frac{a}{\nu}\right)^{1/2} z.
\end{array}\right\}
\tag{10.8}
$$

Equation (10.1) is trivially justified and Eqs. $(10.2) - (10.7)$ are reduced to

$$
f''' + (1 + \lambda_1)\left(ff'' - f'^2 + 2\Omega g\right) + \beta\left(f''^2 - ff^{iv}\right) = 0,
\tag{10.9}
$$

$$
g'' + (1 + \lambda_1)\left(fg' - f'g - 2\Omega f'\right) + \beta\left(f''g' - fg'''\right) = 0,
\tag{10.10}
$$

$$
\frac{1}{\Pr}\theta'' + N_t\theta'^2 + \theta'f + +S_1\theta + N_b\theta'\phi' = 0,
\tag{10.11}
$$

$$
\frac{1}{Sc}\phi'' + f\phi' + \frac{1}{Sc}\frac{N_t}{N_b}\theta'' - \sigma\left(1 + \delta\theta\right)^n \phi\exp\left(-\frac{E}{1 + \delta\theta}\right) = 0,
\tag{10.12}
$$

$$
f(0) = g(0) = 0, \ f'(0) = 1, \ \theta'(0) = -\gamma(1 - \theta(0)), \ N_b\phi'(0) + N_t\theta'(0) = 0,
\tag{10.13}
$$

$$
f'(\infty) \to 0, \ g(\infty) \to 0, \ \theta(\infty) \to 0, \ \phi(\infty) \to 0.
\tag{10.14}
$$

In above expressions Ω, δ, γ, N_t, β, N_b, Pr, Sc, σ, E and S_1 stand for rotation parameter, temperature difference parameter, Biot number, thermophoresis parameter, Deborah number, Brownian movement parameter, Prandtl parameter, Schmidt number, chemical reaction parameter, nondimensional activation energy and heat generation/absorption parameter. We define

$$
\left.\begin{array}{l}
\Omega = \frac{\omega}{a}, \ \beta = \lambda_2 a, \ \Pr = \frac{\nu}{\alpha^\star}, \ \gamma = \frac{h_f}{k}\sqrt{\frac{\nu}{a}}, \ N_b = \frac{(\rho c)_p D_B C_\infty}{(\rho c)_f \nu}, \ Sc = \frac{\nu}{D_B}, \\
N_t = \frac{(\rho c)_p D_T\left(T_f - T_\infty\right)}{(\rho c)_f \nu T_\infty}, \ E = \frac{E_a}{\kappa T_\infty}, \ \sigma = \frac{k_r^2}{a}, \ S_1 = \frac{Q_0}{a(\rho c)_f}, \ \delta = \frac{T_w - T_\infty}{T_\infty}.
\end{array}\right\}
\tag{10.15}
$$

Non-dimensional form of heat transfer rate is

$$
(\mathrm{Re}_x)^{-1/2} Nu_x = -\theta'(0).
\tag{10.16}
$$

Here local Reynolds number is $\mathrm{Re}_x = U_w x/\nu$. Note that dimensionless mass flux exhibited by Sherwood number Sh_x is now identically zero.

10.2   Initial guesses

The suitable initial assumptions and auxiliary linear operators for OHAM solutions are selected as

$$f_0(\zeta) = 1 - e^{-\zeta}, \quad g_0(\zeta) = 0, \quad \theta_0(\zeta) = \frac{\gamma}{1+\gamma}e^{-\zeta}, \quad \phi_0(\zeta) = -\frac{\gamma}{1+\gamma}\frac{N_t}{N_b}e^{-\zeta}, \tag{10.17}$$

$$\dddot{\mathcal{L}}_f^\star = \frac{d^3 f}{d\zeta^3} - \frac{df}{d\zeta}, \quad \dddot{\mathcal{L}}_g^\star = \frac{d^2 g}{d\zeta^2} - g, \quad \dddot{\mathcal{L}}_\theta^\star = \frac{d^2\theta}{d\zeta^2} - \theta, \quad \dddot{\mathcal{L}}_\phi^\star = \frac{d^2\phi}{d\zeta^2} - \phi. \tag{10.18}$$

The above operators have characteristics

$$\left. \begin{array}{l} \dddot{\mathcal{L}}_f^\star \left[\tilde{B}_1^{\star\star\star} + \tilde{B}_2^{\star\star\star}e^\zeta + \tilde{B}_3^{\star\star\star}e^{-\zeta} \right] = 0, \quad \dddot{\mathcal{L}}_g^\star \left[\tilde{B}_4^{\star\star\star}e^\zeta + \tilde{B}_5^{\star\star\star}e^{-\zeta} \right] = 0, \\[2mm] \dddot{\mathcal{L}}_\theta^\star \left[\tilde{B}_6^{\star\star\star}e^\zeta + \tilde{B}_7^{\star\star\star}e^{-\zeta} \right] = 0, \quad \dddot{\mathcal{L}}_\phi^\star \left[\tilde{B}_8^{\star\star\star}e^\zeta + \tilde{B}_9^{\star\star\star}e^{-\zeta} \right] = 0, \end{array} \right\} \tag{10.19}$$

in which $\tilde{B}_j^{\star\star\star}$ $(j = 1 - 9)$ illustrate the arbitrary constants.

10.3   OHAM solutions

The momentum, energy and nano-concentration expressions are tackled by BVPh2.0. These expressions contain non-zero convergence control variables $\hbar_f$, $\hbar_g$, $\hbar_\theta$ and $\hbar_\phi$ which perform a key role of homotopic solutions. We can figure out the optimal values of $\hbar_f$, $\hbar_g$, $\hbar_\theta$ and $\hbar_\phi$ by taking minimum error. In order to save CPU time, average minimal errors are employed at mth-order of deformation which was suggested by Liao [87] as follows:

$$\varepsilon_{\mathring{m}^\star}^f = \frac{1}{\check{k}^\star + 1} \sum_{j=0}^{\check{k}^\star} \left[\mathcal{N}_f \left(\sum_{\mathring{i}=0}^{\mathring{m}^\star} \tilde{f}(\zeta), \sum_{\mathring{i}=0}^{\mathring{m}^\star} \tilde{g}(\zeta) \right)_{\zeta = j\delta\zeta} \right]^2, \tag{10.20}$$

$$\varepsilon_{\mathring{m}^\star}^g = \frac{1}{\check{k}^\star + 1} \sum_{j=0}^{\check{k}^\star} \left[\mathcal{N}_g \left(\sum_{\mathring{i}=0}^{\mathring{m}^\star} \tilde{f}(\zeta), \sum_{\mathring{i}=0}^{\mathring{m}^\star} \tilde{g}(\zeta) \right)_{\zeta = j\delta\zeta} \right]^2, \tag{10.21}$$

$$\varepsilon_{\mathring{m}^\star}^\theta = \frac{1}{\check{k}^\star + 1} \sum_{j=0}^{\check{k}^\star} \left[\mathcal{N}_\theta \left(\sum_{\mathring{i}=0}^{\mathring{m}^\star} \tilde{f}(\zeta), \sum_{\mathring{i}=0}^{\mathring{m}^\star} \tilde{g}(\zeta), \sum_{\mathring{i}=0}^{\mathring{m}^\star} \tilde{\theta}(\zeta), \sum_{\mathring{i}=0}^{\mathring{m}^\star} \tilde{\phi}(\zeta) \right)_{\zeta = j\delta\zeta} \right]^2, \tag{10.22}$$

$$\varepsilon_{\mathring{m}^\star}^\phi = \frac{1}{\check{k}^\star + 1} \sum_{j=0}^{\check{k}^\star} \left[\mathcal{N}_\phi \left(\sum_{\mathring{i}=0}^{\mathring{m}^\star} \tilde{f}(\zeta), \sum_{\mathring{i}=0}^{\mathring{m}^\star} \tilde{g}(\zeta), \sum_{\mathring{i}=0}^{\mathring{m}^\star} \tilde{\theta}(\zeta), \sum_{\mathring{i}=0}^{\mathring{m}^\star} \tilde{\phi}(\zeta) \right)_{\zeta = j\delta\zeta} \right]^2. \qquad (10.23)$$

By Liao [87] :

$$\varepsilon_{\mathring{m}^\star}^t = \varepsilon_{\mathring{m}^\star}^f + \varepsilon_{\mathring{m}^\star}^g + \varepsilon_{\mathring{m}^\star}^\theta + \varepsilon_{\mathring{m}^\star}^\phi, \qquad (10.24)$$

in which $\varepsilon_{\mathring{m}^\star}^t$ expresses total squared residual error, $k = 20$ and $\delta\zeta = 0.5$. At 2nd order of approximations, the optimal data of convergence control variables is $\hbar_f = -1.42072$, $\hbar_g = -1.29840$, $\hbar_\theta = -1.52891$ and $\hbar_\phi = -0.930447$ and total averaged squared residual error is $\varepsilon_{\mathring{m}^\star}^t = 8.22 \times 10^{-4}$. Figure 10.1 is sketched to characterize the total residual error. Individual average squared residual error at $\mathring{m}^\star = 2$ are presented in Table 10.1. It is interpreted that average residual errors depreciates via higher order deformations.
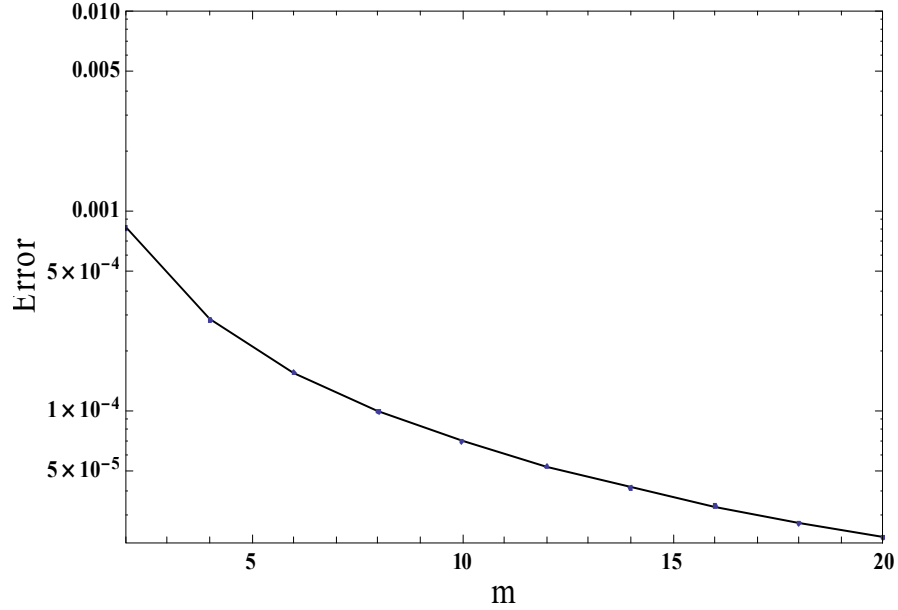

Figure 10.1 : Sketch for total residual error.

Table 10.1. Optimal convergence control variables and total average squared residual errors.

$\mathring{m}^\star$	$\varepsilon_{\mathring{m}^\star}^f$	$\varepsilon_{\mathring{m}^\star}^g$	$\varepsilon_{\mathring{m}^\star}^\theta$	$\varepsilon_{\mathring{m}^\star}^\phi$
2	9.83×10^{-5}	4.87×10^{-4}	1.61×10^{-4}	7.58×10^{-5}
6	3.29×10^{-5}	6.34×10^{-5}	3.09×10^{-5}	2.71×10^{-5}
10	1.82×10^{-5}	2.13×10^{-5}	1.42×10^{-5}	1.62×10^{-5}
16	9.87×10^{-6}	6.83×10^{-6}	7.07×10^{-6}	9.34×10^{-6}
20	7.21×10^{-6}	3.75×10^{-6}	5.11×10^{-6}	7.05×10^{-6}

10.4 Discussion

Here we intend to predict the outcomes of rotation parameter Ω, Biot number γ, Prandtl number Pr, ratio of relaxation to retardation times λ_1, heat source/sink parameter S_1, Deborah number β, thermophoresis parameter N_t, Brownian movement parameter N_b, Schmidt number Sc, nondimensional activation energy E, chemical reaction parameter σ and temperature difference parameter δ on velocities, temperature and nano-concentration. Figure 10.2 presents the outcome of λ_1 for $f'(\zeta)$. Velocity has decreasing trend for higher λ_1. Physically an inverse relation exists between λ_1 and retardation time. Higher λ_1 yields lower retardation time. Such lower retardation time corresponds to reduction of velocity field. Figure 10.3 scrutinizes the change of velocity $f'(\zeta)$ for varying β. Higher estimation of β yield higher velocity field. Basically Deborah number is directly related with retardation time. An increment in Deborah number yields stronger retardation time. Such stronger retardation time correspond to more velocity field. Figure 10.4 analyzes curves of velocity field $f'(\zeta)$ against different values of rotation parameter Ω. One can easily notice the reduction of $f'(\zeta)$ via higher values of Ω. Figure 10.5 delineates the influence of λ_1 on velocity $g(\zeta)$. It is examined that by enhancing λ_1, the velocity $g(\zeta)$ decays. Figure 10.6 portrayed the consequences of β on velocity $g(\zeta)$. It is analyzed that larger β yields an escalation of $g(\zeta)$. Figure 10.7 depicts effect of Ω on velocity $g(\zeta)$. An increasing trend is observed against higher Ω. Figure 10.8 shows how $\theta(\zeta)$ varied for λ_1. Here $\theta(\zeta)$ enhances against stronger λ_1. Basically an increment of λ_1 corresponds to lower retardation and higher relaxation times. Due to this argument, an enhancement is observed in temperature via λ_1. Temperature $\theta(\zeta)$ against higher β is shown in Figure 10.9. Larger β

indicates decay of temperature $\theta(\zeta)$. Figure 10.10 demonstrates the variation of temperature $\theta(\zeta)$ for higher Ω. Temperature $\theta(\zeta)$ is elevated via higher Ω. Figure 10.11 depicts how temperature $\theta(\zeta)$ varied γ. It is noticed that by increasing γ, temperature $\theta(\zeta)$ elevates. Figures 10.12 and 10.13 are developed to analyze the behaviors of the heat generation $(S_1 > 0)$ and absorption $(S_1 < 0)$ parameters. From these Figures it is examined that temperature shows opposite trend while considering $(S_1 > 0)$ and $(S_1 < 0)$. Figure 10.14 is developed to visualize the behavior of Pr on $\theta(\zeta)$. Here $\theta(\zeta)$ decayed for higher Pr. Figure 10.15 displayed behavior of N_t on $\theta(\zeta)$. An enhancement is observed for temperature via higher estimations of N_t. Impact of λ_1 on $\phi(\zeta)$ is presented in Figure 10.16. An elevating impact of $\phi(\zeta)$ is noted for higher λ_1. Figure 10.17 explains the impact of β on nano-concentration field $\phi(\zeta)$. Nano-concentration field $\phi(\zeta)$ depreciates against growing β. Change in $\phi(\zeta)$ against stronger Ω is displayed in Figure 10.18. Clearly $\phi(\zeta)$ is elevated via greater Ω. Nano-concentration field $\phi(\zeta)$ behavior via Sc is depicted through Figure 10.19. One can conveniently see that $\phi(\zeta)$ depreciates via stronger Sc. Figure 10.20 is displayed to analyze the role of N_b on $\theta(\zeta)$. In the boundary layer area, it can be explored that the fluid temperature is boosted up for rising values of N_b. Figure 10.21 is constructed to see the influence of N_t on $\phi(\zeta)$. $\phi(\zeta)$ is elevated through stronger N_t. Figure 10.22 is developed to see the influence of E on the nano-concentration field $\phi(\zeta)$. It is clearly observed from this figure that $\phi(\zeta)$ is an increasing function of E. Figure 10.23 is displayed to deliberate the influence of σ on $\phi(\zeta)$. Higher σ cause a depreciation in $\phi(\zeta)$. Figure 10.24 explores that $\phi(\zeta)$ is a depreciating function of δ. Figure 10.25 displayed the variations of $(\mathrm{Re}_x)^{-1/2} Nu_x$ via higher N_t and N_b. From this Figure it can be observed that $(\mathrm{Re}_x)^{-1/2} Nu_x$ reduces against higher N_t while constant behavior is observed via higher N_b.
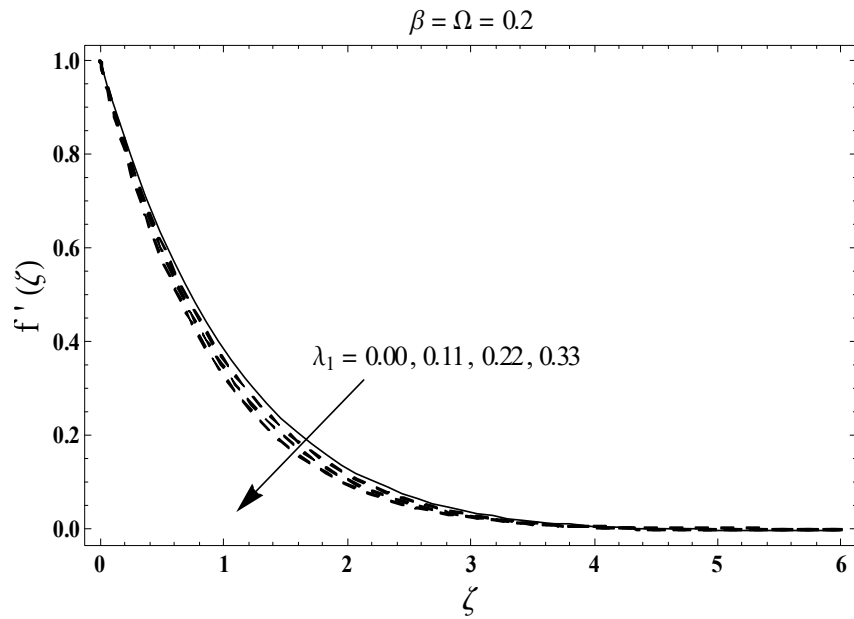
Figure 10.2 : Sketch for $f'(\zeta)$ against λ_1.
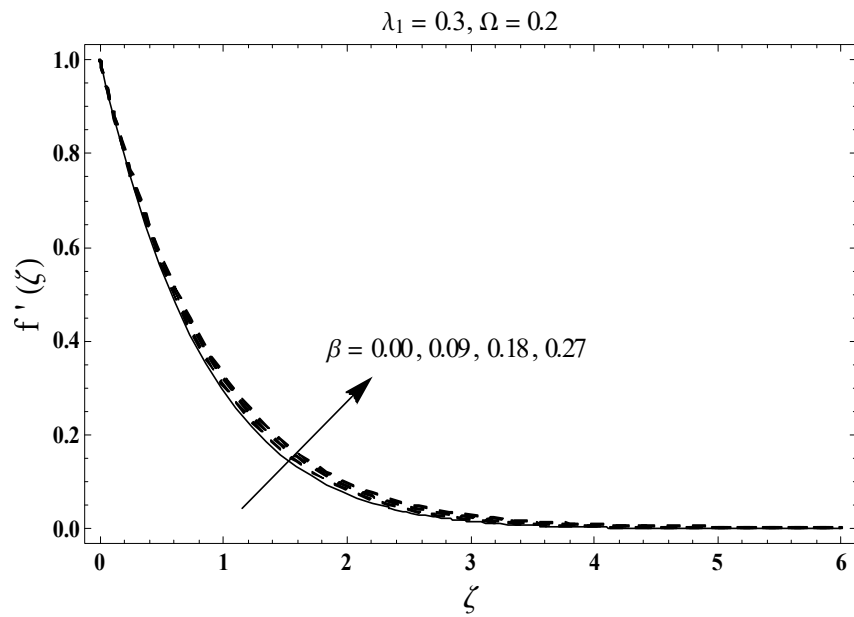
Figure 10.3 : Sketch for $f'(\zeta)$ against β.

189
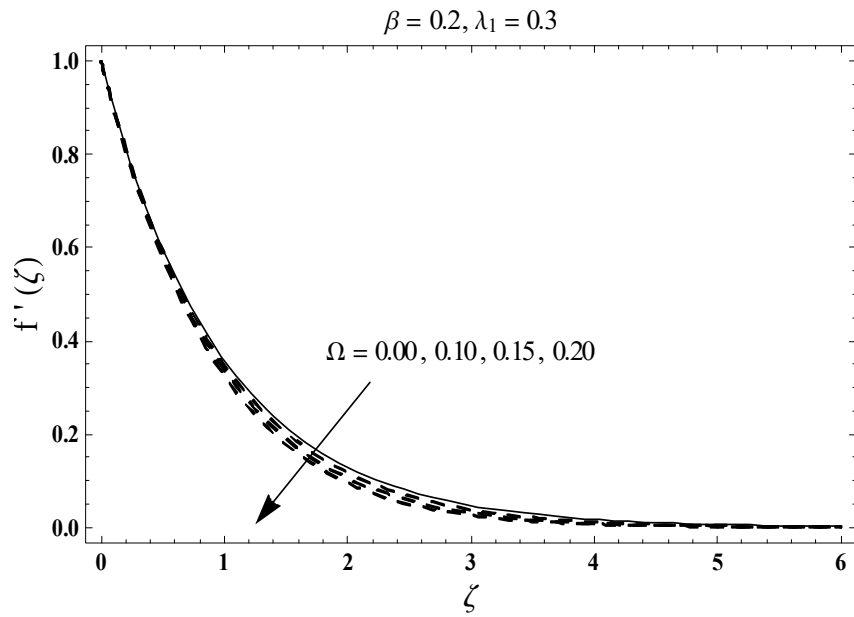
Figure 10.4 : Sketch for $f'(\zeta)$ against Ω.
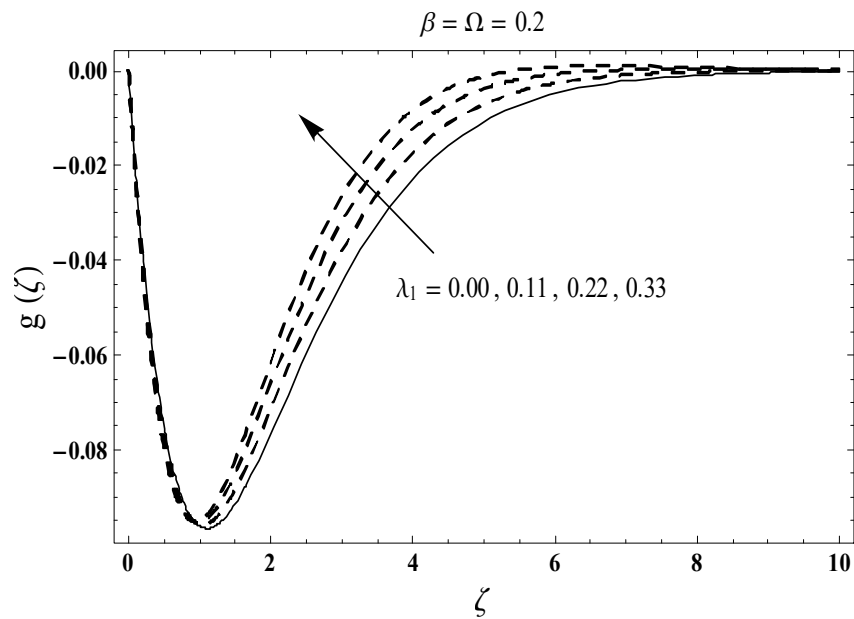
Figure 10.5 : Sketch for $g(\zeta)$ against λ_1.

$\lambda_1 = 0.3$, $\Omega = 0.2$

$\beta = 0.00, 0.07, 0.14, 0.21$
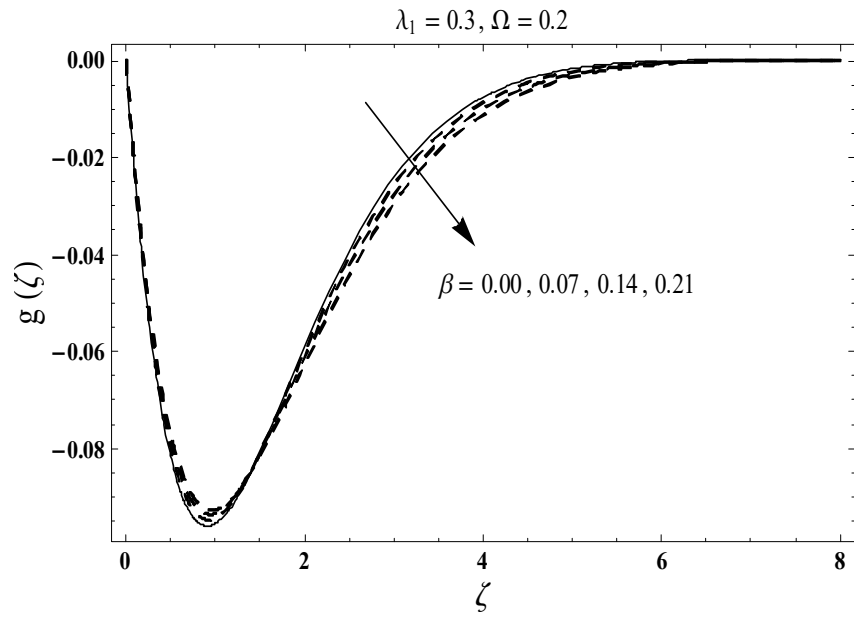
Figure 10.6 : Sketch for $g(\zeta)$ against β.

$\beta = 0.2$, $\lambda_1 = 0.3$

$\Omega = 0.00, 0.10, 0.15, 0.20$
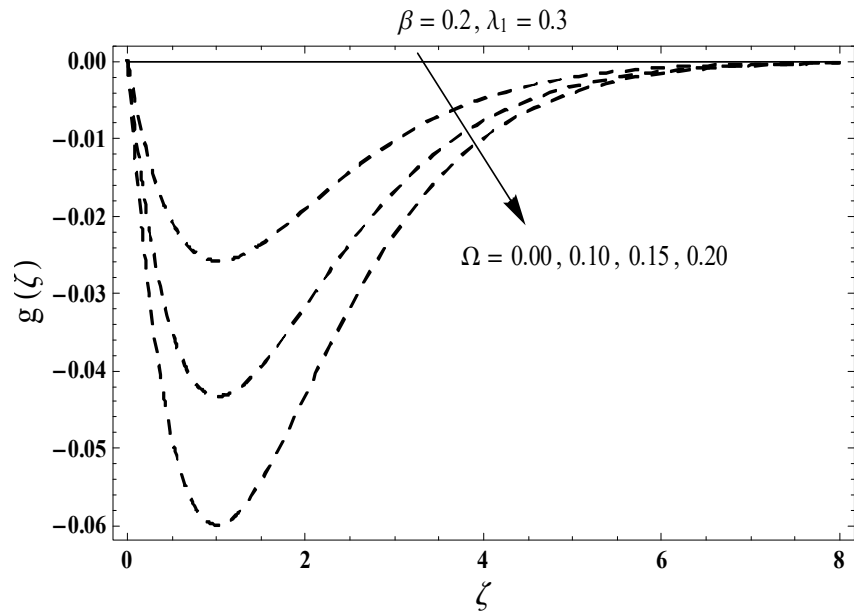
Figure 10.7 : Sketch for $g(\zeta)$ against Ω.

191

$\Omega = E = \beta = \sigma = \delta = 0.2, N_b = \gamma = 0.3, N_t = S_1 = 0.1, Sc = Pr = 1.0, n = 0.5$

$\lambda_1 = 0.0, 0.2, 0.4, 0.6$
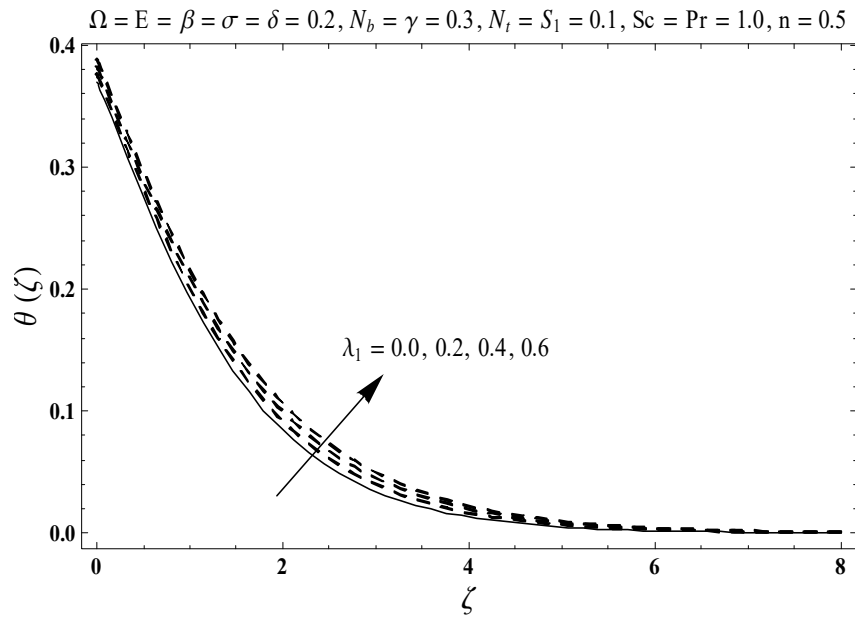
Figure 10.8 : Sketch for $\theta(\zeta)$ against λ_1.

$\Omega = E = \sigma = \delta = 0.2, N_b = \lambda_1 = \gamma = 0.3, N_t = S_1 = 0.1, Sc = Pr = 1.0, n = 0.5$

$\beta = 0.00, 0.25, 0.50, 0.75$

Figure 10.9 : Sketch for $\theta(\zeta)$ against β.

192

$E = \beta = \sigma = \delta = 0.2, N_b = \lambda_1 = \gamma = 0.3, N_t = S_1 = 0.1, \mathrm{Sc} = \mathrm{Pr} = 1.0, \mathrm{n} = 0.5$

$\Omega = 0.00, 0.25, 0.35, 0.45$

Figure 10.10 : Sketch for $\theta(\zeta)$ against Ω.

$\Omega = E = \beta = \sigma = \delta = 0.2, N_b = \lambda_1 = 0.3, N_t = S_1 = 0.1, \mathrm{Sc} = \mathrm{Pr} = 1.0, \mathrm{n} = 0.5$

$\gamma = 0.1, 0.4, 0.9, 1.3$

Figure 10.11 : Sketch for $\theta(\zeta)$ against γ.

193

$\Omega = E = \beta = \sigma = \delta = 0.2, N_b = \lambda_1 = \gamma = 0.3, N_t = 0.1, \text{Sc} = \text{Pr} = 1.0, \text{n} = 0.5$

$S_1 = 0.00, 0.12, 0.24, 0.36$

Figure 10.12 : Sketch for $\theta(\zeta)$ against $(S_1 > 0)$.

$\Omega = E = \beta = \sigma = \delta = 0.2, N_b = \lambda_1 = \gamma = 0.3, N_t = 0.1, \text{Sc} = \text{Pr} = 1.0, \text{n} = 0.5$

$S_1 = 0.00, -0.12, -0.24, -0.36$

Figure 10.13 : Sketch for $\theta(\zeta)$ against $(S_1 < 0)$.

194

$\Omega = E = \beta = \sigma = \delta = 0.2, N_b = \lambda_1 = \gamma = 0.3, N_t = S_1 = 0.1, Sc = 1.0, n = 0.5$

Pr = 0.8, 1.0, 1.2, 1.4

Figure 10.14 : Sketch for $\theta(\zeta)$ against Pr.

$\Omega = E = \beta = \sigma = \delta = 0.2, N_b = \lambda_1 = \gamma = 0.3, S_1 = 0.1, Sc = Pr = 1.0, n = 0.5$

$N_t = 0.1, 0.6, 1.2, 1.8$
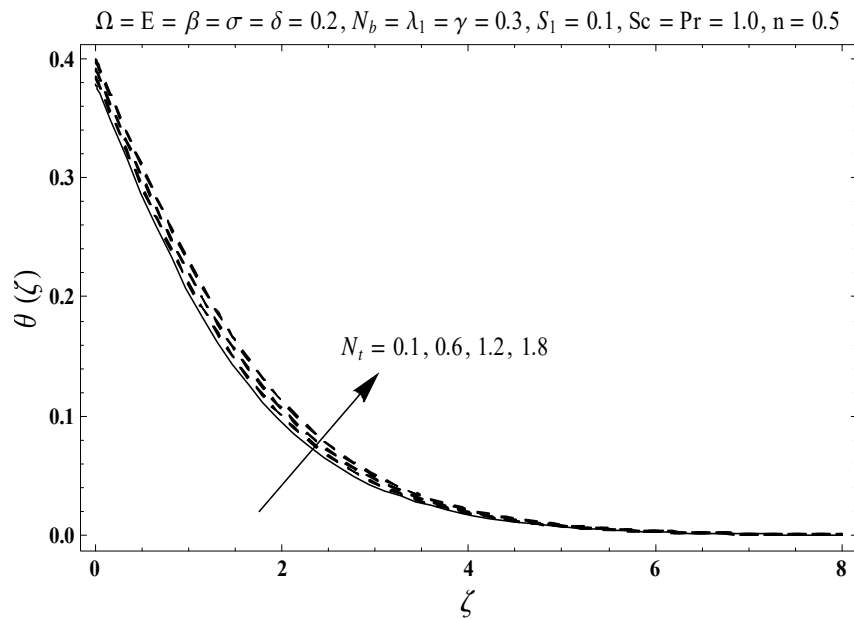
Figure 10.15 : Sketch for $\theta(\zeta)$ against N_t.

195
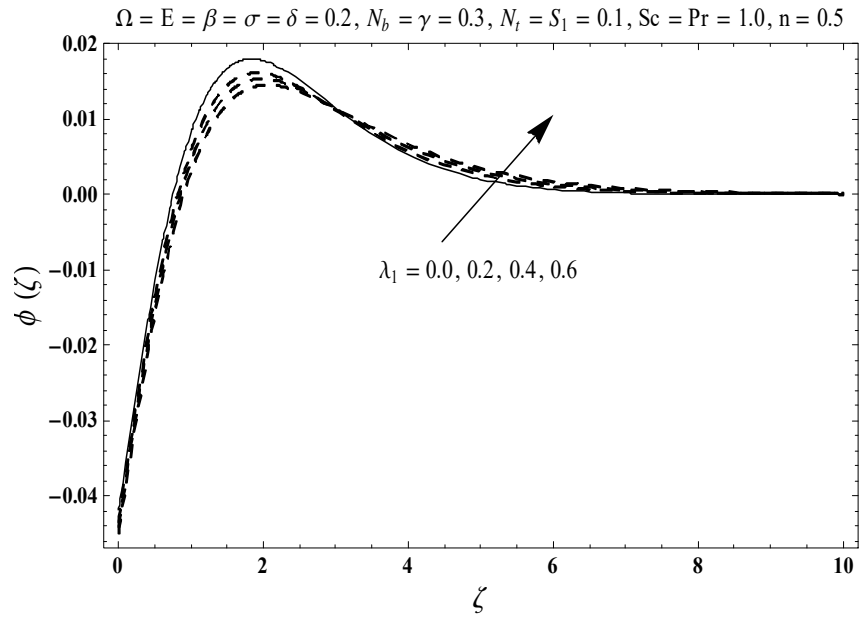
Figure 10.16 : Sketch for $\phi(\zeta)$ against λ_1.
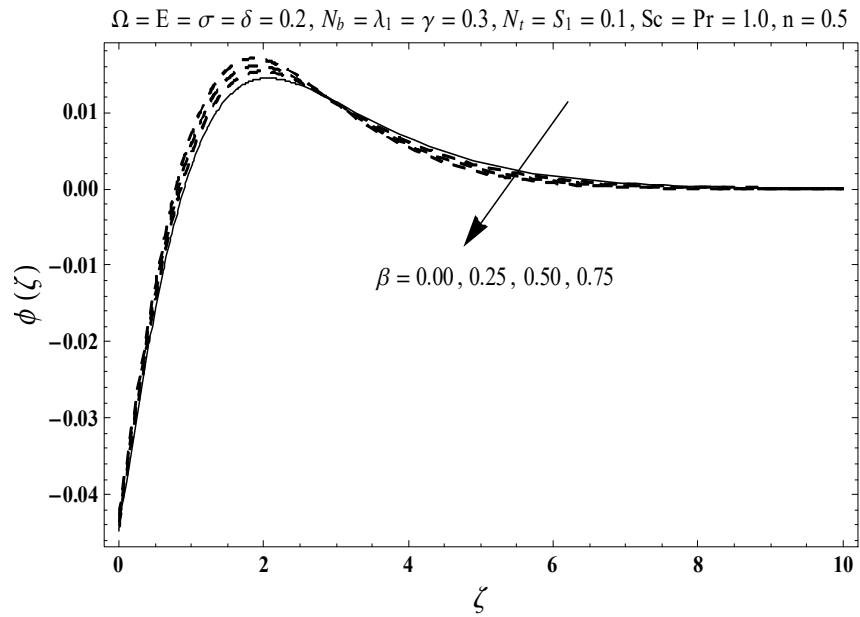
Figure 10.17 : Sketch for $\phi(\zeta)$ against β.
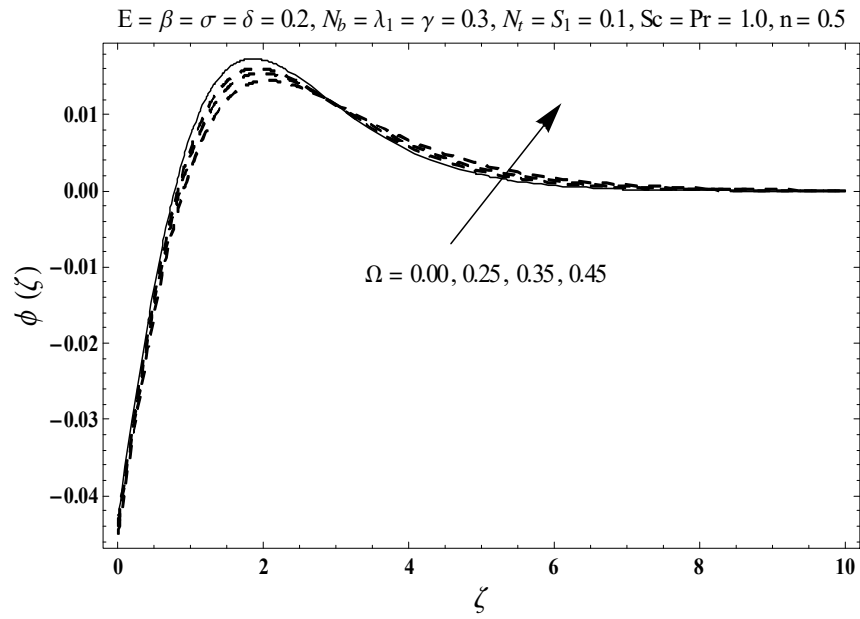
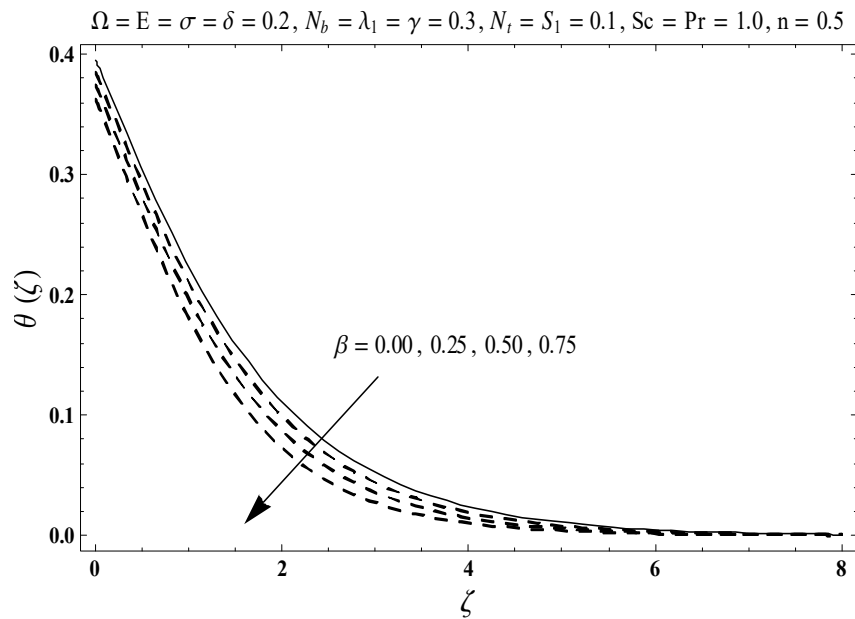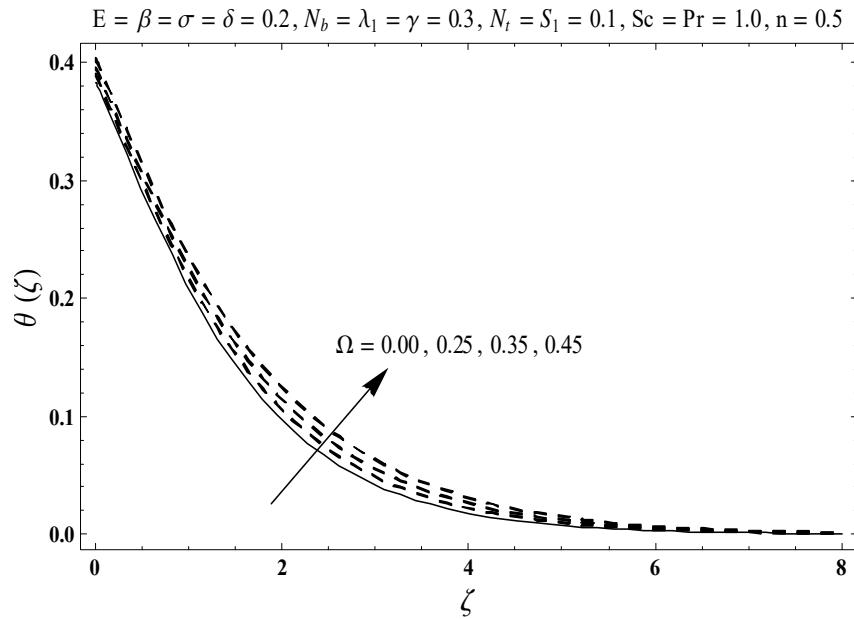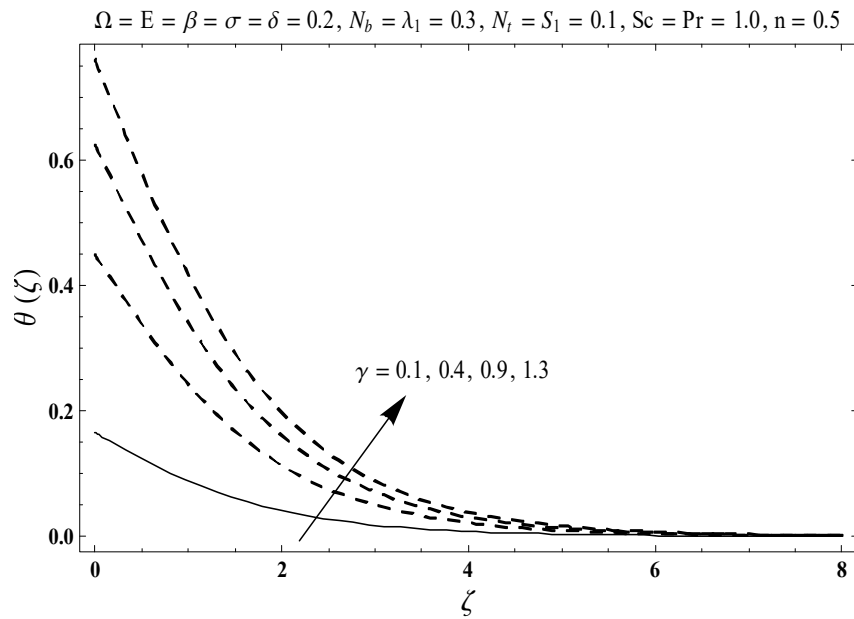Figure 10.18 : Sketch for $\phi(\zeta)$ against Ω.
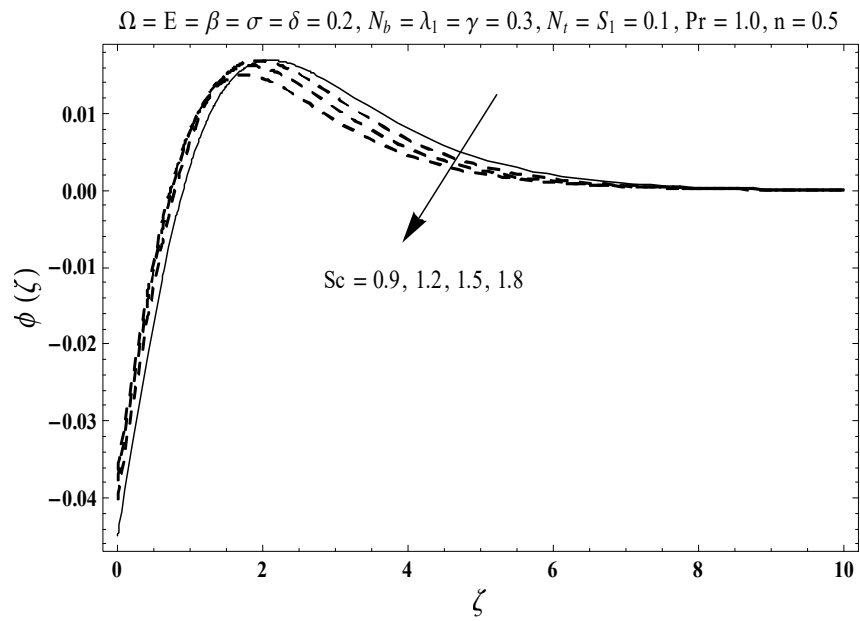
Figure 10.19 : Sketch for $\phi(\zeta)$ against Sc.
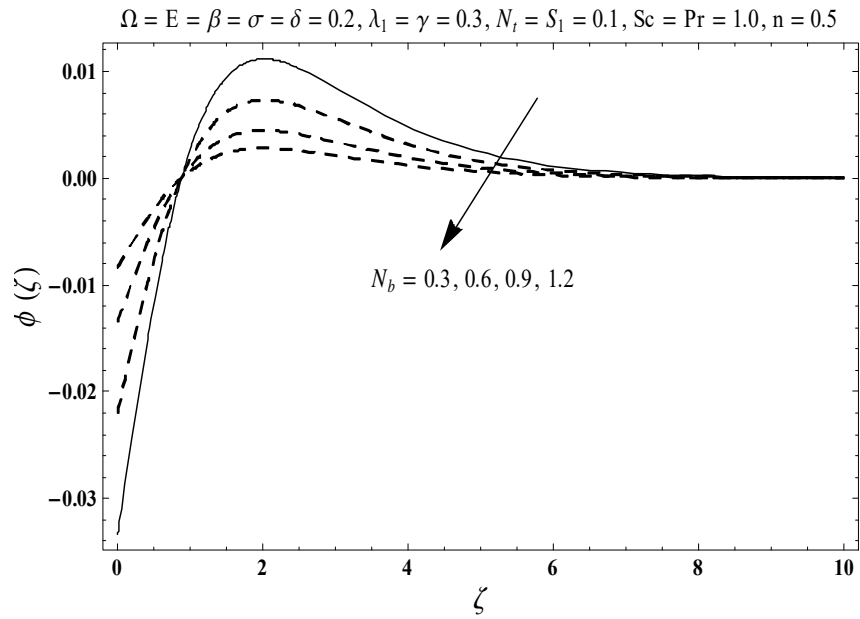
Figure 10.20 : Sketch for $\phi(\zeta)$ against N_b.
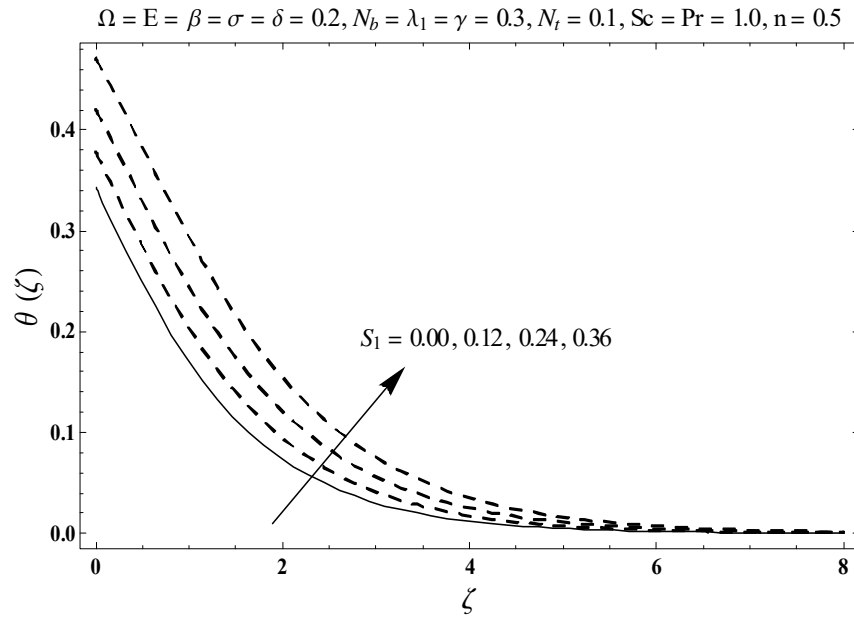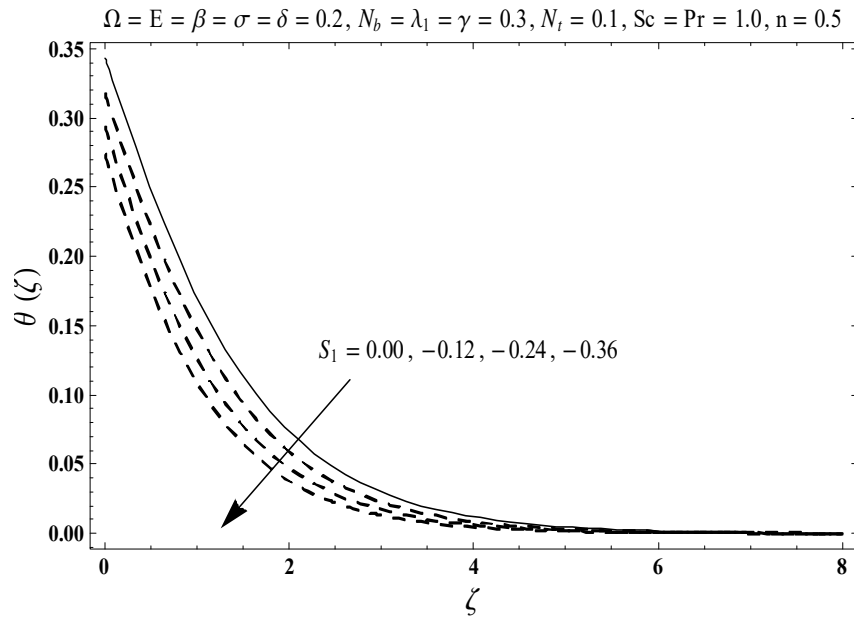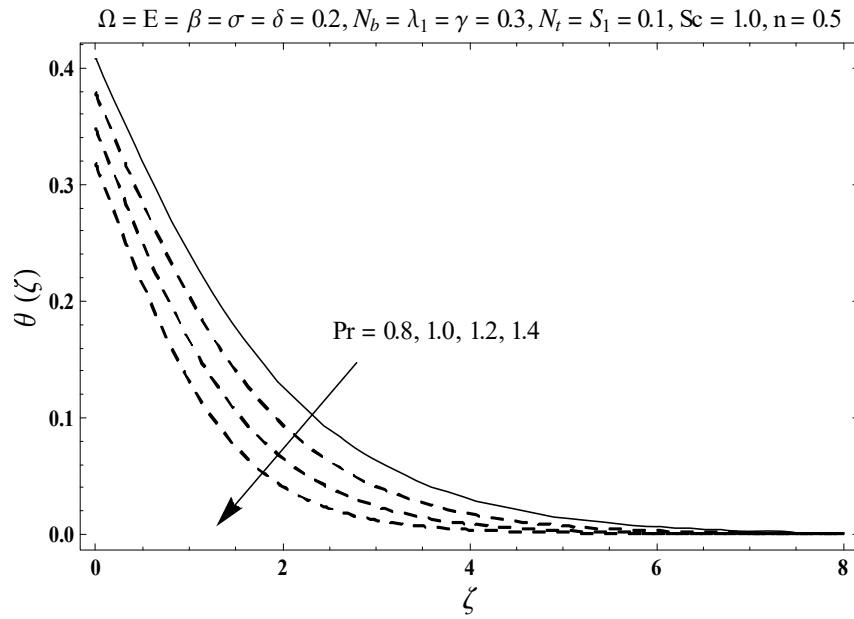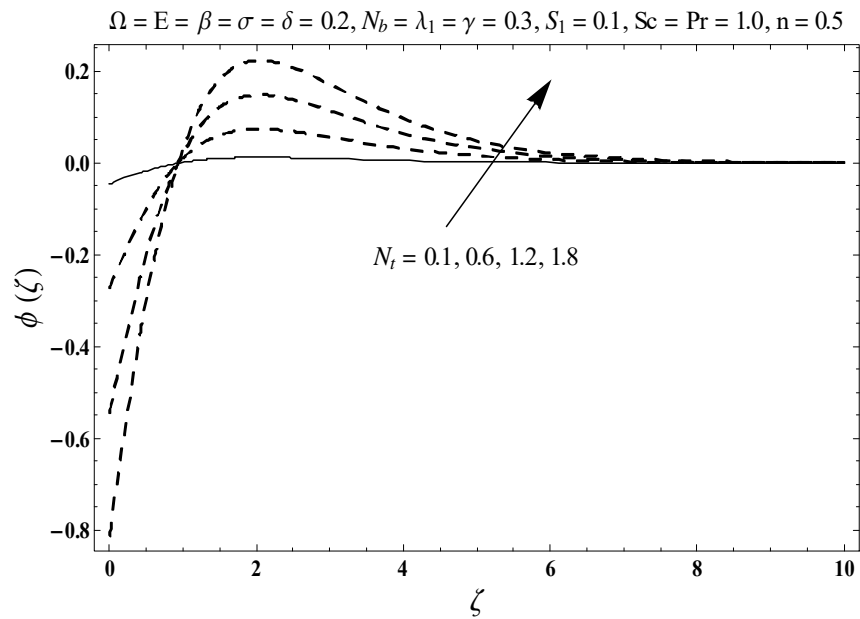

Figure 10.21 : Sketch for $\phi(\zeta)$ against N_t.

198

$\Omega = \beta = \sigma = \delta = 0.2,\, N_b = \lambda_1 = \gamma = 0.3,\, N_t = S_1 = 0.1,\, \text{Sc} = \text{Pr} = 1.0,\, n = 0.5$

$E = 0.1,\, 0.5,\, 1.0,\, 1.5$
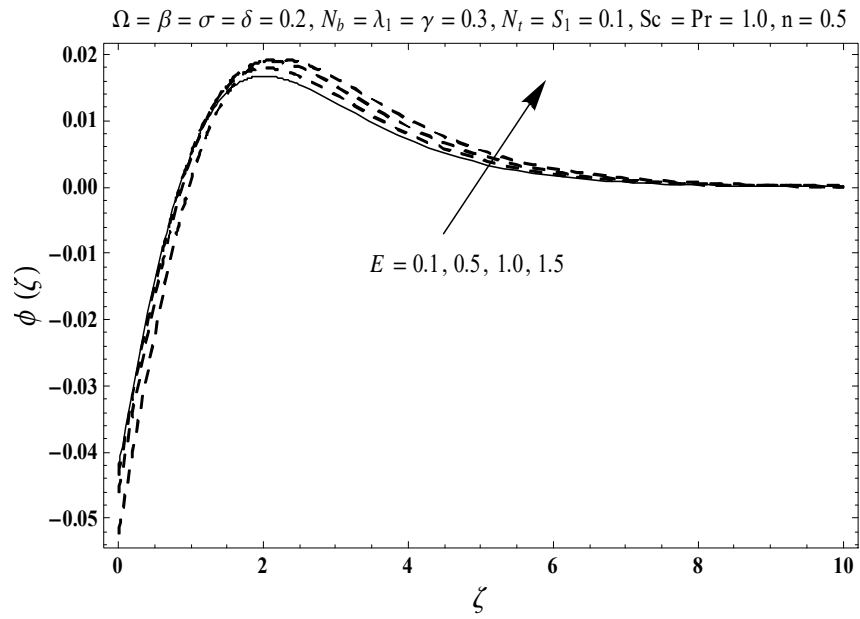
Figure 10.22 : Sketch for $\phi(\zeta)$ against E.

$\Omega = E = \beta = \delta = 0.2,\, N_b = \lambda_1 = \gamma = 0.3,\, N_t = S_1 = 0.1,\, \text{Sc} = \text{Pr} = 1.0,\, n = 0.5$

$\sigma = 0.4,\, 0.6,\, 0.8,\, 1.0$
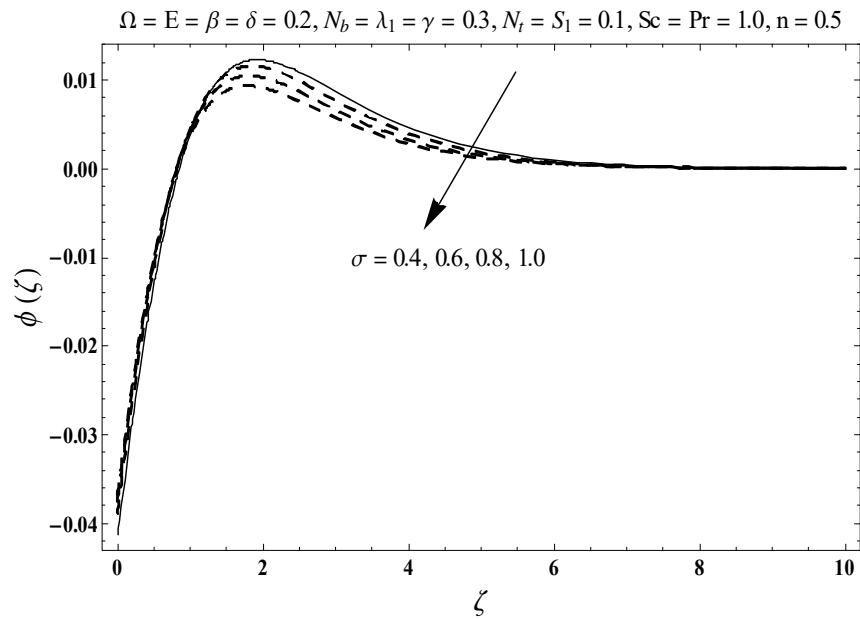
Figure 10.23 : Sketch for $\phi(\zeta)$ against σ.

199

$$\Omega = E = \beta = \sigma = 0.2, \, N_b = \lambda_1 = \gamma = 0.3, \, N_t = S_1 = 0.1, \, Sc = Pr = 1.0, \, n = 0.5$$

$$\delta = 0.0, \, 0.4, \, 0.8, \, 1.2$$
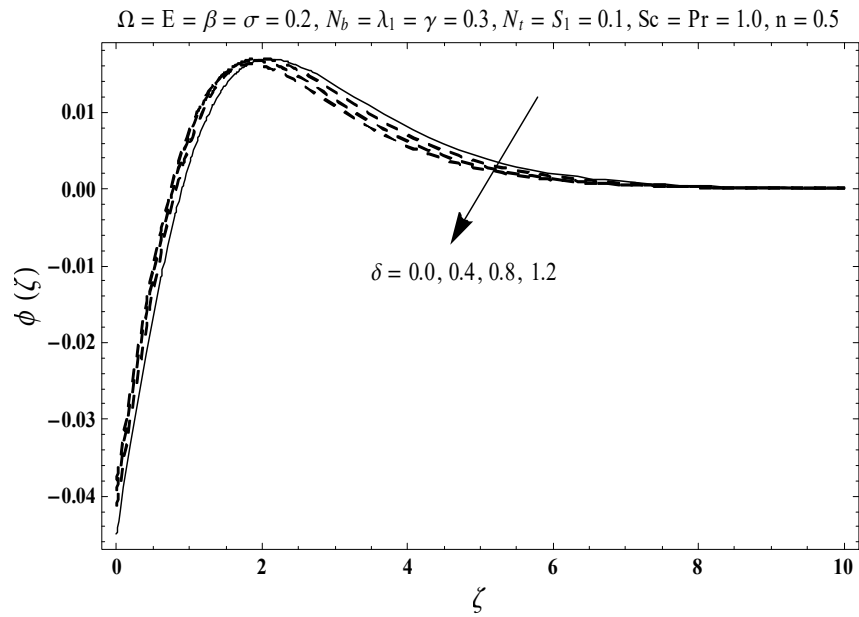
Figure 10.24 : Sketch for $\phi(\zeta)$ against δ.

$$\Omega = E = \beta = \sigma = \delta = 0.2, \, \lambda_1 = \gamma = 0.3, \, S_1 = 0.1, \, Sc = Pr = 1.0, \, n = 0.5$$

$$N_t = 0.1, \, 0.5, \, 1.0, \, 1.5$$
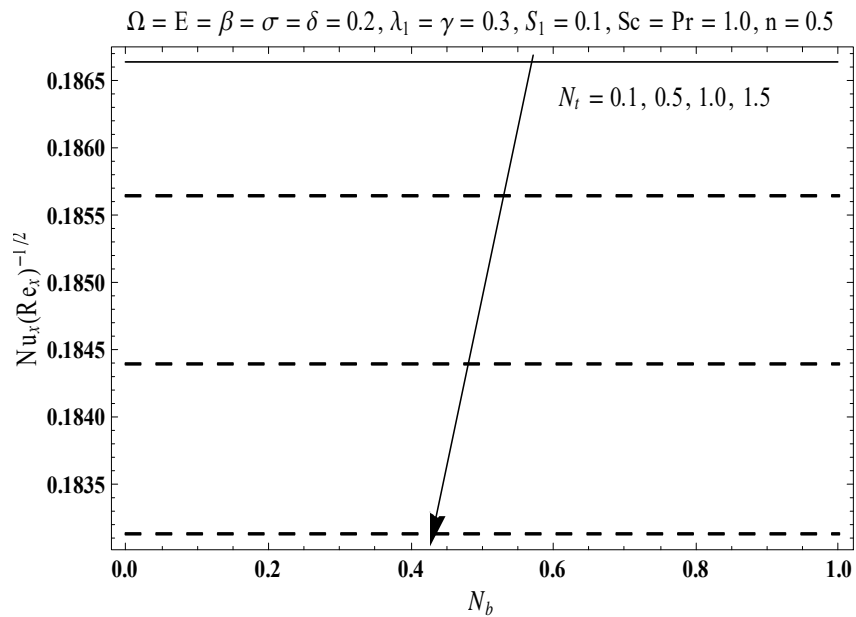
Figure 25 : Sketch for $Nu_x \, Re_x^{\,-1/2}$ against N_t and N_b.

10.5   Major observations

Key observations of present research are given below:

- Both velocities $f'(\zeta)$ and $g(\zeta)$ depict similar trend against stronger β and λ_1 while reverse situation is noticed against rotation parameter Ω.

- An increment in λ_1 and Ω corresponds to stronger temperature $\theta(\zeta)$ and nano-concentration $\phi(\zeta)$ profiles while weaker trend is noted via higher β.

- Temperature enhances via $(S_1 > 0)$ while decaying trend is observed against $(S_1 < 0)$.

- An enhancement of temperature $\theta(\zeta)$ is observed against γ.

- Temperature $\theta(\zeta)$ and nano-concentration $\phi(\zeta)$ have decaying trend via Pr and Sc.

- Higher thermophoresis parameter N_t for temperature $\theta(\zeta)$ and nano-concentration $\phi(\zeta)$ has similar trends while nano-concentration $\phi(\zeta)$ decreases for higher Brownian diffusion parameter N_b.

- Higher E yield stronger $\phi(\zeta)$ while decaying situation is seen for σ and δ.

- Heat transfer rate decays via higher N_t while constant behavior is noted for N_b.

Bibliography

[1] S.U.S. Choi, Enhancing thermal conductivity of fluids with nanoparticles, USA, ASME, FED 231/MD, 66 (1995) 99-105.

[2] J. Buongiorno, Convective transport in nanofluids, ASME J. Heat Transfer, 128 (2006) 240-250.

[3] A.J. Chamkha, A.M. Aly and M.A. Mansour, Similarity solution for unsteady heat and mass transfer from a stretching surface embedded in a porous medium with suction/injection and chemical reaction effects, Chem. Engrg. Comm., 197 (2010) 846-858.

[4] M. Turkyilmazoglu, Exact analytical solutions for heat and mass transfer of MHD slip flow in nanofluids, Chem. Eng. Sci., 84 (2012) 182-187.

[5] M.M. Rashidi, N. Freidoonimehr, A. Hosseini, O.A. Bég and T.K. Hung, Homotopy simulation of nanofluid dynamics from a non-linearly stretching isothermal permeable sheet with transpiration, Meccanica, 49 (2014) 469-482.

[6] T. Hayat, A. Aziz, T. Muhammad and B. Ahmed, Influence of magnetic field in three dimensional flow of couple stress nanofluid over a nonlinearly stretching surface with convective condition, Plos One, 10 (2015) e0145332.

[7] C.S.K. Raju, N. Sandeep, M.J. Babu and V. Sugunamma, Dual solutions for three-dimensional MHD flow of a nanofluid over a nonlinearly permeable stretching sheet, Alex. Engrg. J., 55 (2016) 151-162.

[8] T. Hayat, A. Aziz, T. Muhammad and A. Alsaedi, On magnetohydrodynamic three dimensional flow of nanofluid over a convectively heated nonlinear stretching surface, Int. J. Heat Mass Transfer, 100 (2016) 566-572.

[9] M.K. Nayak, N.S. Akbar, V.S. Pandey, Z.H. Khan and D. Tripathi, 3D free convective MHD flow of nanofluid over permeable linear stretching sheet with thermal radiation, Powder Tech., 315 (2017) 205-215.

[10] T. Hayat, A. Aziz, T. Muhammad and A. Alsaedi, On model for flow of Burgers nanofluid with Cattaneo-Christov double diffusion, Chin. J. Phys., 55 (2017) 916-929.

[11] B. Mahanthesh, B.J. Gireesha, R.S.R. Gorla and O.D. Makinde, Magnetohydrodynamic three-dimensional flow of nanofluids with slip and thermal radiation over a nonlinear stretching sheet: a numerical study, Neural Comp. Appl., 30 (2018) 1557-1567.

[12] T. Hayat, A. Aziz, T. Muhammad and A. Alsaedi, An optimal analysis for Darcy-Forchheimer 3D flow of Carreau nanofluid with convectively heated surface, Results Phys., 9 (2018) 598-608.

[13] M. Sheikholeslami, Numerical approach for MHD Al2O3-water nanofluid transportation inside a permeable medium using innovative computer method, Comp. Meth. Appl. Mech. Engrg., 344 (2019) 306-318.

[14] A. Ali, K. Shehzadi, M. Sulaiman and S. Asghar, Heat and mass transfer analysis of 3D Maxwell nanofluid over an exponentially stretching surface, Phys. Scr., 94 (2019) 065206.

[15] D. Yadav, A. Wakif, Z. Boulahia and R. Sehaqui, Numerical examination of the thermoelectro-hydrodynamic convection in a horizontal dielectric nanofluid layer using the power series method, J. Nanofluids, 8 (2019) 117-131.

[16] J.H. Merkin, A model for isothermal homogeneous-heterogeneous reactions in boundary layer flow, Math. Comp. Modell., 24 (1996) 125-136.

[17] M.A. Chaudhary and J.H. Merkin, A simple isothermal model for homogeneous-heterogeneous reactions in boundary-layer flow. II Different diffusivities for reactant and autocatalyst, Fluid Dyn. Res., 16 (1995) 335-359.

[18] P.K. Kameswaran, S. Shaw, P. Sibanda and P.V.S.N. Murthy, Homogeneous-heterogeneous reactions in a nanofluid flow due to porous stretching sheet, Int. J. Heat Mass Transfer, 57 (2013) 465-472.

[19] M. Imtiaz, T. Hayat, A. Alsaedi and A. Hobiny, Homogeneous-heterogeneous reactions in MHD flow due to an unsteady curved stretching surface, J. Mol. Liq., 221 (2016) 245-253.

[20] T. Hayat, T. Ayub, T. Muhammad and A. Alsaedi, Three-dimensional flow with Cattaneo-Christov double diffusion and homogeneous-heterogeneous reactions, Results Phys., 7 (2017) 2812 - 2820.

[21] M.I. Khan, T. Hayat, M.I. Khan and A. Alsaedi, A modified homogeneous-heterogeneous reactions for MHD stagnation flow with viscous dissipation and Joule heating, Int. J. Heat Mass Transf., 113 (2017) 310-317.

[22] T. Hayat, A. Aziz, T. Muhammad and A. Alsaedi, An optimal analysis for Darcy-Forchheimer 3D flow of nanofluid with convective condition and homogeneous-heterogeneous reactions, Phys. Lett. A, 382 (2018) 2846-2855.

[23] A. Raees, R.Z. Wang and H. Xu, A homogeneous-heterogeneous model for mixed convection in gravity-driven film flow of nanofluids, Int. J. Com. Heat Mass Transf., 95 (2018) 19-24.

[24] A.K. Alzahrani, Darcy-Forchheimer 3D flow of carbon nanotubes with homogeneous and heterogeneous reactions, Phys. Lett. A, 382 (2018) 2787-2793.

[25] T. Hayat, K. Muhammad, A. Alsaedi and S. Asghar, Numerical study for melting heat transfer and homogeneous-heterogeneous reactions in flow involving carbon nanotubes, Results Phys., 8 (2018) 415-421.

[26] F. Almutairi, S.M. Khaled and A. Ebaid, MHD flow of nanofluid with homogeneous-heterogeneous reactions in a porous medium under the influence of second-order velocity slip, Mathematics, 7 (2019) 220.

[27] C.Y. Wang, Stretching a surface in a rotating fluid, Z. Angew. Math. Phys., 39 (1988) 177-185.

[28] T. Javed, M. Sajid, Z. Abbas and N. Ali, Non-similar solution for rotating flow over an exponentially stretching surface, Int. J. Numer. Methods Heat Fluid Flow, 21 (2011) 903-908.

[29] H. Rosali, A. Ishak, R. Nazar and I. Pop, Rotating flow over an exponentially shrinking sheet with suction, J. Mol. Liquids, 211 (2015) 965-969.

[30] M. Mustafa, T. Hayat and A. Alsaedi, Rotating flow of Maxwell fluid with variable thermal conductivity: An application to non-Fourier heat flux theory, Int. J. Heat Mass Transfer, 106 (2017) 142-148.

[31] N. Maqsood, M. Mustafa and J.A. Khan, Numerical tackling for viscoelastic fluid flow in rotating frame considering homogeneous-heterogeneous reactions, Results Phys., 7 (2017) 3475-3481.

[32] T. Hayat, A. Aziz, T. Muhammad and A. Alsaedi, Darcy-Forchheimer flow of nanofluid in a rotating frame, Int. J. Numer. Meth. Heat Fluid Flow, 28 (2018) 2895-2915.

[33] R. Jusoh, R. Nazar and I. Pop, Magnetohydrodynamic rotating flow and heat transfer of ferrofluid due to an exponentially permeable stretching/shrinking sheet, J. Magn. Magn. Mater., 465 (2018) 365-374.

[34] T. Hayat, A. Aziz, T. Muhammad and A. Alsaedi, Numerical simulation for Darcy-Forchheimer 3D rotating flow subject to binary chemical reaction and Arrhenius activation energy, J. Cent. South Univ., 26 (2019) 1250-1259.

[35] T. Hayat, S. Nadeem and A.U. Khan, Aspects of 3D rotating hybrid CNT flow for a convective exponentially stretched surface, Appl. Nanosci., (2019) https://doi.org/10.1007/s13204-019-01036-y.

[36] A. Aziz, T. Muhammad, A. Alsaedi and T. Hayat, An optimal study for 3D rotating flow of Oldroyd-B nanofluid with convectively heated surface, J. Braz. Soc. Mech. Sci. Engrg., 41 (2019) 236.

[37] S. Rashid, M.I. Khan, T. Hayat, M. Ayub and A. Alsaedi, Numerical treatment for rotating Maxwell nanomaterial flow with Arrhenius energy, Appl. Nanosci., (2019) https://doi.org/10.1007/s13204-019-00998-3.

[38] T. Hayat, A. Aziz, T. Muhammad and A. Alsaedi, Numerical simulation for Darcy-Forchheimer three-dimensional rotating flow of nanofluid with prescribed heat and mass flux conditions, J. Therm. Anal. Calorim., 136 (2019) 2087-2095.

[39] M.V. Krishna and A.J. Chamkha, Hall and ion slip effects on MHD rotating boundary layer flow of nanofluid past an infinite vertical plate embedded in a porous medium, Results Phys., 15 (2019) 102652.

[40] A. Bejan, A study of entropy generation in fundamental convective heat transfer, J. Heat Transf., 101 (1979) 718-725.

[41] A. Bejan, Second law analysis in heat transfer, Energy, 5 (1980) 720-732.

[42] A. Noghrehabadi, M.R. Saffarian, R. Pourrajab and M. Ghalambaz, Entropy analysis for nanofluid flow over a stretching sheet in the presence of heat generation/absorption and partial slip, J. Mech. Sci. Tech., 27 (2013) 927-937.

[43] S. Rehman, R.U. Haq, Z.H. Khan and C. Lee, Entropy generation analysis for non-Newtonian nanofluid with zero normal flux of nanoparticles at the stretching surface, J. Taiwan Inst. Chem. Eng., 63 (2016) 226-235.

[44] M.M. Bhatti, T. Abbas and M.M. Rashidi, Entropy generation as a practical tool of optimisation for non-Newtonian nanofluid flow through a permeable stretching surface using SLM, J. Comput. Des. Eng., 4 (2017) 21-28.

[45] H. Sithole, H. Mondal and P. Sibanda, Entropy generation in a second grade magneto-hydrodynamic nanofluid flow over a convectively heated stretching sheet with nonlinear thermal radiation and viscous dissipation, Results Phys., 9 (2018) 1077-1085.

[46] S. Alharbi, A. Dawar, Z. Shah, W. Khan, M. Idrees, S. Islam and I. Khan, Entropy generation in MHD Eyring-Powell fluid flow over an unsteady oscillatory porous stretching

surface under the impact of thermal radiation and heat source/sink. Appl. Sci., 8 (2018) 2588.

[47] S.M. Seyyedi, A.S. Dogonchi, M.H. Tilehnoee, Z. Asghar, M.Waqas and D.D.Ganji, A computational framework for natural convective hydromagnetic flow via inclined cavity: An analysis subjected to entropy generation, J. Mol. Liq., 287 (2019) 110863.

[48] M. Rashid, M.I. Khan, T. Hayat, M.I. Khan and A. Alsaedi, Entropy generation in flow of ferromagnetic liquid with nonlinear radiation and slip condition, J. Mol. Liq., 276 (2019) 441-652.

[49] T. Hayat, R. Riaz, A. Aziz and A. Alsaedi, Analysis of entropy generation for MHD flow of third grade nanofluid over a nonlinear stretching surface embedded in a porous medium, Phys. Scr., 94 (2019) 125703.

[50] A.R. Bestman, Natural convection boundary layer with suction and mass transfer in a porous medium, Int. J. Energy Res., 14 (1990) 389-396.

[51] O.D. Makinde and P.O. Olanrewaju, Unsteady mixed convection with Soret and Dufour effects past a porous plate moving through a binary mixture of chemically reacting fluid, Chem. Engrg. Comm., 198 (2011) 920-938.

[52] K.A. Maleque, Effects of exothermic/endothermic chemical reactions with Arrhenius activation energy on MHD free convection and mass transfer flow in presence of thermal radiation, J. Thermodyn., 2013 (2013) 692516.

[53] D. Lu, M. Ramzan, S. Ahmad, J.D. Chung and U. Farooq, Upshot of binary chemical reaction and activation energy on carbon nanotubes with Cattaneo-Christov heat flux and buoyancy effects, Phys. Fluids, 29 (2017) 123103.

[54] A. Zaib, M.M. Rashidi, A. Chamkha,and K. Bhattacharyya, Numerical solution of second law analysis for MHD Casson nanofluid past a wedge with activation energy and binary chemical reaction, Int. J. Numer. Meth. Heat & Fluid Flow, 27 (2017) 2816-2834.

[55] S. Anuradha and K. Sasikala, MHD free convective flow of a nanofluid over a permeable shrinking sheet with binary chemical reaction and activation energy, Int.J. Engng. Sci. Invent., 7 (2018) 22-30.

[56] G.K. Ramesh, S.A. Shehzad, T. Hayat and A. Alsaedi, Activation energy and chemical reaction in Maxwell magneto-nanoliquid with passive control of nanoparticle volume fraction, J. Braz. Soc. Mech. Sci. Engrg., 40 (2018) 422.

[57] T. Hayat, A. Aziz, T. Muhammad and A. Alsaedi, Effects of binary chemical reaction and Arrhenius activation energy in Darcy-Forchheimer three-dimensional flow of nanofluid subject to rotating frame, J. Ther. Anal. Calor., 136 (2019) 1769-1779.

[58] S.R.R. Reddy, P.B.A. Reddy and K. Bhattacharyya, Effect of nonlinear thermal radiation on 3D magneto slip flow of Eyring-Powell nanofluid flow over a slendering sheet with binary chemical reaction and Arrhenius activation energy, Adv. Pow. Tech., 30 (2019) 3203-3213.

[59] S. Ahmad, M. Farooq, N.A. Mir, A. Anjum and M. Javed, Magnetohydrodynamic flow of squeezed fluid with binary chemical reaction and activation energy, J. Cent. South Univ., 26 (2019) 1362-1373.

[60] H. Darcy, Les Fontaines Publiques De La Ville De Dijon, Victor Dalmont, Paris, (1856).

[61] P. Forchheimer, Wasserbewegung durch boden, Zeitschrift Ver. D. Ing., 45 (1901) 1782-1788.

[62] M. Muskat, The flow of homogeneous fluids through porous media, Edwards, MI, (1946).

[63] M.A. Seddeek, Influence of viscous dissipation and thermophoresis on Darcy-Forchheimer mixed convection in a fluid saturated porous media, J. Colloid Interface Sci., 293 (2006) 137-142.

[64] D. Pal and H. Mondal, Hydromagnetic convective diffusion of species in Darcy-Forchheimer porous medium with non-uniform heat source/sink and variable viscosity, Int. J. Commun. Heat Mass Transf., 39 (2012) 913-917.

[65] M.A. Sadiq and T. Hayat, Darcy-Forchheimer flow of magneto Maxwell liquid bounded by convectively heated sheet, Results Phys.,6 (2016) 884-890.

[66] S.A. Shehzad, F.M. Abbasi, T. Hayat and A. Alsaedi, Cattaneo-Christov heat flux model for Darcy-Forchheimer flow of an Oldroyd-B fluid with variable conductivity and nonlinear convection, J. Mol. Liq., 224 (2016) 274-278.

[67] S.A. Bakar, N.M. Arifin, R. Nazar, F.M. Ali and I. Pop, Forced convection boundary layer stagnation-point flow in Darcy-Forchheimer porous medium past a shrinking sheet, Front. Heat Mass Transf., 7 (2016) 38.

[68] T. Hayat, T. Muhammad, S. Al-Mezal and S.J. Liao, Darcy-Forchheimer flow with variable thermal conductivity and Cattaneo-Christov heat flux, Int. J. Numer. Methods Heat Fluid Flow., 26 (2016) 2355-2369.

[69] T. Hayat, F. Haider, T. Muhammad and A. Alsaedi, On Darcy-Forchheimer flow of viscoelastic nanofluids: A comparative study, J. Mol. Liq., 233 (2017) 278-287.

[70] J.C. Umavathi, O. Ojjela and K. Vajravelu, Numerical analysis of natural convective flow and heat transfer of nanofluids in a vertical rectangular duct using Darcy-Forchheimer-Brinkman model, Int. J. Thermal Sci., 111 (2017) 511-524.

[71] T. Muhammad, A. Alsaedi, S.A. Shehzad and T. Hayat, A revised model for Darcy-Forchheimer flow of Maxwell nanofluid subject to convective boundary condition, Chinese J. Phys., 55 (2017) 963-976.

[72] M. Sheikholeslami, Influence of Lorentz forces on nanofluid flow in a porous cavity by means of Non-Darcy model, Eng. Comput., 34 (2017) 2651-2667.

[73] T. Muhammad, A. Alsaedi, T. Hayat and S.A. Shehzad, A revised model for Darcy-Forchheimer three-dimensional flow of nanofluid subject to convective boundary condition, Results Phys., 7 (2017) 2791-2797.

[74] T. Hayat, A. Aziz, T. Muhammad and A. Alsaedi, Darcy-Forchheimer three-dimensional flow of Williamson nanofluid over a convectively heated nonlinear stretching surface, Commun. Theor. Phys., 68 (2017) 387-394.

209

[75] T. Hayat, F. Haider, T. Muhammad and A. Alsaedi, Darcy-Forchheimer squeezed flow of carbon nanotubes with thermal radiation, J. Phys. Chem. Solids, 120 (2018) 79-86.

[76] T. Hayat, K. Rafique, T. Muhammad, A. Alsaedi and M. Ayub, Carbon nanotubes significance in Darcy-Forchheimer flow, Results Phys., 8 (2018) 26-33.

[77] N.V. Ganesh, A.K.A. Hakeem and B. Ganga, Darcy-Forchheimer flow of hydromagnetic nanofluid over a stretching/shrinking sheet in a thermally stratified porous medium with second order slip, viscous and Ohmic dissipations effects, Ain Shams Eng. J., 9 (2018) 939-951.

[78] T. Hayat, K. Muhammad, A. Alsaedi and M. Farooq, Features of Darcy-Forchheimer flow of carbon nanofluid in frame of chemical species with numerical significance, J. Cent. South Uni., 26 (2019) 1260-1270.

[79] Z. Shah, E.O. Alzahrani, A. Dawar, A. Ullah and I.U. Khan, Influence of Cattaneo-Christov model on Darcy-Forchheimer flow of micropolar ferrofluid over a stretching/shrinking sheet, Int. J. Commu. Heat Mass Transf., 110 (2020) 104385.

[80] R.S. Saif, T. Muhammad and H. Sadia, Significance of inclined MHD in Darcy-Forchheimer flow with variable porosity and thermal conductivity, Phy. A: Stat. Mech. Appl., (2020) In press.

[81] W. Tan, W. Pan and M. Xu, A note on unsteady flows of a viscoelastic fluid with the fractional Maxwell model between two parallel plates, Int. J. Non-Linear Mech., 38 (2003) 645-650.

[82] U. Farooq, D. Lu, S. Munir, M. Ramzan, M. Suleman and S. Hussain, MHD flow of Maxwell fluid with nanomaterials due to an exponentially stretching surface, Scientific Rep., 9 (2019) 7312.

[83] R. K. Bhatnagar, G. Gupta and K.R. Rajagopal, Flow of an Oldroyd-B fluid due to a stretching sheet in the presence of a free stream velocity, Int. J. Non-Linear Mech., 30 (1995) 391-405.

[84] Y. Zhang, M. Zhang and Y. Bai, Flow and heat transfer of an Oldroyd-B nanofluid thin film over an unsteady stretching sheet, J. Mol. Liq., 220 (2016) 665-670.

[85] L.B. Bergstrom, Transient growth of small disturbances in a Jeffrey fluid flowing through a pipe, Fluid Dynamics Research, 32 (2003) 29-44.

[86] N.G. Rudraswamy, K.G. Kumar, B.J. Gireesha and R.S.R Gorla, Combined effects of Joule heating and viscous dissipation on hydromagnetic 3D flow of a Jeffrey nanofluid, J. Nanofluids, 6 (2017) 300-310.

[87] S.J. Liao, An optimal homotopy-analysis approach for strongly nonlinear differential equations, Commun. Nonlinear Sci. Numer. Simulat., 15 (2010) 2003-2016.

[88] M. Dehghan, J. Manafian and A. Saadatmandi, Solving nonlinear fractional partial differential equations using the homotopy analysis method, Numer. Meth. Partial Diff. Eq., 26 (2010) 448-479.

[89] Y. Abd Elmaboud, Kh.S. Mekheimer and M.S. Mohamed, Series solution of a natural convection flow for a Carreau fluid in a vertical channel with peristalsis, J. Hydrodynamics, Ser. B, 27 (2015) 969-979.

[90] T. Hayat, Z. Hussain, T. Muhammad and A. Alsaedi, Effects of homogeneous and heterogeneous reactions in flow of nanofluids over a nonlinear stretching surface with variable surface thickness, J. Mol. Liq., 221 (2016) 1121-1127.

[91] M. Awais, S.E. Awan, K. Iqbal, Z.A Khan and M.A.Z. Raja, Hydromagnetic mixed convective flow over a wall with variable thickness and Cattaneo-Christov heat flux model: OHAM analysis, Results Phys., 8 (2018) 621-627.

[92] A. Kumar, R. Tripathi, R. Singh and G.S. Seth, Three-dimensional magnetohydrodynamic flow of micropolar CNT-based nanofluid through a horizontal rotating channel: OHAM analysis, Ind. J. Phys., (2019) https://doi.org/10.1007/s12648-019-01460-4.

[93] M.Z. Ullah, M. Alghamdi and A.S. Alshomrani, Significance of heat generation/absorption in three-dimensional flow of Prandtl nanofluid with convectively heated surface, Phys. Scr., 95 (2020) 015703.

[94] M. Sheikholeslami, S. Abelman and D.D. Ganji, Numerical simulation of MHD nanofluid flow and heat transfer considering viscous dissipation, Int. J. Heat Mass Trans., 79 (2014) 212-222.

[95] R. Mohebbi and M.M. Rashidi, Numerical simulation of natural convection heat transfer of a nanofluid in an L-shaped enclosure with a heating obstacle, J. Taiwan Inst. Chem. Eng., 72 (2017) 70-84.

[96] A. Aziz, A. Alsaedi, T. Muhammad and T. Hayat, Numerical study for heat generation/absorption in flow of nanofluid by a rotating disk, Results Phys., 8 (2018) 785-792.

[97] T. Hayat, F. Shah, A. Alsaedi, M. Waqas, Numerical simulation for magneto nanofluid flow through a porous space with melting heat transfer, Microgravity Sci. Technol. 30 (2018) 265-275.

[98] M.R. Tavakoli, O.A. Akbar, A. Mohammadian, E. Khodabandeh and F. Pourfattah, Numerical study of mixed convection heat transfer inside a vertical microchannel with two-phase approach, J. Therm. Anal. Calori., 135 (2019) 1119-1134.

[99] T. Hayat, F. Haider, T. Muhammad and A. Alsaedi, Numerical treatment for Darcy-Forchheimer flow of carbon nanotubes due to an exponentially stretching curved surface, J. Cent. South Uni., 26 (2019) 865-872.

[100] T.K. Nguyen, M. Usman, M. Sheikholeslami, R.U. Haq, A. Shafee, A.K. Jilani and I.Tlili, Numerical analysis of MHD flow and nanoparticle migration within a permeable space containing non-equilibrium model, Phy. A: Stat. Mech. Appl., 537 (2020) 122459.